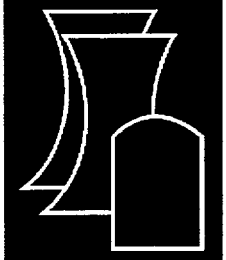

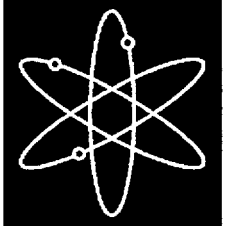

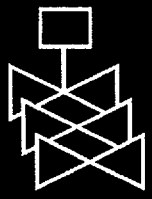

Assessment of Modernization and Integration of BWR Components and Spatial Kinetics in the TRAC-M, Version 3690, Code

U.S. Nuclear Regulatory Commission
Office of Nuclear Regulatory Research
Washington, DC 20555-0001

Assessment of Modernization and Integration of BWR Components and Spatial Kinetics in the TRAC-M, Version 3690, Code

Manuscript Completed: September 2001
Date Published: December 2001

Principal Author: F. Odar (NRC)*

Contributing Authors:
J. Uhle, S. Lu (NRC)*
J. F. Dearing (LANL)**
B. Aktas, R. Shumway, S. Lucas (ISL)***
T. Downar (Purdue University)****

Division of Systems Analysis and Regulatory Effectiveness
Office of Nuclear Regulatory Research
U.S. Nuclear Regulatory Commission
Washington, DC 20555-0001

**Los Alamos National Laboratory
Los Alamos, NM 87545

***ISL, Inc.
11140 Rockville Pike
Rockville, MD 20852

****Purdue University
1290 Nuclear Engineering Building
W. Lafayette, IN 47907-1290

AVAILABILITY OF REFERENCE MATERIALS IN NRC PUBLICATIONS

NRC Reference Material

As of November 1999, you may electronically access NUREG-series publications and other NRC records at NRC's Public Electronic Reading Room at www.nrc.gov/NRC/ADAMS/index.html.
Publicly released records include, to name a few, NUREG-series publications; *Federal Register* notices; applicant, licensee, and vendor documents and correspondence; NRC correspondence and internal memoranda; bulletins and information notices; inspection and investigative reports; licensee event reports; and Commission papers and their attachments.

NRC publications in the NUREG series, NRC regulations, and *Title 10, Energy*, in the Code of *Federal Regulations* may also be purchased from one of these two sources.

1. The Superintendent of Documents
   U.S. Government Printing Office
   Mail Stop SSOP
   Washington, DC 20402–0001
   Internet: bookstore.gpo.gov
   Telephone: 202-512-1800
   Fax: 202-512-2250
2. The National Technical Information Service
   Springfield, VA 22161–0002
   www.ntis.gov
   1–800–553–6847 or, locally, 703–605–6000

A single copy of each NRC draft report for comment is available free, to the extent of supply, upon written request as follows:

Address: Office of the Chief Information Officer,
Reproduction and Distribution
Services Section
U.S. Nuclear Regulatory Commission
Washington, DC 20555-0001
E-mail: DISTRIBUTION@nrc.gov
Facsimile: 301–415–2289

Some publications in the NUREG series that are posted at NRC's Web site address www.nrc.gov/NRC/NUREGS/indexnum.html are updated periodically and may differ from the last printed version. Although references to material found on a Web site bear the date the material was accessed, the material available on the date cited may subsequently be removed from the site.

Non-NRC Reference Material

Documents available from public and special technical libraries include all open literature items, such as books, journal articles, and transactions, *Federal Register* notices, Federal and State legislation, and congressional reports. Such documents as theses, dissertations, foreign reports and translations, and non-NRC conference proceedings may be purchased from their sponsoring organization.

Copies of industry codes and standards used in a substantive manner in the NRC regulatory process are maintained at—

The NRC Technical Library
Two White Flint North
11545 Rockville Pike
Rockville, MD 20852–2738

These standards are available in the library for reference use by the public. Codes and standards are usually copyrighted and may be purchased from the originating organization or, if they are American National Standards, from—

American National Standards Institute
11 West 42nd Street
New York, NY 10036–8002
www.ansi.org
212–642–4900

Legally binding regulatory requirements are stated only in laws; NRC regulations; licenses, including technical specifications; or orders, not in NUREG-series publications. The views expressed in contractor-prepared publications in this series are not necessarily those of the NRC.

The NUREG series comprises (1) technical and administrative reports and books prepared by the staff (NUREG–XXXX) or agency contractors (NUREG/CR–XXXX), (2) proceedings of conferences (NUREG/CP–XXXX), (3) reports resulting from international agreements (NUREG/IA–XXXX), (4) brochures (NUREG/BR–XXXX), and (5) compilations of legal decisions and orders of the Commission and Atomic and Safety Licensing Boards and of Directors' decisions under Section 2.206 of NRC's regulations (NUREG–0750).

ABSTRACT

This report presents an assessment of three different activities which led to the creation of TRAC-M, Version 3690. The first is the modernization of the old Transient Reactor Analysis Code for pressurized-water reactors (TRAC-P), the second is the integration of boiling water reactor (BWR) components from the TRAC-B code and the third is the integration of a spatial kinetics capability from the PARCS Code. The assessment shows that all three aspects of the modernization and integration have been successful.

CONTENTS

FIGURES

TABLES

EXECUTIVE SUMMARY

This report documents assessment findings, which demonstrate that the pressurized-water reactor (PWR) version of the Transient Reactor Analysis Code (TRAC-P) has successfully been modernized. This assessment was performed by comparing the code predictions that were produced using TRAC-P(Version 5.50), which is generically designated as TRAC-M(F77) because it was written in FORTRAN 77, and the modernized TRAC-M(Version 3690), which is generically designated as TRAC-M(F90) because it is written in FORTRAN 90. Specifically, the results reflect the predictions obtained for a series of test cases, which are presented in Chapter 3, "Analytical Test Problems," Chapter 4, "PWR Developmental Assessment," and Chapter 7, "Plant Transient Calculations," of this report.

The test matrix for "Analytical Test Problems" contains 42 cases, all of which are relatively simple and small problems designed to exercise various parts of the code, with an estimated coverage of about 80%. (Chapter 3 discusses five representative test cases. The results of other test cases are available to interested parties.) These test cases are exercised as each version of the code is created, to ensure that new errors have not been introduced as a result of the modernization. The resulting code predictions are then compared, and the comparisons show either "Excellent" or "Reasonable" agreement.

The test matrix for "PWR Developmental Assessment" contains 20 test cases that also exercise various parts of the code. These cases are more complicated than the "Analytical Test Problems," in that they test the coding and modeling of two-phase flow phenomena in PWR plant system transients. Again, comparisons between the code predictions produced using TRAC-M(F77) and TRAC-M(F90) show either "Excellent" or "Reasonable" agreement. Most of these test cases also provide comparison with the test data. Since the modernization did not change the physical models used in the code, agreements between the code predictions and the test data remain the same as those presented in the report prepared by Los Alamos National Laboratory, LA-UR-99-6480, "TRAC-M: FORTRAN 77, Version 5.5, Developmental Assessment Manual, Volume I: Nonproprietary Assessment Sections," dated December 1999. Like the foregoing report, this report finds that the reflood model needs improvement. It should also be noted that the test data obtained in the 2-D/3-D program are not presented in this report, since the data are restricted for exclusive use by 2-D/3-D program participants. When the participants agree to release these test data, this report will be revised accordingly.

Finally, a limited number of plant transients are calculated using both TRAC-M(F77) and TRAC-M(F90). Plant transients are usually long-running; therefore, it is not possible to include a large number of transients in a report that is prepared in relatively a short time. Comparisons between the resulting code predictions for the transients presented show "Excellent" or "Reasonable" agreement.

The consolidated TRAC-M(F90) integrates many boiling water reactor (BWR) components, as well as one component that is designed to provide a capability similar to the Reactor Excursion and Leak Analysis Program (RELAP). In addition, TRAC-M(F90) integrates some BWR-specific models. Specifically, TRAC-M(F90) integrates the following components, models and modules:

Components:

- Channel (CHAN) component
- Containment (CONTAN) component
- Feedwater heater (HEATR) component
- Jet pump (JETP) component
- Separator (SEPT) component
- Single-junction (SJACS) component
- Turbine (TRBN) component

Models:

- BWR control system (CNSYS) model
- Level tracking (LTRCK) model

Modules:

- Power module
- Spatial kinetics module

The assessment of the integration of the CHAN, HEATR, JETP, SJACS, and TRBN components, as well as the CONSYS and LTRCK models and the 3-D Spatial Kinetics module is reported in Chapters 5 and 6 of this report. Verification tests regarding the integration show that these five components, two models, and one module are correctly integrated. The only exception is that the tests revealed an error in the TRBN component, which prevents verification of the control system operation for the turbine. This error will be corrected in a future version of the code, and the assessment will be repeated using the corrected version. Documentation of the SEPT and CONTAN components is not complete; therefore, their assessments are not discussed in this report. The modernization of the power module is complete, and was incorporated into TRAC-M(F90) as part of the BWR consolidation. In addition, heat structure nodes and hydraulic cells were recently aligned, and work was done to ensure that the BWR components use this enhanced heat structure. This work is complete, but there was insufficient time to reflect it in this report. As a result, the assessment of the enhanced heat structure will be included in a future report.

This report also discusses the Peach Bottom Turbine Trip transient, which was used to exercise the BWR components, spatial kinetics, and the BWR control system. Although the resulting calculations are preliminary, the results of these calculations and a comparison with the test data indicate the successful integration of the spatial kinetics module from the Purdue Advanced Reactor Core Simulator (PARCS) code to TRAC-M.

FOREWORD

To advance its current capability, the United States Nuclear Regulatory Commission (NRC) is consolidating the capabilities of its suite of thermal-hydraulic system analysis codes into one code to save resources needed for maintenance and development of four different codes. The base code for the consolidation is the Transient Reactor Analysis Code for pressurized water reactors, TRAC-P. The architecture of the code has been completely revamped to a modular structure using the Fortran90 language. This code is now referred to as TRAC-M to reflect the modernized architecture. The functionality of the predecessor codes are being incorporated into TRAC-M. To date, the functionality of the Transient Reactor Analysis Code for boiling water reactors, TRAC-B, and RAMONA have been incorporated and the consolidation of the Reactor Excursion and Leak Analysis Program, RELAP5, is in progress. Once completed, TRAC-M will have the ability to read both RELAP5 and TRAC-B input decks as well as legacy TRAC-P decks. A developmental assessment will then be performed to select a set of physical models that will allow TRAC-M to simulate the applications of the predecessor code with equivalent fidelity.

The resulting consolidated code, TRAC-M, will enhance the effectiveness and efficiency of the NRC thermal-hydraulic program, since effort will be focused on only one code. Therefore, user needs will be accommodated and improvements, aimed at increasing the code's realism, will be made more efficiently. Analysis capabilities will also improve, as NRC and the user community can focus their attention on one code, thereby developing the collective expertise far more efficiently than is possible when four codes are utilized.

This report demonstrates that the architectural modifications made to TRAC-P to produce TRAC-M have been successful and have not modified the answers. During the development, some code errors in TRAC-P were identified and fixed in TRAC-M. The resulting variation in code results are described and reported in this document. In addition, other analyses presented demonstrate that the functionality of RAMONA and TRAC-B capabilities have been successfully consolidated.

Thomas L. King, Director
Division of Systems Analysis and Regulatory Effectiveness

ACKNOWLEDGMENTS

This project, undertaken under the leadership of Dr. Farouk Eltawila, began in 1996 upon approval of the "Thermal-Hydraulics 5-Year Research Plan." That plan called for the consolidation of TRAC-P and TRAC-B, as well as the inclusion of a spatial kinetics capability similar to that in the RAMONA code. This large-scale project required close coordination between the staff of the U.S. Nuclear Regulatory Commission (NRC) and its contractors. Some staff and management thought that the undertaking was very ambitious.

This report demonstrates that the project has been successful. The authors appreciate the support given by Dr. Eltawila throughout the conduct of this project. Without his support (despite budget cuts), and without many countless hours of hard work by the contractors and NRC staff who are coauthors to this report, this project would not have been successful. The authors also acknowledge contributions by Brent E. Boyack, James F. Lime, David A. Pimentel, Jay W. Spore, and James L. Steiner from Los Alamos National Laboratory; Weidong Wang from the NRC; Glen Mortensen from ISL, Inc.; and Douglas Barber from Purdue University.

The authors also thank Ms. Colleen Amoruso of ISL, Inc., for her word processing, editing, and expertise in preparing the report in FrameMaker format. She has spent many hours (including some weekends) to keep up with the schedule for timely preparation of this report. The authors appreciate the fine manuscript that she prepared.

ACRONYMS

1-D	one-dimensional
2-D	two-dimensional
3-D	three-dimensional
ACC	accumulator
ADS	automatic depressurization system
A/E	architect/engineer
ANS	American Nuclear Society
B&W	Babcock & Wilcox
BE	best-estimate
BN	boron nitride
BOCREC	bottom of core recovery
BWR	boiling-water reactor
CCFL	countercurrent flow limitation
CCTF	Cylindrical Core Test Facility
CDAS	Computer Data Acquisition System
CHF	critical heat flux
CLV	Courant Limit Violating
CMT	core makeup tank
CPU	central processing unit
CSAU	code scaleability, applicability, and uncertainty
DCA	drain cooler approach
DINL	double integrator with XOUT limited
DM1D	Detailed Model One-Dimensional
ECC	emergency core coolant
ECCS	emergency core cooling system

EM	evaluation model
F77	FORTRAN 77
F90	FORTRAN 90
FA	fuel assembly
FLECHT	Full-Length Emergency Core Heat Transfer
GI	General Interface
HEM	Homogeneous Equilibrium Model
HPIS	high-pressure injection system
HSTR	heat structure
HTC	heat-transfer coefficient
IAF	inverted annular flow
IB	intermediate-break
IET	integral effect test
IFDC	interfacial-drag coefficient
I/O	input/output
INEL	Idaho National Engineering Laboratory
INT	integrator
INTM	integrator with mode control
IRWST	in-containment refueling water storage tank
JAERI	Japan Atomic Energy Research Institute
JCELL	junction cell
KWU	Kraftwerk Union Aktiengesellschaft
LAG	first order lag
LANL	Los Alamos National Laboratory
LB	large-break
LBLOCA	large-break loss-of-coolant accident
LDLY	logic delay

L/D	length-to-diameter
LINT	limited integrator
LLAG	lead-lag transfer function
LMTD	logarithmic mean temperature difference
LOCA	loss-of-coolant accident
LOFT	loss-of-fluid test
LOSP	loss-of-offsite power
LPCI	low-pressure coolant injection
LPIS	low-pressure injection system
LRB	Lehigh University rod bundle
LWR	light-water reactor
MATLAB	Matrix Laboratory
MgO	magnesium oxide
MSFCV	main steam flow control valve
MSJACS	multiple-side junction attribute component set
NDM	Neutronics Data Map
NEA	Nuclear Energy Agency
NRC	U.S. Nuclear Regulatory Commission
OECD	Organization for Economic Cooperation and Development
PARCS	Purdue Advanced Reactor Core Simulator
PBL	pressure balance line
PBTT2	Peach Bottom Turbine Trip 2
PCT	peak cladding temperature
PI	proportional plus integral
PID	proportional plus integral plus derivative
PORV	pressure-operated relief valve
PRHR	passive residual heat removal

PVM	parallel virtual machine
PWR	pressurized-water reactor
QA	quality assurance
QATP	Quality Assurance Test Plan
RELAP5	Reactor Excursion and Leak Analysis Program
S/W	steam/water
SB	small-break
SBLOCA	small-break loss-of-coolant accident
SCTF	Slab Core Test Facility
SEASET	Separate-Effects and System-Effects Test
SET	separate effects test
SETS	stability-enhancing two-step
SJACS	single-junction attribute component set
SJC	single-junction component
SOTF	second order transfer function
TDMR	TRAC Data Mapping Routine
T/H	thermal hydraulic
TF	two-fluid
THDM	Thermal-Hydraulic Data Map
TRAC	Transient Reactor Analysis Code
TRAC-B	Generic designation for the Transient Reactor Analysis Code for boiling-water reactors
TRAC-M	Modernized Transient Reactor Analysis Code
TRAC-P	Generic designation for the Transient Reactor Analysis Code for pressurized-water reactors
TSV	turbine stop valve
TT	turbine trip
TTD	terminal temperature difference

UCSP	upper-core support plate
UPTF	Upper-Plenum Test Facility
USAR	Upated Safety Analysis Report
XTV	X-TRAC-View Code

1. Introduction

The first internally-released version (Version 3690) of the consolidated Transient Reactor Analysis Code (TRAC-M) was produced by modernizing TRAC-P, the generic designation for the pressurized-water reactor (PWR) version of the code. As part of the modernization, the PWR components in TRAC-P were consolidated and integrated with the boiling-water reactor (BWR) components from the TRAC-B code, the generic designation for the BWR version of the code. In addition, the modernized version integrates the three-dimensional (3-D) spatial kinetics capability from the Purdue Advanced Reactor Core Simulator (PARCS) code. The TRAC modernization also included changing the programming language from FORTRAN 77 to FORTRAN 90, and reprogramming the code to create new modules. The modernization did *not* involve changing the existing physical models, and did not add any new models for thermal-hydraulics or neutronics. (Chapter 2, "Description of the Consolidated Code," describes the modernization and integration activities in greater detail.)

The purposes of this assessment are to demonstrate that a) the modernization has been successful, and b) BWR components and spatial kinetics have been successfully integrated with the PWR components of the TRAC code. The success of the modernization is demonstrated by comparing the results of calculations produced using TRAC-P(Version 5.5.0), which is generically designated as TRAC-M(F77) because it was written in FORTRAN 77, and the released version (Version 3690) of the modernized and consolidated code, which is generically designated as TRAC-M(F90) because it was written in FORTRAN 90. Specifically, the test plan is designed to use two assessment test matrices and some plant transients to test phenomena of increasing complexity, as well as plant transient calculations involving very large input decks and a good number of plant components. The first matrix is the Standard Assessment Test Matrix presented in Ref. 1.1, and the second is the PWR Developmental Assessment Test Matrix presented in Ref. 1.2. For plant calculations, some of the existing plant input decks are used.

The Standard Assessment Test Matrix contains 42 short, mostly analytical, test cases, all of which represent relatively simple phenomena designed to exercise various parts of the code, with an estimated coverage of about 80%. This matrix was used to test each internal (not released) version of the consolidated code, as the modernization progressed. This testing was used to ensure that new errors have not been introduced, and that the scope of the modernization for that version has been successful. The criterion for success was that differences between the test results for two sequential versions would be "small." These differences occurred because of truncation errors, compiler differences, changes in numerics, and error corrections. Acceptance was based on the subjective judgment of the authors.

This report uses the same acceptance criterion in comparing the released version of the consolidated code, TRAC-M(F90) and TRAC-M(F77), when the Standard Assessment Test Matrix is exercised. Graphics comparing the results from these two codes will be presented to support the authors' conclusions that the differences in these results are "small." Chapter 3, "Analytical Test Problems," contains the results of these analyses.

The PWR Developmental Assessment Test Matrix, which contains the test problems used to assess TRAC-M(F77) (Ref. 1.2), and the companion document containing proprietary data obtained in the two- and three-dimensional (2-D/3-D) program, increase the test coverage to encompass more than the 80% of the code that is exercised using the Standard Assessment Test

Matrix. In addition, the PWR Developmental Assessment Test Matrix uses long-running test problems that increase the complexity of the phenomena. These problems are not used in the Standard Assessment Test Matrix, and they also include experimental test data from facilities. Since the physical models have not been changed, differences between the predictions obtained using TRAC-M(F77) and TRAC-M(F90) are expected to be "small." If so, the agreement between the calculations will be deemed "Excellent." It is also expected that comparison of code predictions with test data will lead to conclusions similar to those reached in Ref. 1.2 and the companion proprietary document. If corrections of errors or bugs involving thermal-hydraulic models lead to large differences between the two sets of code predictions, such that the conclusions reached in Ref. 1.2 are changed, an assessment of changes in physical models should be performed. The need for this type of assessment will be noted; but, performing this type of assessment is outside the scope of this report. If corrections of errors or bugs lead to some differences that are not "small," but earlier conclusions regarding the assessment of models simulating physical phenomena are not changed, the differences will be deemed "Reasonable," and the modernization and integration for that particular application will be deemed acceptable. Graphics comparing the two sets of code results together with the experimental data, when available, will be presented to support the conclusion that differences between two code predictions are "Excellent" or "Reasonable." Chapter 4, "PWR Developmental Assessment," contains these analyses. Results show that agreements are "Excellent" or "Reasonable."

PWR plant transient calculations are performed using two codes, and the results of two sets of predictions are compared with each other. Differences between predictions should be "Excellent" or "Reasonable." If they are not, the reasons for these differences will be understood and noted. Graphics comparing the two sets of predictions will be presented to demonstrate that any differences are generally "small" or "reasonable." Chapter 7, "Plant Transient Calculations," contains the results of these analyses.

As stated earlier, the consolidated TRAC version contains BWR components that have been integrated from the TRAC-B code. The assessment demonstrates that this integration has been performed correctly. The NRC's Quality Assurance (QA) procedures (Ref. 1.3) has been used as a guidance. As required by the QA procedures, the requirements for functionality of each component were defined. Then, in order to demonstrate that these requirements were met, test cases were designed. The consolidated TRAC version and TRAC-B were then run for these test cases, and two sets of predictions were obtained. Demonstration of a successful integration of a component requires that differences between the two code predictions are "small." These differences occur because of truncation errors, compiler differences, changes in numerics, and error corrections. If the differences are "small," the agreement is deemed "Excellent." Graphics comparing the two sets of predictions will be presented to demonstrate that any differences are generally "small," and the agreements are "Excellent." Chapter 5, "Assessment of Integration of BWR Components," describes the requirements, test cases, and results of these analyses.

The consolidated TRAC version also contains a spatial neutronics capability that was integrated from the PARCS code. At each time step, fuel and thermal-hydraulic data are transferred from TRAC to the spatial kinetics module, and the power data are transferred from the spatial kinetics module to the TRAC code. Successful integration of the spatial kinetics capability requires correct implementation of a new data mapping function. Test cases have been designed, and successful implementation of the mapping function has been demonstrated. Chapter 6,

"Assessment of Integration of Spatial Kinetics," describes the test cases and results of these analyses. Chapter 7, "Plant Transient Calculations," contains preliminary results of calculations for the Peach Bottom Turbine Trip 2 transient, which was used to exercise the BWR components, spatial kinetics, and BWR control system of the modernized TRAC release. The results show successful integration of spatial kinetics.

It should be noted that requirements, tests and test results presented in Chapters 5 and 6 have not been independently reviewed as required by Ref. 1.3. Reviews have been conducted by the contractor management, by the author of this report and by the NRC staff while incorporating code changes. These reviews were not formal and they are not a substitute for a detailed and independent review following software quality assurance procedures as defined in Ref. 1.3. However, it appears that the quality of code development work has been maintained during the code development. Hence, conclusions in Chapters 5 and 6 assume that requirements, tests and test results would not change if an independent formal review as defined in Ref. 1.3 is conducted.

REFERENCES

1.1 Steinke, R.G., "A Description of the Test Problems in the TRAC-P Standard Test Matrix," Los Alamos National Laboratory, LA-UR-96-1475, May 1996.

1.2 Boyack, B.E., J.F. Lime, D.A. Pimentel, J.W. Spore, and J.L. Steiner, NUREG/CR-6730, "TRAC-M/F77, Version 5.5, Developmental Assessment Manual, Volume I: Assessments, Volume II: Appendices," NRC: Washington, D.C. August 2001.

1.3 Odar, F., NUREG-1737, "Software Quality Assurance Procedures for NRC Thermal-Hydraulic Codes," NRC: Washington, D.C. December 2000.

2. Description of the Consolidated TRAC Release and History of its Development

The modernized, consolidated, and internally-released TRAC-M(F90), Version 3690, is an advanced, best-estimate (BE) computer program for calculating the transient reactor behavior of a PWR or BWR. As such, TRAC-M(F90) incorporates a four-component (liquid water, liquid solute, water vapor, and noncondensable gas), two-fluid (liquid and gas) model of the thermal-hydraulic (T/H) processes that are involved in such transients. The complexity of the T/H modeling requires many additional models and correlations with logic imposed into a coherent description of a phenomenon.

TRAC-M(F90), Version 3.0, (Ref. 2.1), is one of the latest in a series of TRAC releases. The manuals for TRAC-M(F90), Version 3690 and later versions are under preparation. The development history represented by earlier versions begins with a very fundamental and important improvement in analyzing the behavior of light-water reactors (LWRs), namely, the decision to separately track the liquid and vapor fields in the reactor coolant system. These earlier versions required the greatly improved computer systems that were becoming available during the 1970s. They also pushed advances in numerical techniques to solve the complex equation set, and to permit the large number of nodes that are required in the BE analysis of some transients of interest.

A preliminary TRAC version for PWRs consisting of only one-dimensional (1-D) components was completed in December 1976. Although this version was neither publicly released nor formally documented, it was used in developing the first publicly released version, TRAC-P1, which was completed in December 1977 (Ref. 2.2), and it formed the basis for the 1-D loop component modules.

The TRAC-P1 program was primarily designed for use in analyzing large-break (LB) loss- of-coolant accidents (LOCAs) in PWRs. Because of its versatility, however, TRAC-P1 could be directly applied to many analyses, ranging from blowdowns in simple pipes to integral LOCA tests in multiloop facilities. A refined version, TRAC-P1A, was released to the National Energy Software Center in March 1979 (Ref. 2.3). Although it still treated the same class of problems, TRAC-P1A was more efficient than TRAC-P1 and incorporated improved hydrodynamic and heat transfer models. It was also easier to implement on various computers. A subsequent version, known as TRAC-PD2 (Ref. 2.4), contained improvements in reflood, heat transfer models, and numerical solution methods. Although it was primarily a LBLOCA code, TRAC-PD2 was also successfully applied to small-break (SB) problems and the Three Mile Island accident.

The 1984 release, known as TRAC-PF1 (Ref. 2.5), was designed to improve the ability of TRAC-PD2 to handle SBLOCAs and other transients. In addition to all of the major improvements of TRAC-PD2, TRAC-PF1 used a two-fluid model with stability-enhancing two-step (SETS) numerics (Ref. 2.6) in the 1-D components. This two-fluid model, in conjunction with a stratified flow regime, modeled countercurrent flow better than the drift flux model that was used in previous versions, and the two-step numerics allowed large time steps for slow transients. Also, the 1-D core component permitted calculations with reduced dimensionality, although the 3-D vessel option was retained. In addition, noncondensable gas field was added to

the 1-D and 3-D hydrodynamics, and significant improvements were made to the trip logic and the input.

The development of TRAC-PF1/MOD1 (Refs. 2.7 and 2.8) maintained the models that were needed to apply the code to LBLOCAs, and added or modified models as necessary to enhance the application of the code to SBLOCAs and operational transients. In particular, many user convenience features were added or enhanced to promote the application of the code to transients involving more complex control of the nuclear plant. Specifically, TRAC-PF1/MOD1 contained generalized, reactivity feedback models (subject to point kinetics assumptions), generalized trip and control system modeling, and necessary components to model the rest of the plant. The code was also applicable to most transients for which large asymmetries in the power generation do not exist, for which the 1-D fluid modeling in the pipe is valid, and for which thermal stratification in the liquid in the 1-D components is not important (the 3-D vessel component can model thermal stratification in a coarse manner). In addition, the code maintained the capability to run in either a 1-D or a mixed 1-D/3-D mode, with SETS numerics in both the 1-D and 3-D components.

TRAC-PF1/MOD2, Version 5.5, is the latest released version of the code for PWRs. This code, with some minor corrections, is used is this report and referred to as TRAC-M(F77). This code differs from the last formal release, Version 5.4.15, in three major features. First, standard FORTRAN 77 (F77) has been implemented throughout the code with a commensurate increase in portability and maintainability. Second, the platform-dependent binary file, named TRCGRF, has been replaced by the XTVGR.b and XTVGR.t files, which can be processed by the X-TRAC-View code (XTV) visualization and plotting tool (Ref. 2.9). Third, the code includes a new option (newrfd=3) for the reflood model (Refs. 2.10 and 2.11). TRAC-M(F77), Version 5.5, was used to perform the developmental assessment calculations in Ref. 1.2.

In 1996, the NRC decided to consolidate the functionality of its suite of codes (TRAC-P, TRAC-B, RAMONA, and RELAP5) into a single, consolidated code that is capable of performing the applications of the four codes. The goal was to minimize the dilution of resources and the fragmentation of the knowledge base that occurs with the existence of four separate codes. TRAC-PF1/MOD2, Version 5.4.25, a version that preceded Version 5.5, was selected as the basis for the consolidation because its architecture was consistent with the ultimate design goal of modularity. It had a 3-D hydraulic modeling capability, and it was a better target for installation of special-purpose BWR component models that were developed for the TRAC-B code series. Before beginning the consolidation, TRAC-PF1/MOD2, Version 5.4.25, was converted to FORTRAN 90 (F90). The container array and integer pointers that were used in Version 5.4.25 as a form of home spun dynamic memory allocation, as well as common blocks to provide communication of the global data, made the coding difficult to decipher. The restrictions in F77 that drove the original TRAC-P data structures were eliminated with the introduction of derived types, allocatable arrays, pointers, and modules in F90. The code was denoted TRAC-M to signify the modernization of its architecture, which enhanced readability, portability, extensibility, and maintainability.

To recover the functionality of the RAMONA code, BWR stability, and 3-D kinetics, a semi-implicit numerics scheme was enabled in TRAC-M in place of SETS in cases where the preservation of property gradients is important. 3-D kinetics capability was recovered by utilizing a parallel virtual machine (PVM) to tightly couple the T/H model to a 3-D neutronics package (PARCS) running outside of TRAC-M.

To recover the functionality of TRAC-B, which included transients and LOCAs in BWRs, the modeling philosophy used in TRAC-B was duplicated in TRAC-M to construct the components that are necessary to model a BWR. The work performed to enhance modularity, and in turn, extensibility in TRAC-M during the modernization activities facilitated the TRAC-B consolidation. The object-oriented programming concept of inheritance was used to consolidate the TRAC-B components with minimal maintenance points and code complexity. The TRAC-M and TRAC-B codes share the same generic components, such as PIPE, TEE, VESSEL, BREAK, and FILL. The BWR components, including the jet pump, feedwater heater, turbine, containment, and BWR fuel channel, were built from these generic components, and only component-specific terms were added to the finite volume equations in order to model the BWR components.

REFERENCES

2.1 Spore, J.W., et al., NUREG/CR-6724, "TRAC-M/Fortran 90 (Version 3.0) Theory Manual," NRC: Washington, D.C. July 2001.

2.2 Safety Code Development Group, "TRAC-P1: An Advanced, Best-Estimate Computer Program for PWR LOCA Analysis," Los Alamos Scientific Laboratory Report LA-7279-MS, NUREG/CR-0063, May 1978.

2.3 Safety Code Development Group, "TRAC-P1A: An Advanced, Best-Estimate Computer Program for PWR LOCA Analysis," Los Alamos Scientific Laboratory Report LA-7777-MS, NUREG/CR-0665, May 1979.

2.4 Safety Code Development Group, "TRAC-PD2: An Advanced, Best-Estimate Computer Program for Pressurized-Water Reactor Loss-of-Coolant Accident Analysis," Los Alamos Scientific Laboratory Report LA-8709-MS, NUREG/CR-2054, April 1981.

2.5 "Computer Program for Pressurized-Water Reactor Analysis," Los Alamos National Laboratory Report LA-9944-MS, NUREG/CR-3567, February 1984.

2.6 Mahaffy, J.H., "A Stability-Enhancing Two-Step Method for Fluid Flow Calculations," *J. Computational Physics* 46, 329–341, 1982.

2.7 Safety Code Development Group, "TRAC-PF1/MOD1 Correlations and Models," Los Alamos National Laboratory Report LA-11208-MS, NUREG/CR-5069, December 1988.

2.8 Safety Code Development Group, "TRAC-PF1/MOD1: An Advanced, Best-Estimate Computer Program for Pressurized-Water Reactor Thermal-Hydraulic Analysis," Los Alamos National Laboratory Report LA-10157-MS, NUREG/CR-3858, July 1986.

2.9 Dearing, J.F., and R. Johns, "XTV User's Guide, Release 2.3c," Los Alamos National Laboratory Report LA-UR-01-921, May 1998.

2.10 Nelson, R.A., Jr., D.A. Pimentel, S. Jolly-Woodruff, and J.W. Spore, "Reflood Completion Report, Volume I, A Phenomenological Thermal-Hydraulic Model of Hot Rod Bundles Experiencing Simultaneous Bottom and Top Quenching and an Optimization Methodology for Closure Development," Los Alamos National Laboratory Report LA-UR-98-3043, April 1998.

2.11 Boyack, B.E., J.F. Lime, D.A. Pimentel, J.W. Spore, and T.D. Knight, "Reflood Completion Report, Volume II, Developmental Assessment of a New Reflood Model for the TRAC-M/F77 Code," Los Alamos National Laboratory Report LA-UR-98-3043, April 1998.

3. Analytical Test Problems

This chapter describes comparisons between the predictions obtained using TRAC-M(F77) and TRAC-M(F90) for analytical test problems selected from the "Standard Assessment Test Matrix." The 42 primarily simple, fast-running test problem-calculation cases in this matrix exercise approximately 80% of the code, and are used when a new version of the code is created in order to ensure that errors are not introduced by the new updates.

The matrix consists of two problem series including (1) a short-running series of 10 test problems with 34 problem-calculation cases, and (2) a long-running series of 5 test problems with 8 problem-calculation cases (Ref. 1.1). The test problem names and their number of calculation cases (shown in brackets) are as follows:

Short-Running Series

1. DRAIN [1]
2. HCOND#; #=1,2,3,4,5 [5]
3. MARVIK [1]
4. MS#&; # = C,P,R,S,T,V; & = 2,L,V; #& = VLR [19]
5. ROD2 [1]
6. TFPIPE2 [1]
7. TIN#; # = DWN,UP [2]
8. UTUBE [1]
9. W4LOOP [2]
10. ZIONPWR [1]

Long-Running Series

11. BANKOFF [1]
12. LEHIGH [1]
13. LOFTL26 [2]
14. UPTF8B [3]
15. UTUBE3D [1]

Each version of the code has been exercised using all 42 problem-calculation cases. Comparisons of the results obtained using TRAC-M(F77) and TRAC-M(F90) show "Excellent" to "Reasonable" agreement between the two codes. The following sections present calculations for a sample of five short-running test problems. The files for all other cases are available for review by interested parties.

In Section 3.1, both codes are compared using steady-state conduction solutions for 1-D radial and 2-D radial and axial geometries. Analytical steady-state conduction solutions have been developed in literature with fixed heat transfer coefficients and fixed fluid conditions.

Comparisons are made with the TRAC predicted temperature distributions for the same boundary conditions.

In Section 3.2, both codes are compared using a drain and fill problem. This analytical test problem demonstrates the TRAC capability to accurately calculate mixture levels and level crossings at cell boundaries without significant numerical instabilities.

In Section 3.3, both codes are compared using a manometer oscillation problem with a known analytical frequency. This test problem indicates that both codes accurately calculate the gravity head and oscillation in this U-tube geometry.

3.1 Steady-State Conduction Problems (HCOND#; # = 1,2,3)

These steady-state conduction problems were provided by the Japan Atomic Energy Research Institute (JAERI) as part of the checkout for their fully implicit axial conduction solution. As discussed in the following subsections, these test problems provide an analytical check to verify that the TRAC conduction solution is accurate. The results for a 1-D radial steady-state conduction solution and a 2-D radial and axial steady-state conduction solution are compared to analytical solutions.

3.1.1 1-D Radial Conduction

The 1-D radial steady-state conduction was determined for a generic nuclear fuel rod, with the dimensions shown in Fig. 3.1.1. For this test problem, the inner material is representative of fuel that is surrounded by a gap that is, in turn, surrounded by cladding. The material from $r = 0$ to $r = r_1$ is a uniform source of 1000 W. From $r = r_1$ to $r = r_2$, a gap occurs with a conductance of 1000 $Wm^{-2}K^{-1}$. From $r = r_2$ to $r = r_3$, the thermal conductivity is 13.8 $Wm^{-1}K^{-1}$. The outside fluid temperature is 300 K, and the rod surface heat transfer coefficient is 2836 $Wm^{-2}K^{-1}$.

The governing differential equation is

$$\frac{1}{r}\frac{d}{dr}\left(rk\frac{dT}{dr}\right) = -q'''.$$

where T is the temperature, q''' is the heat generation rate per unit volume, k is the thermal condictivity and r is the radial coordinate.

The boundary conditions are

$$\frac{dT}{dr} = 0 \ @ \ r = 0,$$

where there is no heat conduction across the centerline of the fuel rod, and

$$\left(-k\frac{dT}{dr}\right)_3 = h_3(T_3 - T_f) = Q/(2\pi r_3 L)$$

where h_3 is the surface heat transfer coefficient, T_3 and T_f are rod surface and outside fluid temperatures respectively, r_3 is the distance between the rod surface and rod centerline, L is the height of the rod and Q is the heat generation rate within the rod.

$$Q = \pi r_1^2 L q''' = 1000W$$

at steady-state, all of the energy produced must appear as surface heat flux.

$q_1 = Q/(2\pi r_1 L), q_2 = Q/(2\pi r_2 L)$ and $q_3 = Q/(2\pi r_3 L)$.

The solution for this problem is

$$T = T_3 - q_1 r_1 ln(r/r_3)/k_3 \qquad \text{for } r_2 < r < r_3$$

$$T = T_1 + q_1(r_1^2 - r^2)/(2k_1 r_1) \quad \text{for } r < r_1 \ ,$$

where

$$T_3 = Q/(2\pi r_3 L h_3) + T_f \ ,$$

$$T_2 = T_3 - q_1 r_1 ln(r_2/r_3)/k_3 \ ,$$

$$T_1 = T_2 + q_1/h_2 \ ,$$

where h_2 is the gap conductance,

$Q = 1000$ W,

$L = 0.1$ m,

$r_1 = 6.35$ mm,

$r_2 = 6.426$ mm,

$r_3 = 7.239$ mm,

$k_1 = 2$ $Wm^{-1}K^{-1}$,

$k_3 = 13.8$ $Wm^{-1}K^{-1}$,

$T_f = 300$ K,

$h_2 = 1000$ $Wm^{-2}K^{-1}$, and

$h_3 = 2836$ $Wm^{-2}K^{-1}$.

A TRAC model using 18 nodes in the radial direction (input model HCOND2) was used to represent the geometry of the analytical test problem described above. Calculations were performed using TRAC-M(F77) and TRAC-M(F90), and the results are compared with the analytical model in Table 3.1.1.

The results given in Table 3.1.1 indicate that the finite-difference solutions of the heat conduction equation are accurate in the radial direction. The surface temperature is exact to four digits of accuracy, which is the number of digits that TRAC edits. The results in Table 3.1.1 also indicate a TRAC error of 0.17% in the centerline temperature, and this error is associated with an

error in the temperature solution across the gap, where the steepest temperature profile occurs. Consequently, inaccuracies in the finite-difference approximation would tend to occur where the temperature profile is steep. Given that the agreement between TRAC-M(F77) and TRAC-M(F90) calculations is "Excellent," the results confirm that the radial heat conduction solution in TRAC is accurate and adequate for LWR safety applications, and that conversion from TRAC-M(F77) to TRAC-M(F90) has been successful.

3.1.2 2-D Radial and Axial Conduction

The analytical solution for the 2-D radial and axial heat conduction problem was developed for a solid rod with a constant and uniform heat source, with a constant heat transfer coefficient in the radial direction, and adiabatic boundary conditions at both ends of the rod (as shown in Fig. 3.1.2). The axial variation in the temperature profile is obtained by having one fluid temperature boundary condition on the lower half of the rod, and another fluid temperature boundary condition on the upper half of the rod.

This problem is solved in Ref. 3.1, and the solution is not repeated here. The analytical solution for this problem is, however, compared with the TRAC solution in Table 3.1.2 for rod temperatures along the centerline of the rod. As presented in Table 3.1.2, the results obtained using TRAC-M(F77) and TRAC-M(F90) with input model HCOND3 indicate that 2-D conduction solutions in both codes are accurate. Again, some inaccuracies appear in the region where the temperature profile is steep; however, the error percentage is quite small (0.05%). The results given in Table 3.1.2 were obtained with the fine mesh option on. That option adds axial levels in regions where the temperature profile is steep, in an attempt to reduce the finite difference error in that region.

Table 3.1.3 presents a comparison between the results obtained using TRAC-M(F77) and TRAC-M(F90) and the analytical solution using 21 fixed axial levels (input model HCOND1). This comparison demonstrates that the fine mesh option improves the accuracy of the finite difference approximations relative to the original differential equation. The maximum error for the fixed node case is 0.75%, whereas the maximum error for the fine mesh case is 0.05%. Agreement between the TRAC-M(F77) and TRAC-M(F90) predictions is "Excellent."

In Table 3.1.4, the radial solutions at z = 100 mm for the 21 fixed axial heat-conduction model (HCOND1) are compared with the analytical solution at the same location. Table 3.1.4 shows that the maximum error of 0.018% along that radius occurs at the outer edge. The results indicate that the 2-D heat conduction solution obtained using both codes is very accurate in both the axial and radial directions. Nevertheless, the accuracy of the axial solution is significantly improved with the fine mesh option turned on. The results also confirm that conversion of the TRAC-M(F77) code to the TRAC-M(F90) code has been successfully performed.

Table 3.1.1 Comparison Between TRAC Codes and Analytical Solutions for a 1-D Heat-Conduction Problem in the Radial Direction at Steady State (TRAC Input Model HCOND2)

Node Location (mm)	Analytical Solution (K)	TRAC-M(F77) Solution (K)	TRAC-M(F90) Solution (K)	Error (K)
0.000	1039.8	1038.0	1038.0	-1.8
1.830	1006.7	1005.0	1005.0	-1.7
2.590	973.6	972.1	972.1	-1.5
3.175	940.3	938.8	938.8	-1.5
3.670	906.9	905.4	905.4	-1.5
4.100	873.9	872.4	872.4	-1.5
4.490	840.9	839.4	839.4	-1.5
4.850	807.7	806.2	806.2	-1.5
5.185	774.5	773.0	773.0	-1.5
5.500	741.3	739.8	739.8	-1.5
5.800	707.8	706.3	706.3	-1.5
6.080	675.0	673.5	673.5	-1.5
6.350	641.9	640.4	640.4	-1.5
6.426	391.3	391.3	391.3	0.0
6.670	387.0	387.0	387.0	0.00
6.840	384.1	384.1	384.1	0.0
7.040	380.7	380.7	380.7	0.0
7.239	377.5	377.5	377.5	0.0

Table 3.1.2 Comparison Between TRAC Codes and Analytical Solutions Along a Center Line of a Rod in a 2-D Heat-Conduction Problem While at Steady State with Fine Mesh (TRAC Input Model HCOND3)

Node Elevation (mm)	Analytical Solution (K)	TRAC-M(F77) Solution (K)	TRAC-M(F90) Solution(K)	Error (K)
0	658.1	658.1	658.1	0.0
10	658.1	658.1	658.1	0.0
20	658.1	658.1	658.1	0.0
30	658.1	658.1	658.1	0.0
40	658.1	658.1	658.1	0.0
50	658.1	658.1	658.1	0.0
60	658.1	658.1	658.1	0.0
70	658.1	658.1	658.1	0.0
80	658.2	658.2	658.1	0.0
90	662.7	662.7	662.6	0.0
100	758.1	758.5	758.5	+0.4
110	853.9	853.6	853.6	−0.3
120	857.5	857.9	857.9	+0.4
130	858.1	858.1	858.1	0.0
140	858.1	858.1	858.1	0.0
150	858.1	858.1	858.1	0.0
160	858.1	858.1	858.1	0.0
170	858.1	858.1	858.1	0.0
180	858.1	858.1	858.1	0.0
190	858.1	858.1	858.1	0.0
200	858.1	858.1	858.1	0.0

Table 3.1.3 Comparison Between TRAC Codes and Analytical Solutions Along a Center Line of a Rod in a 2-D Heat-Conduction Problem While at Steady State with Fixed Noding (TRAC Input Model HCOND1)

Node Elevation (mm)	Analytical Solution (K)	TRAC-M(F77) Solution (K)	TRAC-M(F90) Solution (K)	Error (K)
0	658.1	658.1	658.1	0.0
10	658.1	658.1	658.1	0.0
20	658.1	658.1	658.1	0.0
30	658.1	658.1	658.1	0.0
40	658.1	658.1	658.1	0.0
50	658.1	658.1	658.1	0.0
60	658.1	658.1	658.1	0.0
70	658.1	658.2	658.2	+0.1
80	658.2	658.8	658.8	+0.6
90	662.7	667.7	667.7	+5.0
100	758.1	758.1	758.1	0.0
110	853.9	848.5	848.5	−5.4
120	857.5	857.4	857.4	−0.1
130	858.1	858.0	858.0	−0.1
140	858.1	858.1	858.1	0.0
150	858.1	858.1	858.1	0.0
160	858.1	858.1	858.1	0.0
170	858.1	858.1	858.1	0.0
180	858.1	858.1	858.1	0.0
190	858.1	858.1	858.1	0.0
200	858.1	858.1	858.1	0.0

Table 3.1.4 Comparison Between TRAC Codes and Analytical Solutions Along a Radius at Midplane (Elevation 100 mm) of a Rod in a 2-D Heat-Conduction Problem at Steady State (TRAC Input Model HCOND1)

Node Location (mm)	Analytical Solution (K)	TRAC-M(F77) Solution (K)	TRAC-M(F90) Solution K	Error (K)
0.0	758.1	758.1	758.1	0.0
0.5	756.1	756.1	756.1	0.0
1.0	750.1	750.1	750.1	0.0
1.5	740.2	740.2	740.2	0.0
2.0	726.3	726.3	726.3	0.0
2.5	708.4	708.4	708.4	0.0
3.0	686.5	686.5	686.5	0.0
3.5	660.6	660.6	660.6	0.0
4.0	630.8	630.8	630.8	0.0
4.5	596.9	597.0	597.0	+0.1
5.0	559.1	559.2	559.2	+0.1

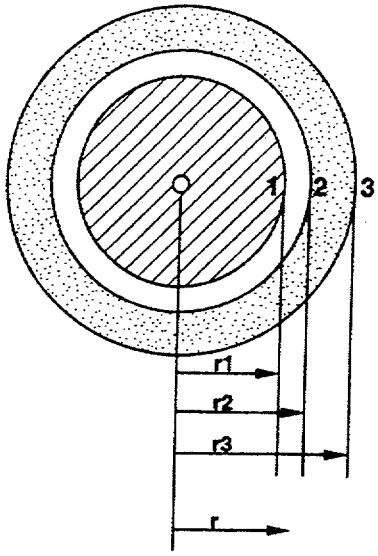

Figure 3.1.1 Boundary Conditions of a 1-D Heat-Conduction Problem in the Radial Direction

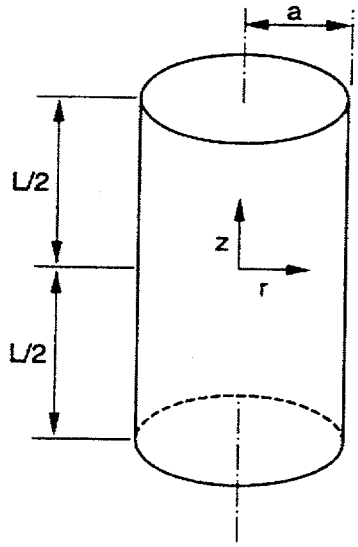

Figure 3.1.2 The 2-D Radial and Axial Heat-Conduction Problem

3.2 1-D Drain and Fill Test Problem (DRAIN)

The drain test problem consists of a vertical PIPE component that is partially filled with water, a FILL component, and a BREAK component, as shown in Fig. 3.2.1. The BREAK component provides a constant pressure boundary condition (1.0e+05 Pa) for the top of the pipe. The FILL component slowly drains water from the pipe, and then refills the pipe to its original level. The purpose of this test problem is to verify that (1) TRAC versions do not calculate numerical instabilities as the cells in a PIPE component slowly drain or fill, and (2) TRAC codes accurately calculate the gravity head.

Figs. 3.2.2 and 3.2.3 show the void fraction and mass flow rate within the pipe as the pipe drains and fills. In particular, these plots show that no numerical problems appear as the level crosses the cell boundaries. In Fig. 3.2.4, the pressure in cell 1 is plotted for the drain and fill transient, and no significant pressure oscillation occurs as the pipe drains and fills.

The PIPE component is made up of 15 cells, with each cell being 1.0 m long. With the PIPE component initially full of 10 m of water, the cell center pressure of the first cell should be the 1.0e+05 Pa plus 9.5 m of water or,

$$p = p(break) + rho*g*h$$

$$= 1.0e+05 + 997.4*9.8*9.5 = 1.929e+05 \text{ Pa}.$$

TRAC calculates the initial cell 1 pressure before the drain starts as 1.92e+05 Pa, and the final cell 1 pressure at the end of the fill transient as 1.93e+05 Pa. The minimum level during this calculation is 4 m of water above the cell 1 center. Given the static head above cell 1, the pressure would be

$$p = p(break) + rho*g*h$$

$$= 1.0e+05 + 997.4*9.8*4.0 = 1.391e+05 \text{ Pa}.$$

TRAC calculates a minimum pressure in cell 1 of 1.387e+05 Pa.

From these calculations and Figs. 3.2.3 and 3.2.4, it is apparent that both TRAC-M(F77) and TRAC-M(F90) accurately calculate the gravity head as the cells slowly drain and fill. It is also apparent that the codes encounter no significant numerical problems when a liquid level crosses a cell boundary. Agreement between TRAC-M(F77) and TRAC-M(F90) predictions is also "Excellent."

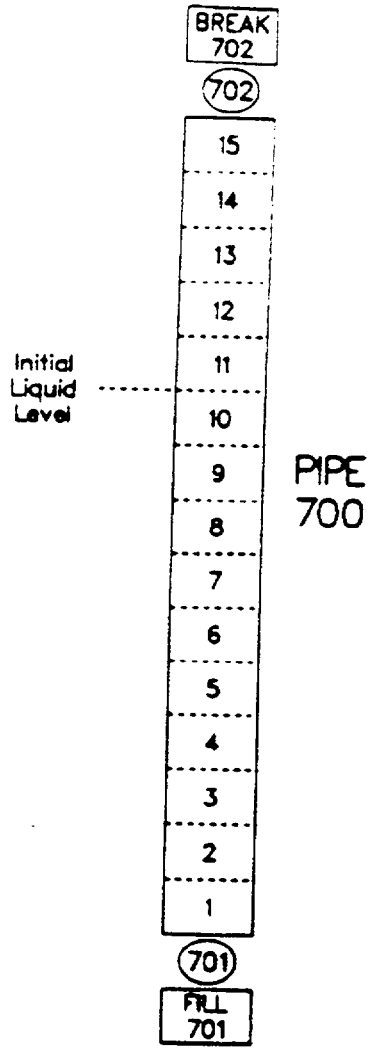

Figure 3.2.1 TRAC Model of the DRAIN Test Problem

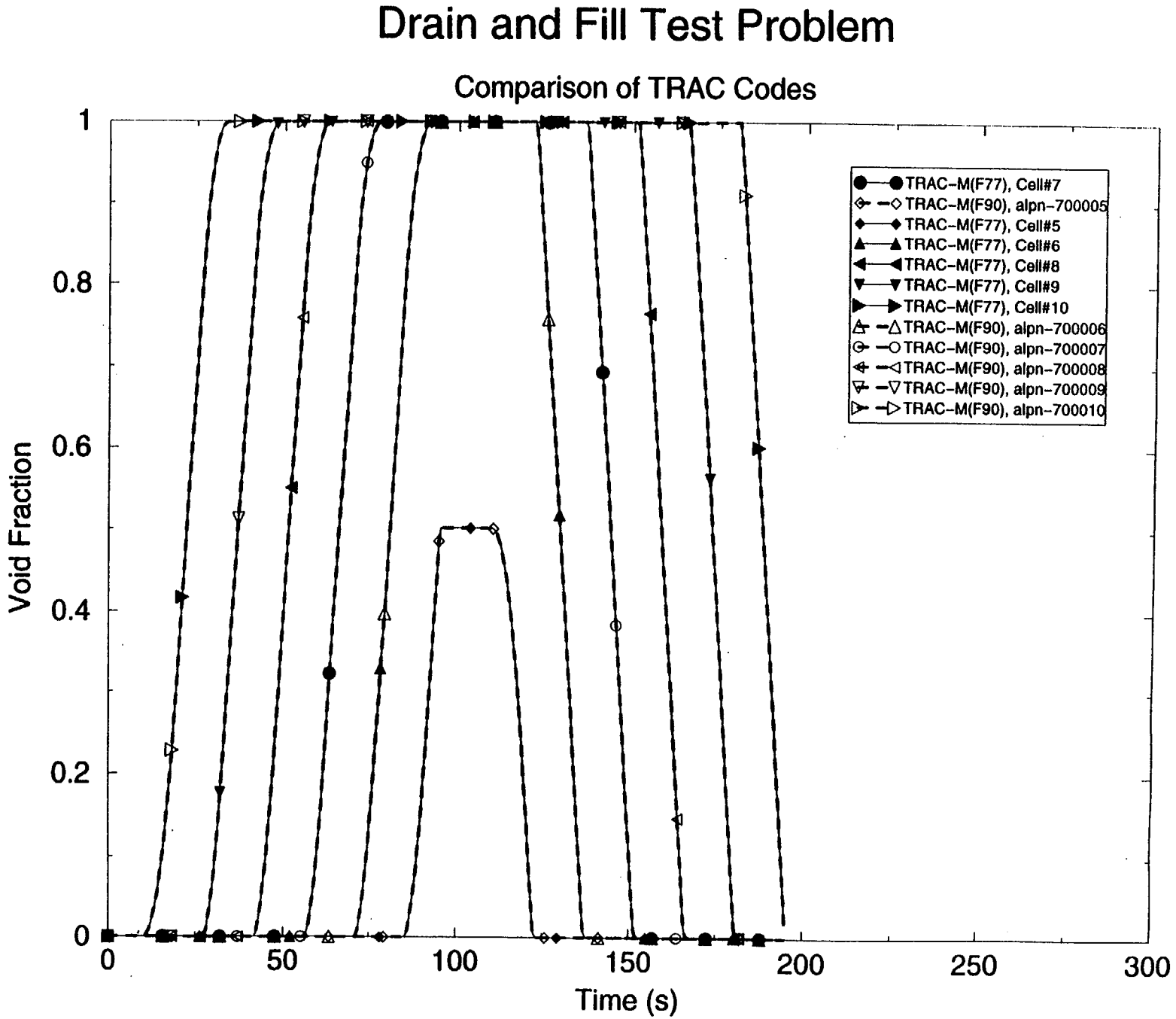

Figure 3.2.2 Comparison of Void Fraction Predictions in DRAIN and FILL Test Problem

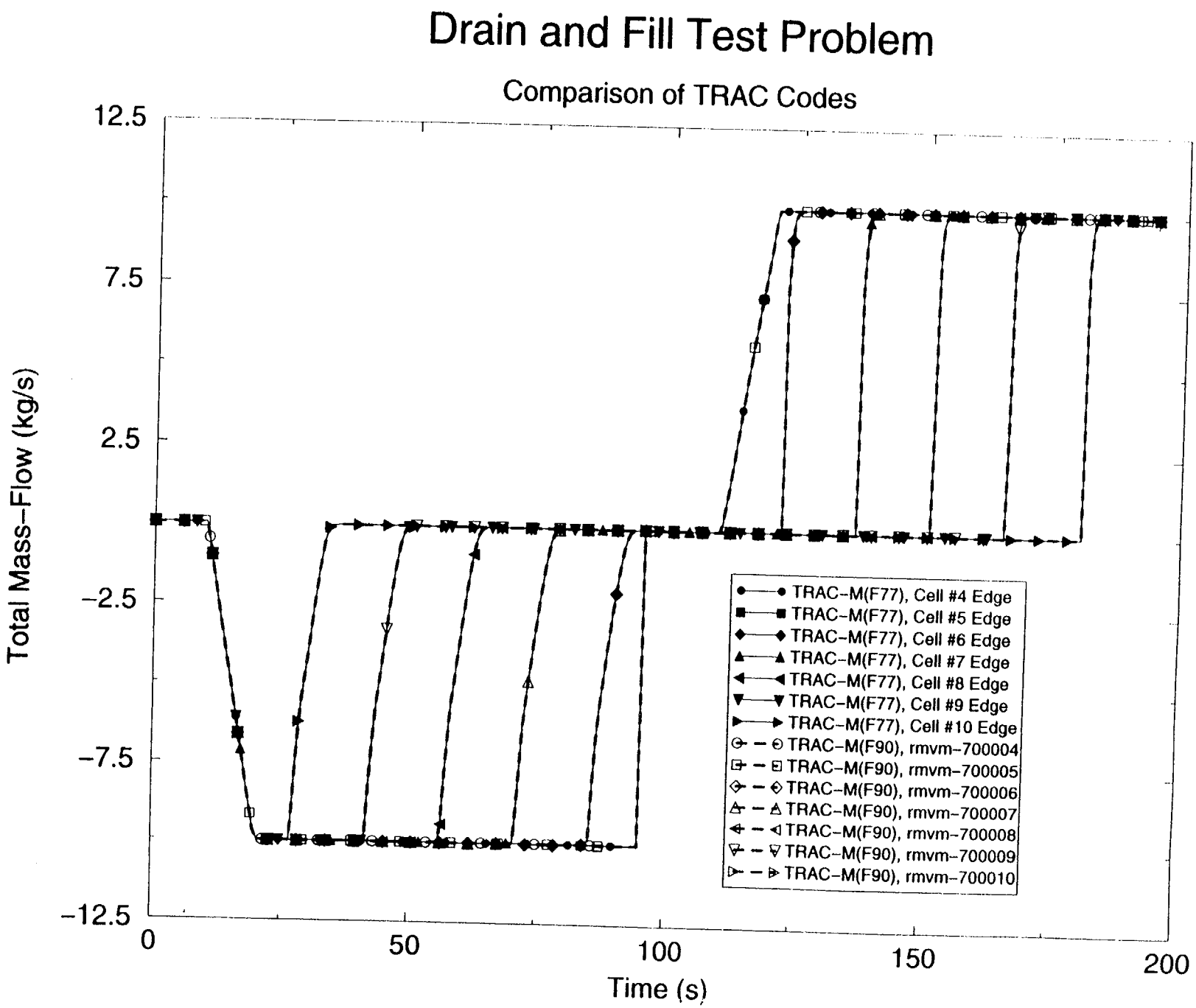

Figure 3.2.3 Comparison of Mass Flow Predictions in DRAIN and FILL Test Problem

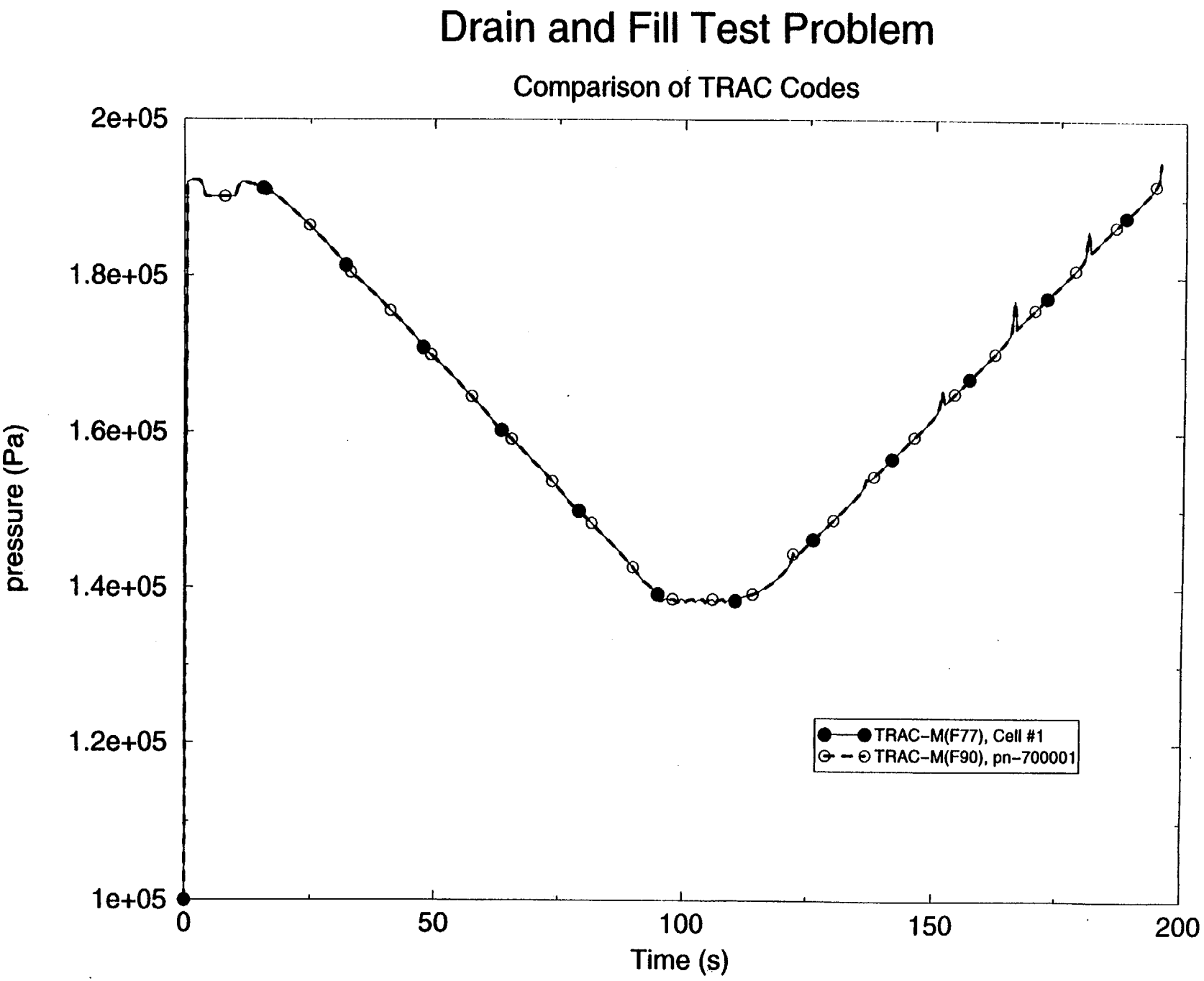

Figure 3.2.4 Comparison of Pressure Predictions in DRAIN and FILL Test Problem

3.3 U-Tube Test Problem (UTUBE)

This test problem (illustrated in Fig. 3.3.1) consists of a single pipe representing a U-tube that is ~6.8 m high. Both legs of the U-tube are connected to constant-pressure BREAK components. Under the initial conditions, the liquid level in one leg is 0.3 m higher than the liquid level in the other leg. This results in a U-tube oscillation that has a period (Ref. 3.2) of

$$\tau = 2\pi\sqrt{L/2g} = 2.954s$$

Fig. 3.3.2 shows that the periods calculated by TRAC-M(F77) and TRAC-M(F90) for the U-tube oscillation are almost identical. The period is ~3.1 s. In addition, it is apparent that the gas volume fraction oscillation in cell 6 is the same as the gas volume fraction oscillation in cell 10, with the exception that the oscillations in cells 6 and 10 are out of phase. That is, when the cell 6 gas volume fraction peaks high, the cell 10 gas volume fraction peaks low, and conversely. However, because of wall friction in the pipe, the amplitude of the gas volume fraction oscillation should decay to zero. However, the gas volume fraction oscillation does not completely dampen out in either calculation because of the time and spatial averaging used to calculate the interfacial shear between cells 6 and 7 and between cells 9 and 10. For relatively large time-steps, the time averaging model for the interfacial shear tends to move closer to the new time interfacial shear. Some time averaging of the interfacial shear is required for stability. The oscillations can be reduced through finer noding, reduced maximum time-step size, or increased wall drag. Fig. 3.3.3 shows that the oscillations dampen out considerably when the maximum time-step size is reduced from 0.05 s to 0.01 s. Overall, the agreement between TRAC-M(F77) and TRAC-M(F90) predictions is "Excellent."

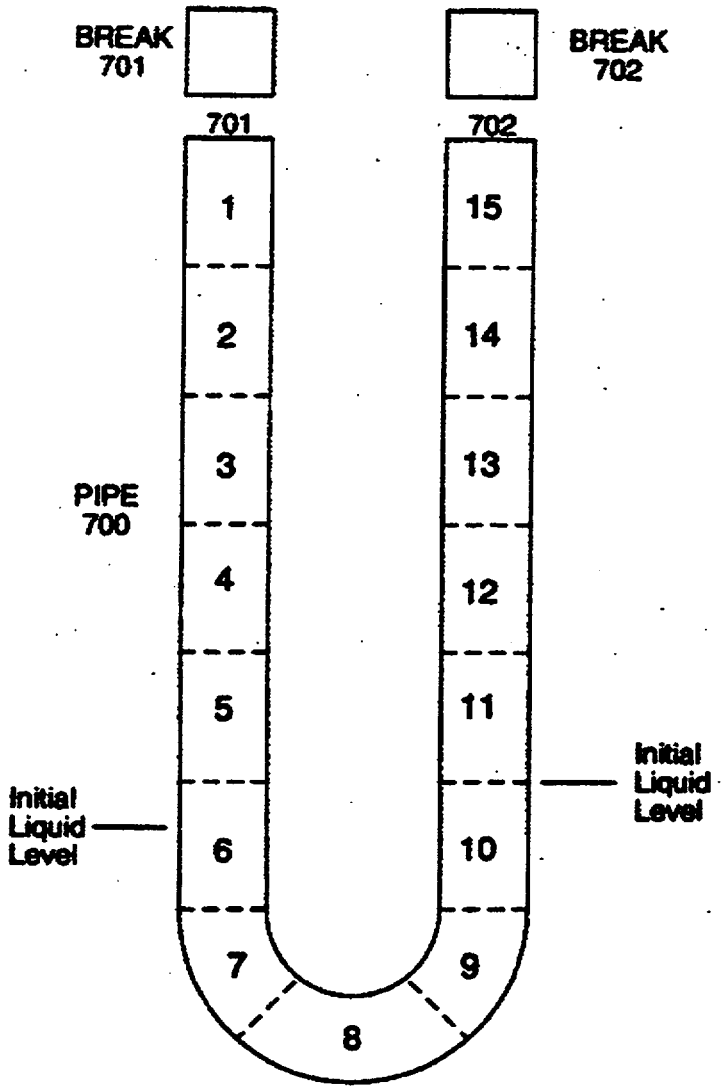

Figure 3.3.1 TRAC Model of the UTUBE Test Problem

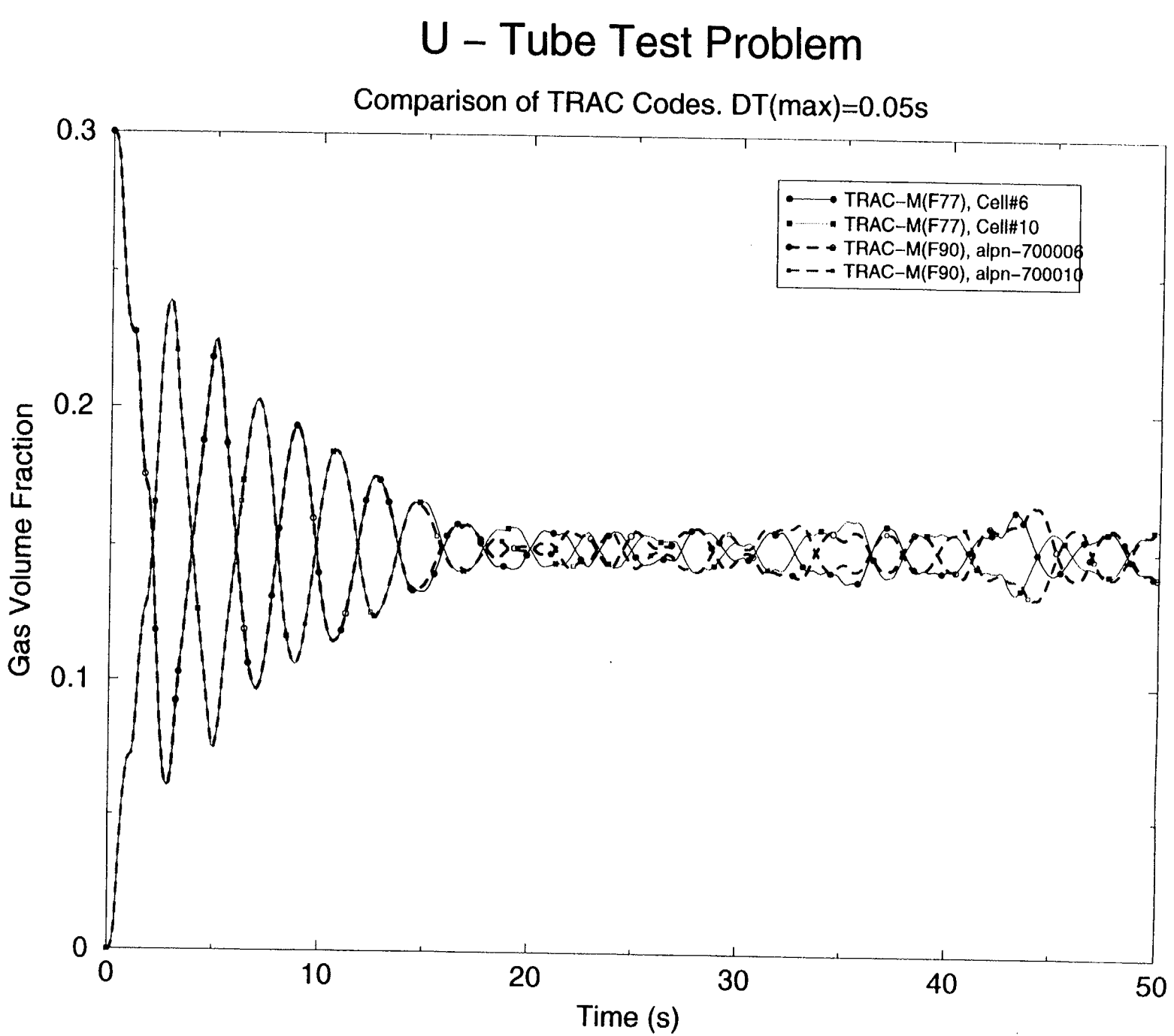

Figure 3.3.2 Comparison of Gas Volume Fraction Oscillations in the UTUBE Test Problem, DT(max)=0.05s

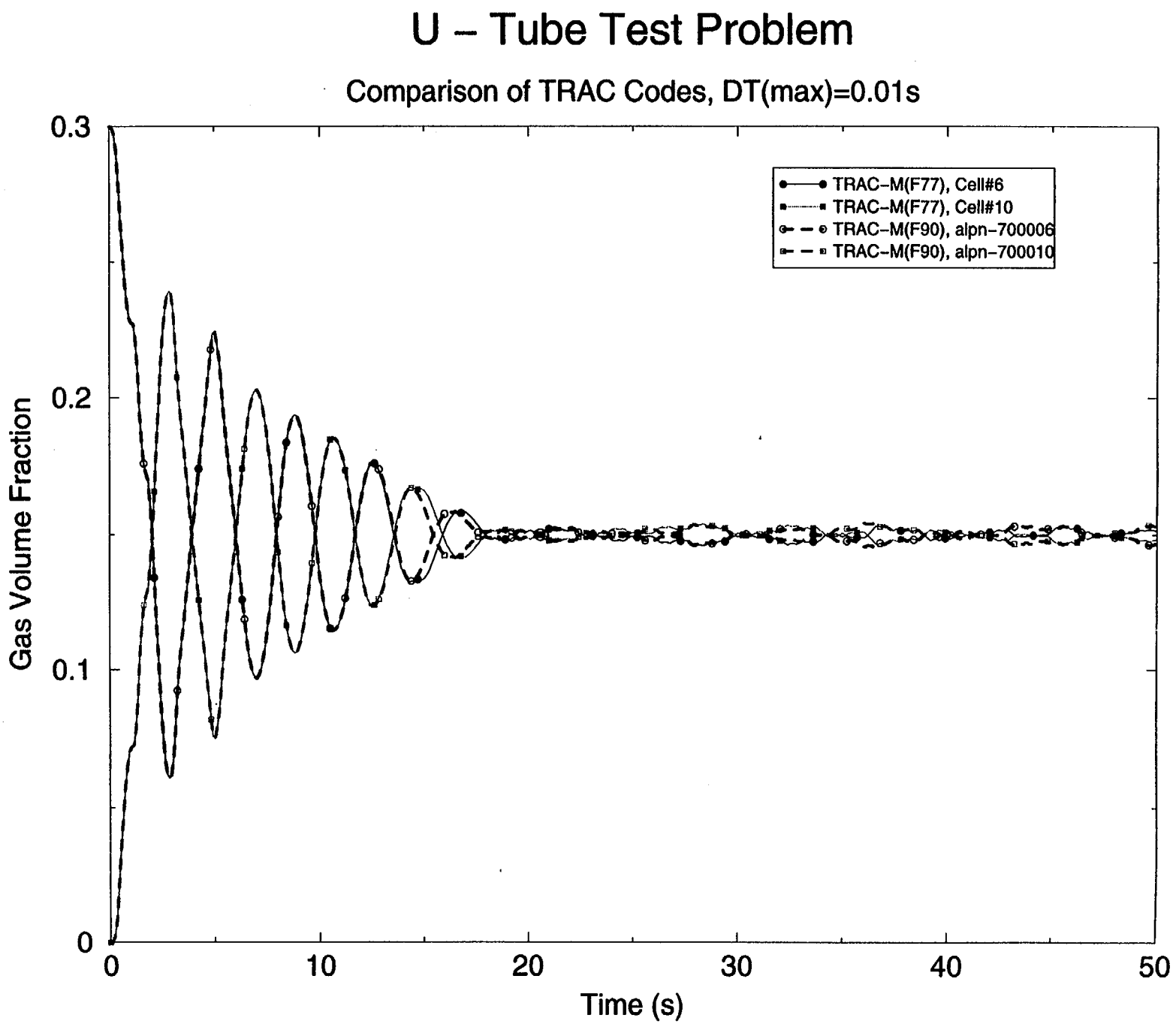

Figure 3.3.3 Comparison of Gas Volume Fraction Oscillations in the UTUBE Test Problem, DT(max)=0.01s

3.4 Conclusions

Analytical test problem comparisons show that the TRAC finite-difference solution to the heat conduction equations in rod geometries is accurate. The hydro models are also accurate and stable during the filling and draining of cells. The conversion from TRAC-M(F77) to TRAC-M(F90) has been successful for these applications and other cases in the Standard Assessment Test matrix. The files for all other cases are available for review by interested parties.

REFERENCES

3.1 Carslaw, H.S., and J.C. Jaeger, *Conduction of Heat in Solids*, Clarendon Press, Oxford, 1959.

3.2 Streeter, V.L., and E.B. Wylie, *Fluid Mechanics*, McGraw-Hill Book Company, New York, 1975.

4. PWR Developmental Assessment

This chapter presents results of a developmental assessment of TRAC-M(F77), Version 5.50 and TRAC-M(F90), Version 3690 using the separate effects test (SET) and integral effects test (IET) data for PWRs. The test matrix has been used in Ref. 1.2 in the developmental assessment of TRAC-M(F77). Since no physics modeling has been changed between these two codes, it is expected that calculations obtained from exercising these two versions should be close to each other. There will be some differences because of some error corrections in TRAC-M(F90). As long as these error corrections do not change conclusions on the capabilities of the codes to predict the separate effects phenomena and integral effects test results, conversion of TRAC-M(F77) to TRAC-M(F90) will deem acceptable. As the results of calculations show, the comparisons are "Excellent" or "Reasonable."

4.1 Countercurrent Flow Limitation

The countercurrent flow limitation (CCFL) is defined when the downward flowing liquid in a countercurrent flow is about to change its direction to flow upward. This condition can be attained if the upward steam flow rate is increased, while the liquid is flowing downward. Depending upon the geometry of the equipment used, the occurrence of the CCFL varies. In reactor applications, CCFL can occur at flow area restrictions when liquid flows downward through rising gas or vapor. For example, in the upper tie-plate region of a PWR during reflood, the upward flow of steam can prevent or limit the downflow of liquid, thereby causing the rods to cool less than they otherwise would.

In TRAC-M, a special model allows the user to invoke characteristic CCFL correlations at specific locations. Rather than try to develop a new mechanistic CCFL model that could predict the complex behaviors in a variety of geometrical configurations, TRAC enables the user to apply a CCFL correlation for a specific geometry and apply it at a specific location.

4.1.1 Bankoff Tests

This section assesses the CCFL model against the data of Bankoff et al. (Ref. 4.1.1).

4.1.1.1 Test Facility

As illustrated in Fig. 4.1.1, the experimental apparatus used by Bankoff et al. was a vertical channel with a flow area of 31 cm^2. The air-water experiments were used to determine CCFL independent of the effects of phase change. The air was introduced below a perforated plate, while the water was introduced to the upper-plenum chamber and overflowed to drain. This test was used to assess the capability of TRAC to predict CCFL with a 15-hole geometry corresponding to a small segment of the upper tie plate of a PWR.

Pressure and temperature measurements were available at various places, and air and water flow rates were measured using rotameters. The test procedure used in the air-water tests consisted of establishing the water inlet flow rate, increasing the air flow rate, and determining the water delivery rate at each step until a point of essentially zero downward delivery was finally obtained. That point is defined as the CCFL.

4.1.1.2 TRAC Model

Fig. 4.1.2 illustrates the TRAC CCFL model. The test section is modeled with a 1-D VESSEL component with 11 axial cells. The rectangular perforated plate is located at the interface between the fifth and sixth cells, and the flow area of all 15 holes is specified at this interface. The hydraulic diameter of 10.5 mm is the same as that of the hole diameter. The water injection PIPE component is connected to the middle of the water pool that initially existed in cells 6 through 9. The height of this water pool is controlled by the drain tube, which is modeled by a PIPE component, and horizontally connected to cell 9. The other side of the drain tube is connected to an atmospheric BREAK component. Downward flowing water is collected at the bottom of the vessel, which is connected to a zero FILL boundary condition. The volume of the bottom level of the VESSEL component is sufficient for water flowing through the tie plate to accumulate. The air flows through an air outlet pipe to a BREAK component.

The TRAC CCFL model allows the user to input the characteristic flooding curve parameters for a specific geometry applied at a particular location. Typically, these parameters have been developed from experimental data for the geometry of interest, or for hardware of at least similar dimensions. Bankoff et al. have shown that the data correlate well with the relationship

$$H_g^{1/2} + MH_l^{1/2} = C, \tag{4.1.1.1}$$

where

H_g is the dimensionless gas flux,

H_l is the dimensionless liquid delivery,

C is the abscissa intercept, and

M is the slope.

The Bankoff relationship is sufficiently general that either Wallis scaling for diameter dependence, Kutaleladze scaling for surface-tension dependence, or a combination of the two can be implemented. The scaling is performed by defining a variable length scale in the determination of the dimensionless flux:

$$H_k = j_k\left(\frac{\rho_k}{g_c w \Delta\rho}\right)^{\frac{1}{2}} \tag{4.1.1.2}$$

$$w = HD^{1-B}L^B, \tag{4.1.1.3}$$

$$L = \left(\frac{\sigma}{g_c \Delta\rho}\right)^{\frac{1}{2}}, \tag{4.1.1.4}$$

where

k	refers to the phase (gas or liquid),
j	is the superficial velocity,
HD	is the hydraulic diameter,
g_c	is the gravitational constant,
σ	is the surface tension,
ρ	is the density,
$\Delta\rho$	is the difference between the phasic densities, and
B	is a factor between 0 and 1.

The correlation reverts to the Wallis scaling for $B = 0$, and to the Kutaleladze scaling for $B = 1$. For B between 0 and 1, the user can input the scaling proposed by Bankoff et al., which can be used for tie plate geometry even when no experimental data are available.

4.1.1.3 Comparison of Predicted and Measured Results

Parametric calculations have been performed by varying both TRAC-M(F77) and TRAC-M(F90). Figs. 4.1.3 and 4.1.4 show the liquid and air mass flow rates calculated by two codes. The agreement between predictions is "Excellent," and the frequency of oscillations of water downflow and air upflow agree with each other every well. The amplitudes also agree quite well. From these two figures, we conclude that the conversion from TRAC-M(F77) to TRAC-M(F90) has been successful for this type of application.

The rest of the analysis has been performed using the results obtained from TRAC-M(F77). Smoothing functions are applied to the mass flows as shown in Figs. 4.1.5 and 4.1.6, and the smoothed mass flows are then used to calculate the dimensionless fluxes $H_l^{1/2}$ and $H_g^{1/2}$, which are shown in Fig. 4.1.7.

Fig. 4.1.8 shows the TRAC-M(F77) results for the flow of air and water at 1 atm, along with the correlation of the Bankoff data. The TRAC input parameters for the Bankoff data are B = 0.884, M = 1, and C = 1.92. As demonstrated, the TRAC results agree quite well with the experimental data of Bankoff. Thus, it is expected that when the TRAC CCFL option is used at a given location with appropriate input parameters for the flooding curve, the liquid downflow will be predicted reasonably well for plates that are similar to those used in the Bankoff experiment (as well as other types of plates). Since liquid and air mass flow rates calculated by TRAC-M(F90) are in excellent agreement with those calculated by TRAC-M(F77), we expect similar agreement with the experimental data of Bankoff when the TRAC-M(F90) code is used.

4.1.1.4 Conclusions

The TRAC CCFL model allows the user to input the characteristic flooding curve parameters for a specific geometry applied at a particular location. When used to predict the air-water CCFL data obtained by Bankoff et al., this model gave reasonable results in predicting the CCFL. The assessment is limited to air-water mixtures at atmospheric conditions, and the current code CCFL model for steam-water mixtures is not assessed. The assessment will be extended to cover steam-water mixtures in a future program.

The conversion from TRAC-M(F77) to TRAC-M(F90) has been successful for this type of application.

REFERENCES

4.1.1 Bankoff, S.G., R.S. Tankin, M.C. Yuen, and C.L. Hseih, "Countercurrent Flow of Air/ Water and Steam/Water Through a Horizontal Perforated Plant," *Int. J. Heat Mass Transfer* 24(8), 1381–1385, 1981.

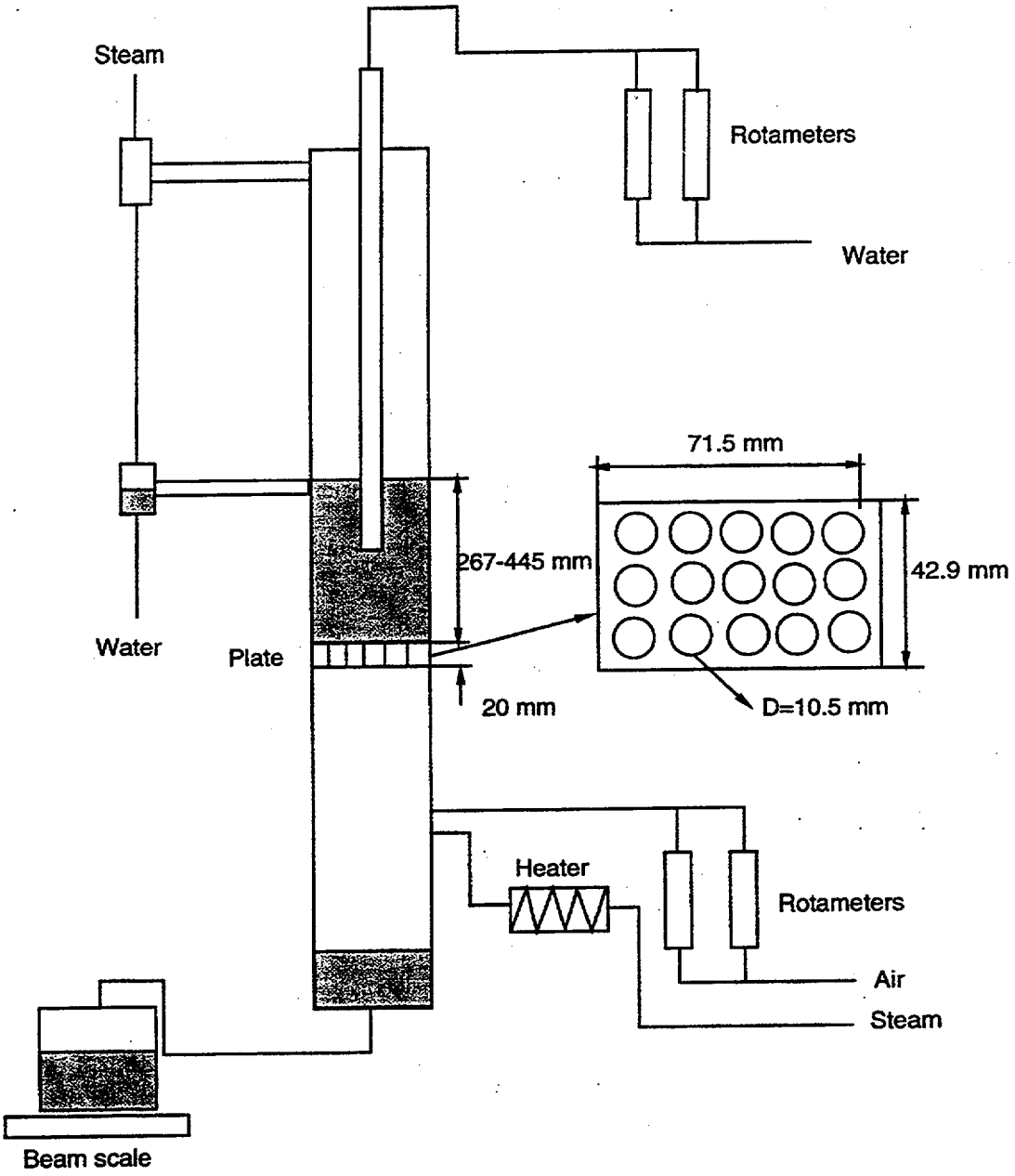

Figure 4.1.1 Sketch of the Perforated Plate Air-Water Countercurrent Flow System Used by Bankoff et al.

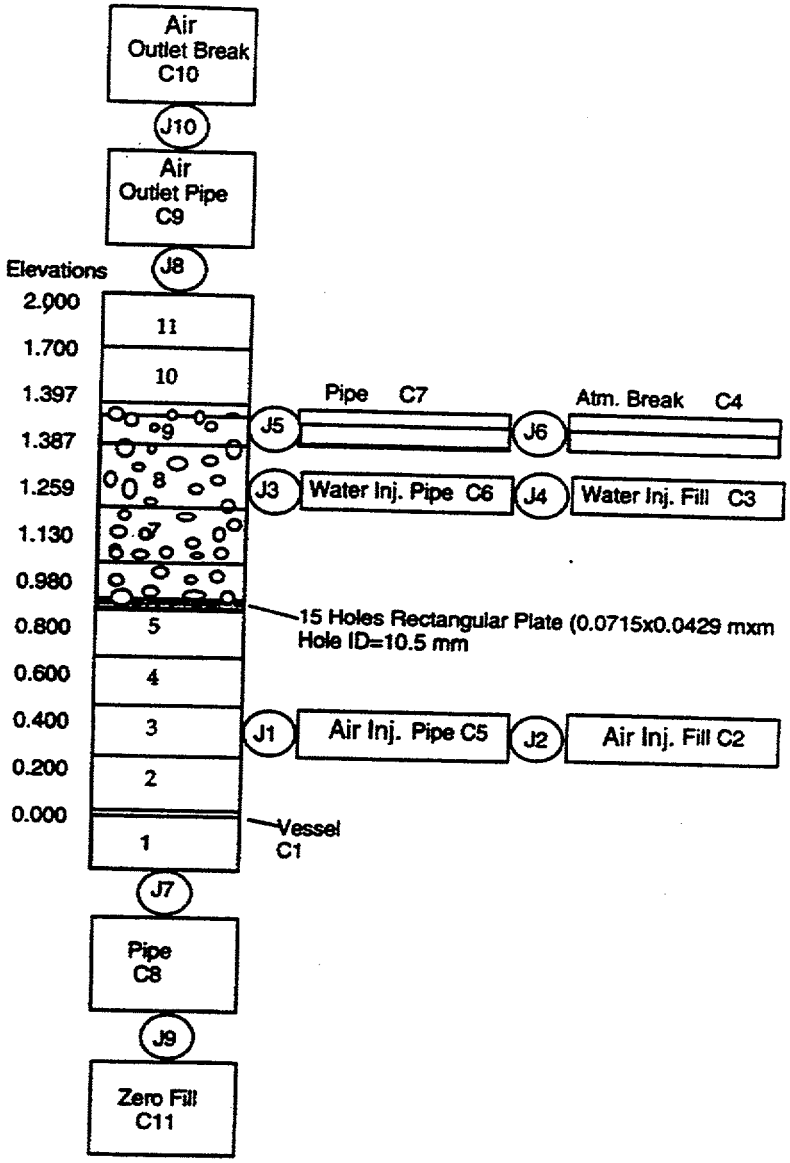

Figure 4.1.2 TRAC Model for the Test Apparatus Used by Bankoff et al.

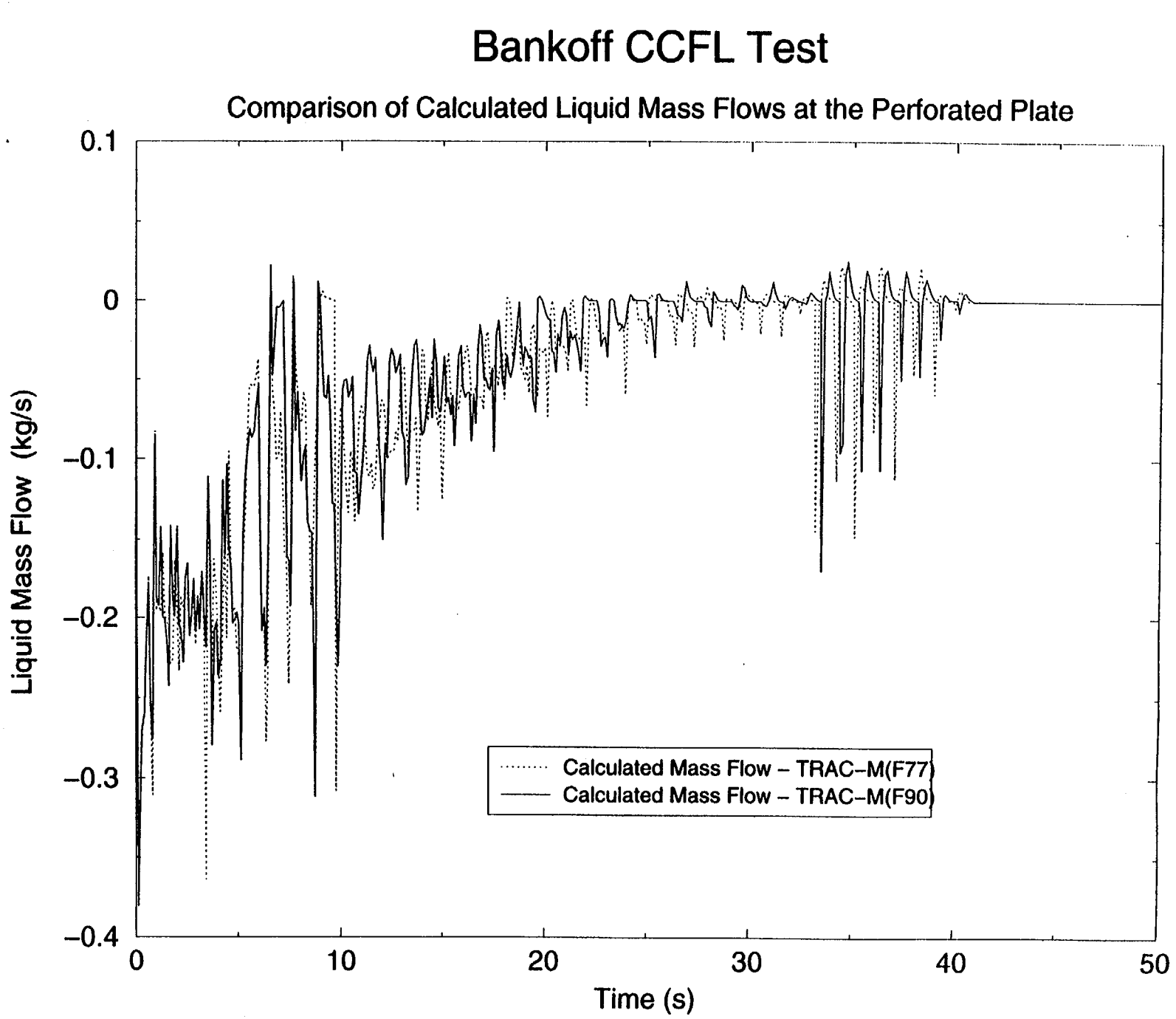

Figure 4.1.3 Comparison of Calculated Liquid Mass Flows at the Perforated Plate in the Bankoff CCFL Test

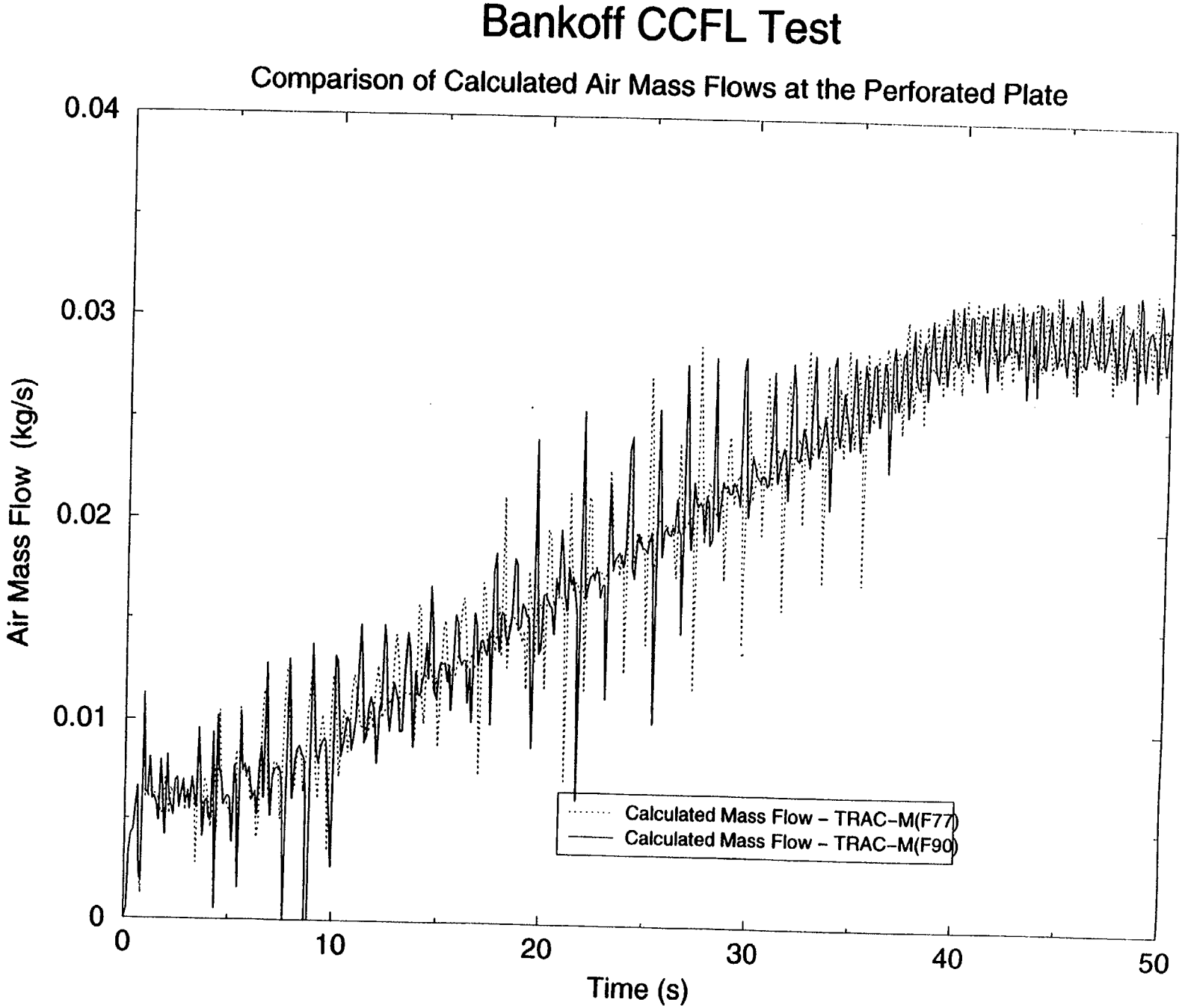

Figure 4.1.4 Comparison of Calculated Air Mass Flows at the Perforated Plate in the Bankoff CCFL Test

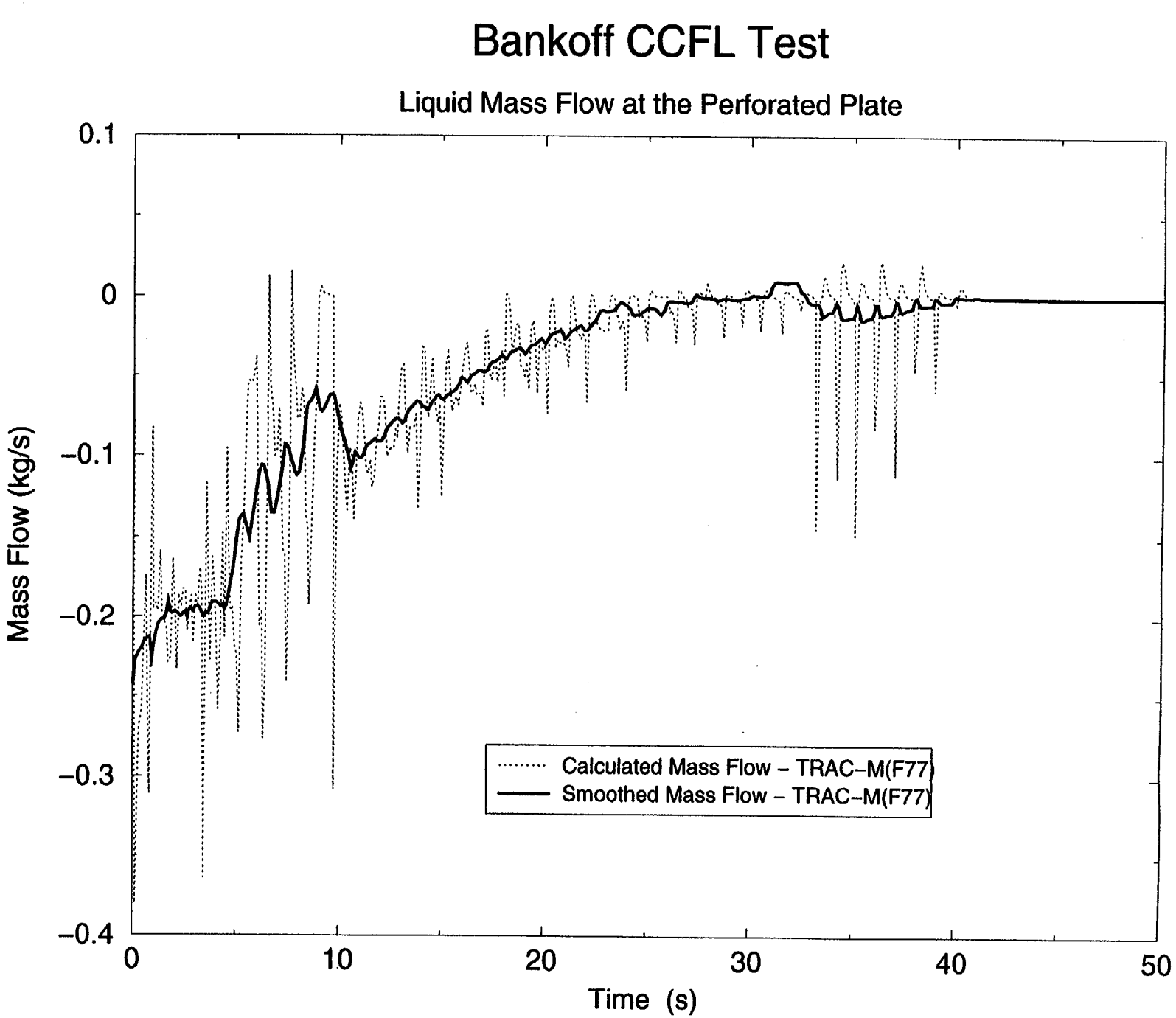

Figure 4.1.5 Liquid Mass Flow at the Perforated Plate in the Bankoff CCFL Test

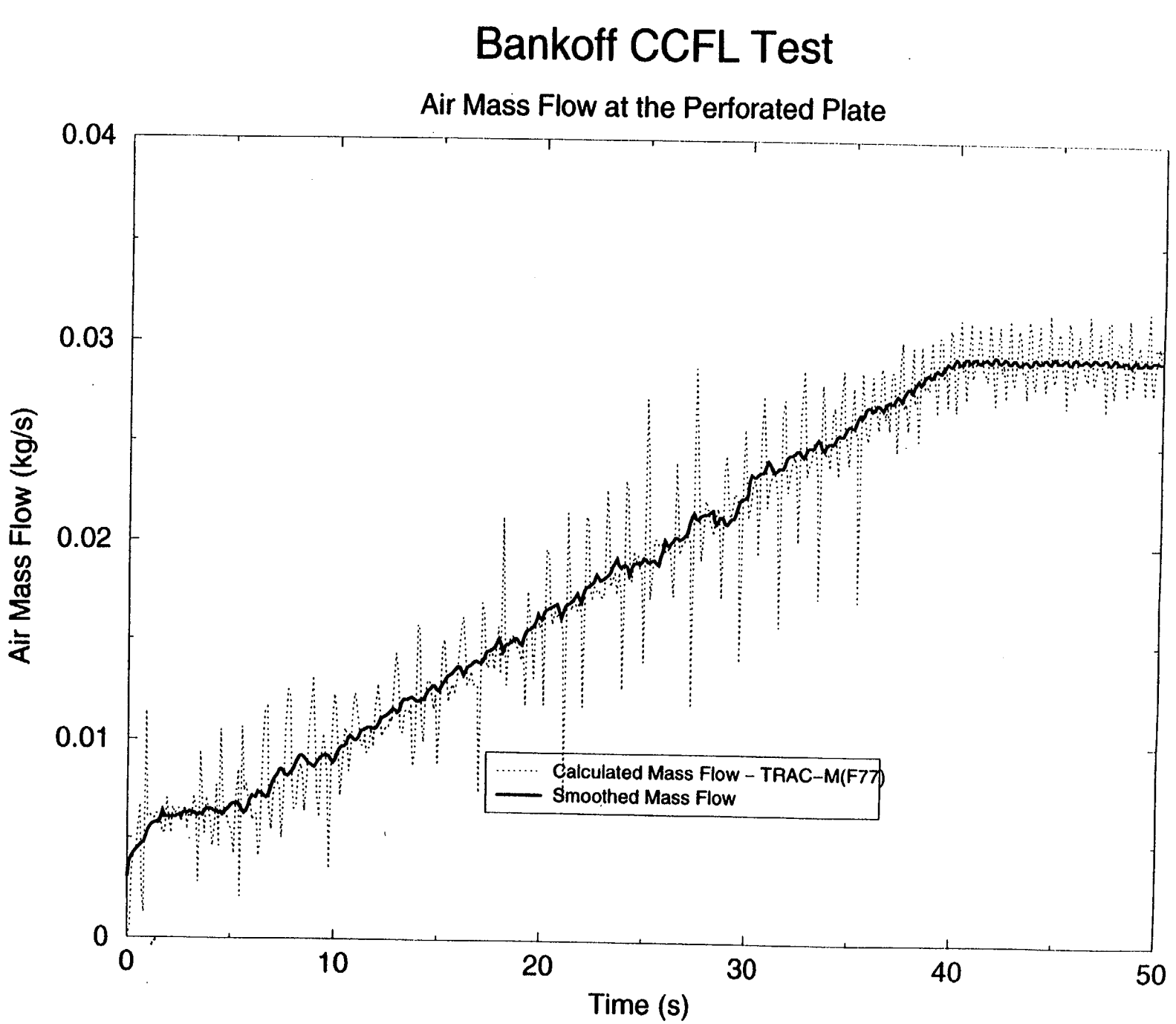

Figure 4.1.6 Air Mass Flow at the Perforated Plate in the Bankoff CCFL Test

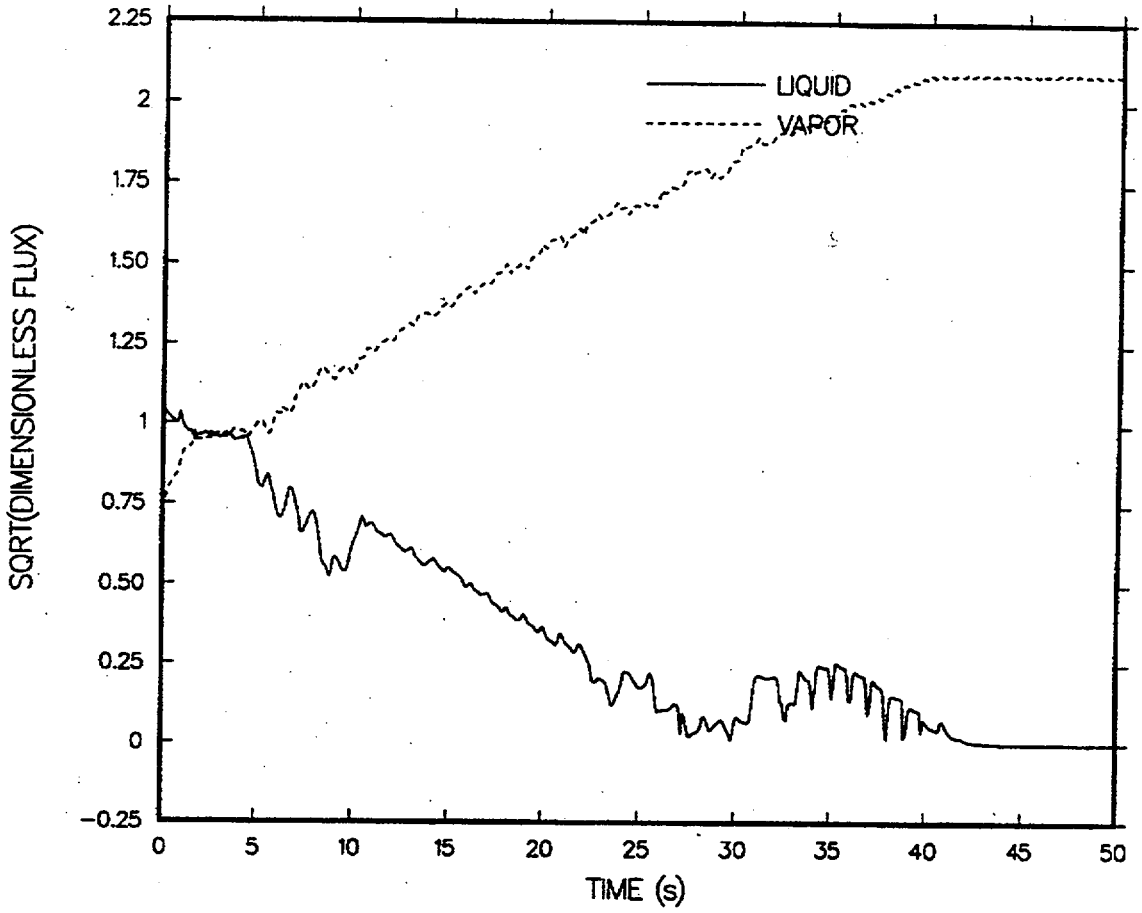

Figure 4.1.7 Liquid and Air Dimensionless Fluxes at the Perforated Plate in the Bankoff CCFL Test

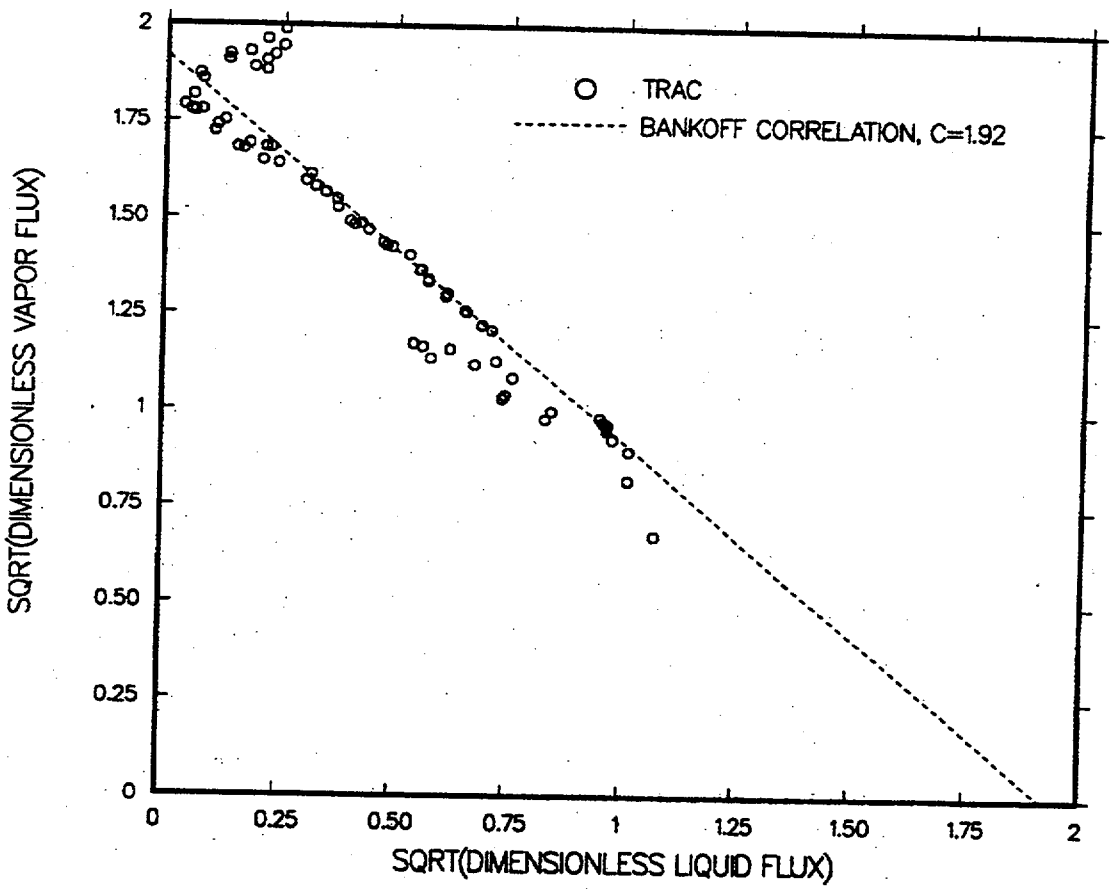

Figure 4.1.8 Comparison of TRAC Results with Bankoff Correlation

4.2 Condensation

When a thermal-hydraulic (T/H) analysis of PWRs is performed to calculate the consequences of a small-break loss-of-coolant accident (SBLOCA) or a large-break loss-of-coolant accident (LBLOCA), direct contact occurs between subcooled liquid and steam after the emergency injection system is turned on. This contact causes a violent pressure transient and a phenomenon similar to a water hammer. Consequently, the prediction of the correct interfacial condensation rate for a variety of flow regimes is very important for LOCA analyses. The condensation model used in TRAC-M is founded upon the Chen-Mayinger condensation correlation. The details of the model with its limitations and applicability range are discussed in the TRAC-M/FORTRAN 90 (Version 3.0) Theory Manual (Ref. 2.1). The assessment of the model against small-scale, separate effect data will be discussed in the following subsections.

4.2.1 Akimoto Tests

The data and correlations for this assessment are taken from Akimoto et al. (Refs. 4.2.1 and 4.2.2), and the same test section was used in all experiments. The experimental facility is illustrated in Fig. 4.2.1. The test section was horizontal, 3.35 m long, and 0.02 x 0.05 m in rectangular cross-section. The steam produced by a steam generator was injected at one end of the test section after it was metered. The subcooled water was injected 1.5 m downstream of the steam entrance, with an injection tee along the entire width of the test section. The test section was transparent, which allowed flow visualizations. The two-phase fluid was emptied to an exit tank that was exhausted to the atmosphere.

4.2.1.1 Condensation Experiments

Akimoto et al. observed distinct oscillatory and stable wavy flow regimes. The water was injected after the steam flow rate was established. When the steam flow rate was small relative to the liquid injection rate, the downstream of the test section was plugged by water while the upstream of the section was filled with steam. The liquid plug traveled back and forth from the liquid injection point to the channel exit. Oscillations were caused by changing condensation rates and pressures, and their frequencies and amplitudes changed with the steam injection rate. When the liquid injection point was fully exposed to the steam, rapid condensation led the local pressure to drop below that of the channel exit. This forced the liquid plug to move toward the channel entrance. When the plug moved upstream of the liquid injection point, this movement insulated the injected liquid from the steam. The decreasing condensation rate caused the local pressure to increase until the plug moved toward the channel exit, and a new oscillation began.

When the steam flow rate was sufficiently large relative to the liquid injection rate, the liquid plug was swept away from the test section, and a stratified flow regime with mist flow on top and stable wavy liquid film flow at the bottom was established in the test section.

Akimoto et al. (Refs. 4.2.1 and 4.2.2) reported the following simple relation for the boundary between the oscillatory and stable flow regimes:

$$M_v = 0.84 M_{c,max} \tag{4.2.1.1}$$

and

$$M_{c,max} = \frac{C_{pl}\{T_{sat}(P_{exit}) - T_{li}\}}{h_{lg}} M_{li} \qquad (4.2.1.2)$$

where

M_v is the mass flux of the injected steam,

M_{li} is the mass flux of the injected liquid through the steam flow channel,

C_{pl} is the specific heat of the injected liquid,

h_{lg} is the injected liquid's latent heat of vaporization,

$T_{sat}(P_{exit})$ is the saturation temperature at atmospheric pressure,

T_{li} is the injected liquid's temperature, and

$M_{c,max}$ is defined by Akimoto et al. as the condensability of the injected water.

The condensability is a measure of the maximum mass flux of the steam that the injected water can condense before reaching thermal equilibrium, assuming a complete mixing of water with steam (Ref. 4.2.2).

4.2.1.2 TRAC Model

The TRAC input model for this facility is shown in Figs. 4.2.2 and 4.2.3. Two TEE components were used to simulate the horizontal test section and the exit tank. The rectangular cross-section is considered to be a circular geometry, with a hydraulic diameter of 0.286 m and actual flow area of 0.001 m^2. The node sizes are selected in such a way that the length-to-diameter (L/D) ratio is similar to that used in full plant analyses.

4.2.1.3 Comparison of Measured and Predicted Results

The following subsections discuss the assessment results and the analysis of the stratified mist flow, oscillatory plug flow, and transition from stable to oscillatory flows. Both TRAC-M(F77) and TRAC-M(F90) were run to predict the test data.

4.2.1.3.1 Stratified-Mist Flow

When the steam flow rate is high ($M_v/M_{c,max} > 0.84$), Akimoto et al. observed that the injected liquid was quickly atomized into droplets immediately downstream of the injection nozzle. The mixing process in the injection region was described as very rapid and complicated. Some coalesced droplets eventually reattached to the wall, and formed a wavy liquid film at the bottom of the test section.

The liquid film temperature is determined by the condensation rate of steam, and was measured as a function of distance from the injection nozzle. For the purpose of this assessment, we chose the test results given in Fig. 4 of Ref. 4.2.1, with the following test conditions:

steam mass flux =40 $kgm^{-2}s^{-1}$

injected liquid mass flux =330 $kgm^{-2}s^{-1}$

injected liquid temperature =323 K

The predicted and measured liquid film temperatures are plotted in Fig. 4.2.4 as a function of the distance from the injection nozzle. The predicted temperatures correspond to t = 150 s because they remain constant. The liquid entering the test section is subcooled to 323 K. Shortly downstream (0.1 m), experimental data indicate that the liquid is heated up to 361.6 K, whereas, the calculated liquid temperature at this location is 358.0 K (indicating a disagreement of only 3.6 K between calculated and measured data). The predicted and measured values at 0.2 m downstream of the injection point are almost the same (366.4 and 365.7 K, respectively). At 0.3 m downstream of the injection point, the predicted and measured values (369.6 and 368.8 K) also agree very well. The correct prediction of the liquid film temperature indicates that the TRAC condensation model (including the heat transfer coefficient and the interfacial area) for the mist flow adequately predicts the rate of condensation and is expected to predict a reasonably correct rate of condensation for the stratified-mist flow regime encountered in LOCA situations. Since both code predictions are essentially the same, the conversion of TRAC-M(F77) to TRAC-M(F90) for this application is successful.

4.2.1.3.2 Oscillatory Plug Flow

Unstable flow with regular oscillations occurred when the liquid injection rate was increased. Akimoto et al. classified the oscillatory flow regime into three subregimes, identified as Type-A, Type-B, and Type-C. Type-A flow included very well-defined oscillatory behavior. The test reported in Fig. 5 of Ref. 4.2.2, performed with 20 $kgm^{-2}s^{-1}$ steam and 600 $kgm^{-2}s^{-1}$ water mass fluxes, exhibited well-defined oscillatory behavior. This test was selected for assessment. Type-B flow included not so well-defined oscillatory behavior, while Type-C flow exhibited only small interface fluctuations and did not exhibit any periodicity.

The predicted pressure trace at the injection location shown in Fig. 4.2.5 indicates that the pressure oscillated between 36.8 to 335.8 kPa. Table 4.2.1 lists the measured and calculated frequencies and amplitudes of the pressure. Notably, the amplitudes of the predicted pressure oscillation are higher than those measured. Nonetheless, a count of the number of oscillations between 15 and 40 s yielded a predicted oscillation frequency of 1.73 s^{-1}, which agrees reasonably well with the measured data of 1.67 s^{-1}. (See Fig. 4.2.6.)

As seen in Figs. 4.2.7 and 4.2.8, a pressure increase near the liquid injection point (cell 4) corresponds to both a decrease in the void fraction in cell 4 and an increase in the void fraction in cell 13, clearly indicating that a plug of water is moving toward the steam injection point. When the plug moves upstream of the injection point, the condensation at the liquid-steam interface continues, heating up the liquid and eventually reducing the condensation rate. The pressure then continues to rise, and causes the plug movement to reverse, thereby exposing the injection point to the steam. When the injection point is exposed to the inflowing steam, a rapid condensation

occurs and the pressure drops below that of the exit tank. The plug of water then starts to move toward the injection point again, and a new oscillation follows the same history.

Despite the complexity of the phenomenon described above, the frequencies and minimum pressures predicted by both codes agree reasonably well with the measured data. The overprediction of the maximum pressures can be explained if the condensation rate is underpredicted when the liquid steam interface passes the liquid injection point, where the condensation rate should reach a maximum. Inadequate modeling of the pressure losses can be another reason for the overprediction of the maximum pressure. Further investigation is needed to correctly identify the cause.

4.2.1.3.3 Stable-to-Oscillatory Flow Transition

This section assesses the ability of TRAC to predict oscillatory condensation, and compares the results with the transition correlation of Akimoto et al. (Eq. 4.2.1.1). In order to assess this capability, a test was designed in which the liquid flow rate for a given steam flow rate in the stable flow region is increased until the flow starts to show some oscillations. It is assumed that an oscillatory flow occurs when the amplitude of the pressure oscillations is $>\pm 15\%$.

Fig. 4.2.9 shows how the steam and ECC injection flow rates were varied during this test, while Fig. 4.2.10 shows the results of oscillations calculated by TRAC-M(F77) and TRAC-M(F90). Figs. 4.2.11 through 4.2.13 contain the pressure oscillation traces for different portions of the transient. The predicted results and experimental observations are presented in Fig. 4.2.14, which plots the steam mass flux as a function of the condensability, given by Eq. 4.2.1.1.

When the ratio $M_v/M_{c,max}$ becomes smaller than the experimental value of 0.84 at a given liquid flow rate, the liquid plugs the channel because the steam provided is not sufficient to overcome the condensate energy of the injected liquid. As shown in Fig. 4.2.14, the experimental constant of 0.84 in Eq. 4.2.1.1 is reasonably predicted for the stable-to-oscillatory flow transition for lower mass fluxes. However, for the higher steam flux, both versions of TRAC overpredict the condensability. The prediction of condensation rate depends on predictions of the condensation heat transfer coefficient (HTC) and the interfacial area. Unfortunately, no experimental data are available from Akimoto's tests to determine which parameter is overpredicted.

4.2.1.4 Conclusions

In both stable and mist-flow regimes, the TRAC condensation model yielded good predictions of the liquid temperature along the test section measured by Akimoto et al. The results indicated that the rate of condensation in the mist-flow regime was predicted reasonably well; therefore, it is expected that the model will also give reasonable results for a similar range of operating parameters in the mist-flow regime (i.e., *lower* steam mass flux) when it is used in full-plant simulations.

The model also predicted the frequency of oscillations when the plug flow is considered. The motion of the plug in the predictions was similar to that described by Akimoto et al. and the mimimum pressure agreed with the data; however, the predicted pressure amplitude disagreed with the measured data, and the maximum peak pressure was overpredicted. The overpredicted

maximum pressure could be attributable to the overprediction of the condensation rate when the steam-water interface was upstream of the injection point. In addition, the transition from stable to oscillatory flow was reasonably predicted for a steam mass flux at or below 40 $kgm^{-2}s^{-1}$. For a higher steam flux, the condensability was overpredicted.

Since predictions obtained using both TRAC-M(F77) and TRAC-M(F90) are essentially the same, the conversion of TRAC-M(F77) to TRAC-M(F90) is successful for this application.

REFERENCES

4.2.1 Akimoto, H., Y. Tanaka, T. Kozwa, A. Inoue, and S. Aoki, "Oscillatory Flows Induced by Direct-Contact Condensation of Flowing Steam with Injected Water," *J. Nucl. Sci. Tech.* 22(4), 269–283, 1985.

4.2.2 Akimoto, H., Y. Kozawa, A. Inoue, and S. Aoki, "Analysis of Direct Contact Condensation of Flowing Steam onto Injected Water with Multifluid Model of Two-Phase Flow," *J. Nucl. Sci. Tech.* 20 (12), 1006–1022, 1983.

Table 4.2.1 Data Comparison in the Junction Cell of the Test Section

Type	Experiment	TRAC-M(F77)	TRAC-M(F90)
Oscillation Frequency (s^{-1})	1.67	1.58	1.65
Maximum Pressure (kPa)	140	335	400
Minimum Pressure (kPa)	40	37	37

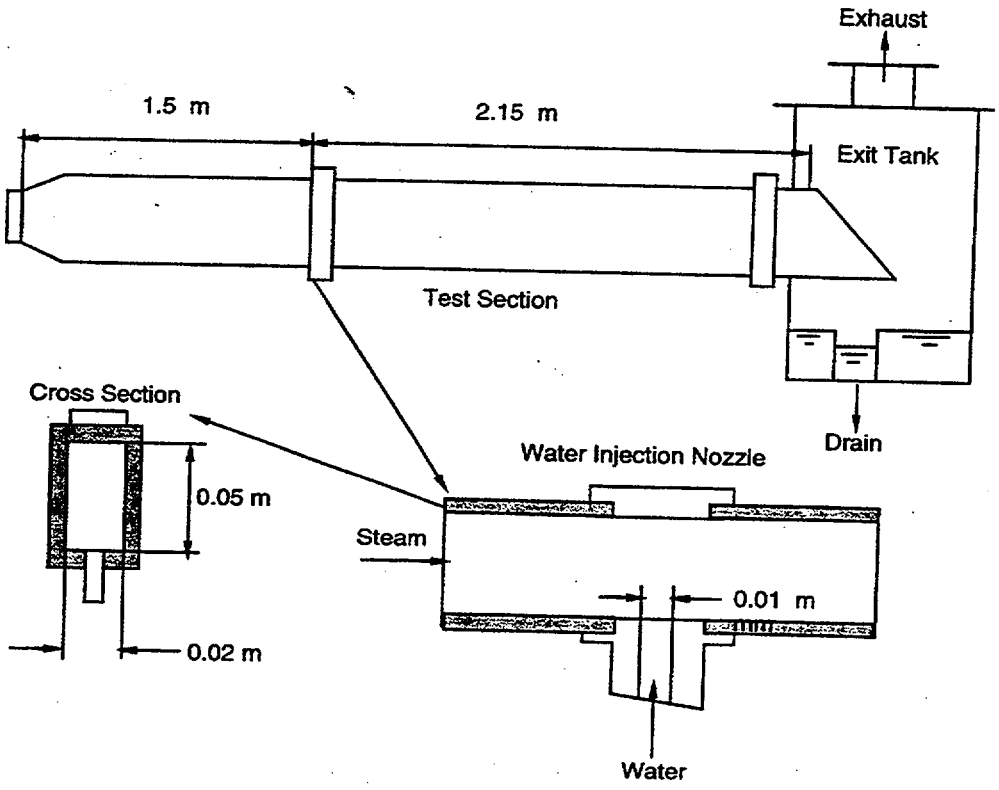

Figure 4.2.1 Sketch of the Experimental Apparatus of Akimoto et al.

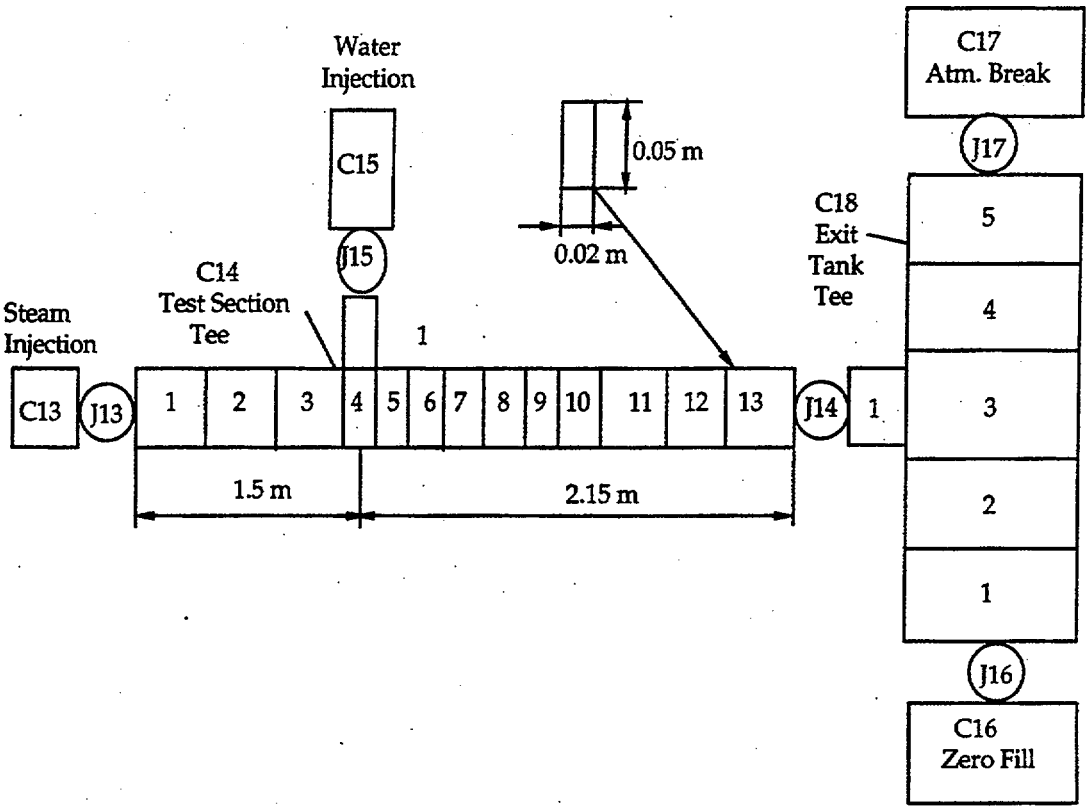

Figure 4.2.2 TRAC Input Model

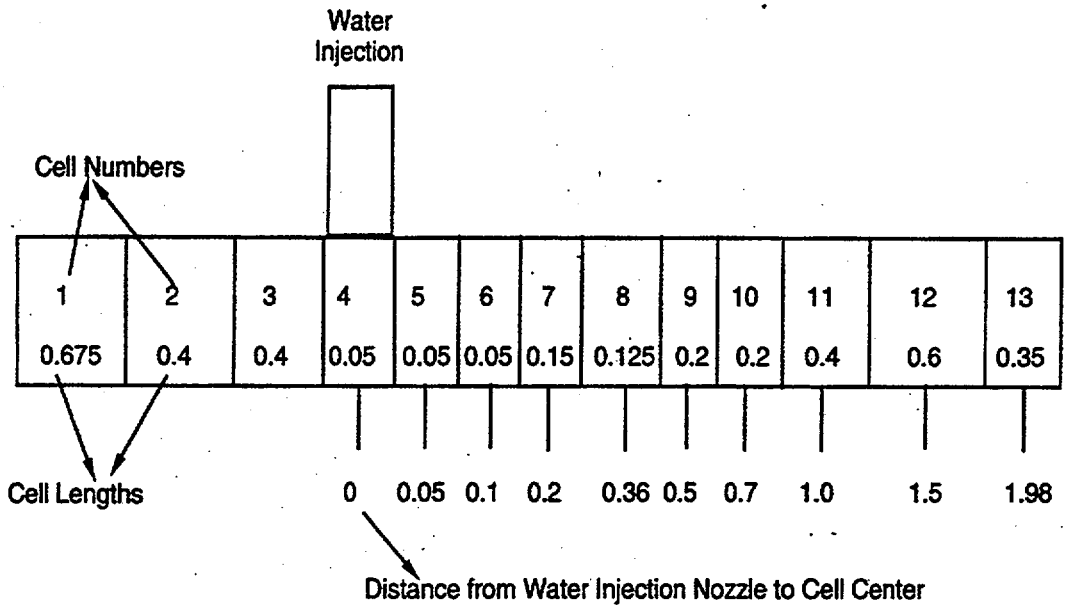

Figure 4.2.3 Noding Cell Lengths of the Test Section

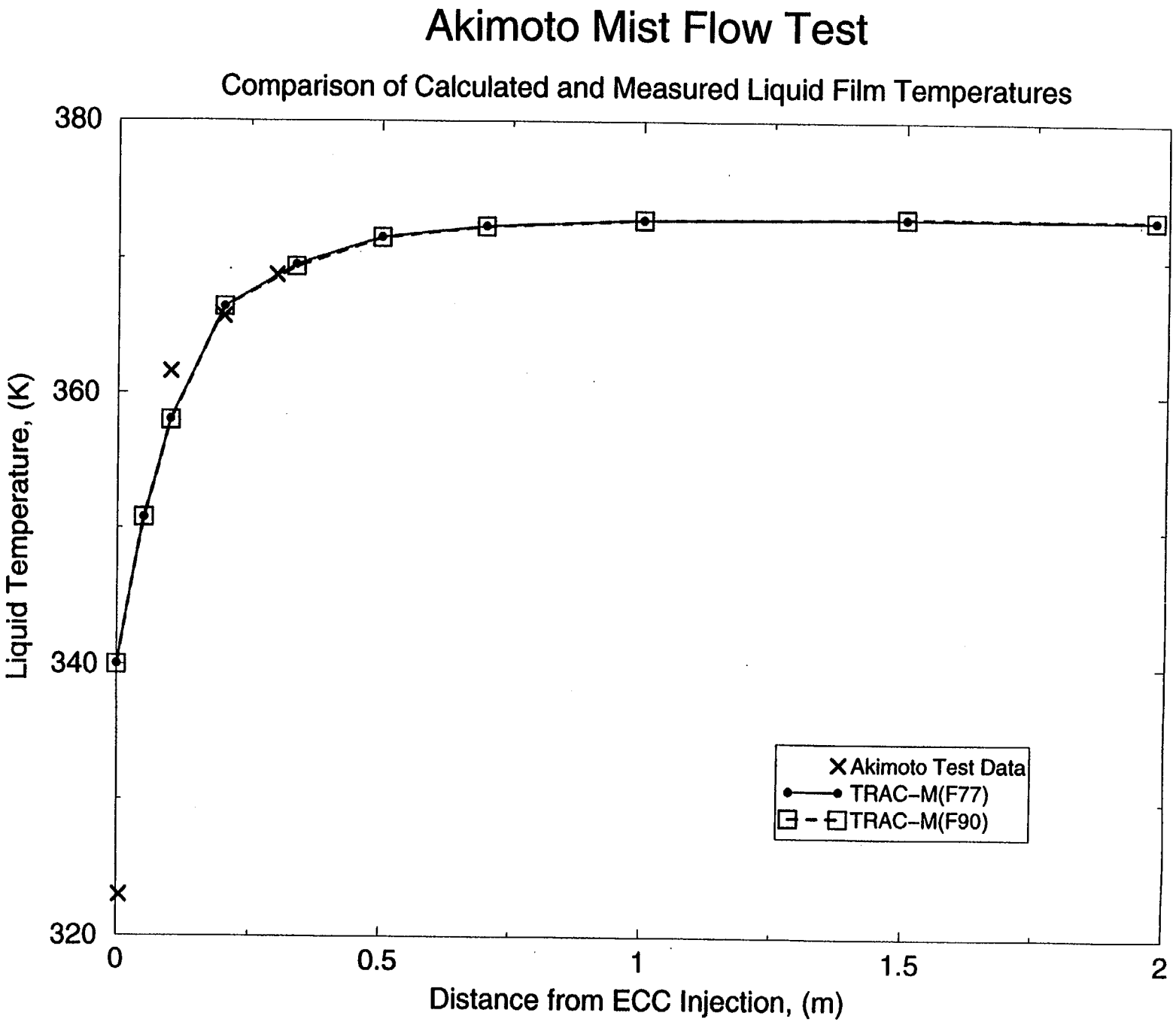

Figure 4.2.4 Comparison of Calculated and Measured Liquid Film Temperatures in the Akimoto Stratified-Mist Flow Test

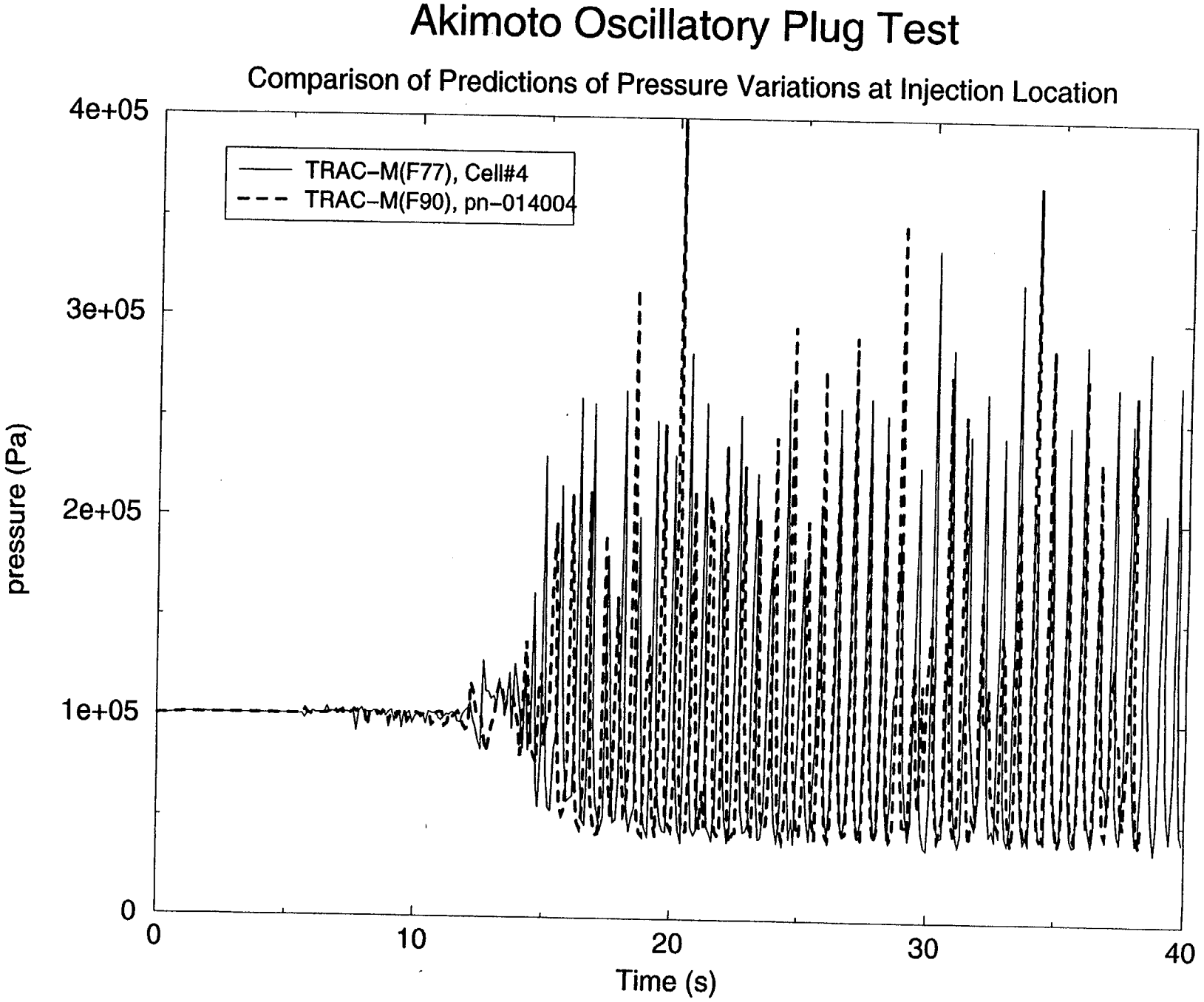

Figure 4.2.5 Comparison of Predictions of Pressure Variations at Injection Location in the Akimoto Oscillatory Plug Test

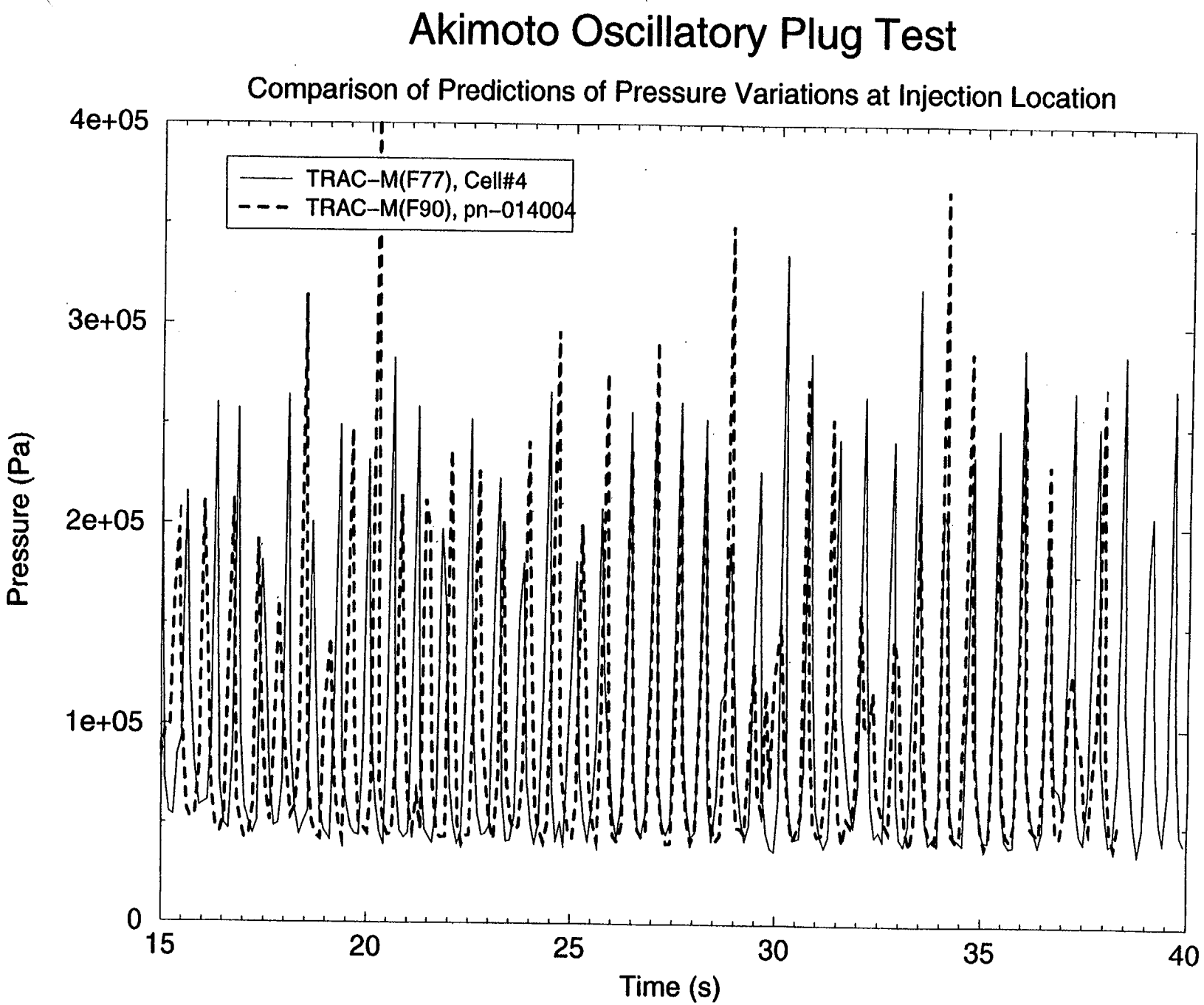

Figure 4.2.6 Comparison of Predictions of Pressure Variations at Injection Location in the Akimoto Oscillatory Plug Test

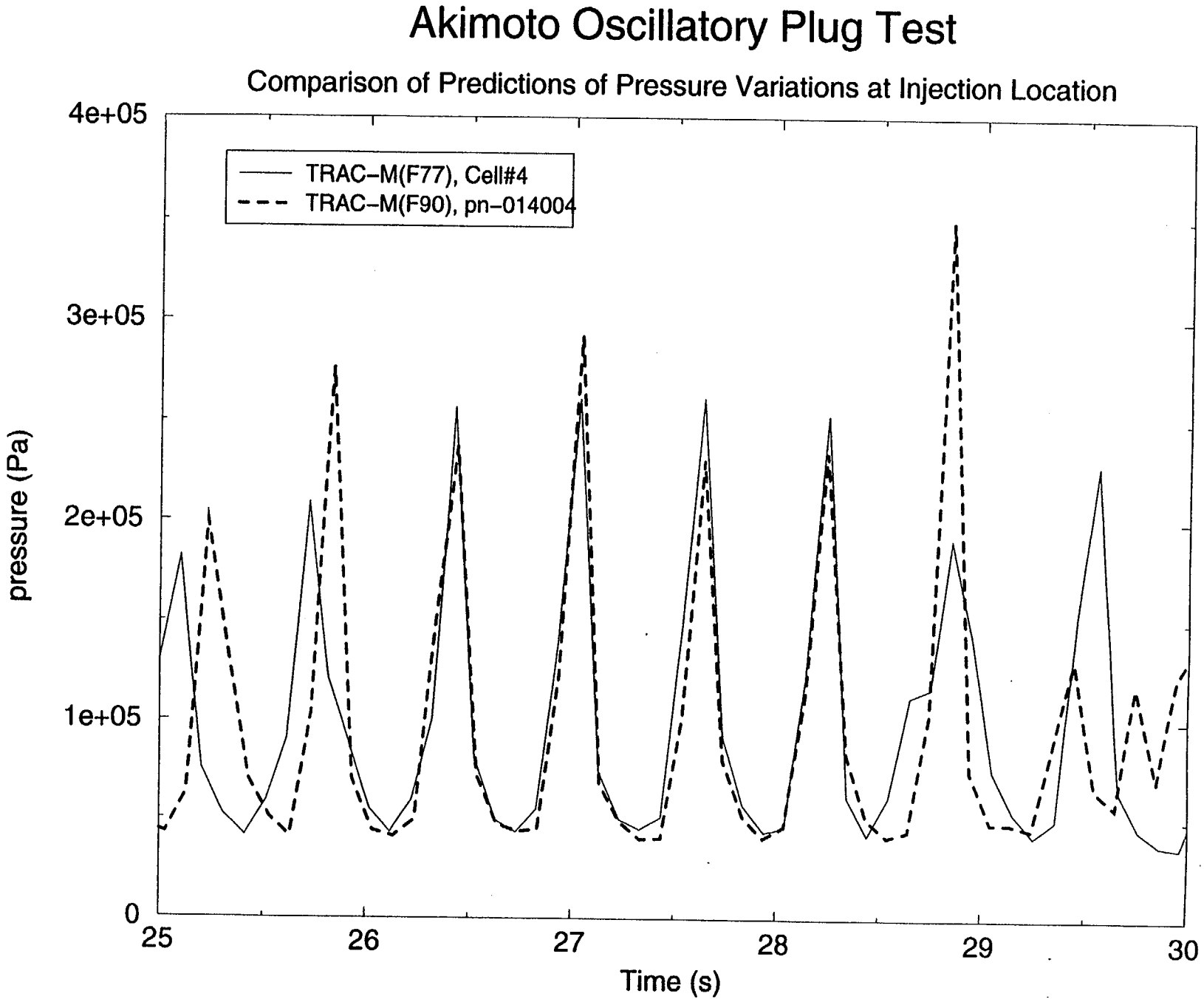

Figure 4.2.7 Comparison of Predictions of Pressure Variations at Injection Location in the Akimoto Oscillatory Plug Test

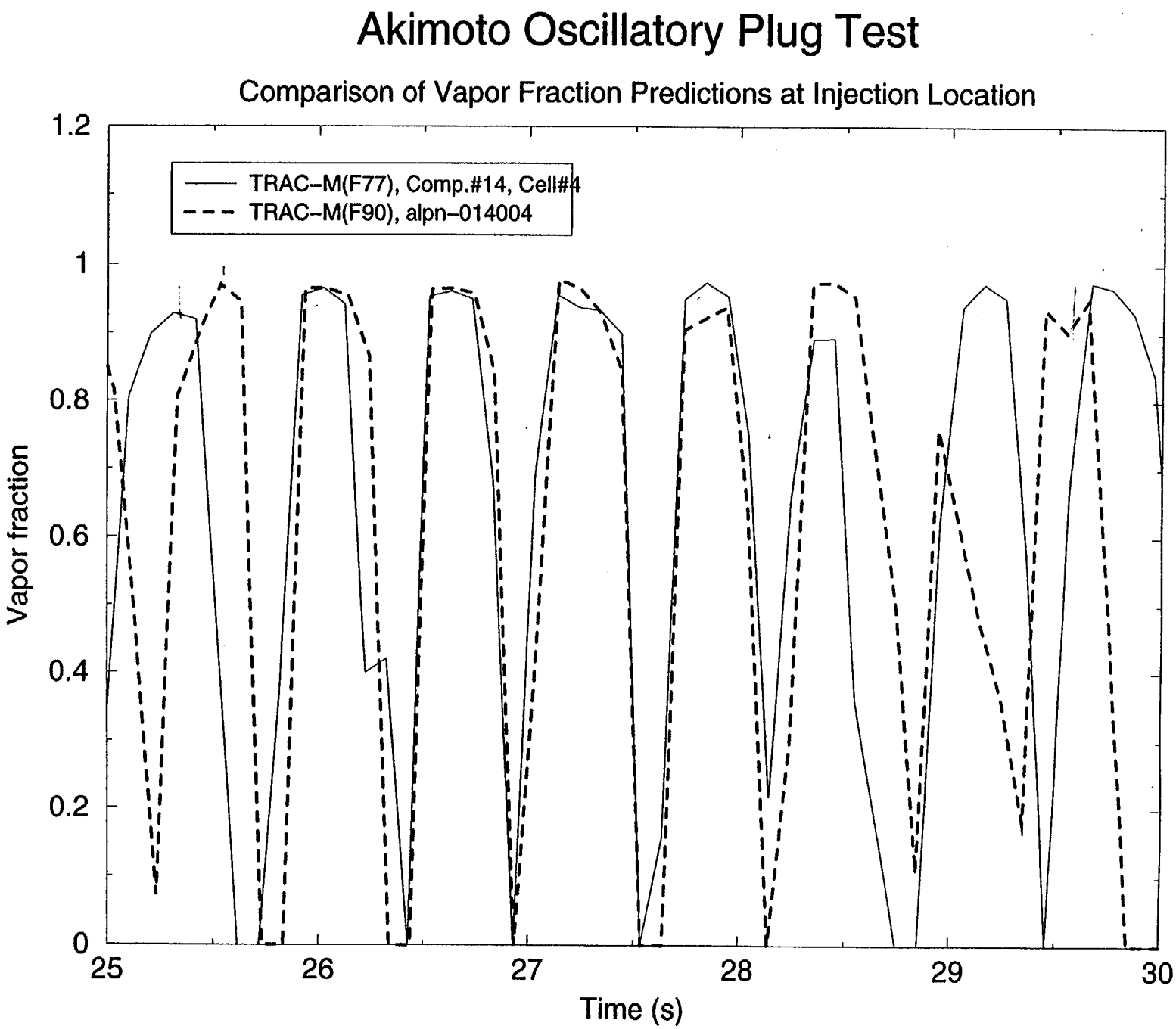

Figure 4.2.8 Comparison of Vapor Fraction Predictions at Injection Location in the Akimoto Oscillatory Plug Test

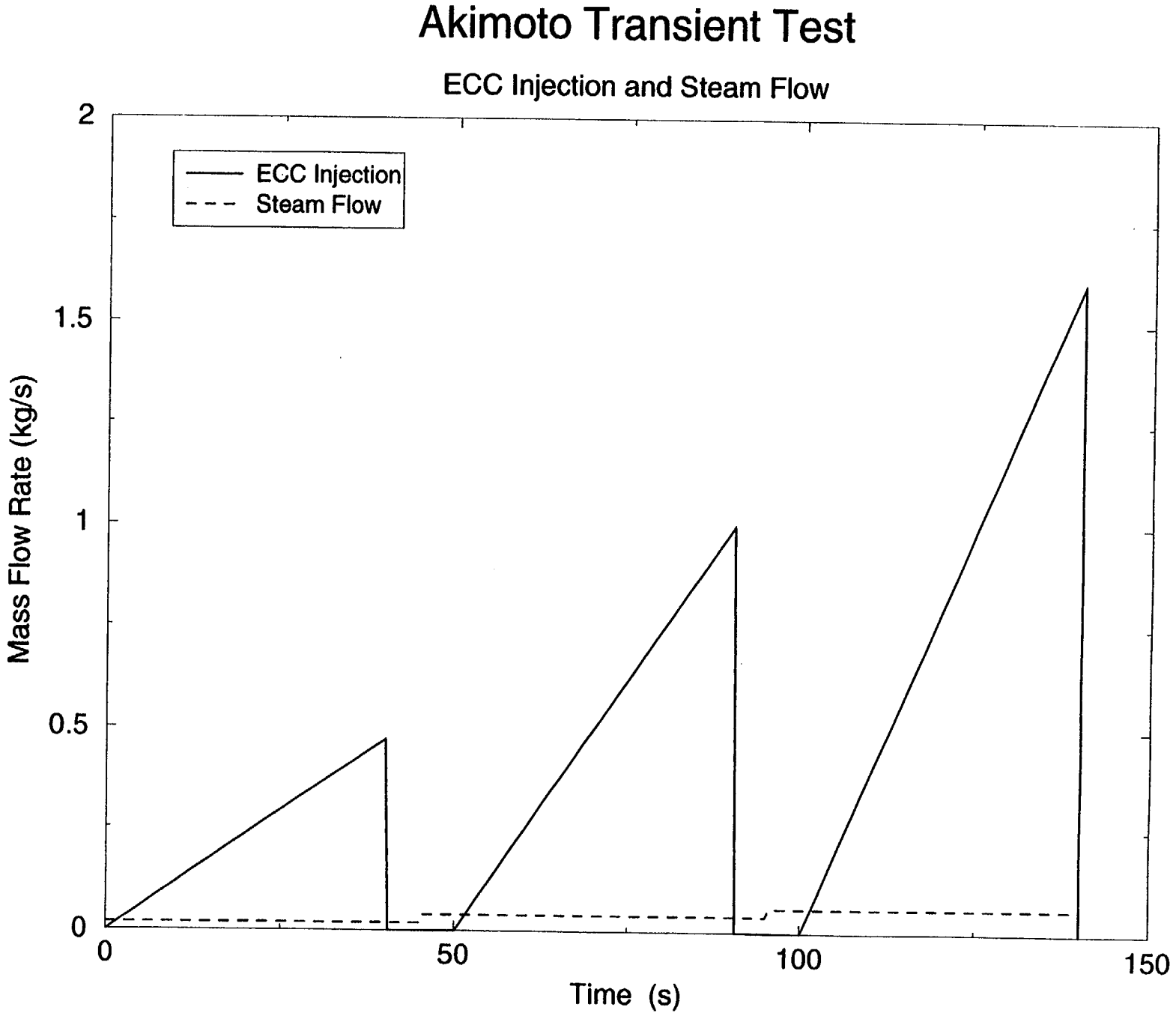

Figure 4.2.9 ECC Injection and Steam Flow in the Akimoto Transient Test

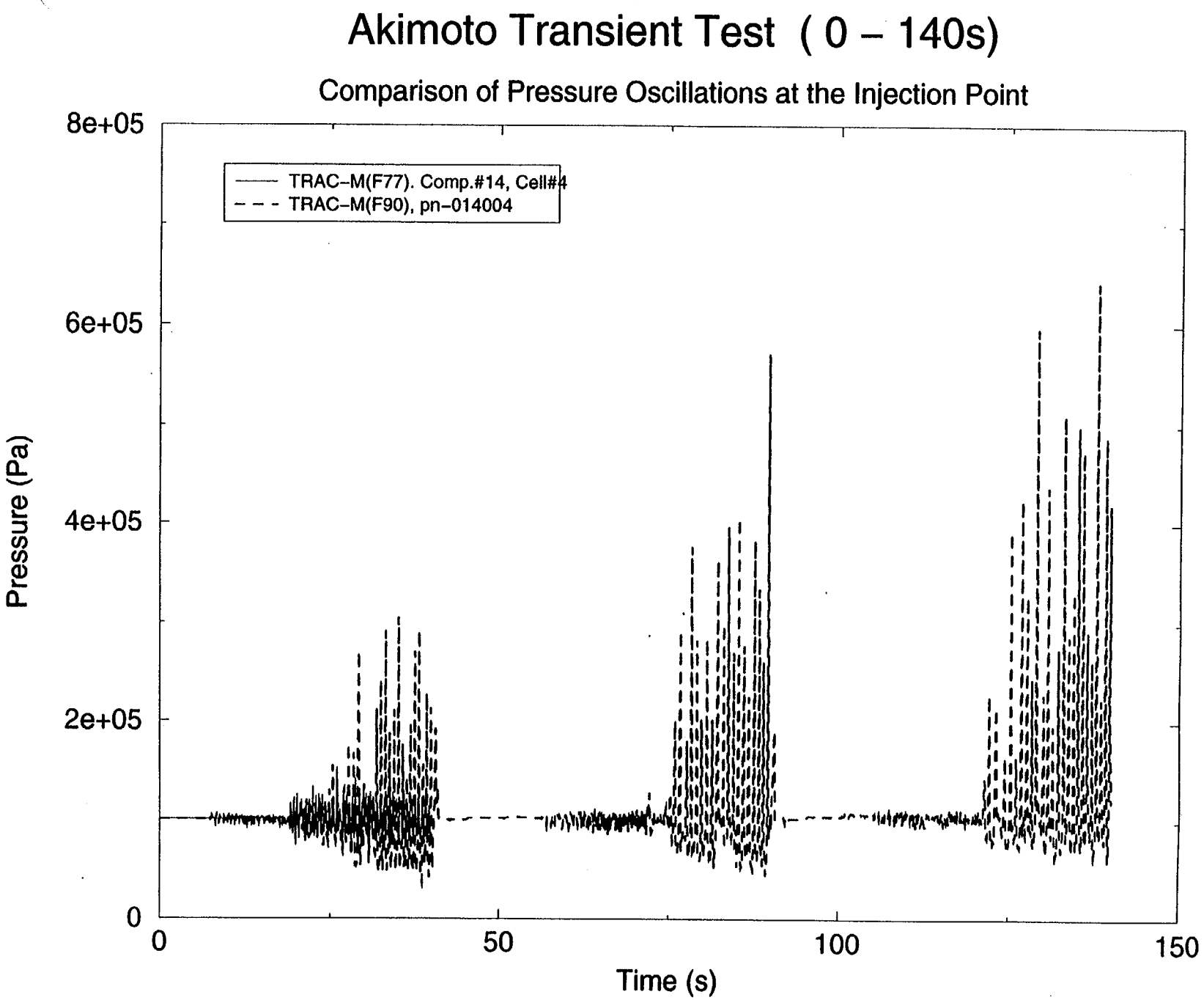

Figure 4.2.10 Comparison of Pressure Oscillations at the Injection Point in the Akimoto Transient (0 – 140s)

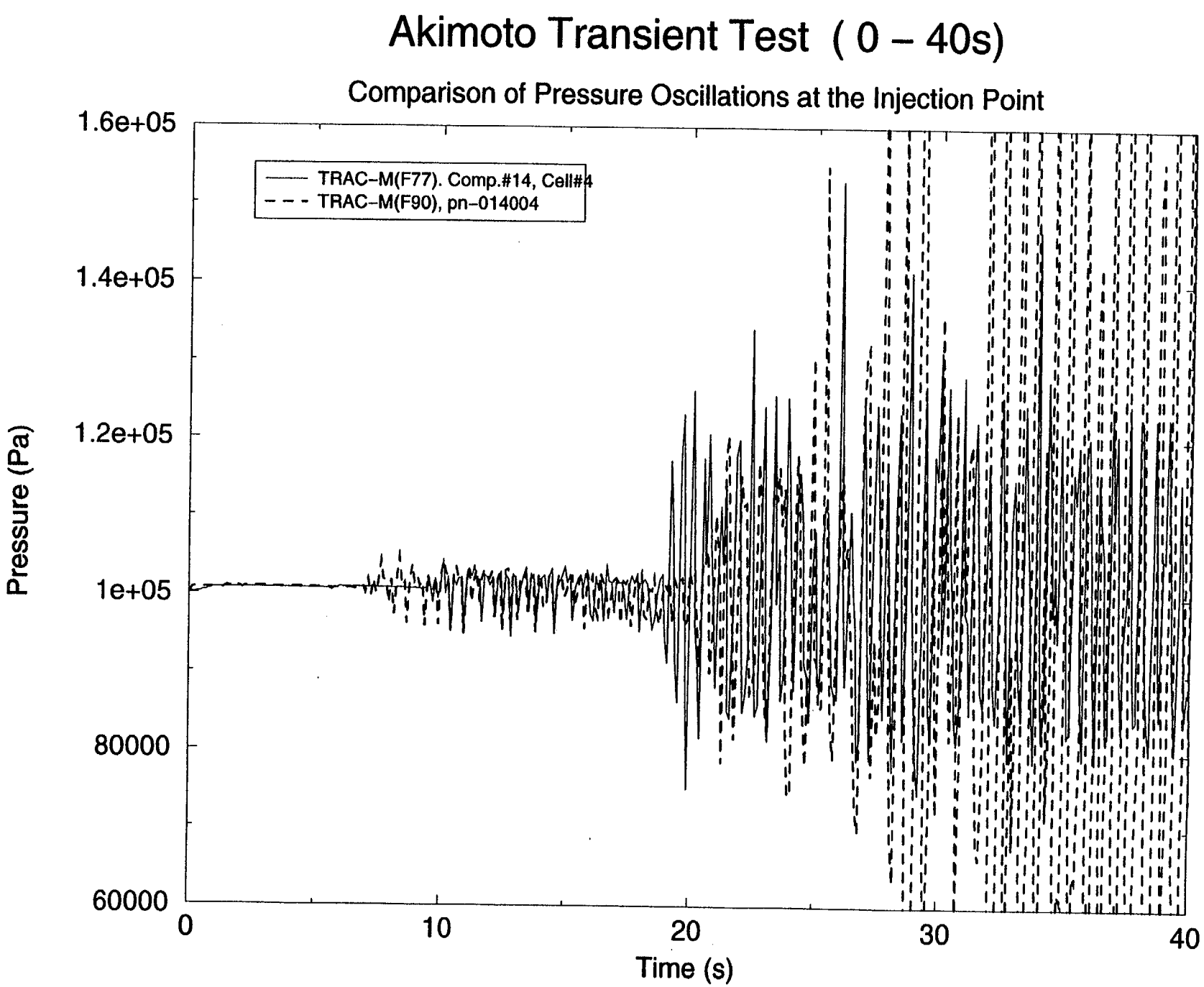

Figure 4.2.11 Comparison of Pressure Oscillations at the Injection Point in the Akimoto Transient Test (0 – 40s)

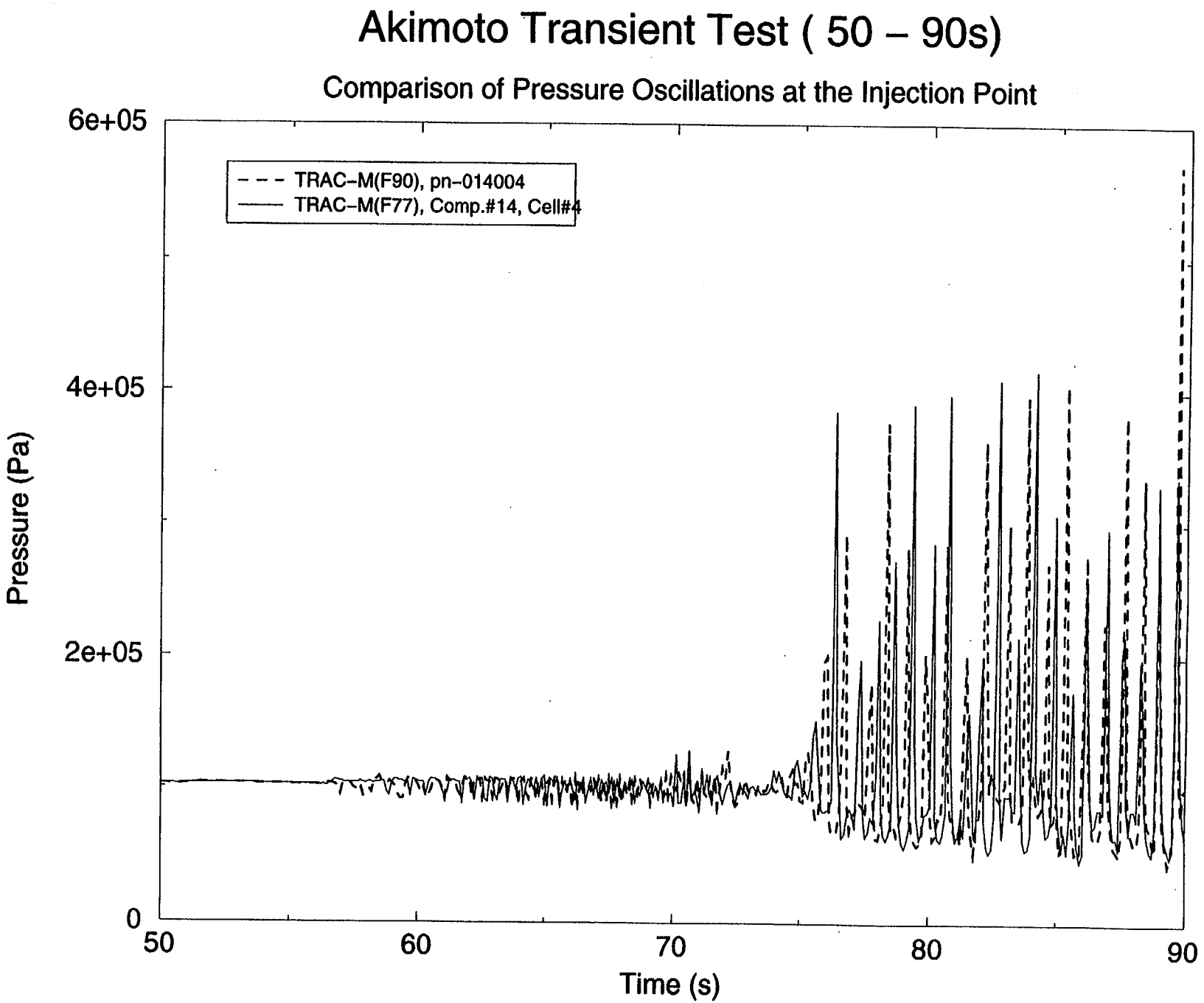

Figure 4.2.12 Comparison of Pressure Oscillations at the Injection Point in the Akimoto Transient Test (50 – 90s)

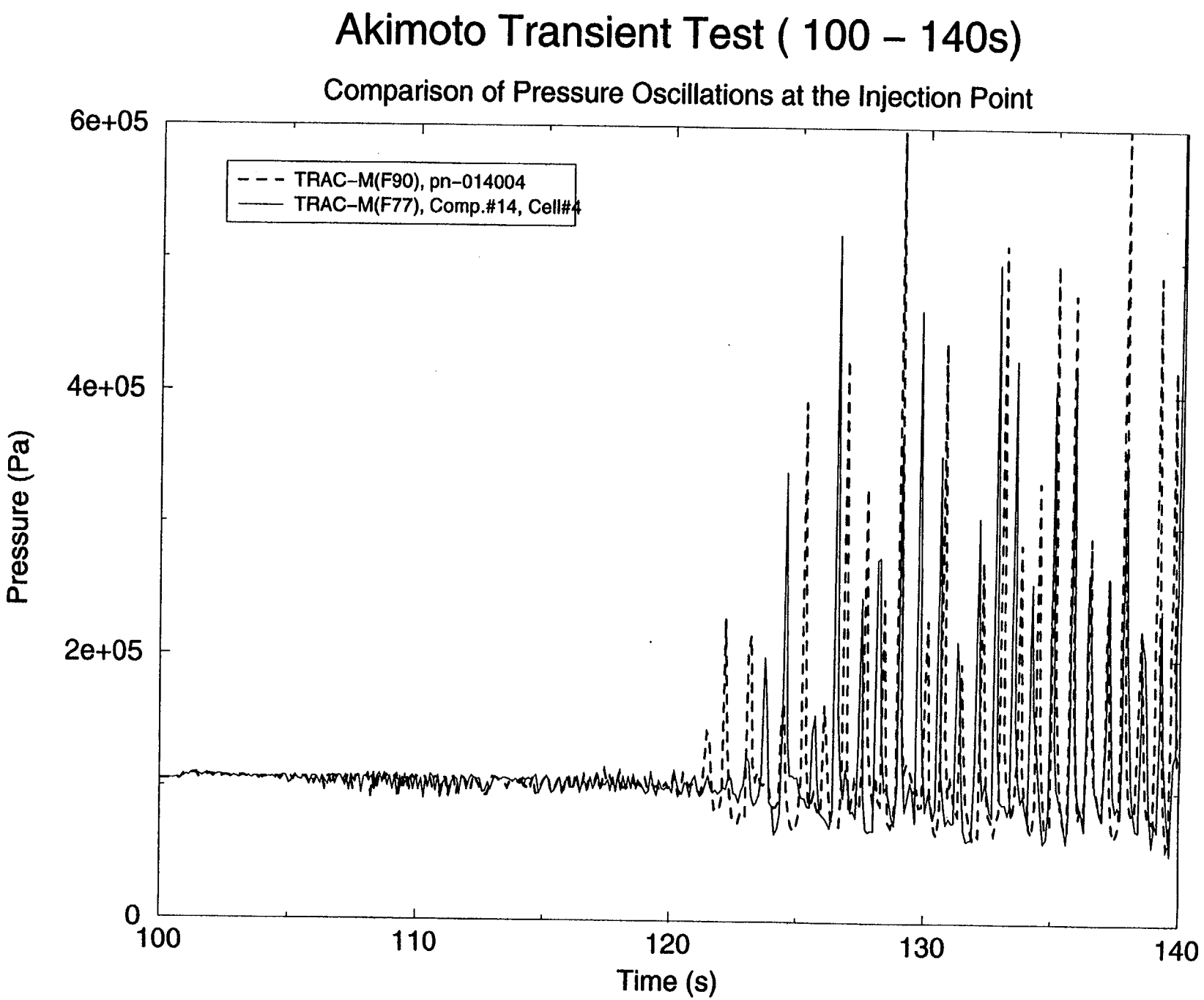

Figure 4.2.13 Comparison of Pressure Oscillations at the Injection Point in the Akimoto Transient Test (100 – 140s)

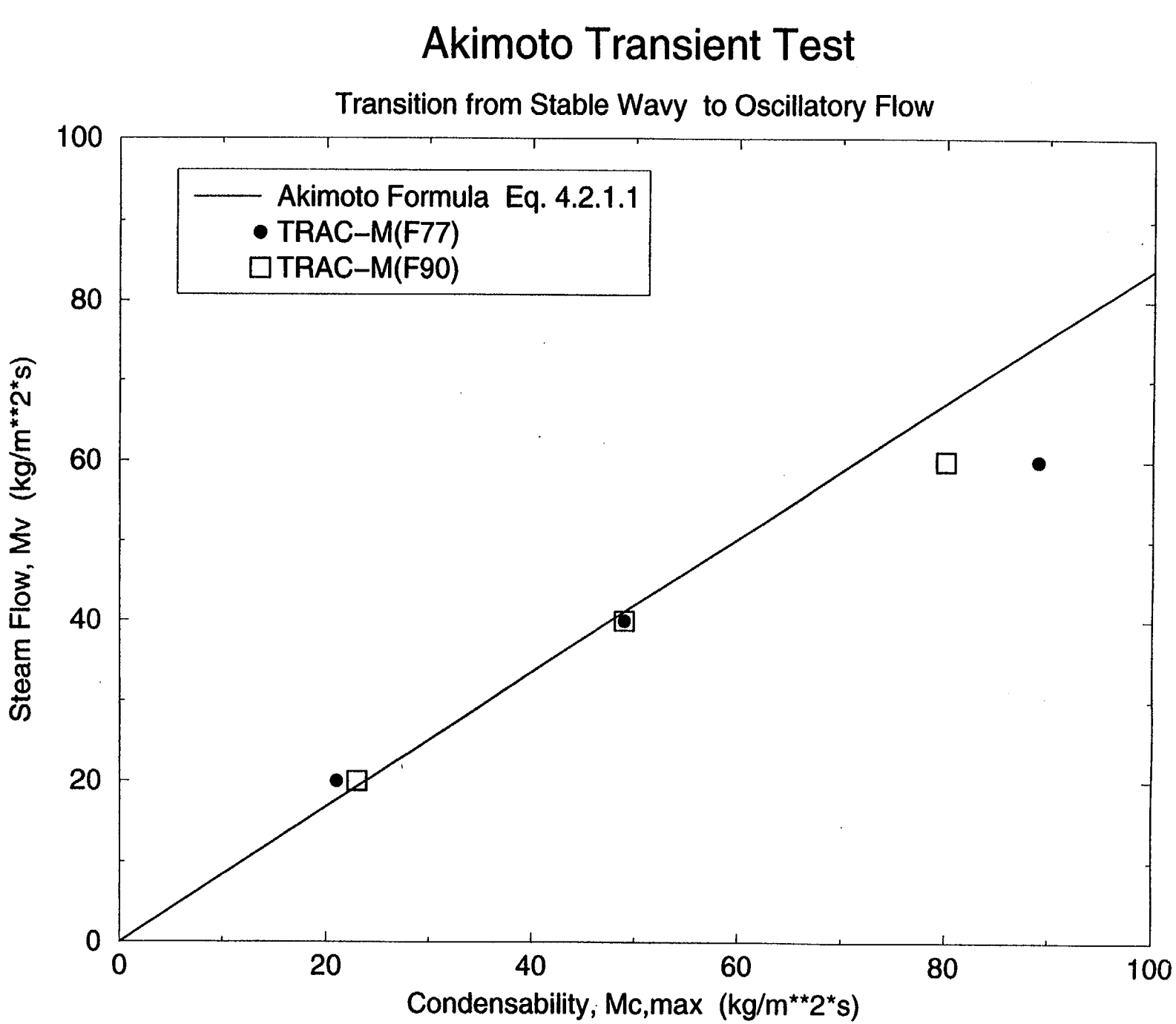

Figure 4.2.14 Transition from Stable Wavy to Oscillatory Flow in the Akimoto Transient Test

4.3 Critical Flow

The TRAC critical flow model is described in Ref. 2.1. The 1-D critical flow model was programmed in TRAC-PF1 to evaluate choked flow conditions with a coarse spatial mesh. Without the critical flow model, a fine mesh is required to accurately evaluate choking from the hydrodynamic equations. However, evaluating choking with a fine mesh is accurate only for smooth flow area changes between upstream mesh cells. The TRAC critical flow model improves computational efficiency by allowing a coarse mesh, and it also allows abrupt upstream flow area changes to be modeled while accurately predicting choked flow conditions.

The critical flow model comprises three separate models, including a single-phase subcooled-liquid choked flow model, a two-phase liquid and gas choked flow model, and a single-phase gas, choked flow model. The single-phase subcooled liquid choked flow model is a modified form of the Burnell model (Ref. 4.3.1) for an upstream gas volume fraction <0.01, and it incorporates a nucleation delay model developed by Jones (Ref. 4.3.2). The two-phase liquid and gas choked flow model is an extension of the model developed by Ransom and Trapp (Ref. 4.3.3), on the basis of first principles and a characteristic analysis approach for an upstream gas volume fraction between 0.1 and 0.999. This model assumes thermal equilibrium between the gas and liquid phases. Because there is a discontinuity in the sound speed during the transition from liquid to two-phase flow, linear interpolation is used between the subcooled liquid and two-phase models for an upstream gas volume fraction between 0.01 and 0.1. The single-phase gas choked flow model assumes ideal gas isentropic expansion for an upstream gas volume fraction >0.999.

4.3.1 Marviken Tests

The Marviken facility, located in Sweden, was originally designed to be part of a nuclear plant and, thus, is a full scale facility. The Marviken blowdown tests provide data for assessing the ability of computer codes to predict subcooled and saturated critical flow in large-diameter pipes.

4.3.1.1 Facility Description

The Marviken test facility consists of a pressure vessel and a discharge pipe, which contains a test nozzle with the minimum flow area, a rupture disk assembly, and a ball valve that is used to isolate the vessel after testing. The pressure vessel and discharge pipe are shown in Figs. 4.3.1 and 4.3.2. The vessel includes part of the core superstructure and three gratings to limit vortex formation. Pressure and temperature transducers are located in the vessel and discharge pipe, as shown in Figs. 4.3.1 and 4.3.2. The break flow is measured with a pitot tube, and is also calculated from differential pressure measurements. The data uncertainties are 90 kPa for the pressure data, 2 K for the temperatures, 10% and 15% for subcooled and saturated break flows determined by the pitot-static method, and 15% and 20% for subcooled and saturated break flows derived from differential pressure.

4.3.1.2 TRAC Model

Five critical flow experiments (Marviken Tests 4, 13, 20, 22, and 24) from the Marviken blowdown test facility are selected for assessment calculations.

The TRAC model of the Marviken facility has four components. Two PIPE components are used to represent the vessel and discharge pipe, a BREAK component provides the pressure

boundary condition downstream of the break, and a zero-velocity FILL closes the top of the vessel. The vessel, discharge pipe, and break nozzle noding for Test 4 are typical of the input models, and are shown in Figs. 4.3.3 and 4.3.4. The internally set default subcooled and saturated break flow multipliers of 1.0 were used for all calculations.

The initial and boundary conditions were varied in the remaining Tests 13, 20, 22, and 24. Table 4.3.1 summarizes the differences in the Marviken tests and the TRAC models. Both TRAC-M(F77) and TRAC-M(F90) were run to predict test data.

4.3.1.3 Comparison of Predictions and Measurements for Test 4

The calculated pressures, fluid temperatures, and break flow are in reasonable agreement with the measured data from Test 4. Calculated values are within the data uncertainties for most of the 50 s test duration. The values calculated by TRAC-M(F90) closely agree with the results that were previously calculated by TRAC-M(F77).

The calculated break flow is compared with the break flow measurements from the pitot tube and the vessel differential pressure in Fig. 4.3.5. It should be noted, however, that the break flow derived from the vessel differential pressure is not valid for the first ~5 s because of momentum effects on the measured pressures. As a result, the pitot tube measurements should be used for comparison purposes. The TRAC break flow underpredicts the subcooled critical flow for the first 19 s of the test, but was in reasonable agreement with the test data during the saturated blowdown after that time. The underprediction of the break flow results when the flow conditions at the nozzle become saturated even though the upstream incoming flow is subcooled.

The vessel pressure comparison is shown in Fig. 4.3.6. Except for the initial pressure dip in the test data caused by delayed nucleation, the calculated pressure is just under the lower uncertainty limit until ~27 s, and then is within the uncertainty limit for the rest of the test. A similar comparison was obtained for the discharge line pressure shown in Fig. 4.3.7. Again, the calculated pressure is very close to the lower uncertainty of the measured pressure for most of the time. Both the calculated and measured fluid temperatures are very close to saturation for most of the time.

The fluid temperature comparison in the lower vessel shown in Fig. 4.3.8 is very similar to comparisons in the middle of the vessel and the discharge pipe. A temperature increase occurs in the first 20 s as warmer fluid from the upper vessel drains into the lower vessel. The calculated temperature increase is smoother because of the averaging of the liquid temperature within a hydraulic cell. The fluid temperature comparison in the upper vessel is very similar to the pressure comparison because both the measured and calculated fluid temperatures are very close to saturation.

4.3.1.4 Comparison of Predictions and Measurements for Test 13

The Test 13 nozzle was shorter, and had a smaller throat diameter than the nozzle in Test 4. Test 13 also had more initial subcooling at the nozzle inlet. The lower velocities and pressure drops upstream of the nozzle, along with the higher subcooling, were sufficient to prevent vapor formation from reducing the subcooled break flow in the calculation for Test 13.

Fig. 4.3.9 compares the calculated and measured break flows in the first 75 s. When the break flow is subcooled, the calculated flow is generally within the uncertainty of the test data. Voiding at the nozzle exit remains below 0.01, which allows delayed nucleation in the subcooled critical flow model to take effect. As warmer liquid from the vessel enters the discharge line, the calculated break flow is reduced by vapor formation, and the break flow is underpredicted for the remainder of the test. As suggested in Ref. 4.3.1, the nonequilibrium effects in Test 13 were more pronounced during the saturated flow because of the short nozzle length. In addition, there is a large underprediction of the flow because the two-phase TRAC critical flow model assumes thermal equilibrium between phases.

The upper vessel pressure comparison for Test 13 is shown in Fig. 4.3.10. Except for the initial dip in pressure caused by the delayed nucleation in the test, the calculated pressure is within the uncertainty of the test data. Similar comparisons were obtained at lower vessel elevations and in the discharge pipe.

The fluid temperature predictions in the upper vessel are within the uncertainty of the test data, with the exception of the initial dip that was caused by delayed nucleation in the test. When the fluid reaches saturation, the measured and calculated fluid temperatures closely follow saturation. As in Test 4, the calculated lower vessel fluid temperature for Test 13 increased to saturation more smoothly than the data, as shown in Fig. 4.3.11. Calculations by both TRAC-M(F77) and TRAC-M(F90) are essentially the same.

4.3.1.5 Comparison of Predictions and Measurements for Test 20

The break nozzle in Test 20 was shorter than in Test 4, but it had the same throat diameter. Test 20 also had less initial subcooling in the bottom of the vessel. With the reduced initial subcooling, the subcooled break flow was again underpredicted by both codes during the first 7 s of the test, as shown in Fig. 4.3.12. However, the saturated break flow predictions obtained using both codes were within the uncertainty of the test data for the remainder of the test after 7 s.

Fig. 4.3.13 shows the upper-vessel pressure comparison for Test 20. The pressure calculated by both codes is within the measurement uncertainty, with the exception of the initial pressure dip that was caused by the delayed nucleation in the test. Calculated pressures at lower vessel elevations and in the discharge pipe compared similarly with the measured data from Test 20. The fluid temperature comparisons for Test 20 were much like those of the other Marviken tests, in that (1) the predicted temperatures in the vessel are generally within the data uncertainty except for the initial dip, (2) the discharge line temperatures increase to saturation more smoothly in calculations and are within the uncertainty afterward, and (3) calculations produced by TRAC-M(F90) are essentially the same as those produced by TRAC-M(F77).

4.3.1.6 Comparison of Predictions and Measurements for Test 22

Test 22 had the same break nozzle as Test 20, which was shorter than the Test 4 nozzle but had the same throat diameter as the Test 4 nozzle. Test 22 had the maximum initial subcooling, both in the bottom of the vessel and in the discharge pipe. The duration of the subcooled break flow was prolonged until ~30 s in Test 22 (Fig. 4.3.14) because of the high initial subcooling. Fig. 4.3.14 shows that both codes underpredict portions of the subcooled break flow, but are consistently within the data uncertainty during the saturated blowdown after 30 s.

The vessel pressure comparison for Test 22 is shown in Fig. 4.3.15. The initial dip in the pressure is not predicted because the codes do not have delayed nucleation in the vapor generation model. After the initial pressure dip, pressures are generally underpredicted for the remainder of the subcooled blowdown. However, during the saturated blowdown after 30 s, the break flow and nonequilibrium effects are reduced, and the predicted pressures are within the data uncertainty. Pressures calculated by both codes at lower vessel elevations and in the discharge pipe compared similarly with the measured data from Test 22. Fluid temperature comparisons for Test 22 are very much like those of the other Marviken tests.

4.3.1.7 Comparison of Predictions and Measurements for Test 24

Test 24 had the shortest break nozzle, but its throat diameter was the same as the Test 4 nozzle. Test 24 also had the same initial subcooling in the bottom of the vessel as Test 4, and greater subcooling in the discharge pipe. The short nozzle increases the acceleration and magnitude of nonequilibrium effects upstream of the throat, and the codes do not correctly calculate the nonequilibrium effects. As a result, both codes underpredict the subcooled break flow to a greater degree than in the other tests, as shown in Fig. 4.3.16. The calculated break flows are within the data uncertainty during the saturated blowdown after 30 s, but the vessel emptied ~15 s late in the calculation because of the underprediction of the subcooled break flow.

Fig. 4.3.17 shows the upper vessel pressure comparison for Test 24. Again, both codes fail to predict the initial pressure dip, and underpredict the pressures during much of the subcooled blowdown. The pressure comparisons are closer after the transition to saturated break flow at ~30 s. Similar pressure comparisons were obtained in the lower vessel and discharge pipe. Fluid temperature comparisons for Test 24 are very much like those of the other Marviken tests.

4.3.1.8 Conclusions

Calculations were performed using TRAC-M(F90) and TRAC-M(F77) codes, and the results were compared with test data to assess the TRAC critical flow model. Results of the comparisons for the Marviken tests with larger nozzle diameters generally showed that both codes correctly predict the saturated critical flow, but sometimes predict an early transition from subcooled to saturated critical flow. For Marviken Test 13, which has a smaller nozzle diameter, both codes underpredict the saturated critical flow. The early transition to the saturated critical flow is a result of the vapor generation model, which does not model delayed nucleation. The depressurization and break flow rates are both adversely affected by the early transition in the calculations. The comparisons are best for the tests with higher initial subcooling, longer break nozzle inlet sections, and larger nozzle diameters.

Comparisons of code predictions with the Marviken tests indicate that whereas both codes generally calculate saturated break flow correctly, the absence of nucleation delay in the vapor generation model over most of the two-phase flow regime can cause differences in the break flow and depressurization rate during the subcooled break flow. The differences seem to correspond to nonequilibrium conditions just upstream of the break, and result in a brief period when both the break flow and pressure are underpredicted. For the short-nozzle and small-diameter tests, Marviken Test 13 and Test 24, nonequilibrium effects become dominant. In these tests, during the period where the measured flow is highly underpredicted by both codes, the measured mass-flux generally agrees with that predicted by the Henry-Fauske Critical-Flow Model (Ref. 4.3.4). This

can be seen in Table 4.3.2, which compares the TRAC calculated and measured critical mass fluxes at selected test times to the mass fluxes calculated by three different critical flow models, including (1) Homogeneous Equilibrium Model (HEM), (2) Moody Model, and (3) Henry-Fauske Model. For Tests 13 and 24, the measured mass fluxes agree more closely to those predicted by the Henry-Fauske model. It is recommended that a nonequilibrium critical-flow model, such as the Henry-Fauske Model, be implemented into the code as a user option for modeling the critical flow for small-diameter nozzles, orifices, and short tubes.

The magnitude of the initial pressure dip in the Marviken tests, which is not calculated, seemed to depend on the rate of depressurization more than any other single parameter. Comparisons are generally better for the tests with slower depressurization rates. It is clear that additional modeling of nonequilibrium effects is needed. Plausible solutions might be to extend the Jones nucleation delay model to higher void fractions and/or to develop an improved thermal nonequilibrium model for the two-phase flow.

All calculations performed using TRAC-M(F90) are essentially the same as those performed using TRAC-M(F77), demonstrating that the conversion of TRAC-M(F77) from FORTRAN 77 to FORTRAN 90 has been successful for this type of application.

4.3.2 Edwards Blowdown Test

The Edwards blowdown test facility (Ref. 4.3.5) is a separate-effects facility that was built in England in the late 1960s to study depressurization phenomena associated with subcooled water that is initially stagnant. This facility is much smaller than any component of a full-scale reactor system.

4.3.2.1 Facility Description

The Edwards blowdown test apparatus (shown in Fig. 4.3.18) consists of a horizontal pipe that is sealed at one end, an orifice at the pipe exit, and a glass rupture disk. The pipe, which is initially filled with subcooled liquid, is electrically heated and insulated with asbestos. Pressures are measured at four locations along the pipe, and the void fraction and fluid temperature are measured at a point near the middle of the pipe. The break flow rate and pipe wall temperatures are not measured.

4.3.2.2 TRAC Model

The TRAC-M model of the Edwards blowdown test facility has three components, as shown in Fig. 4.3.19. A PIPE component represents the blowdown pipe, a zero-velocity FILL terminates the closed end of the blowdown pipe, and a BREAK component provides the pressure boundary condition downstream of the break.

4.3.2.3 Comparison of Predicted and Measured Results

Pressures, fluid temperature, and void fractions in the middle of the blowdown pipe are calculated using both TRAC-M(F77) and TRAC-M(F90). The predictions reasonably agree with the measured data from the test. Although the calculated parameters are sometimes outside the data uncertainty, the major trends in the data were predicted.

The pressure comparisons at the closed end and the break end of the blowdown pipe are shown in Figs. 4.3.20 and 4.3.21, respectively. Measurement uncertainties were not given in the original publication for the Edwards blowdown test; however, an uncertainty of ~0.3 MPa has been suggested in Ref. 4.3.3. Figs. 4.3.20 and 4.3.21 show that the initial subcooled depressurization lasted ~0.1 s in both the test and the calculation. However, the predictions are frequently outside the data uncertainty during the saturated blowdown after 0.01 s. The pressure comparisons for the other two pressure measurements, in the midsection of the pipe, are very similar to those shown in Figs. 4.3.20 and 4.3.21.

The fluid temperature measured near the center of the pipe is compared with the corresponding calculated temperature in Fig. 4.3.22. After ~0.1 s, the liquid and vapor temperatures in the calculation are equal to the saturation temperature. Thus, the fluid temperature comparison is very similar to the pressure comparisons shown in Figs. 4.3.20 and 4.3.21 after this time. The void fraction was measured at the same location as the fluid temperature, and the void fraction comparison is shown in Fig. 4.3.23. The overall trend in the void fraction is captured in the calculations; however, there are significant differences between the measured and calculated void fractions in the first half of the test when the flows and depressurization rate are higher. Also, the oscillations in the measured void fraction from 0.15 to 0.25 s do not occur in the calculations.

4.3.2.4 Conclusions

The parameters calculated by both codes for the Edwards blowdown test followed the same trends as the test data, and correctly predicted the timing of major events. However, there are periods when the calculated parameters noticeably differ from the measured values, and the oscillations in the measured void fraction are not captured in the calculations. Sparse data from the facility and the lack of data uncertainty information make it difficult to determine which models in the code contribute most to the differences between the test results and predictions, or whether the differences are attributable to incorrect initial conditions in the input model.

The Edwards blowdown test comparison shows that although the major trends and timing of events in the test data are captured in calculations, the calculated parameters do not always match the values measured during the test. Also, the oscillations in the measured pressure upstream of the break and in the void fraction in the middle of the pipe are not completely captured in the calculations. Uncertainties in the initial temperature distribution and the lack of break flow and pipe wall temperature measurements make it difficult to attribute differences to a specific model in the code.

Calculations performed using TRAC-M(F77) and TRAC-M(F90) are reasonably close, but they are not identical. TRAC-M(F90) contains some updates that may affect the critical flow calculations. Consequently, it is necessary to incorporate the same updates in TRAC-M(F77) to make precise comparisons. At this point, we can say that the predictions are reasonably close, and that the conversion from TRAC-M(F77) to TRAC-M(F90) has been successful for this type of application.

REFERENCES

4.3.1 Ransom, V.H., R.K. Wagner, J.A. Trapp, K.E. Carlson, D.N. Kaiser, H. Kuo, H. Crow, R.A. Nelson, and S.W. James, "RELAP/MOD1 Code Manual, Volume 1: System Models and Numerical Methods," Idaho National Engineering Laboratory Report EGG-2070, NUREG/CR-1826, March 1982.

4.3.2 Jones, O.C., "Flashing Inception in Flowing Liquids," Brookhaven National Laboratory report BNL-NUREG-51211, 1980.

4.3.3 Ransom, V.H., and J.A. Trapp, "The RELAP5 Choked Flow Model and Application to a Large-Scale Flow Test," in *ANS/ASME/NRC International Topical Meeting on Nuclear Reactor Thermal-Hydraulics*, pp. 799–819, Saratoga Springs, New York, 1980.

4.3.4 Henry, R.E., and H.K. Fauske, "The Two-Phase Critical Flow of One-Component Mixtures in Nozzles, Orifices, and Short Tubes," *Journal of Heat Transfer, Transactions*, 93, May 1971.

4.3.5 Edwards, A.R., and T.F. O'Brien, "Studies of Phenomena Connected with the Depressurization of Water Reactors," *Journal of British Nuclear Energy Society*, 9, 125–135, April 1970.

Table 4.3.1 Marviken Tests and TRAC Noding

	Test 4	Test 13	Test 20	Test 22	Test 24
Nozzle straight section length (m)	1.500	0.590	0.731	0.731	0.166
Nozzle diameter (m)	0.509	0.200	0.500	0.500	0.500
Length-to-diameter ratio	2.95	2.95	1.46	1.46	0.33
Initial pressure (MPa)	4.94	5.09	4.987	4.93	4.96
Initial subcooling near vessel bottom (K)	37	31	7	52	33
Initial subcooling at nozzle inlet (K)	63	95	77	95	83
Initial liquid level above vessel bottom (m)	17.59	17.52	16.65	19.64	19.88
Number of cells in PIPE representing vessel	15	15	38	38	15
Number of cells in PIPE representing lower vessel and discharge pipe	17	13	14	14	17

Table 4.3.2 Comparison of Measured Mass Fluxes and the Mass Fluxes Calculated by TRAC-M(F77) and Different Critical Flow Models

Marviken Test No.	4	13	20	22	24
Test Time (s)	41	100	40	40	15
Measured Mass Flux (pitot) ($kg/(s\text{-}m^2)$[a] (Δp)	15971 16428	34364 34841	18640 21279	14860 17045	40881 41171
TRAC-M(F77) Calculations					
Exit Pressure (MPa)	3.281	3.963	3.676	2.394	2.855
Exit Void Fraction	0.2941	0.0608	0.3321	0.2581	0.0448
Mass Flux ($kg/(s\text{-}m^2)$)	18466	23130	21448	15854	30805
Mass Flux ($kg/(s\text{-}m^2)$) determined from:					
HEM	14782	17679	15851	11910	14022
Moody Model	26635	29558	27978	22982	25233
Henry-Fauske Model	27668	35641	28391	24285	30549

[a] The first value given is the mass flux determined from measured pitot tube data. The second value is the mass flux determined from differential vessel pressure measurements.

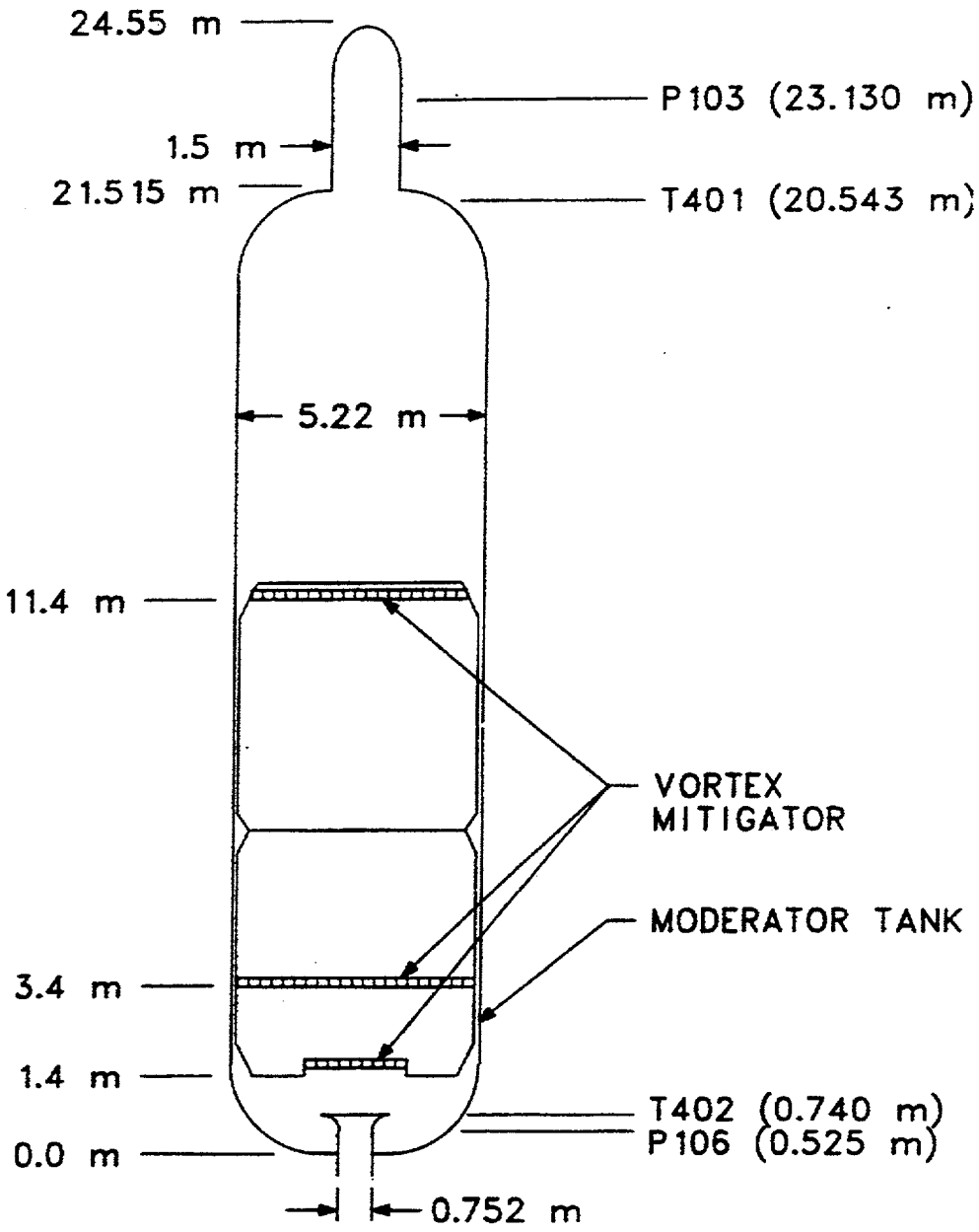

Figure 4.3.1 Marviken Pressure Vessel

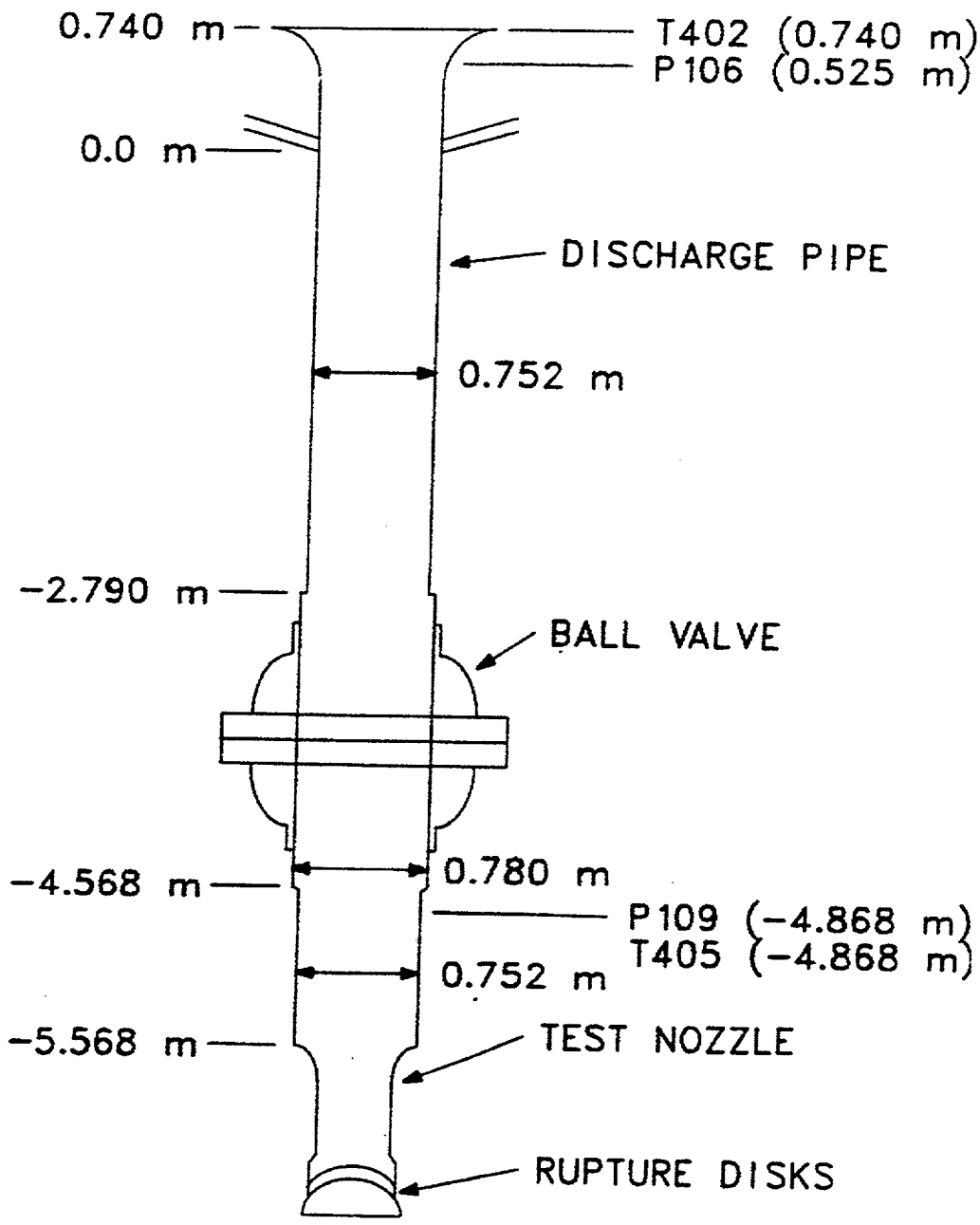

Figure 4.3.2 Marviken Discharge Pipe, Test Nozzle, and Rupture Disk Assembly

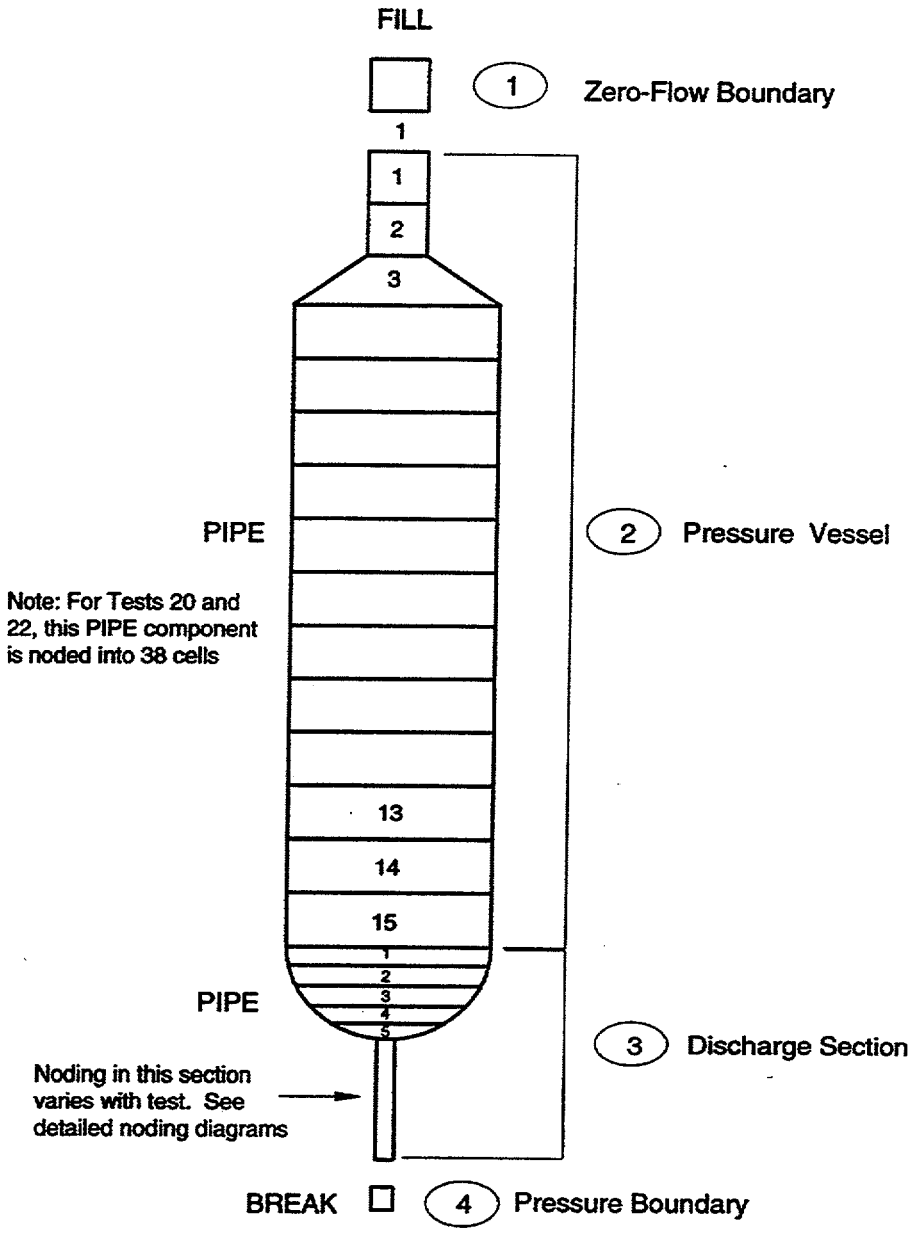

Figure 4.3.3 Pressure-Vessel and Discharge-Pipe Noding

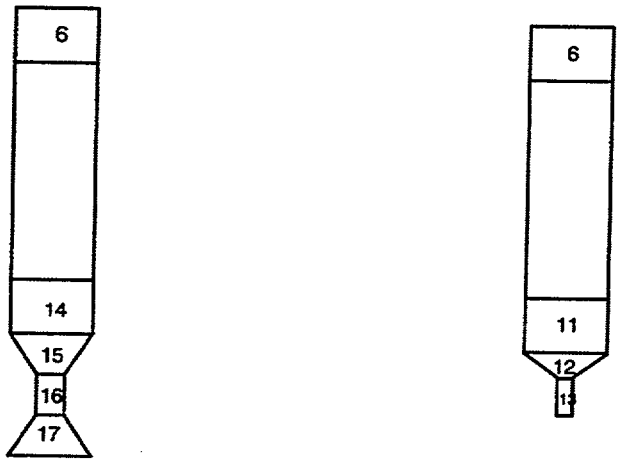

(a) Test 4

(b) Test 13

Note: Not to scale

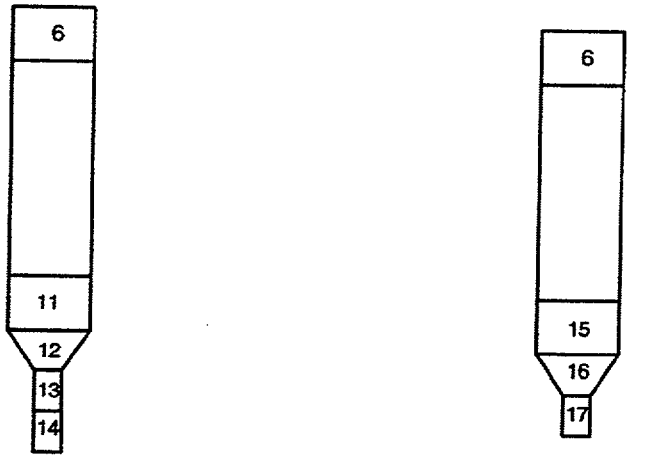

(c) Tests 20 and 22

(d) Test 24

Figure 4.3.4 Nozzle and Rupture-Disk Assembly Noding for Marviken Tests

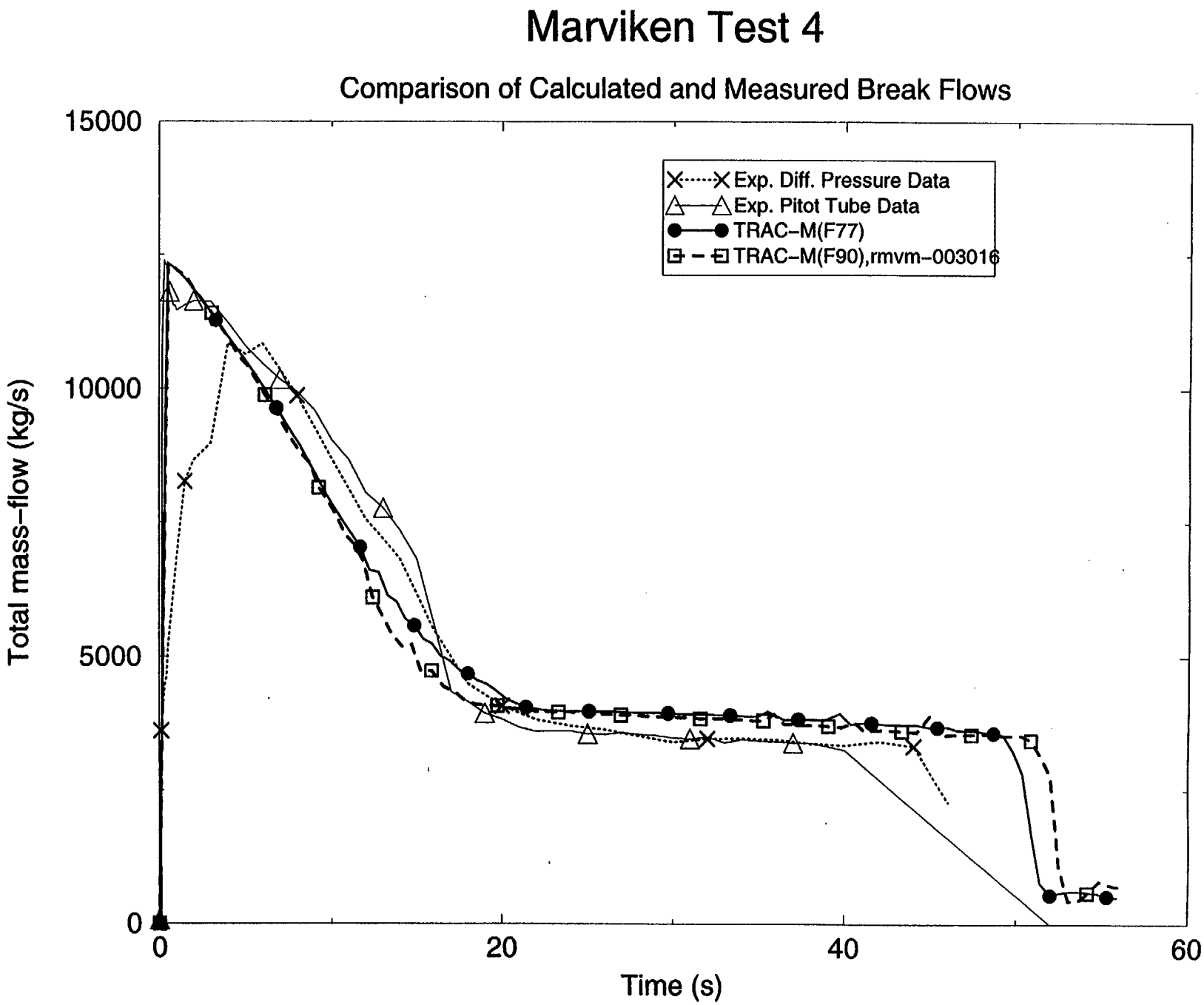

Figure 4.3.5 Comparison of Calculated and Measured Break Flows for Marviken Test 4

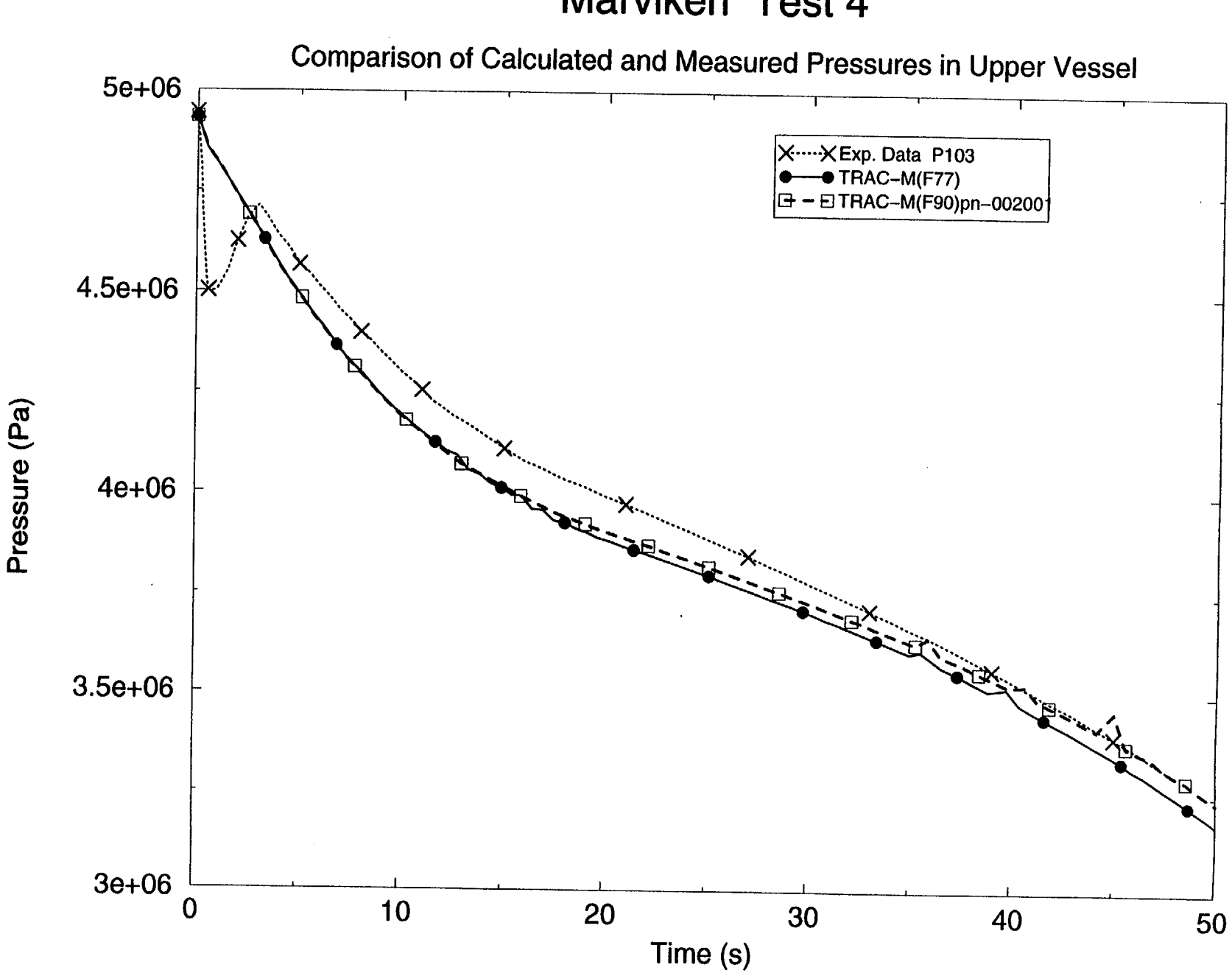

Figure 4.3.6 Comparison of Calculated and Measured Pressures in the Upper Vessel for Marviken Test 4

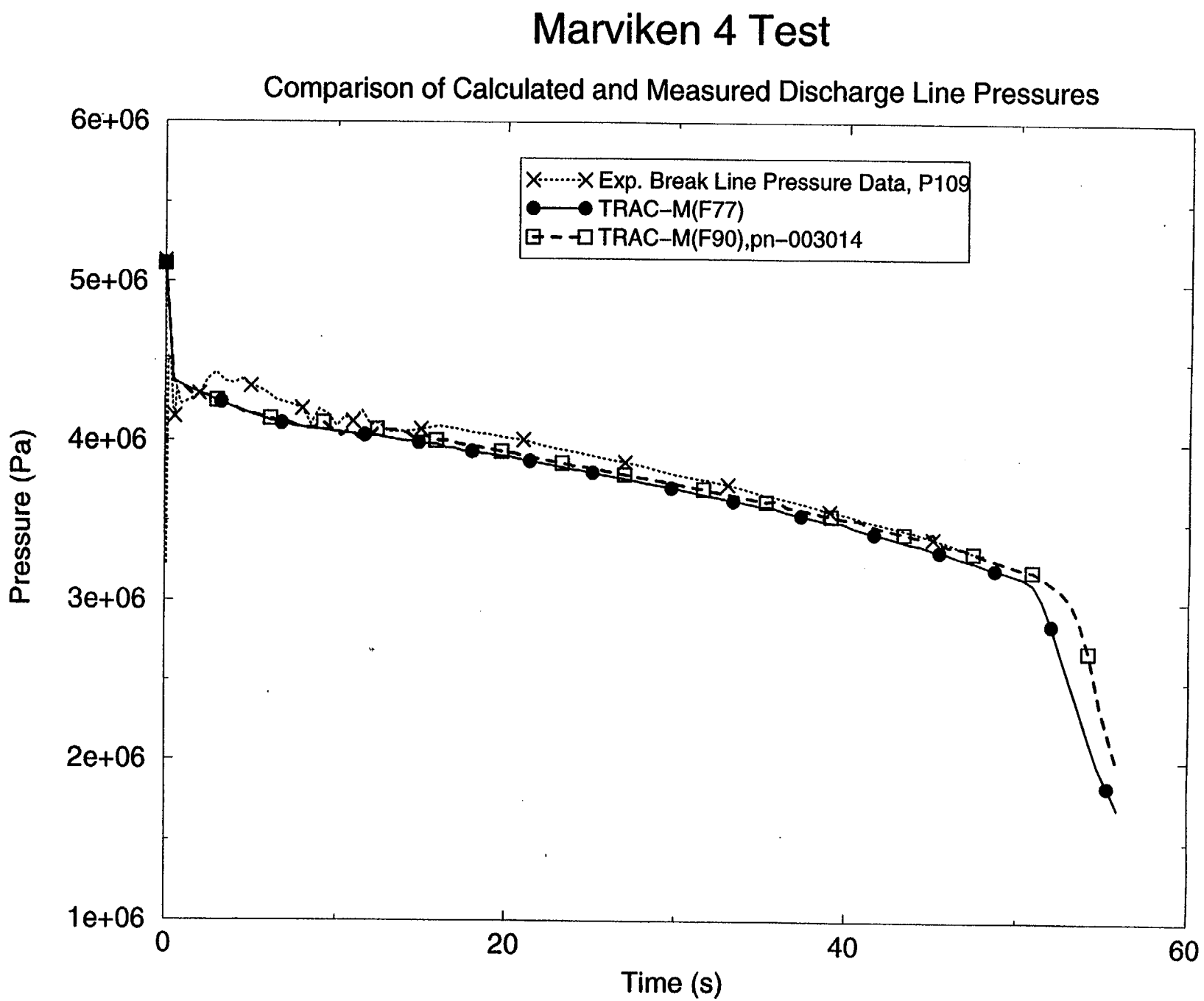

Figure 4.3.7 Comparison of Calculated and Measured Discharge Line Pressures for Marviken 4 Test

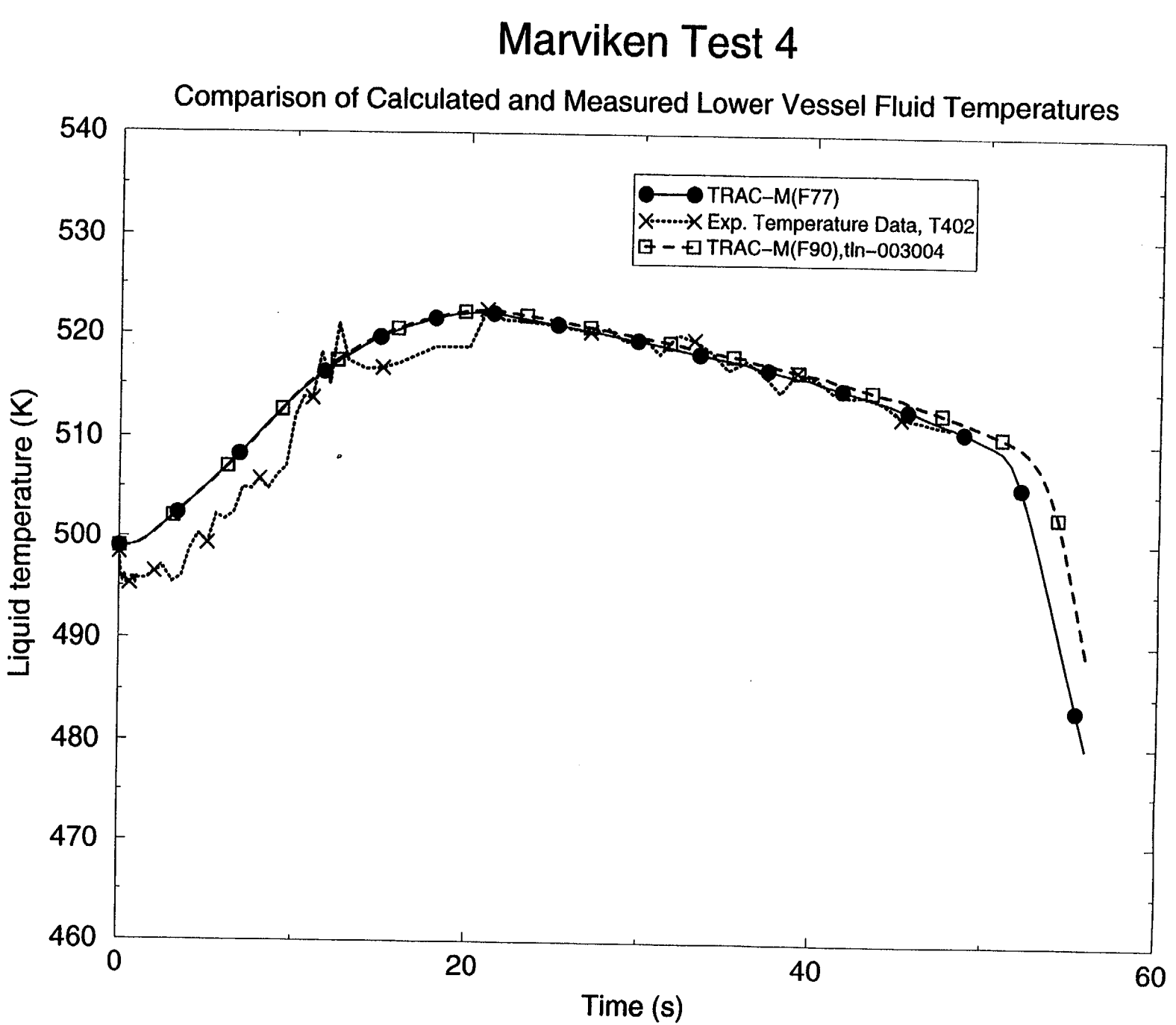

Figure 4.3.8 Comparison of Calculated and Measured Lower Vessel Fluid Temperatures for Marviken Test 4

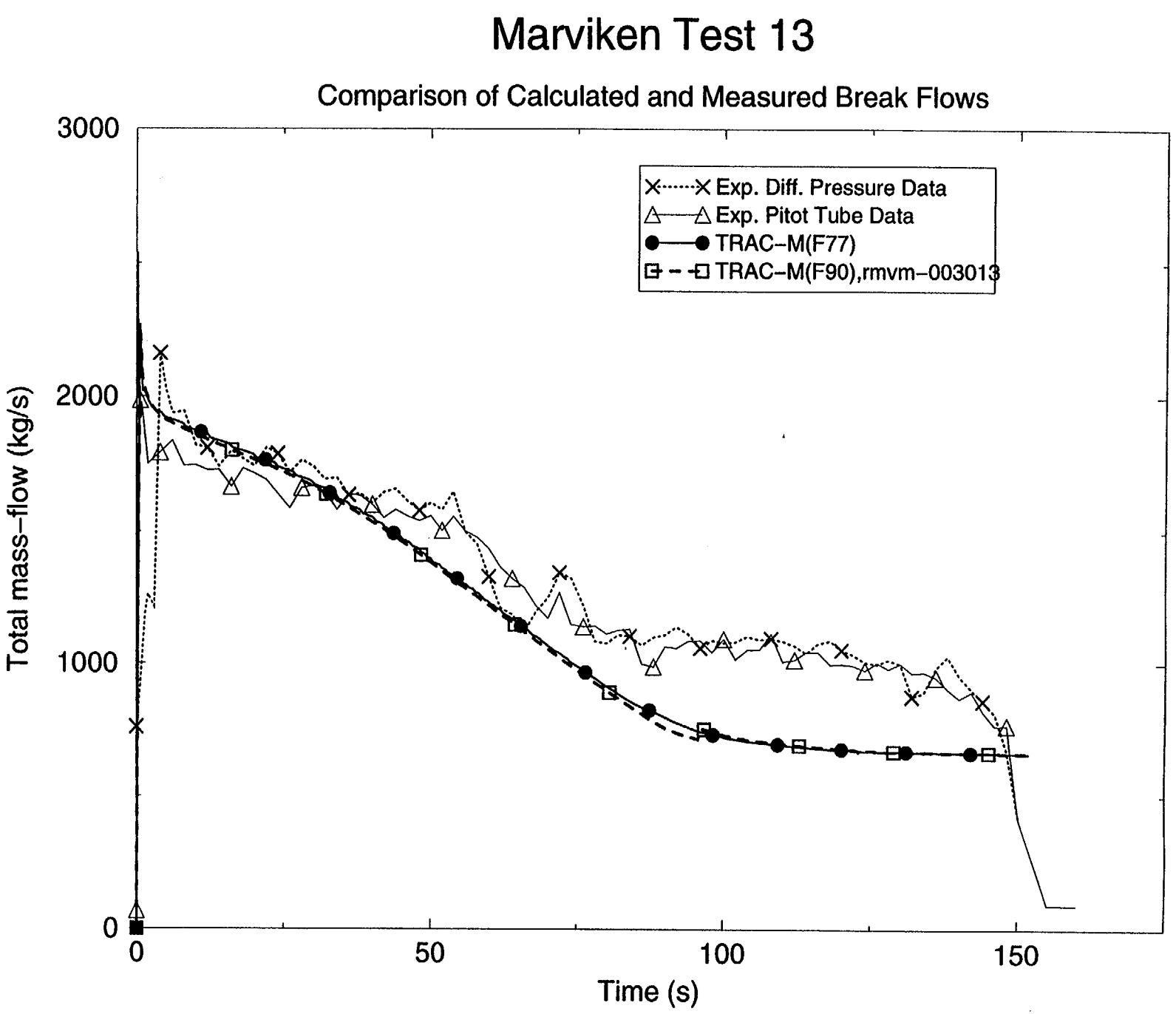

Figure 4.3.9 Comparison of Calculated and Measured Break Flows for Marviken Test 13

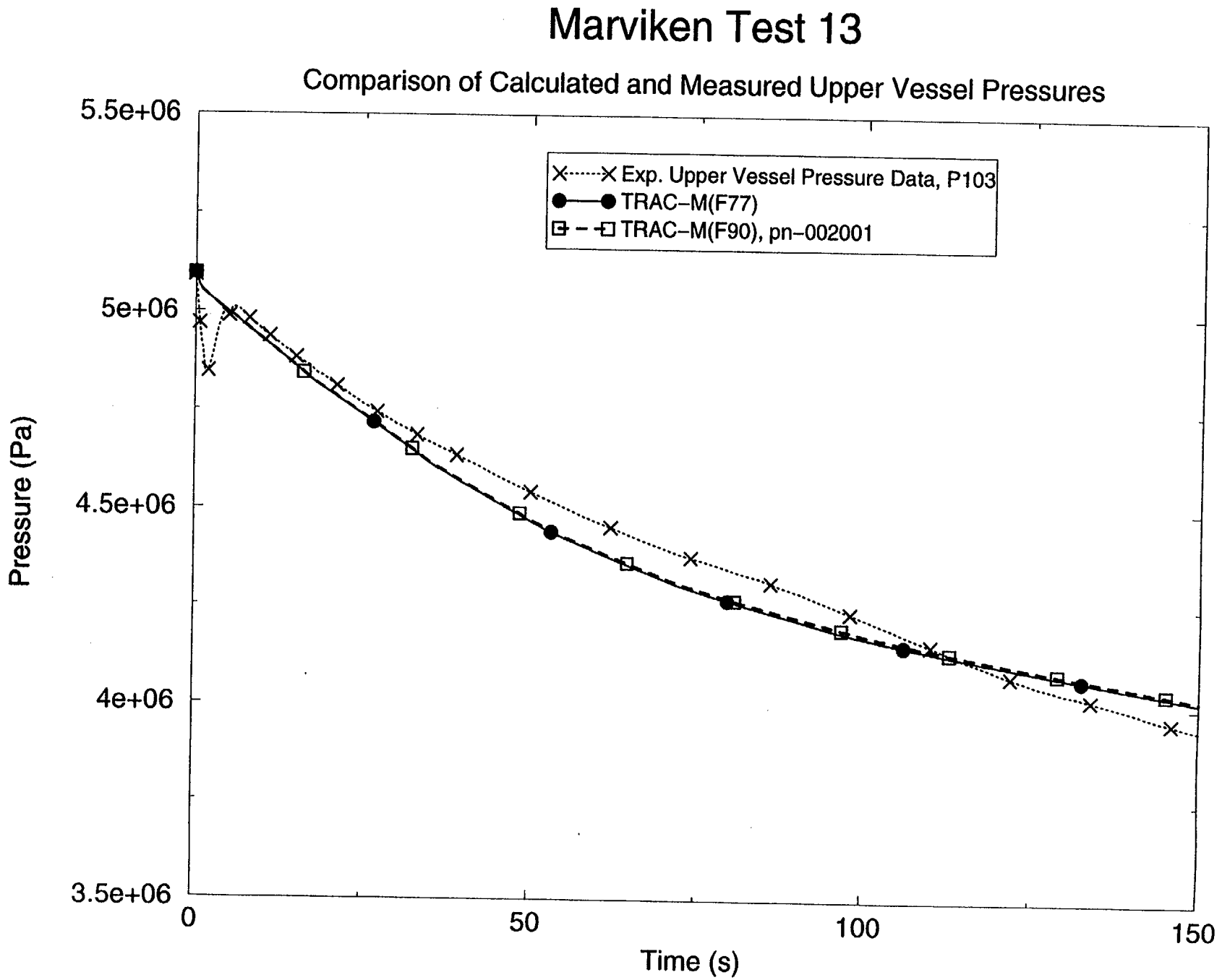

Figure 4.3.10 Comparison of Calculated and Measured Upper Vessel Pressures for Marviken Test 13

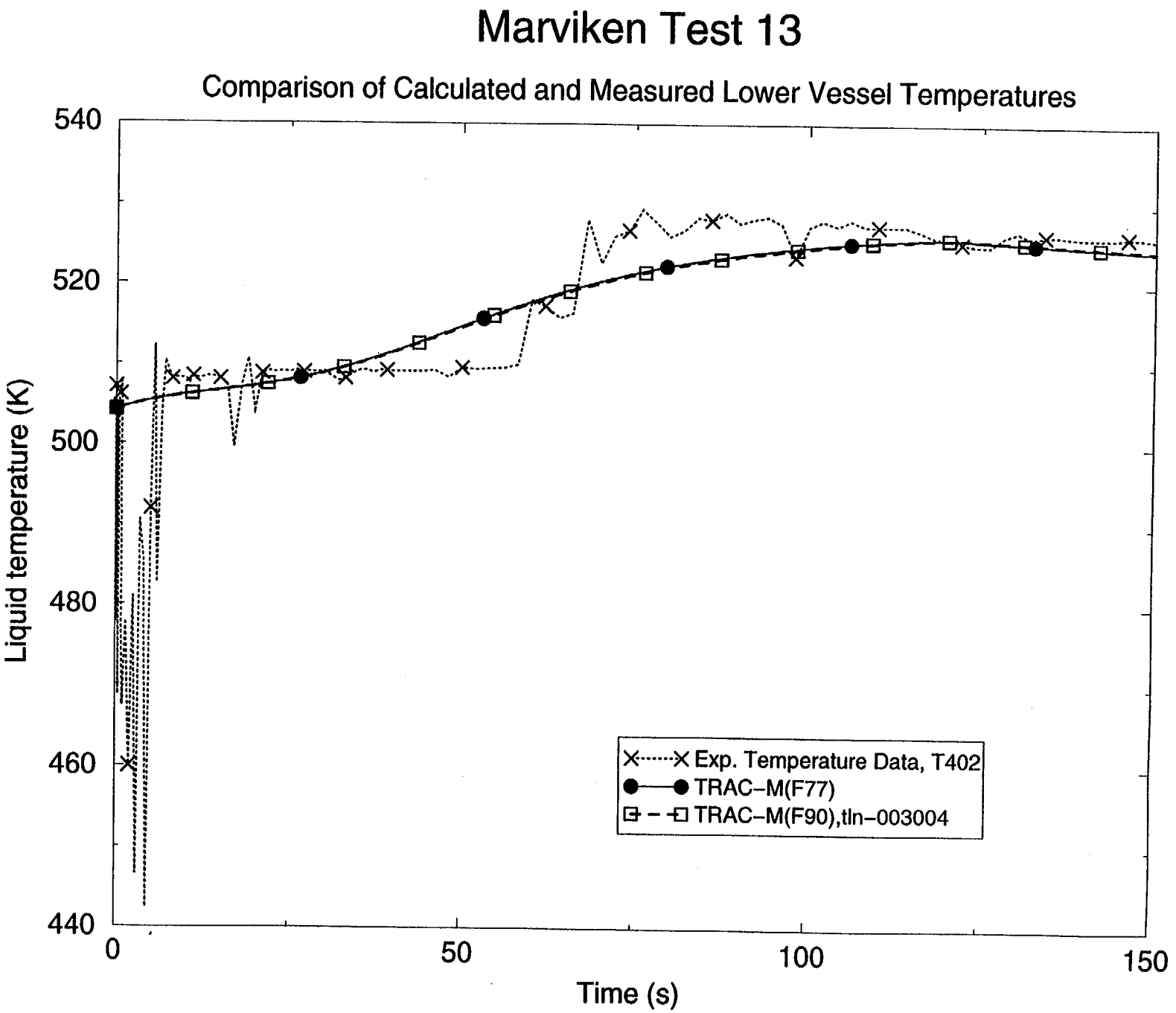

Figure 4.3.11 Comparison of Calculated and Measured Lower Vessel Temperatures for Marviken Test 13

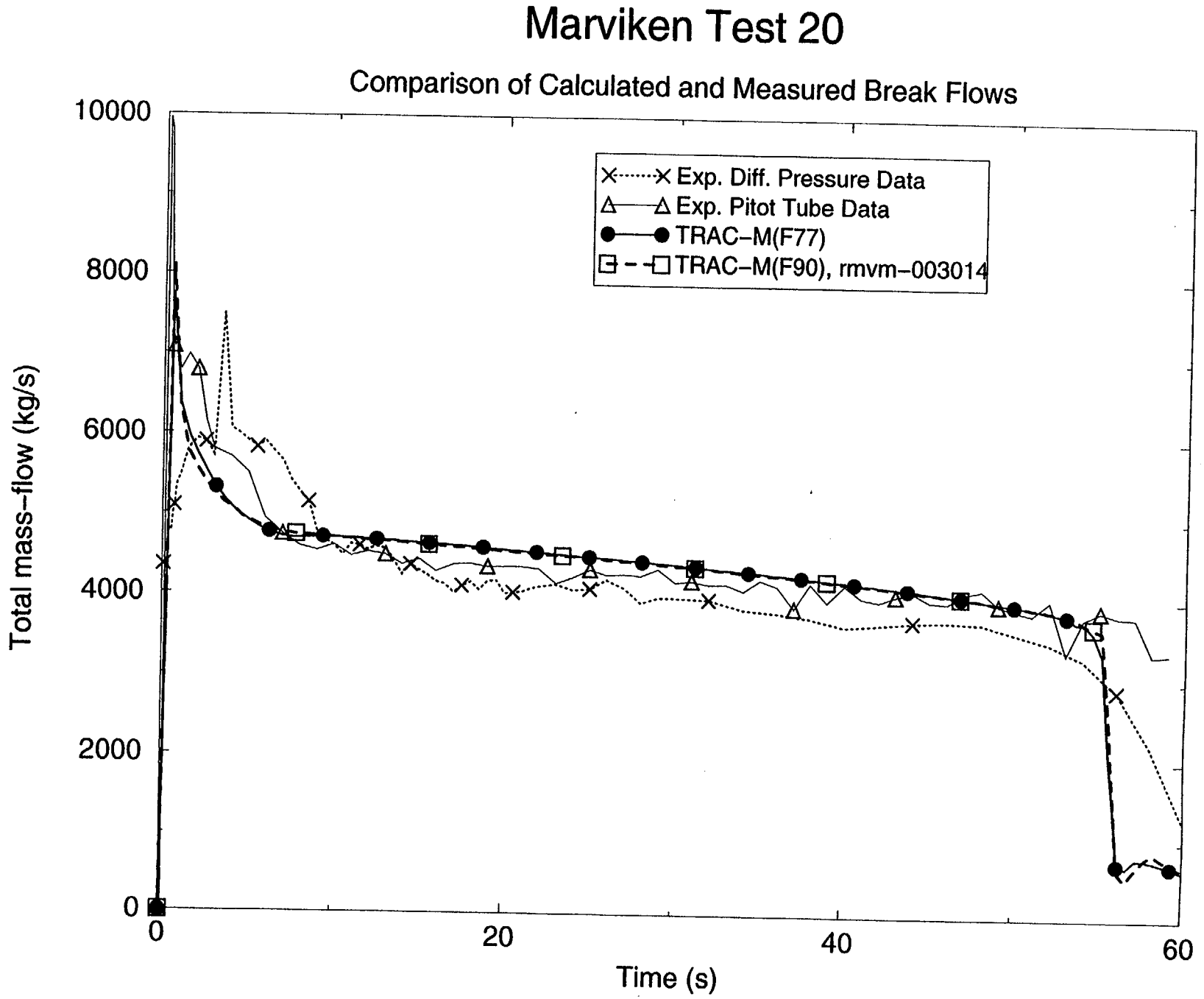

Figure 4.3.12 Comparison of Calculated and Measured Break Flows for Marviken Test 20

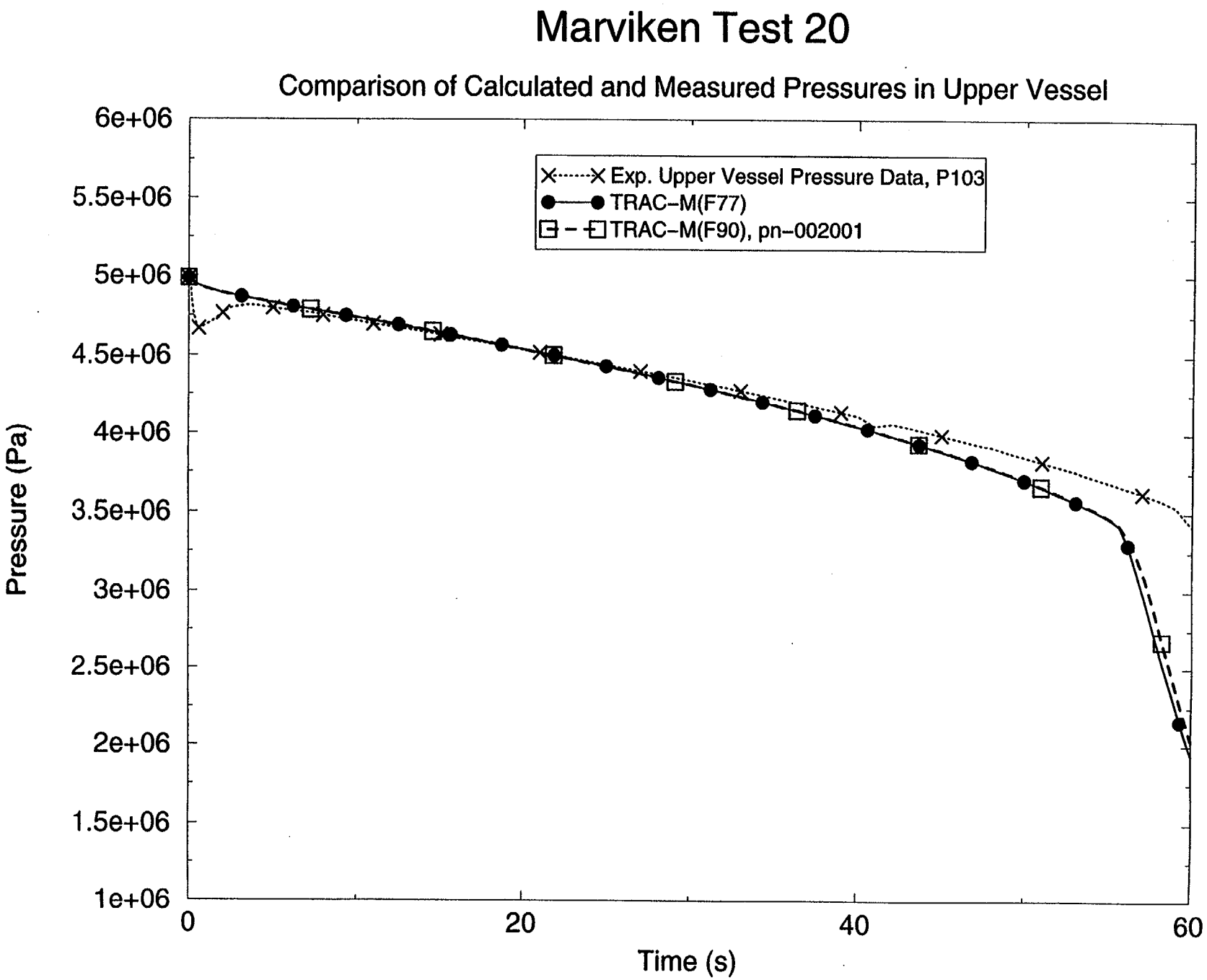

Figure 4.3.13 Comparison of Calculated and Measured Pressures in the Upper Vessel for Marviken Test 20

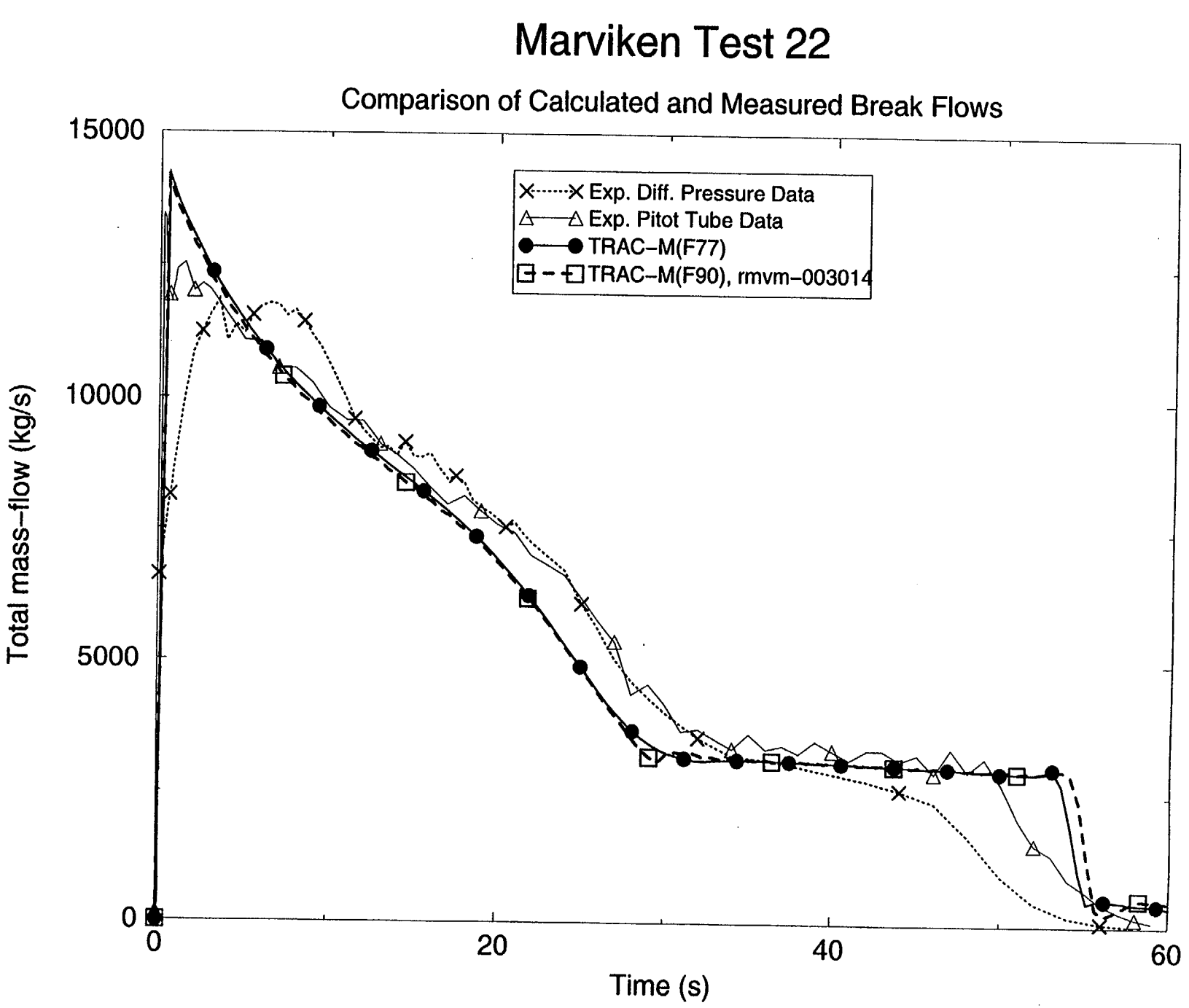

Figure 4.3.14 Comparison of Calculated and Measured Break Flows for Marviken Test 22

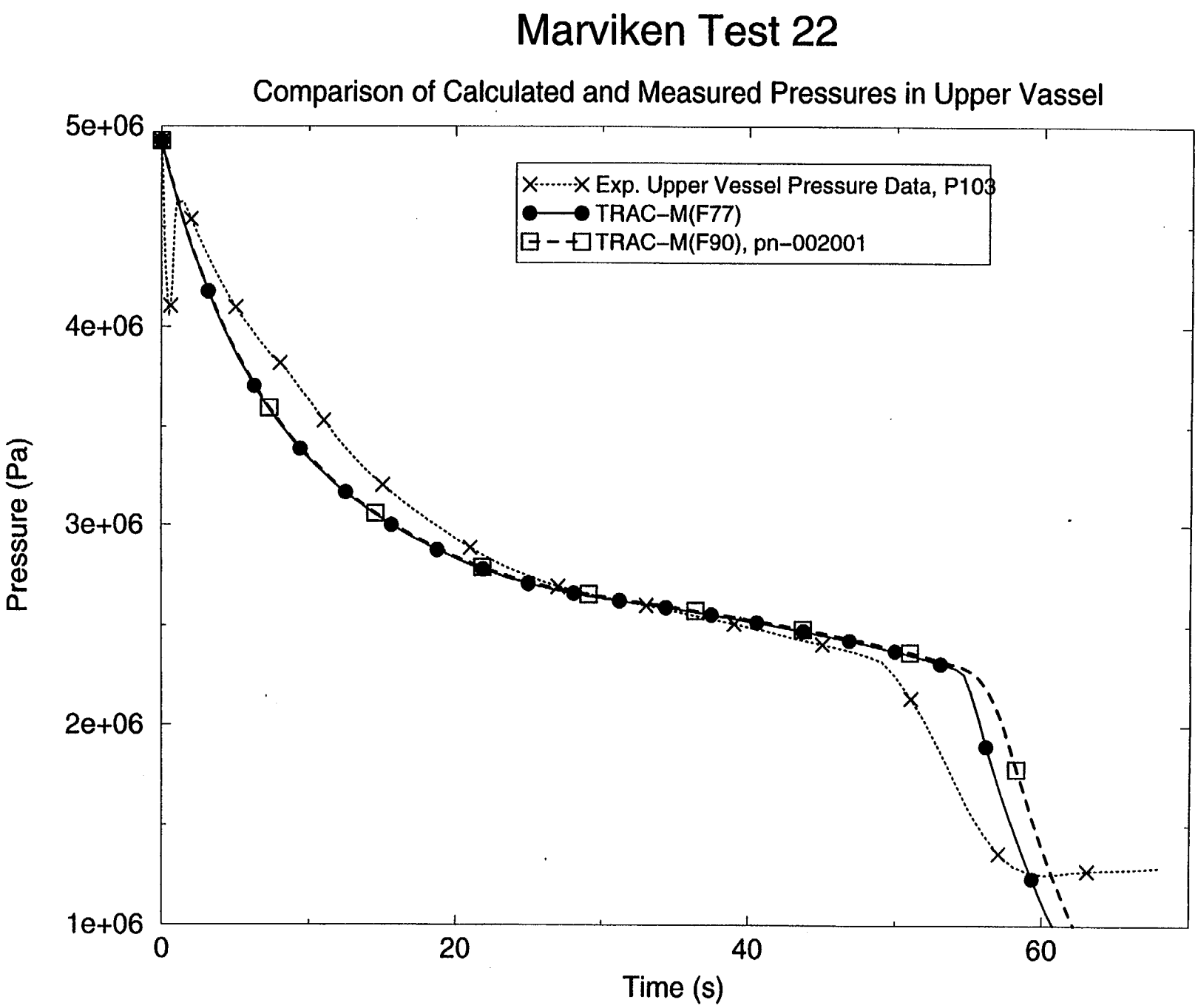

Figure 4.3.15 Comparison of Calculated and Measured Pressures in Upper Vessel for Marviken Test 22

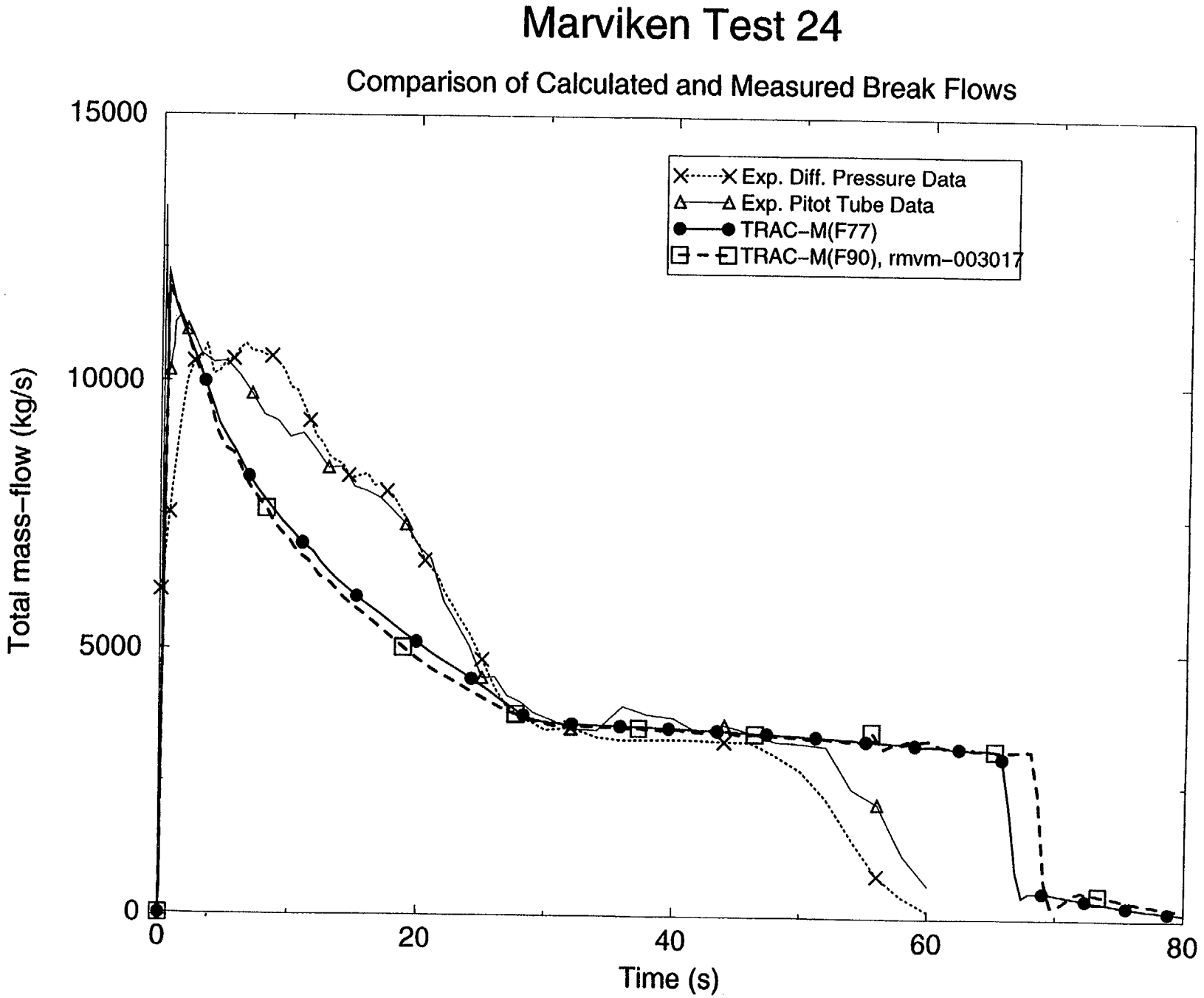

Figure 4.3.16 Comparison of Calculated and Measured Break Flows for Marviken Test 24

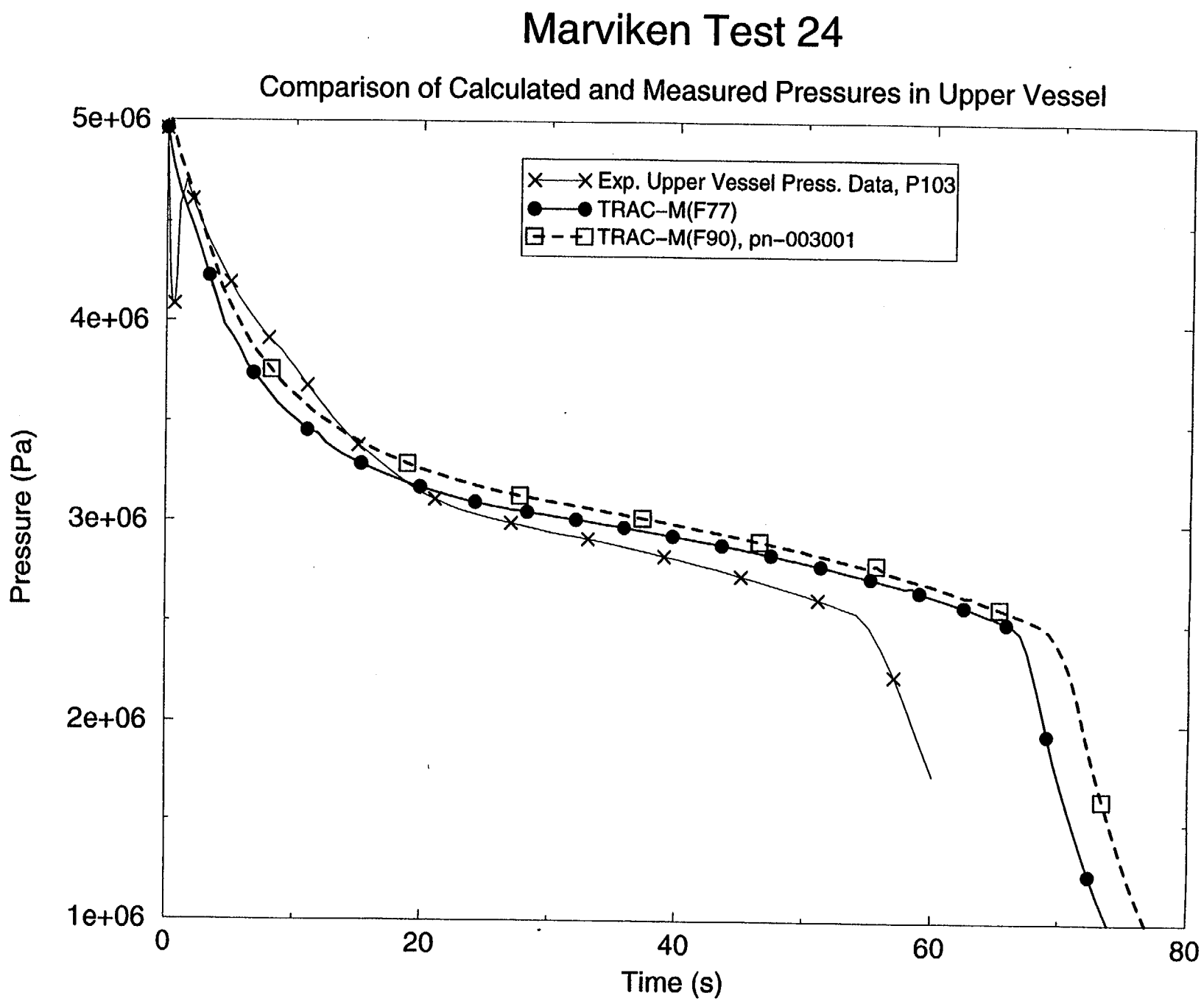

Figure 4.3.17 Comparison of Calculated and Measured Pressures in the Upper Vessel for Marviken Test 24

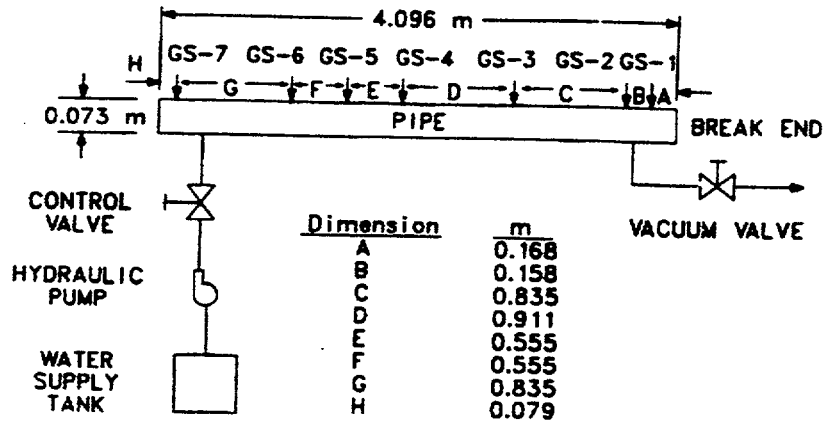

Figure 4.3.18 Edwards Blowdown Test Apparatus

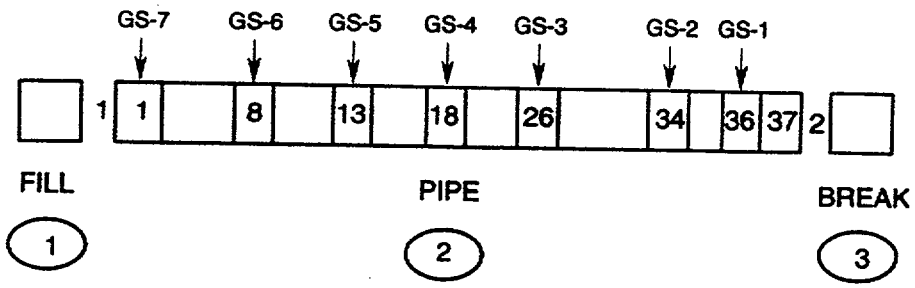

Figure 4.3.19 TRAC Model from the Edwards Blowdown Test

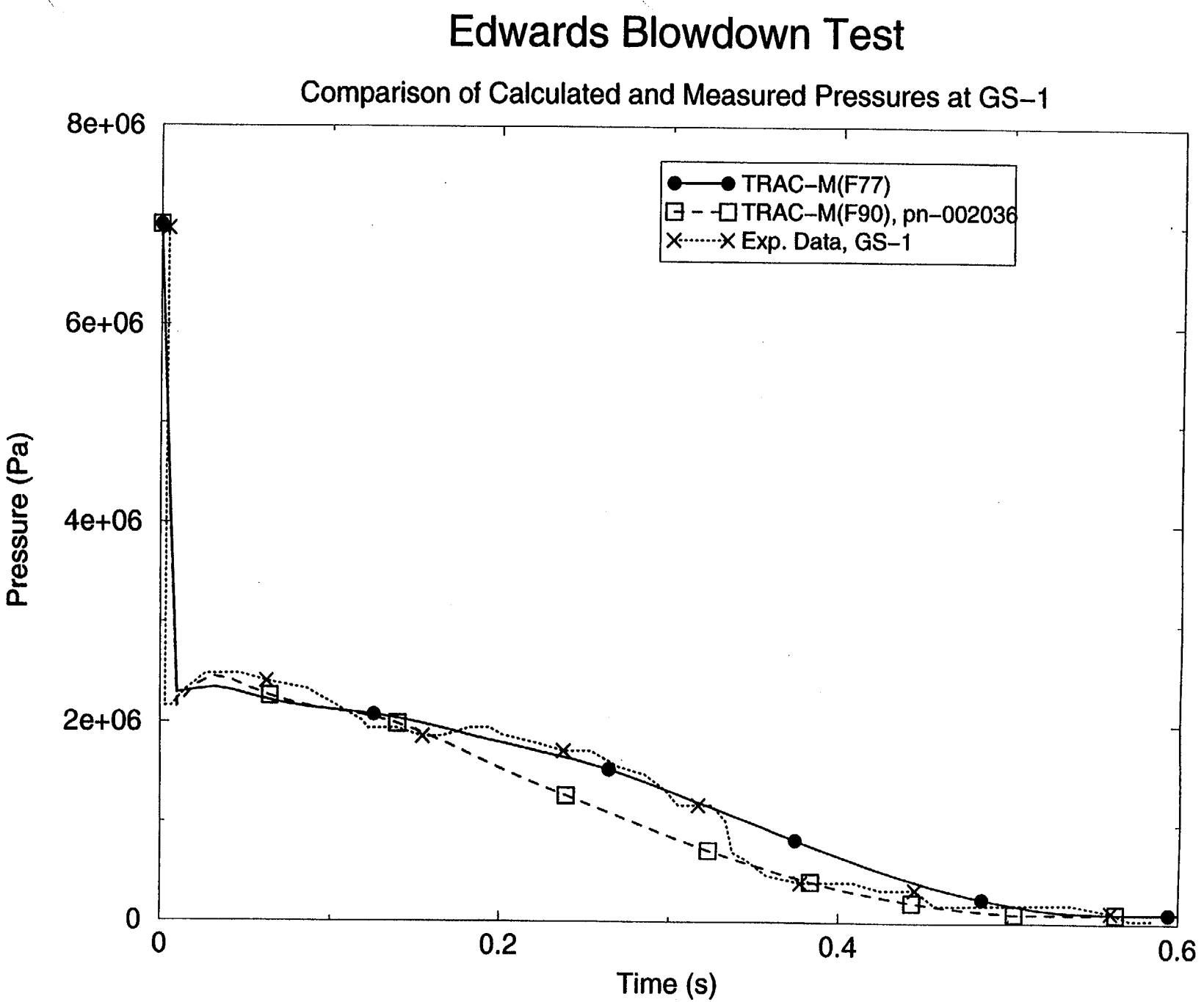

Figure 4.3.20 Comparison of Calculated and Measured Pressures at GS-1 for the Edwards Blowdown Test

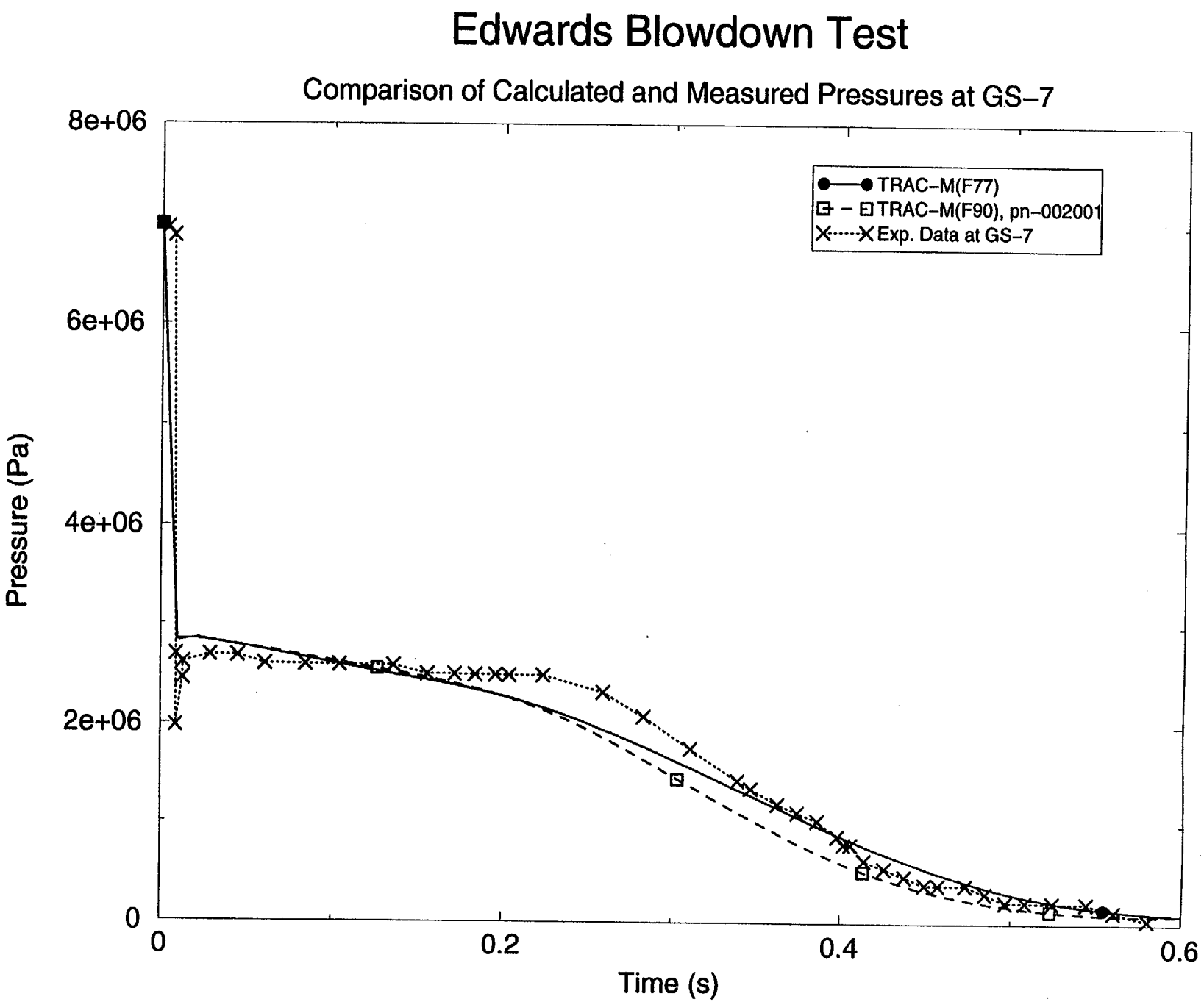

Figure 4.3.21 Comparison of Calculated and Measured Pressures at GS-7 for the Edwards Blowdown Test

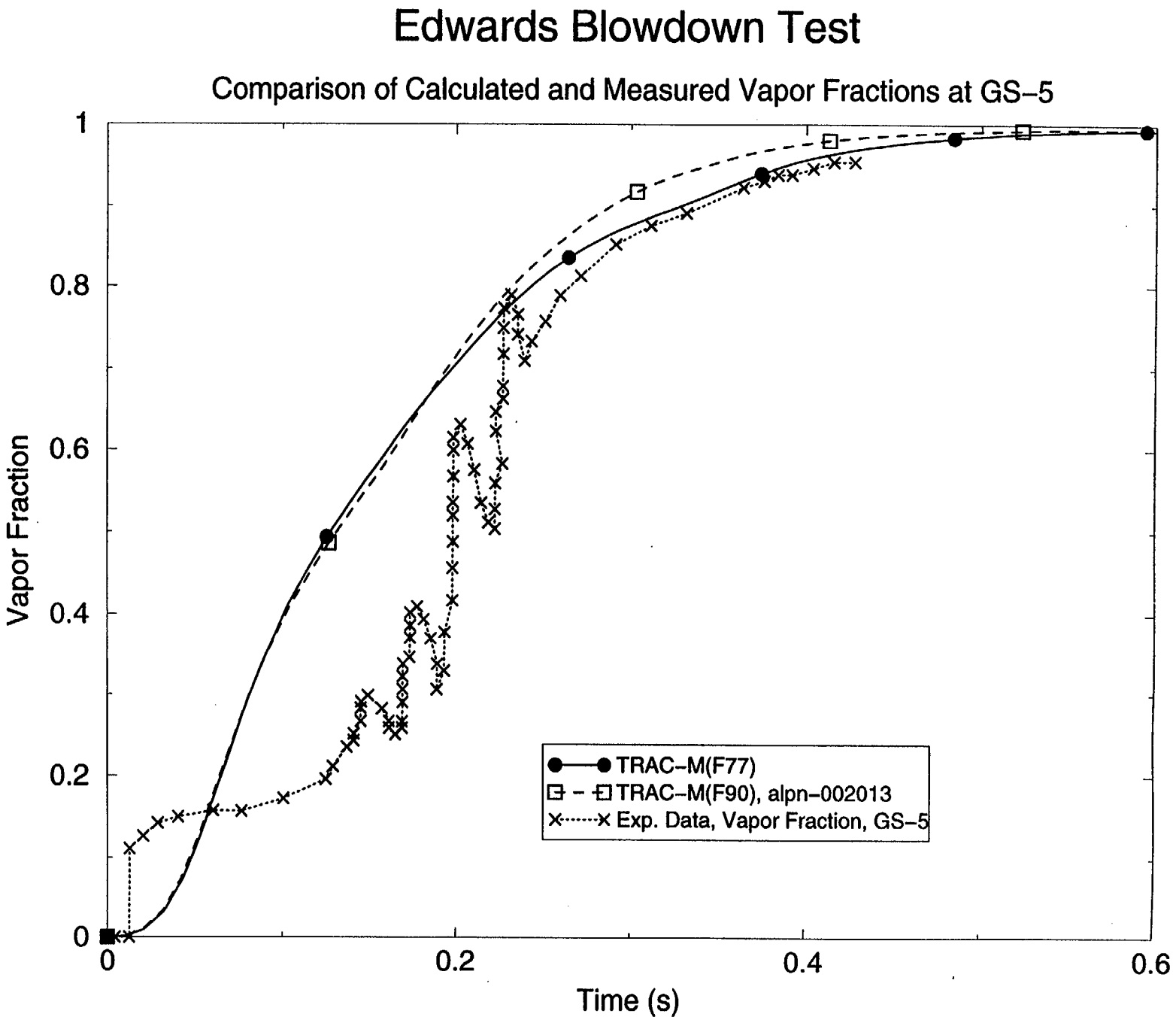

Figure 4.3.22 Comparison of Calculated and Measured Vapor Fractions at GS-5 for the Edwards Blowdown Test

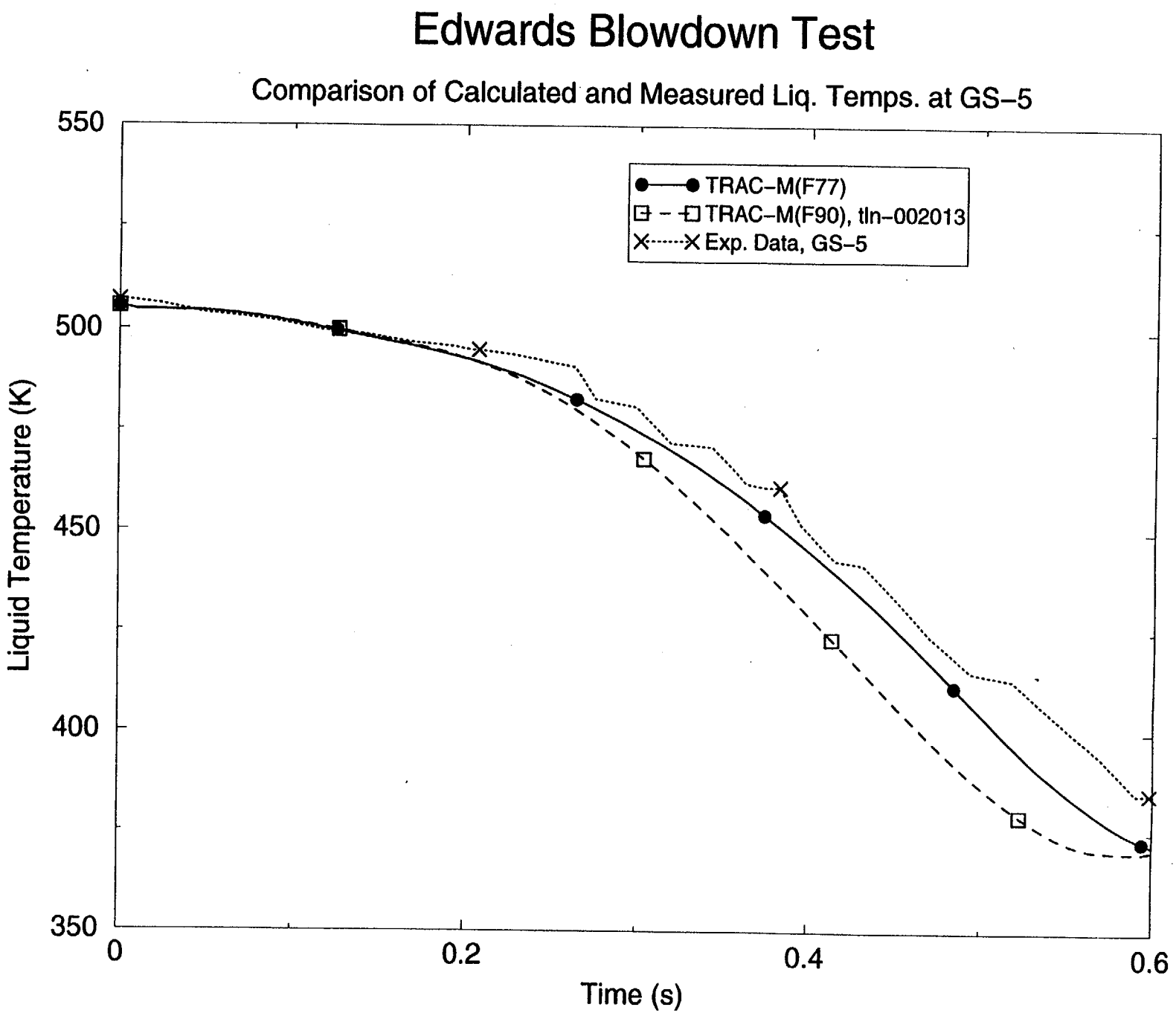

Figure 4.3.23 Comparison of Calculated and Measured Liquid Temperatures at GS-5 for the Edwards Blowdown Test

4.4 Reflood

This section presents the results of an assessment of the capabilities of two codes, namely TRAC-M(F77), Version 5.5, and TRAC-M(F90), Version 3670, to predict reflood phenomenon and provides some conclusions on the conversion of TRAC-M(F77) to TRAC-M(F90). The assessment of the predictive capability of reflood is based on some of the tests performed in the Lehigh University test facility, the FLECHT-SEASET test facility, the Cylindrical Core Test Facility (CCTF) and the Slab Core Test Facility (SCTF). An assessment with Run 31504 from the FLECHT-SEASET test facility shows that the predictions of the reflood phenomenon by the TRAC codes are not accurate, but will yield conservative results although agreements in other tests are better. One reason for better agreement is that some of the TRAC reflood modeling parameters are based on test results of Run 14 performed at CCTF (Ref. 2.1).

The Office of Nuclear Regulatory Research has a research program in place at Pennsylvania State Univeristy (PSU) to improve the agency's capability to model reflood phenomena using its system analysis codes. The findings in this report provide guidance on how future modeling of reflood should proceed. Cases in this report exhibit the overall trend that TRAC-M(F90) overpredicts peak clad temperature (PCT), even though some predictions are more in reasonable agreement in some runs made at the CCTF, SCTF, and LOFT (IET) facilities than in Run 31504 in the FLECHT-SEASET facility. The TRAC-P code series has been used by NRC to perform LOCA analysis because of this conservative trend. However, as the agency begins to risk-inform its regulations, new designs are submitted and licensees request further uprates. NRC would be better equipped to audit licensee submittals with a less conservative, more accurate reflood model. In order to model reflood accurately for all designs, conditions, and test facilities, the proper physics must be modeled mechanistically. This assessment provides a guidance for the development of more accurate models.

4.4.1 Lehigh Rod Bundle Test 02/24/85-20

The Lehigh University rod bundle (LRB) test facility was designed, built, and operated by Lehigh University to simulate post-critical heat flux (CHF) phenomena under nonequilibrium conditions in a rod bundle at low mass fluxes, low to moderate vapor qualities, and near atmospheric pressures. A total of 467 data points were generated from 144 experimental runs, which were executed with the following range of conditions:

Coolant mass flux	0.1 to 26 $kgm^{-2}s^{-1}$
Inlet temperature/quality	40°C subcooled to 0.4
Pressure	105 to 120 kPa
Heat Flux	5 to 43 kWm^{-2}

Post-CHF experiments were conducted in three different modes, including (1) steady state experiments with a fixed CHF location, (2) reflood experiments with slowly advancing CHF locations (propagating quench front), and (3) boiloff experiments with retreating CHF locations. The test used for this assessment, LRB Run 02/24/85-20, was one in a series of advancing quench front tests.

4.4.1.1 Facility Description

The LRB test facility was designed and built for convective boiling and heat transfer studies using steam/water mixtures. The purpose of this research was to obtain post-CHF heat transfer data with nonequilibrium vapor temperature measurements at two axial positions and several radial positions downstream from a fixed or advancing CHF point. A detailed facility description is provided in Ref. 4.4.1, and much of the descriptive information that follows was taken directly from that document. A sketch of the facility is provided in Fig. 4.4.1.

Water was drawn from a surge tank, passed through filters to remove solid impurities, through a flow metering station and pumped to a vertical boiler that produced the desired flow quality to the test section. After passing through the test section, the fluid passed to a tank where the water and steam were separated. A regulating valve on the steam outlet was varied to produce the desired test section pressure. The two-phase fluid was then condensed and cooled by a water-cooled condenser, and returned to the surge tank.

The test section consisted of a heated shroud containing a 3 × 3 rod bundle assembly that was representative of a PWR rod bundle. A cross-section of the bundle is shown in Fig. 4.4.2. The dimensions of the rods and the shroud were selected to provide equal hydraulic diameters in all subchannels. The shroud, made of 2-mm thick Inconel 625 alloy, was heated by radiation from a tubular furnace with three independently controlled zones. The shroud heat flux was to be equal to the test rod heat flux, and 12 chromel alumel thermocouples were brazed onto the outside surface of the shroud at different axial locations. The test section had a length of 1.220 m, and incorporated four ports for vapor temperature and pressure probes. A rod spacer was located 762 mm from the test section inlet, as shown in Fig. 4.4.3, and the inlet contained a strainer to provide uniform flow across the bundle cross-section.

The test rods (9.5-mm O.D.) were heated internally by electric resistance ribbons that were embedded in boron nitride. The rod clad was made of stainless steel. A hot patch was also available to condition the thermal state of the inlet two-phase flow, and to stabilize the quench front in tests for which a fixed CHF point was desired. The hot patch technique was used to produce dryout at the test section inlet. The bottom hot patches consisted of an outer copper block surrounding the shroud and nine short hot rods, each of which acted as an individual hot patch for one of the nine rods in the test bundle. The hot rods were similar to test rods in construction, but provided higher heat fluxes and were individually temperature controlled.

The test section had 108 thermocouples on the test rods in the 3 x 3 bundle assembly. Each of the 9 test rods was equipped with 12 internal thermocouples at different axial elevations. There were also 2 thermocouples in the aspirated vapor probes to measure the vapor superheat temperature. Because the clearance between test bundle rods was only 3 mm, the vapor probes were of a small size (2.13-mm-diameter outer tube) to minimize disruption of the flow as it passed the probe. The probe was also traversable in the cross-sectional plane to enable the measurement of lateral variations in vapor superheat.

Absolute pressure in the test bundle was measured, as well as the pressure drop between the four taps on the shroud walls. Flow rates were measured with variable area flow meters. Power fed to all components of the test loop was measured by power transducers. The loop was designed and instrumented to collect the desired data on flow conditions.

4.4.1.2 Test Procedure and Description

With single-phase water flow in the test section, the furnace power was turned on. It took about 1 to 2 hours to reach the steady-state furnace operating temperature, because of its large thermal mass. When the steady-state operating temperature was reached, the single-phase water flow was diverted from the test section to the bypass line by closing the test section inlet and outlet, and opening the bypass valves. At the same time, the pre-test cooling fluid (steam) was introduced to the test section. (Pre-test cooling was necessary to keep the shroud temperatures within limits, because of the radiation from the furnace, while the hot patches and the test section were preheated.) The steam flow rate was manually adjusted to maintain the shroud temperatures and test section pressure in the ranges of 300–400°C and 1–10 psig, respectively. The hot-patch was heated to approximately 500°C, while the test rods and hot rods were heated to approximately 600°C.

During this pre-heating period, the boiler power was adjusted to obtain the desired test section inlet quality, while the flow was passing through the bypass line. Finally, when all temperatures were high enough to initiate the test, the two-phase fluid was diverted to the test section.

At the time of flow diversion, all instrumentation was activated and recorded until the quench front passed the second vapor probe. Each experimental run was stopped when all of the thermocouples on the test section were quenched.

4.4.1.3 TRAC Model

The TRAC model included only the test section of the Lehigh University two-phase flow facility and LRB Run 02/24/85-20, because the T/H conditions in the other components of the two-phase loop were not of interest. Also, it was possible to specify the necessary boundary condition time histories using experimental data. This approach permitted a more direct assessment of the core T/H models that are used in TRAC. As shown in the schematic in Fig. 4.4.4, the model consisted of 7 components, including 13 fluid cells. For reference, the entrance to the component 1 model in Fig. 4.4.4 corresponds to the bottom of the test section in the schematic presented in Fig. 4.4.3 (i.e., the interface between the copper block/hot patch and the test section).

A 1-D VESSEL model (Component 1) was used to simulate the heated test section, which was divided into 11 fluid cells with node sizes between 0.1 and 0.11-m (3.9 to 4.3-in.) to facilitate detailed modeling of the grid spacer and the locations of vapor probes. The superheated vapor temperatures were measured at locations corresponding to the middle of the sixth and ninth cells in this model. A grid spacer that was 0.79 cm (2 in.) long was located in cell 8. The constant power-generation option was used to simulate the electrically heated test rods. The radiation heated square shroud was modeled with a cylindrical slab having the same perimeter as the shroud. The energy transfer from the radiation furnace was modeled by specifying a proper heat transfer coefficient and a sink temperature at the outside of the cylindrical slab.

The axial noding of ~0.1m used in the LRB Run 02/24/85-20 model is finer than the noding used in standard full-plant models. Core nodes in an AP600 model, for example, are ~0.6 m high. The fine nodalization is used to simulate the phenomena occurring in this test and to accurately predict experimental data.

To model the unheated part of the test section (hot patch), a PIPE (Component 2) was connected to the lower end of the vessel. This extension PIPE consisted of only one fluid cell, and is considered to be very well insulated against heat losses to the environment. At the inlet end of this PIPE component, a FILL (Component 3) was used to model the constant mass injection to the test section. The upper end of the test section was open to a plenum. A BREAK (Component 5) was connected to the upper end via an exit PIPE to specify the boundary conditions at this location.

The boundary conditions input to the model were the test section inlet mass flux, void fraction, inlet temperature (FILL Component 3), and the outlet pressure (BREAK Component 5). The initial wall temperatures were also specified for the ROD and SLAB components.

4.4.1.4 Comparison of Predicted and Measured Results

Lehigh Rod Bundle Test 02/24/85-20 was one of a series of advancing quench front tests conducted in the LRB facility. Specifically, this test was a subcooled reflood experiment, with a slowly moving quench front. The inlet mass flux was 25.13 kg/m^2s, and the inlet coolant temperature of 351.9 K was subcooled 21.1 K relative to the saturation temperature of 373 K at 101.3 kPa. Calculations were performed using both TRAC-M(F77) and TRAC-M(F90).

The prediction of the clad cooling rate throughout the core strongly depends upon the prediction of the correct void fraction distribution, which is primarily determined by the core reflood interfacial drag coefficient (IFDC) model. The IFDC model was developed from the inverted annular flow (IAF) regime map suggested by Ishii and his coworkers (Ref. 4.4.2), in which the IAF regimes along the core are determined from a capillary number defined at the quench front location. In addition to the criteria suggested by Ishii, TRAC also forces IAF regimes to occur within certain void fraction ranges (Ref. 2.1). In some IAF regimes, the core reflood IFDC model uses weighting functions, as well as empirical constants, to make transitions between them. (The empirical constants are used because the experimental pressure drop or void fraction data for each IAF regime are not available in the literature to assess each IFDC model. The available information is usually the pressure drop over a certain length of the core that may experience several IAF regimes, depending upon the distance between the pressure taps.) The pressure drop data of Cylindrical Core Test Facility (CCTF) Run 14 (Ref. 4.4.3) was used to determine the empirical constants.

The TRAC model included the single grid spacer in the Lehigh rod bundle facility, which is located 0.762 m above the test section inlet (the same axial position as in the test facility).

In Figs. 4.4.5 through 4.4.7, the predicted and measured heater rod wall temperatures at elevations 0.15, 0.3, and 0.45 m above the core inlet are plotted against the transient time. The predicted and measured heater rod wall and vapor temperatures at an elevation of 60 cm are shown in Fig. 4.4.8. This is the elevation of the first vapor temperature probe (see Figs. 4.4.3 and 4.4.4). The predictions of wall temperatures tend to increase until ~70 s, whereas the measured data show an immediate decrease at a very small rate. The wall temperature is overpredicted by ~80 K, while the vapor temperature at this location is underpredicted by ~200 to 300 K. Note that the measured vapor temperatures are the maximum possible values and are obtained by drawing a tangent to the peak values of the recorded trace.

At the axial level of 96 cm, the vapor temperature is also underpredicted as shown in Fig. 4.4.9. After 65 s, the predicted vapor temperature comes close to the saturation temperature of the fluid, well below the measured vapor temperature, which remains between 800 and 900 K. The predicted wall temperatures are less than the measured temperatures, indicating that the predicted cooling rate is higher than in the test at this elevation. Whereas the wall temperature is overpredicted at the 60 cm level, it is underpredicted at the 96 cm level. The change from undercooling at the 60 cm level to overcooling at the 96 cm level is caused by the TRAC grid-spacer model implemented at the 76.2 cm level.

We have used the measured and predicted quench times at three levels to calculate an average quench front velocity over the time intervals (Tables 4.4.1 and 4.4.2). The quench-front velocity is not correctly predicted. The main controlling mechanism in determining the rate of quench front propagation is the axial distance dependent transition model. From this assessment, it seems that the empirical constants used in the transition boiling correlation should be reviewed.

As a result of this assessment, it is obvious that the TRAC grid spacer model is seriously flawed. The grid spacer model for interfacial heat transfer is activated when the code finds that a grid spacer is located within a hydro cell, the hydro cell is above the transition boiling regime for bottom-up reflood and the vapor temperature in this hydro cell is above the saturation temperature. The TRAC grid spacer model for interfacial heat transfer is:

$$h_{ig}A_i = C_s H_D/(\text{vol}(T_v - T_{sat}))$$

where

h_{ig} = interfacial heat transfer coefficient from the vapor phase to the interface

A_i = interfacial area

C_s = correlation constant = 10^6

H_D = hydraulic diameter

vol = volume of the hydro cell

T_v = vapor temperature

T_{sat} = saturation temperature

When a grid spacer is modeled in the input deck, and the conditions governing its initiation are satisfied, the grid spacer model for interfacial heat transfer is actuated.

A constant interfacial heat transfer rate from the vapor phase to the interface continues until the vapor temperature reaches approximately the saturation temperature. The TRAC grid spacer model for interfacial heat transfer in the TRAC reflood model is ad hoc; it was developed on the basis of the Lehigh test rod surface temperatures, which showed significant levels of cooling in the vicinity of the grid spacer.

The absence of the grid spacer model can most easily be observed in the vapor superheat comparisons beyond the grid spacer location and in all the axial cladding temperature

comparisons. As discussed above, the grid spacer model, when activated, reduces the vapor temperature to near saturation (Figs. 4.4.8 and 4.4.9). Calculations have also been made without the grid spacer model using TRAC-M (F77), Ref. 1.2. Without the grid spacer model, the predicted superheat temperature, although fluctuating, is near the measured value. With the grid spacer model, the vapor superheat varies between values near measured to saturation for the first 70 s with the saturation temperatures resulting from the grid spacer model. In addition, the wall temperature is significantly higher when the grid spacer model is absent. The impact of the grid spacer model on the wall temperatures is more graphically illustrated in the series of wall axial temperature profiles with and without the grid spacer model, Ref. 1.2. Without the grid spacer model, the predicted wall temperatures remain much higher than measured.

We have concluded that the TRAC grid spacer model is severely flawed; and therefore, it should not be used. However, the results of LRB Test 02/24/85-20 clearly show that the grid spacer is a highly significant component in reflood cooling, and a good grid spacer model is clearly needed. The impact of the grid spacer varies from facility to facility. However, the assessment shows that the grid spacers have a first order impact on the measured cladding temperature. We emphasize that the grid spacer model, used in these calculations does not model the key physical processes associated with a grid spacer.

4.4.1.5 Conclusions

Overall, the agreement between the predicted and measured parameters, with or without the grid spacer model, is minimal or insufficient for both codes.

Early in the transient, the code predicted a rapid advancement of the quench front. However, the predicted rate of quench front advancement slowed as the transient progressed, and the predicted and measured axial locations of the quench front were identical by 149 s. Subsequently, the predicted position of the axial quench front fell behind the measured position.

With the grid spacer model activated, the vapor temperatures were underpredicted throughout the transient. Further, the predicted vapor superheats were highly variable, with short periods of high superheat temperatures approaching the measured superheated vapor temperatures, interspersed with intervals during which the steam is at saturation temperatures. This behavior was directly related to the TRAC grid spacer model.

The TRAC grid spacer model lacks an appropriate physical basis and, therefore, its use is not recommended. The Lehigh data clearly shows enhanced wall cooling caused by the bundle grid spacer. Therefore, it is clear that a well-founded grid spacer model should be developed for TRAC. This assessment also shows that the predictions produced by TRAC-M (F77) and TRAC-M (F90) are very close to each other. We therefore conclude that the conversion from TRAC-M (F77) to TRAC-M(F90) is successful for this type of application.

4.4.2 FLECHT-SEASET Test 31504

This section presents assessment studies of TRAC-M using the data from the 161-rod unblocked test section at the Full-Length Emergency Core Heat Transfer/Separate-Effects and System-Effects Test (FLECHT-SEASET) facility. The FLECHT-SEASET facility simulates only 1-D reflood phenomena, but it allows visual observations through view ports located at several elevations of the bundle. Since the hydraulics and heat transfer are closely coupled, the interactions of such system parameters as flooding rates, pressure, subcooling, initial cladding temperature, heat transfer, and mass effluent fraction have been studied. Among these parameters, the flooding rate was found to be the most influential. Different flooding rates give rise to different flow regimes which, in turn, determine the cladding temperature rise and the quenching of the core. A detailed assessment of the code capabilities is presented in Ref. 4.4.4.

4.4.2.1 Facility Description

The FLECHT-SEASET test facility was developed by modifying the existing FLECHT test facility. A detailed description of the facility is presented in Ref. 4.4.5.

A cross-section of the test bundle with the heater rod instrumentation groups is shown in Fig. 4.4.10. The bundle comprised 161 heater rods (93 uninstrumented and 68 instrumented), 4 instrumented thimbles, 12 steam probes, 8 solid triangular fillers, and 8 grids. The triangular fillers were welded to the grids to maintain the proper grid location. The fillers also reduced the amount of excess flow area from 9.3 to 4.7 percent.

Locations of electrically heated rods, thimbles, and steam probe tubes are identified by alpha numeric coordinates indicated in Fig. 4.4.11. Each heater rod is identified by a circle. Some heater rods are instrumented by thermocouples welded inside its cladding, and such instrumented rods are identified by a group number shown in the circle. These group numbers are associated with the locations of thermocouples.

The heater rods were designed to provide an axial cosine shaped power profile. As a run started, a computer provided decay power to the rods. Figs. 4.4.12 and 4.4.13 show the axial power shape and variation of decay power with time, respectively.

Steam probe tubes and thimbles are identified by double circles in Fig. 4.4.10. Steam probe tubes contain steam probes designed to measure superheated steam temperatures. These steam probes were located in the bundle, as well as the test section outlet pipe, and the bundle steam probes were located in thimble tubes. The probes were designed to separate moisture from the high-temperature steam, and to aspirate the steam across the thermocouple into an ice bucket.

4.4.2.2 Test Procedure

The following is a general procedure used to establish the initial test conditions and to perform a typical FLECHT-SEASET unblocked bundle reflood test. The accumulator was filled with water, and heated to the desired coolant temperature of 53 °C (127 °F) nominal. The boiler was turned on and brought up to the nominal gage pressure of 0.62 MPa (75 psig). The carryover vessel, entrainment separator, separator drain tank, test section upper plenum, and test section outlet piping (located before the entrainment separator) were heated while empty to slightly above the saturation temperature corresponding to the test run pressure. The exhaust line between the

separator and the exhaust orifice was heated to 260°C (500°F) nominal, and the test section lower plenum was heated to the temperature of the coolant in the accumulator. The above component heating was accomplished using clamp-on strip heaters. A Computer Data Acquisition System (CDAS) was used to provide controls for component action and to measure test data during a test procedure.

The test section, carryover vessel, and exhaust line components were pressurized to the desired system pressure of 0.14 to 0.41 MPa (20 to 60 psia) by valving the boiler into the system and setting an exhaust line air-operated control valve to the desired pressure. The coolant in the accumulator was pressurized to 2.76 MPa (400 psia). Water was then injected into the test section lower plenum until it reached the beginning of the heated length of the bundle heater rods. Coolant was circulated and drained to ensure that the water in the lower plenum and injection line were at the specified temperature before the run. Power was then applied to the test bundle, and the rods were allowed to heat up. When the temperature in any two designated bundle thermocouples reached a preset value between 260°C and 871°C (500°F to 1600°F), the computer automatically initiated flooding and controlled power decay. Solenoid valves, in conjunction with a hydraulic control valve, controlled coolant injection into the test section.

During an experimental run, the boiler was valved out of the system, and the pressure was maintained by the control valve located in the exhaust line. Liquid effluent leaving the test section was separated in the upper plenum and collected in a carryover tank. A baffle assembly in the upper plenum was used to improve liquid carryout separation and to minimize liquid entrainment in the exhaust vapor. An entrainment separator (located in the exhaust line) was used to separate any remaining liquid carryout from the vapor. Dry steam flow leaving the separator was measured by an orifice before exhausting to the atmosphere. In order to ensure single-phase flow measurement, the piping upstream of the orifice was heated to a temperature well above the saturation temperature. After all of the designated heater rods were quenched, as indicated by the rod thermocouples, power to the heater rods and coolant injection to the test section were terminated. The entire system was depressurized by opening a control valve, and the CDAS was deactivated. Water stored in all components was then drained and weighed.

4.4.2.3 TRAC Model

Figure 4.4.14 shows a schematic of the TRAC input model that was used to model the forced flow reflood in FLECHT-SEASET Run 31504. The input deck contains one 1-D VESSEL component (Component 5) to model the test section and plenums, one FILL component (Component 1) where the flow rate is defined, one BREAK component (Component 4) where the system pressure is defined, and two PIPE components (Components 2 and 3) connecting the FILL and BREAK components, respectively. The fuel (heater) rods are modeled using a ROD component (Component 6), and the test section housing wall is modeled using another ROD component (Component 7).

A 1-D VESSEL component is used because the reflood phenomenon that occurs in the FLECHT-SEASET test section is one-dimensional. The component contains 18 cells. The lower plenum is modeled with cells 1 and 2, the rod bundle occupies cells 3 through 17, and the upper plenum is modeled with cell 18. The 161 heater rods are modeled as a single ROD component. The input deck does not model grid spacers, since the effects of grid spacers on T/H phenomena

are not correctly modeled in TRAC. Coolant injection was applied to the lower plenum through the PIPE and FILL components, and the flow exits from the BREAK component.

The axial power shape modeling using 18 axial cells accurately duplicated the axial power shape constructed in heater rods (including all steps indicating different power levels). This was done in order to accurately compare the temperature predictions with the measured values. This is much finer nodalization than used for standard reactor fuel rod modeling. Normally, fuel rods are modeled using three or four axial elevations. However, such coarse nodalization introduces an additional uncertainty in calculations that should be accounted for.

4.4.2.4 Comparisons of Predictions with Experimental Data

Calculations were performed using both TRAC-M(F77) and TRAC-M(F90). Both calculations used the newrfd=1 option, which specifies the bottom-up quenching reflood model.

FLECHT-SEASET Run 31504 is one of a series of forced reflood tests that was conducted in the facility. The initial test conditions and key results are presented in Table 4.4.3.

The input deck models the initial conditions reasonably well. Figs. 4.4.15 and 4.4.16 compare the calculated initial heater rod cladding and steam temperatures along the test section with experimental data, respectively. The calculated temperatures agree very well with the experimental data.

The uncertainty of experimental measurements was on the order of 100 K in a two-phase flow. Figs. 4.4.15 and 4.4.16 illustrate the initial experimental clad and steam temperatures, as well as the calculations produced by TRAC-M(F77). The experimental data shown in Fig. 4.4.15 include all of the thermocouples, including those that gave erroneous readings. One reading seems to be an outlier, and can be eliminated. The data spread seems to be larger than 100 K (on the order of 150 K), probably as a result of natural circulation of the steam before the testing was initiated. Such natural circulation would occur because of heat losses from the test section wall, and nonuniformity of the axial power shape. This is also substantiated in Fig. 4.4.16, which depicts the initial axial variation of steam temperatures. Calculations were performed using a 1-D model, which did not model the natural circulation. Considering this limitation, the agreement between the temperature calculations and the measured data is "Excellent" for the initial conditions.

This test was initiated by applying the decay power and forcing the specified inlet flow, which simulated the emergency core cooling system (ECCS) injection into the test section full of steam when the temperature in any rod at any location reached the specified level. As the inlet flow progressed, water slugs and droplets provided precursory cooling to the rods. As the flow progressed, the rods quenched. Comparisons between the calculated clad temperatures and the experimental data are illustrated at different elevations of the test section in Figs. 4.4.17 through 4.4.20. Clad temperatures were calculated using both TRAC-M(F77) and TRAC-M(F90). Only bounding experimental temperature curves are shown. At t=0.0, the clad temperatures are at their initial values.

Temperatures initially increase because the precursory cooling is not sufficient to immediately cool down the rods. As the time progresses, the quench front propagates, precursory cooling increases, and both decay power and rod power decrease. At a chosen elevation, clad temperatures first increase until they attain their maximum values, and then turn around as

precursory cooling increases, and finally drop to the saturation value as the rod quenches. Fig. 4.4.21 illustrates the propagation of the quench front. Quench times predicted by TRAC-M(F77) during the first 200 s of the transient are slightly delayed, but they meet the acceptance criterion of a 120-s spread. (See Ref. 4.4.4.) After 200 s but before 500 s, the predictions indicate substantially earlier quench, and do not meet the acceptance criterion. Between 500 and 620 s, quenching occurs within the acceptance criterion. Quench times predicted by TRAC-M(F90) are always delayed. Except for a short time in the beginning of the transient (about the first 150 s of the transient), the delay does not meet the acceptance criterion (Ref. 4.4.4).

Figs. 4.4.17 through 4.4.20 illustrate the clad temperatures predicted by both codes, as well as the bounding experimental data for various elevations of the test section. The bounding experimental data traces bound the spread of the experimental data, which is 100 K. Since the tests were run with grid spacers, and grid spacers are not modeled in the codes, the codes should predict hotter temperatures (up to 100 K), which is the expected bias (Ref. 4.4.4). Figs. 4.4.17 through 4.4.20 show that the maximum clad temperatures predicted by TRAC-M(F77) meet the acceptance criterion of 100 K ± 100 K for all elevations (Ref. 4.4.5). Those predicted by TRAC-M (F90) meet the acceptance criterion for low elevations (below ~2.00 m), but not at higher elevations.

Fig. 4.4.22 illustrates experimental differential pressure data taken along the test section. These data were taken at 1-foot increments, starting from the 0-foot reference and ending at a height of 10 feet. Note that the data indicate orderly and monotonic progression of a sharp quench front (suggested by rapid increases of pressure drops at lower elevations). The sharpness of the quench front disappears at higher elevations; however, progression of the quench front is still orderly and monotonic (i.e., the height of the quench front increases with increasing time).

Fig. 4.4.23 illustrates calculations of vapor fraction along axial distance with TRAC-M(F77). Although the calculations show predictions of quench fronts at different times, they indicate that progression is not orderly and monotonic. Calculations and animation of the calculated results with the XTV code show that the quench front and vapor fractions along the test section continuously oscillate, indicating that the code does not correctly predict the phenomenon.

Figs. 4.4.24 through 4.4.29 present comparisons between the experimental data and the code predictions of differential pressure drops. Both codes predict large-amplitude, high-frequency oscillations, while the measurements show relatively smooth conditions. The predictions of large-amplitude, high-frequency oscillations are not considered realistic. Qualitatively, there is "Insufficient" agreement between the calculations and the test data.

Figs. 4.4.30 through 4.4.32 present comparisons between the experimental data and the calculated steam temperatures at various elevations. There are very few steam temperature measurements; hence, it is not possible to estimate their uncertainties. However, the comparisons indicate that the calculated values differ by *several hundred degrees* from the experimental data. Hence, the agreement is "Insufficient."

These comparisons indicate that both codes are not correctly predicting the reflood phenomena. Although peak clad temperature predictions produced using TRAC-M(F77) are excellent, the rest of the clad temperature predictions minimally agree with the data, and there is insufficient agreement between the test data and the code predictions of differential pressures and

steam temperatures. One can conclude that the predictions of peak clad temperatures are fortuitous.

A big surprise in the code calculations was the very large differences between the TRAC-M(F77) and TRAC-M(F90) predictions of almost any parameter. Examination of the output files indicates that TRAC-M(F77) was predicting choked flow conditions at the exit of the test section. There were some corrections in the algorithm of the choked flow model in TRAC-M(F90); therefore, TRAC-M(F90) was not predicting choked flow conditions.

Fig. 4.4.33 demonstrates the effects of choked flow predictions. The choking of the flow produces high pressures in the test section, as predicted by TRAC-M(F77) while the test section pressures predicted by TRAC-M(F90) (without choked flow) remain almost constant at 40 psia, which was the pressure level at which the experiments were conducted.

Choking should not have been predicted, since this phenomenon does not occur during reflood. It is clear that the TRAC-M(F77) predictions are completely incorrect, and the code is predicting different phenomena. Prediction of choking implies high two-phase velocities. It is expected that predictions by both codes would indicate substantially more liquid carryout than in testing. This would lead to higher clad temperature predictions, since less liquid would contact the surface of the rods and less cooling would occur. Figs. 4.4.34 and 4.4.35 show comparisons between the experimental data and the liquid and steam carryouts (integrated liquid and steam outflows) predicted by both codes.

To evaluate the effect of choking on the predictions, the choking model was artificially turned off during a sensitivity study performed using TRAC-M(F77). Figs. 4.4.36 through 4.4.39 compare the calculations produced using TRAC-M(F77) with and without the choking model, and those produced using TRAC-M(F90) with the experimental data. As expected, the predictions produced using TRAC-M(F77) without the choking model are very close to those produced using TRAC-M(F90). Some differences are expected as a result of the bug fixes in TRAC-M(F90) and the results seem to be "close enough." This comparison shows that the conversion to TRAC-M(F90) is successful for this type of application.

4.4.2.5 Discussion of TRAC Models

Excessive liquid carryout, which has been predicted in many reflood tests (Ref. 1.2), is an indication that the interfacial area used by the code is larger than in tests. This raises the question of how well the flow regime maps have been modeled in the code.

Fig. 4.4.40 shows the flow regime map used in the TRAC code (which depicts "inverted annular flow") during reflood when the inlet conditions are subcooled or low-quality. Figs. 4.4.41 and 4.4.42 show the relative velocities calculated using TRAC-M(F77) and TRAC-M(F90) at Cell 10 (at about the middle of the test section) and Cell 17 (almost at the end of the test section). Note that these relative velocities are very high. High steam velocities may tear the liquid away from the liquid core and also carry large slugs of liquid out of the test section without permitting the liquid to contact heated walls for a long time. Consequently, these high relative velocities explain why the liquid carryout from the test section is higher than the measured data and why the calculated clad temperatures, in general, are higher than the experimental values.

The TRAC flow regime maps are predicated on the work performed by Ishii and his coworkers (Ref. 4.4.2), which indicates that these flow regime maps exist at relatively low relative velocities. For example, Ref. 4.4.2 states that if the relative velocity is increased to 2.0 m/s, smooth and rough wavy sections are nonexistent; however, the relative velocities shown in Figs. 4.4.41 and 4.4.42 are much higher than 2.0 m/s (up to 20.0 m/s). This would lead to the conclusion that, at these predicted velocities, the flow regime maps used by TRAC-M(F77) or TRAC-M(F90) cannot be consistent with the flow regimes that actually occur in tests.

According to Ref. 4.4.2, the inverted annular flow regime has four different regions with distinct characteristics, 1) smooth, 2) rough-wavy, 3) agitated flow, and 4) dispersed flow. Fig. 4.4.40 depicts these regions, as well as the transition flow region (i.e., the transition boiling region between the CHF point and the T(min)). The tests in Ref. 4.4.2 were performed under conditions that did not simulate the transition flow region.

Ref. 4.4.2 defines the boundaries of four different regions on the basis of the Capillary number with restrictions on their applicability. The regions of applicability are predicated on the Weber number and vapor fraction, and the Weber number is founded on the relative velocity. Examination of the documentation on the TRAC code (Ref. 2.1 and Ref. 4.4.6) indicates that although the same Ishii correlations based on the Capillary number have been used, the regions of applicability are not the same, because they are based on the vapor fraction alone and not on the Weber number.

Table 4.4.4 shows the Capillary number criteria and the Weber number restrictions in Ref. 4.4.2 and TRAC code application in Ref. 4.4.6 and Ref. 2.1, where in Ref. 4.4.2, Z is the average break-up length measured from the inlet of the test section, D is the liquid jet hole diameter, Ca is the Capillary number defined using fluid jet properties (viscosity, velocity, and surface tension) at the inlet ($Ca = \mu_l V_l/\sigma_l$), We is the Weber number defined using fluid jet and gas properties at the inlet ($We = \rho(V_g - V_l)^2 D/\sigma_l$), and α_i is the void fraction at the inlet of the test section. In Ref. 4.4.2, for a constant inlet jet flow and a constant inlet gas flow, which is injected from a nozzle at the periphery of the test section, all breakout points (boundaries of flow regimes) are determined by the relationships in the second and third columns. Experiments were run at the steady state. Flow regimes vary axially but the boundaries remain constant with time. The void fraction at the inlet of the section is determined by the test section geometry alone, and does not change with changing jet liquid velocity or gas injection velocity. Hence, for a given test section, the breakout points are determined only by the liquid velocities (i.e., Capillary numbers, provided that the gas velocities are within the ranges determined by the correlations with Weber numbers). Note that both liquid and gas velocities are quantities measured at the inlet, not local quantities. It is surprising that the breakout points do not vary with the amount of power or power profile applied to the test section. This can be true only if the amount of power and power profile did not change during the tests. Hence, power or power profile did not enter into the correlations. However, heating and power profile can be a major factor in reactor applications.

The TRAC modeling is different, in that the Capillary number is calculated using fluid properties at the CHF point, and the criteria for the applicability of Ishii correlations (i.e., breakout points) are founded on local void fractions. Details concerning the calculations of the local void fractions, presented in Ref. 2.1, do not include any restriction on the basis of Weber numbers calculated using relative velocities.

It is clear that the flow regime maps modeled by Ishii in Ref. 4.4.2, have not been correctly implemented in TRAC. On the other hand, Ishii correlations may have an important shortcoming in that breakout points are independent of power input to the test section, and relative velocities are predicated on quantities measured at the inlet. It is clear that new experiments should be performed, and a new reflood model should be developed. Determination of the type of reflood modeling in the TRAC code and the type of experiments to be performed for accurate reflood modeling is outside of the scope of the present assessment.

4.4.2.6 Conclusions

The top-level requirement in the development of a T/H code is that the code should correctly model the physics of the phenomena. This assessment shows that TRAC does not correctly model the flow regime maps during the reflood and, consequently, it cannot correctly model the interfacial areas between phases, and cannot correctly predict vapor fractions, phasic velocities, and temperatures. Almost none of the important parameters (such as clad temperatures, steam temperatures, differential pressures, and liquid and steam carryouts) are consistently predicted with acceptable accuracy throughout the range. The predictions in ranges where clad temperatures are predicted within accuracy limits, are accidental. Also, the predicted clad temperatures are higher than the experimental data because predictions of liquid carryout by the codes during reflood have consistently been high (Ref. 1.2). Hence, these predictions are conservative.

Comparison between TRAC-M(F77) and TRAC-M(F90) code calculations is favorable. The sensitivity study performed with TRAC-M(F77) without the choking model indicates that the calculations agree reasonably well with the calculations performed with TRAC-M(F90). The observed differences are probably attributable to many error fixes in TRAC-M(F90). We believe that the conversion from TRAC-M(F77) to TRAC-M(F90) has been successful for this application.

4.4.3 Cylindrical Core Test Facility (CCTF), Core I Test C1-5 (Run 14)

The Cylindrical Core Test Facility (CCTF) was designed, built, and operated by the Japan Atomic Energy Research Institute (JAERI) to provide information on thermal-hydraulic behavior during the refill and reflood phases of a LOCA in a PWR. The CCTF was used to run two test series, which were designated as CCTF Core I (CCTF-I) and CCTF Core II (CCTF-II) tests. The blowdown period was not simulated for either series, and the facility configuration was slightly modified for the second series.

The CCTF tests were conducted with the following objectives:

- Demonstrate ECC behavior during refill and reflood phases.
- Verify reflood analysis codes.
- Collect information to improve the T/H models in such analysis codes as (a) multidimensional core thermal-hydrodynamics including the radial power distribution effect, fallback effect, and spatial oscillatory behavior; (b) flow behavior in the upper plenum and hot legs; (c) behavior of accumulated water at the bottom of the upper plenum, including possible countercurrent flow and sputtering effects; (d) hydrodynamic behavior of the injected ECC water and water passing through the steam generator; (e) multidimensional T/H behavior in the hot annular downcomer; and (f) overall oscillatory behavior in the system.

4.4.3.1 Facility Description

The CCTF is a full-height, experimental facility designed to model a four-loop, 1100-MWe PWR. Figs. 4.4.43 and 4.4.44 show a schematic of the CCTF facility and a top view of the primary system piping, respectively. Fig. 4.4.45 shows a top view of the pressure vessel, and the configuration of bundle assemblies. Additional descriptive information regarding the facility can be found in Refs. 4.4.7 and 4.4.8. All pertinent PWR components have been modeled. Vessel and primary-loop components are full height and their dimensions are volume-scaled in a ratio of 1/21.4, as compared with a 1100-MWe PWR. The pressure vessel downcomer annulus is larger than the width that results from an exact 1/21.4 scaling because the scaled core bypass area is included as part of the downcomer area. The upper plenum internals are reduced in radial dimension by the ratio of 8/15. Depending on facility configuration and operation, tests in the CCTF have been variously defined as either separate effects tests (SETs) or integral effect tests (IETs) (Refs. 4.4.9 and 4.4.10, respectively).

The CCTF vessel contains a core, an annular downcomer, and upper and lower plena. The CCTF core contains thirty-two 8 x 8 bundles, each containing 57 electrically heated rods and 7 nonheated rods (a total of 1824 heated rods and 224 unheated rods). Bundles are assembled to form different powered zones, as shown in Fig. 4.4.45. In CCTF-I, each bundle includes rods with three different power densities, resulting in local peaking factors. The heated rods are held in place by grids, as in a PWR. Each heated rod consists of a nichrome heating element, magnesium oxide and boron nitride insulators, and an Inconel sheath. The heated length and outer diameter of the heater rods are 3.66 m and 10.7 mm, respectively. The average axial power profile is simulated by a 17-step chopped cosine profile, with an axial peaking factor of 1.492. The unheated rods simulate the guide and instrument thimble tubes in PWR fuel assemblies.

The primary loops consist of three intact loops and a broken loop. Each loop consists of hot leg and cold leg piping, a steam generator simulator, and a pump simulator. The 200% cold leg break is simulated in the broken loop. The two ends of the broken loop are connected to two containment tanks through blowdown valves. The steam generator simulators are of the U-tube and shell type. Each steam generator simulates two loops that are housed in a single shell assembly having two compartments, one simulator for each loop in a single compartment. The primary coolant passes through the tube side, and the secondary coolant is stagnant in the shell side. The steam generator tubes are 25% shorter than those in a commercial reactor.

The ECCS consists of two accumulators and a low-pressure coolant injection (LPCI) system. The instrumentation consists of detectors, signal conditioners, signal processors, recording equipment, and display equipment. Temperature measurements are made with alumel chromel thermocouples having an expected error of 0.5%. Pressure and differential pressure measurements are made with differential pressure cells, with an expected error of 0.3%. In the pressure vessel, liquid level measurements are made in two ways. Differential pressure measurements are used to determine the collapsed liquid level. The liquid level is also directly measured using conductivity or optical detectors. ECC water mass flow rate measurements are made with electromagnetic flow meters, with an expected error of 0.5%. Mass flow rate measurements in the outlet nozzles of the steam generators are made with pitot tubes. Mass flow rate measurements from the downcomer into the core are made with four drag disks. The steam mass flow rate from containment tank II is measured with a venturi tube. Two-phase flow measurements in the primary loops are made at spool pieces. A spool piece is installed in each hot and cold leg. Each spool piece consists of a three-beam gamma densitometer, a turbine flowmeter, three drag transducers attached to a drag screen, fluid and metal temperature thermocouples, an absolute pressure transducer, and a differential pressure transducer across the drag screen. The fluid densities, velocities, mass flow rates, and void fraction can be obtained using data processing software. Velocimeters were installed in the lower plenum to measure the core flooding rate.

4.4.3.2 Test Procedure

CCTF Test C1-5 (Run 14), hereafter referred to as CCTF Run 14, was the CCTF Core-I facility base case (Ref. 4.4.7). CCTF Run 14 does not correspond to either a best-estimate (BE) or evaluation model (EM) condition (Ref. 4.4.11). The power level for this test is 7% greater than the value used in the current EM licensing analyses, and 35% higher than a realistic BE case. ECC flows are 25% lower than the scaled ECC flow that is expected in a PWR. Pump simulator orifices are sized to provide an equivalent locked rotor pump resistance. The 0.2-MPa containment pressure chosen for this test is lower than that used in most licensing calculations.

In preparation for the test, the accumulator tank, LPCI tank, saturated water tank, and secondary sides of the steam generator simulators were filled with purified water. The instruments were checked for their zero points and sensitivities.

After these preparatory operations, the primary system was heated with the preheaters to its specified temperatures (downcomer wall, core internals, and primary-loop piping wall), and was pressurized to the specified pressure using steam. The water in the accumulator tank was electrically heated to its specified temperature, and pressurized with nitrogen gas to provide sufficient head to drive the required injection flow. The water in the LPCI tank was also heated to

its specified temperature, and was circulated through the delivery lines to preheat the lines to the same temperature as the water. The water in the secondary side of each steam generator simulator was also heated and pressurized to the specified temperature and pressure. The water in the saturated water tank was heated to approximately the saturation temperature of the expected primary pressure.

After establishing the initial test conditions, the electric power for preheating was turned off and the lower plenum was filled with water to the specified level (0.9 m) from the saturated water tank. When the initial test conditions were stabilized at allowable tolerances, electric power was applied to the heater rods in the core and the data recording was started. The temperature increases in the rods were monitored by a computer. When a specified initial cladding temperature was reached, direct injection of the accumulator water into the lower plenum was initiated. The system pressure was maintained at the specified initial pressure throughout the test by controlling the outlet valve of containment tank II. The decay power input to the rods was programmed to begin when the water reached the bottom of the heated region of the core. The specified initial cladding temperature of the heater rods was predetermined by interpolation between the cladding temperature after preheating and the cladding temperature assumed for the time of bottom of core recovery (BOCREC). When the water reached the specified level below the core, the injection port for the accumulator water was switched from the lower plenum to the three intact cold-leg ECC ports. The accumulator (ACC) injection flow rate was then reduced during the cold-leg injection. At a specified time after BOCREC, the valves in the accumulator lines and the LPCI circulation lines were closed, and the valves in the LPCI injection lines were opened. These actions transferred the ECC injection from the ACC mode (high flow rate) to the LPCI mode (lower flow rate). The steam and entrained water flowed via the broken and intact loops to the containment tanks. The steam was then vented to the atmosphere to maintain a constant pressure in the containment tanks. The test was terminated after all of the thermocouples on the surface of the heater rods indicated quenching of the rods.

CCTF Run 14 proceeded as described in the previous paragraph. Direct injection of ACC water into the previously filled lower plenum began after power was applied to the core, and after the cladding temperature at a specified location reached 506°C. When the lower plenum filled with water and the level reached the bottom of the heated core, the core power followed a programmed transient to simulate decay power. The injection port was changed from the lower plenum to the three intact cold-leg ECC ports 14 s after the start of ACC injection. As specified, 22 s after the initiation of ACC injection, ECC injection was transferred from the ACC injection mode (high flow rate) to the LPCI mode (lower flow rate). Operating parameters for CCTF Run 14 are presented in Table 4.4.5.

4.4.3.3 TRAC Model

Several TRAC input models have been developed for simulation of CCTF Run 14. These include (1) a finely noded, 3-D vessel model with 16 axial levels, 4 radial sectors, and 4 azimuthal sectors; (2) a coarsely noded, 3-D vessel model with 16 axial levels, 2 radial sectors, and 2 azimuthal sectors; and (3) a finely noded 1-D vessel model with 24 axial levels, 1 radial sector, and 1 azimuthal sector. Of these three versions of the CCTF Run 14 input model, only the latter has been updated for TRAC-M(F77). This model has also been used for assessment of an earlier

code version by JAERI (Ref. 4.4.12). The noding schematic for the input model is presented in Fig. 4.4.46. The power profile is illustrated in Fig. 4.4.47.

The CCTF Run 14 1-D TRAC input model used in this assessment directly models only the core and upper plenum of the CCTF-I facility. The boundaries of the model have been reduced by artificially limiting the model to a limited region of the larger test facility (i.e., not modeling the downcomer and cold legs), thereby permitting a more direct assessment of the core reflood T/H modeling. The added degrees of freedom associated with the downcomer and cold legs have also been eliminated. However, this approach requires application of appropriate boundary conditions if the simplified model is to be acceptable. Toward this end, the core inlet boundary conditions are specified by a FILL component with time-dependent, core inlet mass flow and fluid temperature. The core outlet boundary conditions are specified by a single BREAK component, with the time-dependent pressure specified. The total power supplied to the heater rods is also provided.

The CCTF core and upper plenum are modeled with 24 axial levels, and the model included grids. The fine axial noding used in the CCTF Run 14 model (~0.2-m high axial levels) is coarser than the noding used in standard full-plant models. (For example, core nodes in an AP600 model are ~0.6-m high.)

The inlet FILL (Component 1) is connected via the PIPE (Component 2) to axial cell 1. The BREAK (Component 5) is connected to axial cell 23 via the PIPE (Component 4). The core extends axially from level 2 through 19.

4.4.3.4 Comparison of TRAC-M(F77) and TRAC-M(F90) Calculations

Calculations were performed using both TRAC-M(F77) and TRAC-M(F90). Figs. 4.4.48 through 4.4.52 compare the clad temperatures calculated at different elevations in the core. In these figures, experimental data are not shown, since the data were obtained under the 2-D/3-D program, and are not publicly available. When an agreement with other partners is reached to release these data, this report will be revised to include the experimental data and to illustrate the comparisons between the data and the code predictions.*

Figs. 4.4.48 through 4.4.52 show comparisons of code predictions, which demonstrate "Excellent" to "Reasonable" agreement. There are some differences between the predictions in some areas; however, these differences are attributable to error corrections and bug fixes in the TRAC-M(F90) code, and we can conclude that the conversion from TRAC-M(F77) has been successful for this application.

4.4.3.5 Conclusions

The conversion from TRAC-M(F77) has been successful for this type of application.

---

* 2-D/3-D partners agreed to the release of data on CCTF-14, CCTF-54, SCTF-719, UPTF 6, and UPTF 8b in NRC developmental assessment reports. These data will be included in future reports.

4.4.4 Cylindrical Core Test Facility (CCTF), Core-II Run 54

The CCTF is an experimental test facility designed to model a full-height core section and four primary loops with components of a PWR. The facility was completed on March 10, 1979, and 22 tests were performed with CCTF Core-I by April 1981. For the CCTF Core-II test series, the first core was replaced by the new second core on November 1981, and six tests, including two acceptance tests and two shakedown tests, were performed with CCTF Core-II by April 1982. Although there were some differences between the core designs in the CCTF Core-I and CCTF Core-II programs, the special purposes of the CCTF Core-II program were to investigate the effects of an alternative ECCS (such as the combined and downcomer injections), and to extend the experimental range of the CCTF Core-I test series.

Core-II Run 54 was successfully conducted on March 30, 1982. The objectives of the test were to check the functions of the modified CCTF Core-II facility, to confirm the similarities between Core-I and Core-II, and to study the effect of the lower power supplied into the core. The test was conducted under the same initial and boundary conditions as in the base case of the CCTF Core-II test series (Run 62), which simulated EM conditions, except for the lower power. The ECC flow conditions were the same as those of the EM tests in CCTF Core-I.

4.4.4.1 Facility Description

Fig. 4.4.53 shows an isometric view of the facility, which was designed and operated by JAERI to provide information regarding fluid behavior in the core, downcomer, and upper plenum, including steam and water carryover (steam binding) and integral system (steam generator and pump simulator) effects during the refill and reflood phases of a hypothetical LOCA in a PWR. The central part of the test facility is a nonnuclear core that consists of 1824 electrically heated rods and 224 nonheated rods arranged in a cylindrical array. The core is housed in a test vessel that includes a downcomer, lower plenum, upper plenum, and core region. The core design is based on 8 x 8 rod assemblies that model the typical 15 x 15 fuel assembly of a PWR. Volumetric scaling is based on core flow area scaling.

The scaled dimensions of the components are given in Table 4.4.6, and elevations of the components are given in Table 4.4.7.

4.4.4.1.1 Pressure Vessel and Internals

The pressure vessel is a cylindrical type, as shown in Fig. 4.4.54. The height is the same as the reference reactor pressure vessel. The radial direction is scaled down in proportion to the core flow area scaling (that is, 1/21.44). The upper ring was newly installed in the Core-II facility for the upper plenum ECC water injection nozzles (called core flooding nozzles). Core flooding nozzles were not used in the Run 54 test. The vent valves and core flooding nozzles are intended to simulate a Babcock & Wilcox (B&W) type PWR. This facility includes the following features:

- The cross-section of the pressure vessel is shown in Fig. 4.4.55. The core consists of thirty-two 8 x 8 electrically heated rod bundles, arranged in a cylindrical configuration, to simulate Westinghouse 15 x 15 fuel assemblies.

- The downcomer is an annulus of a 61.5-mm gap. In determining the gap size, the flow area of the core baffle flow area is included in the downcomer region. Thus, the core baffle flow area is included in the downcomer simulation, and is not simulated separately in this vessel.

- The vessel wall is constructed of carbon steel that is clad with a stainless steel lining. The wall is 90 mm thick to simulate the stored energy as closely as is reasonably possible during ECC water injection.

- The design of upper plenum internals is based on that of the Westinghouse 17 x 17 fuel assemblies. The internals consist of 10 control rod guide tubes, 10 support columns, and 12 open holes. Flow resistance baffles are inserted into the guide tubes. The radius of each internal is scaled down by a factor of 8/15 from that of an actual reactor.

- The end box and the upper-core support plate (UCSP) are installed between the core and upper plenum. The end box tie plate is 10 mm thick, and perforated with round flow holes. Plugging devices are installed in the Core-II facility to simulate the flow resistance. The UCSP is a 60-mm thick perforated plate. The geometry of the perforation is analogous to that of an actual reactor.

4.4.4.1.2 Heater Rod Assembly

The heater rod assembly that simulates the fuel assembly consists of thirty-two 8 x 8 array rod bundles. Each bundle consists of 57 electrically heated rods and 7 unheated rods. The core is usually subdivided into three regions to achieve the desired radial power distribution. The local peaking factor of heated rods in a bundle is unity; that is, all heated rods in a bundle have the same power density in the Core-II facility.

A heater rod consists of a nichrome heating element, magnesium oxide (MgO) and boron nitrite (BN) insulators, and an Inconel-600 sheath. BN is used only for the central part of the heated region, and MgO is used for the other part. The heated length and outer diameter of the heater rods (3.66 m and 10.7 mm, respectively) are identical to the corresponding dimensions of actual PWR fuel rods. The sheath-wall thickness is 1.0 mm, which is thicker than the actual fuel cladding because of the requirements for thermocouple installation. The heating element is a helical coil with a varying pitch to generate a 17-step, chopped cosine axial power profile, as shown in Fig. 4.4.56. Nonheated rods are either stainless steel pipes or solid bars of 13.8-mm outside diameter. All of the pipes are used to install such instruments as steam superheat probes and thermocouples, and to carry the assembly loads.

The heater rods and nonheated rods are held in a radial position by grid spacers that are located at six elevations along the axial length, as shown in Fig. 4.4.56. A grid spacer is a lattice structure composed of stainless steel plates. The top and bottom edges of the stainless steel plates are sharpened in CCTF Core-II. The rod pitch is 14.3 mm, which is same as that of the reference PWR.

The heater rods penetrate through the bottom plate to facilitate lead out of the power cables from the bottom of the vessel. The outer diameter of the rods in the lower plenum is reduced to 8.6 mm. Three-phase electric current is used to heat the heater rods, and the electrical neutral point is at the top of the rods (where they are interconnected to each other).

4.4.4.1.3 Primary Loops and the Emergency Core Cooling System (ECCS)

The primary loop consists of three intact loops and a broken loop. Each loop consists of hot- and cold-leg piping, a steam-generator simulator, and a pump simulator. The cold-leg break is simulated for the broken loop. The broken cold leg is connected to two containment tanks through blowdown valves. The primary loop arrangement is shown in Fig. 4.4.57.

The inner diameter of the piping is scaled down in proportion to the core flow area scaling. The length of each piping section is almost the same as the corresponding sections of the reference PWR.

The steam generator simulators are the U-tube and shell type. The tube length is ~5 m shorter than in the reference PWR, and the vertical height of the steam generator simulators is ~5 m lower than in the reference PWR. The primary coolant passes through the tube side, and the secondary coolant is stagnant in the shell side. The steam generator simulators of two loops are housed in a single shell assembly that has two sets of separated inlet and outlet headers for the two loops. The wall thickness of the U-tube is 2.9 mm (instead of 1.27 mm for the reference PWR) because of a higher pressure difference between the primary and secondary sides in the steam-generator simulator. The pump simulator consists of the casing and vane simulators and an orifice plate.

The resistance of each looop is simulated with the orifice plate, and has a hole with a diameter of 95 mm and a thickness of 10 mm.

The ECCS consists of an ACC and an LPCI. The injection points are at each cold leg and at the lower plenum. The upper plenum and downcomer injection system are available for further alternative ECCS tests.

4.4.4.1.4 Instrumentation

The instrumentation is divided into two groups. One group consists of JAERI-supplied instruments that measure the temperatures, absolute pressure, differential pressures, water levels, and flow rates. Thermocouples measure the temperatures of the rod surface, fluid, and structure. The absolute pressures are measured in the upper and lower plena, steam generator plena, and containment tanks. The differential pressure measurements are carried out at many locations that almost completely cover the entire system. The liquid levels are measured in the ECC water supply tanks and containment tank 1. The flow meters measure the ECC water flow rates, and flow rates in the downcomer and loop seal piping vent line from containment tank 2 to the atmosphere are measured with the drag disk flow meter, Pitot tubes, and venturi tube, respectively. The total number of JAERI-supplied instruments are 1316 channels, and the signals from these instruments are recorded on a magnetic tape.

The other instrumentation group consists of NRC-supplied advanced instruments totaling 536 channels for the two-phase flow measurement.

4.4.4.2 Test Procedure

In preparation for the test, the ACC tank, LPCI tank, saturated water tank, and secondary sides of the steam generator simulators were filled with water purified with ion exchange resin. The instruments were checked for their zero points and sensitivity after all of the components and instruments were inspected for mechanical and electrical leakage.

After the preparatory operations, the primary system was heated to its specified temperatures (downcomer wall, 468 K; core internals, 423 K; and primary loop piping wall, 406 K) with the preheaters, and pressurized to 0.2 MPa by substituting steam for nitrogen gas in the system. The water in the ACC tank was electrically heated to 310 K, and pressurized with nitrogen gas to provide sufficient head to drive the required injection flow. The water in the LPCI tank was also heated to 310 K, and was circulated through the circulation line (including the LPCI line) to preheat the line to the same temperature as the water. The water in the saturated water tank was heated close to the saturation temperature (394 K) of the expected primary system pressure (0.2 MPa). The water in the secondary side of each steam-generator simulator was heated to 539 K, and and pressurized to 5.3 Mpa.

After the initial conditions of the test were established, the electric power for preheating was turned off, and the lower plenum was filled to 0.86 m directly from the saturated water tank. Electric power was applied to the heater rods in the core, and the data recording was started when the water level in the lower plenum reached the specified level and other initial conditions of the test stabilized at the allowable tolerance. A computer was used to monitor the temperature increases of the rods. When a specified initial clad temperature (1003 K) was reached, direct injection (0.104 m^3s^{-1}) of the ACC water into the lower plenum was initiated. The system pressure was maintained at 0.2 MPa throughout the test by controlling the outlet valve of containment tank 2. The decay of power input to the rods was programmed to begin when the water reached the bottom of the heated region of the core. The specified initial clad temperature (995 K) of the heater rods for initiation of coolant injection was predetermined by interpolation between the clad temperature (394 K) after preheating and the clad temperature (1073 K) assumed for the time of core bottom recovery. The specified power decay was obtained by normalizing the 1.0 X ANS standard + U^{238} - capture decay curve at 30 s after shutdown.

When the assumed water level reached the specified level (0.5 m from the bottom of the heated region of the core), the injection port was changed from the lower plenum to the three intact cold-leg ECC ports. This water level was assumed to be the level at which considerable steam generation occurs in the core to minimize oscillatory behavior caused by the condensation at the ECC ports. The ACC injection flow rate was then reduced to 0.088 m^3s^{-1} in the cold-leg injection period. At a specified time (16.5 s) after the time of core bottom recovery, the valves in the ACC lines and LPCI circulation lines were closed, and the valves in LPCI injection lines were opened. These actions transferred the ECC injection from ACC injection mode to LPCI mode. A specified LPCI flow rate (0.0116 m^3s^{-1}) was maintained constantly until the ECC injection was turned off.

The generated steam and the entrained water flowed via broken and intact loops to the containment tanks. The steam was then vented to the atmosphere to maintain a constant pressure in the containment tanks. After all thermocouples on the surface of the heater rods indicated quenching of the rods, the power supply to the heater rods decreased linearly. The linear power decay was performed to study any particular reflood phenomena under very low power supply. The linear power decay was initiated at 690.5 s, and the power was turned off at 898 s. After the ECC injection was turned off, the recording system was stopped, thus terminating the test.

4.4.4.3 TRAC Input Model

The input model was a straightforward conversion of an earlier TRAC model that was used for the analysis of CCTF Run 54, which was conducted as part of the 2-D/3-D program. This input model used the intermediate-node model of the CCTF reactor vessel, as shown in Fig. 4.4.58. The vessel nodalization includes 2 azimuthal zones, 4 radial rings, and 16 axial levels.

The three CCTF intact loops are combined and modeled as a single loop. The intact loop components are shown in Fig. 4.4.59, and Fig. 4.4.60 shows the noding for the broken loop components.

Initial thermal and hydraulic parameter values are generally consistent with the initial values listed in Table 4.4.8. In most instances, initial pressures and temperatures are at the nominal values given in the table. The axial and radial distribution of the power in the core agree with the distribution given in the Run 54 data report. Table 4.4.9 presents the chronology of testing events.

The seven time-dependent boundary conditions used for these calculations included the total core power, lower plenum injection velocity and ECC temperature, cold leg injection velocity and ECC temperature, and both containment tank pressures. The inputs were tabulated from instrument records.

4.4.4.4 Comparison of TRAC-M(F77) and TRAC-M(F90) Predictions

Calculations are performed using both TRAC-M(F77) and TRAC-M(F90), and the results are compared in Figs. 4.4.61 through 4.4.65. Since CCTF data are restricted to 2-D/3-D program participants, this report does not contain any graphics of CCTF test data.* These figures compare code to code results. The figures show clad temperature predictions of the hot rod at various elevations. Agreements between code calculations are considered "Excellent" to "Reasonable" for this test. Predictions of peak clad temperatures are almost the same. There are some differences in quenching times. Considering all error corrections and changes that have been implemented in TRAC-M(F90), the agreement between predictions is deemed to be "Reasonable."

4.4.4.5 Conclusions

The conversion from TRAC-M(F77) to TRAC-M(F90) has been successful for this type of application.

---

* See footnote on page 4-79.

4.4.5 Slab Core Test Facility (SCTF), Run 719

The Slab Core Test Facility (SCTF) is designed to investigate the 2-D thermal-hydraulic phenomena that occur in a PWR during the end of the blowdown, refill, and reflood phases of a postulated LBLOCA. The SCTF is a full-height facility; most major vessel and primary loop dimensions are volume scaled in a ratio near 1/21 relative to a four-loop PWR with lower plenum and cold-leg ECC injection. A description of the SCTF Core-III facility is provided in Section 4.4.5.1. Fig. 4.4.66 shows an overview of the SCTF Core-III system. A major feature of the SCTF is that it contains a full-height and full-radius heated core with a width of one tube bundle. The current configuration of the core is designated as Core-III, with the upper plenum and upper head representative of a German PWR. The facility is operated by JAERI.

4.4.5.1 Facility Description

Fig. 4.4.67 shows a vertical cross-sectional view of the SCTF pressure vessel. The vessel contains a downcomer, lower plenum, electrically heated core simulator, core baffle region, upper plenum, and upper head. The core simulator models a sector of the core from the centerline to the outer wall of the vessel. The name of the facility, "slab core," is descriptive of the core simulator arrangement. A slab-like sector of the vessel from the core centerline to the vessel outer wall contains eight heater rod bundles arranged in a row, the core baffle region, and the downcomer. Whereas the design of the Core-II upper plenum was based on that of a Westinghouse plant with 17 x 17 array fuel assemblies, the design of the Core-III upper plenum is based on that of a German PWR.

Each heater rod bundle contains 236 electrically heated rods and 20 unheated rods. A heater rod consists of a Nichrome heater element wound in a helix about a ceramic core rod (magnesium hydroxide), and a Nichrofer 7216 (equivalent to Inconel 600) sheath, with boron nitride (central region) or magnesium hydroxide (upper and lower regions) packed between the heater element and the sheath. The pitch of the heater element winding is varied to produce a 17-step, chopped-cosine axial power profile, as shown in Fig. 4.4.68.

Simplified models of the primary coolant loops are provided in the facility. The facility is equipped with a hot leg that is equivalent to four hot legs in a PWR. The hot leg cross-sectional shape is not typical of a PWR, in that it is tall and narrow rather than circular in shape. The hot leg connects the vessel upper plenum to a steam/water (S/W) separator. The S/W separator simulates single-phase steam flow downstream of a steam generator in a PWR, and also facilitates the measurement of liquid carryover from the upper plenum, through the hot-leg simulator, and into the S/W separator. The S/W separator inlet plenum models a steam generator inlet plenum to simulate the flow characteristics of carryover water into the U-tubes. The intact cold leg in the SCTF is equivalent to three intact loops in a PWR. A pump simulator and a loop seal are provided in the intact cold leg simulator. Two broken loop components are provided, and each of these is connected to a separate containment tank through a break valve. The loop resistance is adjusted with orifice plates that can be placed in the intact cold leg, the S/W separator side and pressure vessel side broken cold legs, and the pump simulator in the intact loop.

The coolant flows delivered by the ECCS are also modeled. These simulate flows from the ACC, an LPCI system, and a combined injection system. ECC water injection ports are at the cold leg, the hot leg, through the upper head into the top of the upper plenum, into the upper

plenum at the UCSP, into the downcomer, and into the lower plenum. The specific injection ports are selected according to the objectives of the given test.

4.4.5.2 Test Procedure

SCTF Run 719 (Test S3-15) was an integral, lower plenum injection test that simulated the condition of a US/Japan-type PWR during the reflood phase of a 200% cold leg LBLOCA. The test objective of Run 719 was to investigate the effect of radial power distribution shape and ratio on 2-D heat transfer behavior. The radial power distribution was inclined, and the peak-to-average power ratios were 1.36, 1.20, 1.20, 1.00, 0.91, 0.86, 0.81, and 0.76 for bundles 1 through 8, respectively. Before test initiation, the facility was filled with saturated steam at 0.2 MPa. The lower plenum was filled with saturated water (393 K) to a height of 1.2 m. The core then began to heat in near adiabatic conditions. The core power was tripped and ECC initiated when a preselected number of rod cladding temperatures exceeded 1134 K. The maximum cladding temperature reached was 1183 K; this temperature was measured at the midplane of bundle 1 (the bundle receiving the highest power). The entire core was quenched at 574.5 s. The core T/H behavior was strongly 2-D in Run 719. A single recirculating flow was established with upflow through the high-power bundles and downflow through the low-power bundles. A summary of the test conditions for this test is presented in Table 4.4.10.

4.4.5.3 TRAC Input Model

The pressure vessel noding is shown in Fig. 4.4.69. The heated core section is noded into six axial levels. Fig. 4.4.70 shows the heater rod noding, along with the thermocouple locations and the modeled axial power shape. The hot leg and the S/W separator are shown in Fig. 4.4.71; the intact cold leg noding is shown in Fig. 4.4.72; the broken cold leg noding from the pressure vessel to containment tank 1 is shown in Fig. 4.4.73; and the broken cold leg noding from the S/W separator to containment tank 2 is shown in Fig. 4.4.74. The primary features of each element in the TRAC input model are discussed in the following sections.

4.4.5.3.1 Pressure Vessel

The pressure vessel is modeled with the TRAC VESSEL component in 2-D Cartesian coordinates with 12 sectors in the horizontal direction and 15 levels in the vertical direction, as shown in Fig. 4.4.69. All of the major elements in the experimental facility are modeled in the input. The lower plenum is modeled in sectors 1 through 9 and levels 1 through 3. The lower core support plate is modeled at the top of level 3. The lower plenum is noded into three axial levels to capture the geometry below the tube bundles, and to model the opening between the lower plenum and downcomer. The electrically heated core is modeled in sectors 1 through 8 and axial levels 4 through 9. Each of the eight sectors represents a heater rod bundle. The core baffle occupies sectors 9 and 10 and the same axial levels as the core. The upper plenum is modeled in sectors 1 through 9 and axial levels 10 through 14. The upper tie plate, which contains the minimum flow area between the core and upper plenum, is located in level 10, and the upper core support plate is located in level 11. The support columns connecting the upper head and the upper plenum are modeled with PIPE components in sectors 1, 3, 5, 6, and 7 to provide a flow path between the upper plenum and the upper head. The upper head is modeled in sectors 1 through 12 at level 15. The downcomer is modeled in sectors 11 through 12 and axial levels 2 through 14.

The intact cold leg and broken cold leg connections to the pressure vessel are in level 12 of sectors 11 and 12, respectively. The hot leg connections to the upper plenum are at the outer interface of sector 10 in level 13. The lower plenum ECC injection point is located in sector 10 at level 1.

4.4.5.3.2 Heater Rods

Heater rods in the test facility were fabricated to provide a 17-step, chopped-cosine distribution for the axial power. The TRAC fuel rod model, shown in Fig. 4.4.70, has only six axial sectors. This presented several challenges in modeling the electrically heated core as described in earlier SCTF Run 179 assessment calculations. To model the axial power distribution, the areas under the power distribution of the heater rods in the test facility and that of the TRAC model were set equal to preserve the total power. Also, the TRAC six-level axial power shape had to be adjusted to match the pre-ECC injection axial cladding temperatures of the test. Several parametric runs were made to determine the axial power shape and peak power so that the axial distribution of calculated cladding temperatures compared well with those provided by JAERI.

A second problem encountered with the earlier SCTF assessment calculations involved specifying the correct heater rod material properties. SCTF Core-I studies showed that the heater-rod material properties had a large effect on cladding temperature. A parametric study was conducted by varying the density and specific heat of magnesium hydroxide. To verify the input, the cladding temperature was calculated for the adiabatic heatup conditions of Run 719, and then compared with the initial and boundary condition data provided by JAERI. For case 1, the values for density and specific heat provided by the heater rod manufacturer were used (density = 2500 kg/m^3, with specific heat defined from a temperature-dependent table). For case 2, the values for density and specific heat selected for use in the TRAC Core-I and Core-II models were used (density = 2800 kg/m^3, with specific heat defined from a temperature-dependent table increased by 2800/2500 from the manufacturer's recommended values). For case 3, intermediate values were used (density = 2625 kg/m^3). For this study, a MgO density of 2650 kg/m^3 and corresponding specific heat were used for the Run 719 analysis.

To ensure that TRAC was correctly calculating the adiabatic heatup, a TRAC calculation that could be verified with a hand calculation was performed. The SCTF Core-III model was used with the following changes. The axial and radial relative power profiles were set to unity, all rod material properties were set equal to the properties for Nichrome, and the core power was set at a constant value of 10 MW. The heatup period was 20 s. The hand-calculated lumped parameter energy balance predicted a uniform temperature of 488.5 K (no radial distribution); TRAC calculated a heater rod centerline temperature of 487.7 K, and a cladding temperature of 485.5 K. The difference represents the slight heat losses from the heater rod to the steam environment during the adiabatic heatup. Because the heater rod material properties are important in determining the cladding temperature, further effort may be required to ensure that the correct material properties are being used in other assessment analyses.

4.4.5.3.3 Hot-Leg and S/W Separator

The hot leg and S/W separator noding are shown in Fig. 4.4.71. The hot leg is modeled with a PIPE component containing four cells, and the outer surface of the hot leg is assumed to be insulated.

The S/W separator is modeled with a 3-D VESSEL component with four axial levels, one radial sector, and two azimuthal sectors. The hot leg connection to the S/W separator is in the outer radial face of cell 1 at level 3. The respective intact and broken cold leg connections to the S/W separator are made at level 2 to the outer radial faces of cells 1 and 2.

4.4.5.3.4 Intact Cold Leg

The intact cold leg noding is shown in Fig. 4.4.72. The intact cold leg is modeled with a TEE component consisting of seven cells in the primary side, and one cell in the secondary side. The secondary side of the TEE component is connected to the primary side at cell 7. The primary side includes the loop seal and the pump simulator. The intact cold leg orifice and pump simulator orifice are located at cell faces 2 and 6. The secondary side models the ECC injection port.

4.4.5.3.5 Broken Cold Leg (Pressure Vessel Side) and Containment Tank 1

The broken cold leg noding between the pressure vessel and containment tank 1, shown in Fig. 4.4.73, is modeled with a VALVE component containing six cells. The break valve is at the interface between cells 3 and 4. The opening and closing actions of the valve are modeled with the trip and control logic in TRAC. For Run 719, the valve was set fully open and not actuated. Containment tank 1 is modeled as a BREAK component using the measured containment pressure as the boundary condition.

4.4.5.3.6 Broken Cold Leg (S/W-Separator Side) and Containment Tank 2

The broken cold leg noding between the S/W separator and containment tank 2, shown in Fig. 4.4.74, is modeled with a VALVE component containing eight cells. The break valve for this segment of the broken cold leg is at the interface between cells 3 and 4. The opening and closing actions of the valve are modeled with the trip and control logic in TRAC. For Run 719, the valve was set fully open and not actuated. Containment tank 2 is modeled as a BREAK component using the measured containment pressure as the boundary condition.

4.4.5.4 Comparison of TRAC-M(F77) and TRAC-M(F90) Calculations

Calculations were performed using both TRAC-M(F77) and TRAC-M(F90). Figs. 4.4.75 through 4.4.83 compare the clad temperatures calculated at different elevations in the core. In these figures, experimental data are not shown since the data are obtained under 2-D/3-D program and the data are not publicly available. When an agreement is reached with other partners to release these data, this report will be revised to include comparisons between the data and the code predictions.*

---

* See footnote on page 4-79.

As shown in Figs. 4.4.75 through 4.4.83, the agreement between the code predictions is "Excellent" to "Reasonable." Differences between the predictions are small, considering that some error corrections were implemented in the TRAC-M(F90) code. Consequently, we consider the conversion from TRAC-M(F77) to TRAC-M(F90) to be successful for this application.

4.4.5.5 Conclusions

The conversion TRAC-M(F77) to TRAC-M(F90) has been successful for this application.

REFERENCES

4.4.1 Tuzla, K., C. Unal, O. Badr, S. Neti, and J. C. Chen, "Thermodynamic Nonequilibrium in Post-Critical-Heat-Flux Boiling in a Rod Bundle," U.S. Nuclear Regulatory Commission Document NUREG/CR-5095, Vols. 1–4, July 1987.

4.4.2 Obot, N.T., and M. Ishii, "Two-Phase Flow Regime Transition Criteria in Post-Dryout Region Based on Flow Visualization Experiments," *Int. J. Heat Mass Transfer*, Vol. 31, No. 12, pp. 2559–2570, 1988.

4.4.3 Hirano, K., et al., "Data Report on Large-Scale Reflood Test-14, CCTF Test C1-5 (Run 014)," Japan Atomic Energy Research Institute Document JAERI-memo 57-214, August 1982.

4.4.4 Odar, F., NUREG-1744, "Assessment of the TRAC-M Codes Using FLECHT-SEASET Reflood and Steam Cooling Data," NRC: Washington, D.C. May 2001.

4.4.5 Loftus, M.J., et al., "PWR FLECHT-SEASET Unblocked Bundle Forced and Gravity Reflood Task Data Report," Westinghouse Electric Corporation Report, WCAP-9699, NUREG/CR-1532, Vols. 1 and 2, 1980.

4.4.6 Nelson, R.A., D.A. Pimentel, S.J. Jolly-Woodruff, and J.W. Spore, "A Phenomenological Thermal-Hydraulic Model of Hot Rod Bundles Experiencing Simultaneous Bottom and Top Quenching and Optimization Methodology for Closure Development,"Los Alamos National Laboratory Report, LA-UR-98-3043, April 1998.

4.4.7 Damerell, P.S., and J.W. Simons, Eds., "2-D/3-D Program Work Summary Report," U.S. Nuclear Regulatory Commission Document NUREG/IA-0126, June 1993.

4.4.8 Sugimoto, J. and Y. Murao, "Evaluation Report on CCTF Core I Reflood Tests C1-5 (Run 14), C1-7 (Run 16) and C1-14 (Run 23) – Effects of Initial Clad Temperature," Japan Atomic Energy Research Institute Document JAERI-M-83-026, February 1983.

4.4.9 Aksan, N., F. D'Auria, H. Glueser, R. Porchard, C. Richards, and A. Sjoberg, "Separate Effects Test Matrix for Thermal-Hydraulic Code Validation, Volume I —

Phenomena Characterization and Selection of Facilities and Tests," Organization for Economic Cooperation and Development Nuclear Energy Agency Document NEA/CSNI/R(93)/Part. 1/Rev., and "Volume II — Facility and Experiment Characteristics," Organization for Economic Cooperation and Development Nuclear Energy Agency Document NEA/CSNI/R(93)/Part 2/Rev., September 1993.

4.4.10 "CSNI Integral Test Facility Validation Matrix for the Assessment of Thermal-Hydraulic Codes for LWR LOCA and Transients," Organization for Economic Cooperation and Development Nuclear Energy Agency Draft Document 132, Rev. 6, June 1995.

4.4.11 Motley, F., "Research Information Report Results from TRAC Analysis of Cylindrical Core Test Facility Core I Test Series," Los Alamos National Laboratory Report, LA-20130-TN-85-5, January 1986.

4.4.12 Akimoto, H., "Analysis of TRAC-PF1 Calculated Core Heat Transfer for a CCTF Test," *Nuclear Engineering and Design* 88, 215–227, 1985.

Table 4.4.1 Predicted and Measured Quench Times

Location (m)	Experimental Quench Time (s)	Predicted Quench Time, TRAC-M(F77) (s)	Predicted Quench Time, TRAC-M(F90) (s)
0.15	65.5	31.5	27.5
0.30	114.7	111.0	100.0
0.45	178.0	200.0	184.0

Table 4.4.2 Predicted and Measured Quench Velocities

Location (m)	Experimental Quench Velocity (mm/s)	Predicted Quench Velocity, TRAC-M(F77), (mm/s)	Predicted Quench Velocity, TRAC-M(F90), (mm/s)
0.15	2.3	2.5	1.8
0.30	3.0	1.4	1.3
0.45	2.4	2.9	2.5

Table 4.4.3 Conditions and Key Results for Run 31504

Parameter	Test Condition Value
Upper Plenum Pressure	0.28 MPa
Rod Initial Clad Temperature at the 1.83 m Level	1136 K
Rod Peak Power	2.3 kW/m
ECCS Injection Rate	~0.37 kg/s
Coolant Temperature	324 K
Radial Power Distribution	Uniform
Initial Temperature of Hottest Rod	1093 K
Elevation of Maximum Temperature of Hottest Rod	1.98 m
Maximum Temperature of Hottest Rod	1423 K
Temperature Rise	330 K
Turnaround Time of Hottest Rod	130 s
Quench Time of Hottest Rod	325 s
Bundle Quench Time	594 s

Table 4.4.4 Flow Regime Transition Criteria

Regime	Ishii's Correlation	Region of Applicability	TRAC Application
Smooth Inverted Annular Flow (IAF)	$Z/D = 60\sqrt{Ca}$	$We/\alpha^2{}_i \leq 10^{-2}$	$0.05 < \alpha < 0.3$
Rough Wavy IAF	$Z/D = 295\sqrt{Ca}$	$We/\alpha^2{}_i \leq 10^{-1}$	$0.3 < \alpha < 0.4$
Agitated IAF	$Z/D = 595\sqrt{Ca}$	$We/\alpha^2{}_i \leq 3.5$	$0.4 < \alpha < 0.75$
Dispersed Section	$Z/D = 595\sqrt{Ca}$	$We/\alpha^2{}_i \leq 10$	$0.75 < \alpha < 0.98$

Table 4.4.5 Operating Parameters for CCTF Run 14

System Pressure	2.02 kg/cm^2
Total Power	9.36 MW_t
Radial Power Distribution	1.07:1.0:0.82
Downcomer Wall Temperature	182°C
Primary Piping Wall Temperature	120°C
Steam-Generator Secondary-Side Liquid Temperature	262°C
Peak Clad Temperature at ECC Injection Initiation	502°C
ECC Liquid Temperature	114°C
Lower-Plenum Liquid Level	0.87 m
ACC Injection Rate	278 m^3/h
Low-Pressure Coolant Injection Rate	30.2 m^3/h

Table 4.4.6 CCTF Component Scaled Dimensions

Component	PWR	CCTF	Ratio
Pressure Vessel			
Vessel inside diameter (mm)	4394 (173 in.)	1084	
Vessel thickness (mm)	216 (8.5 in.)	90	
Core barrel outside diameter (mm)	3874	961	
Core barrel inside diameter (mm)	3760	929	
Thermal shield outside diameter (mm)	4170		
Thermal shield inside diameter (mm)	4030		
Downcomer length (mm)	4849	4849	1/1
Downcomer gap (mm)	114.3	61.5	
Downcomer flow area (m^2)	4.23	0.197	1/21.44
Lower-plenum volume (m^3)	29.6	1.38	1/21.44
Upper-plenum volume (m^3)	43.6	2.04	1/21.44
Fuel (heater-rod) Assembly			
Number of bundles	193	32	
Rod array	15x15	8x8	
Rod heated length (mm)	3660	3660	1/1
Rod pitch (mm)	14.3	14.3	1/1
Fuel rod outside diameter (mm)	10.72	10.7	1/1
Thimble tube diameter (mm)	13.87	13.8	1/1
Instrument tube diameter (mm)	13.87	13.8	1/1
Number of heater rods	39372	1824	1/21.58
Number of nonheated rods	4053	244	1/18.09
Core flow area (m^2)	5.29	0.25	1/21.2
Core fluid volume (m^3)	17.95	0.915	1/19.6
Primary Loop			
Hot-leg inside diameter (mm)	736.6 (29 in.)	155.2	1/4.75
Hot-leg flow area (m^2)	0.426	0.019	1/22.54
Hot-leg length (mm)	3940	3940	1/1
Pump-suction inside diameter (mm)	787.4 (31 in.)	155.2	1/5.07
Pump-suction flow area (m^2)	0.487	0.019	1/25.77
Pump-suction length (mm)	9750	7950	1/1
Cold-leg inside diameter (mm)	698.5 (27.5 in.)		155.21/4.50
Cold-leg flow area (m^2)	0.383	0.019	1/20.26
Cold-leg length (mm)	5600	5600	1/1

Table 4.4.6 (cont) CCTF Component Scaled Dimensions

Component	PWR	CCTF	Ratio
Containment tank 1 (m^3)		30	
Containment tank 2 (m^3)		50	
Storage tank (m^3)		25	
Accumulator tank (m^3)		5	
Saturated water tank (m^3)		3.5	
Steam-generator Simulator			
Number of tubes	3388	158	1/21.44
Tube length (average) (m)	20.5	15.2	1/1.35
Tube outside diameter (mm)	22.225 (0.875 in.)	25.4	
Tube inside diameter (mm)	19.7 (0.05 in.)	19.6	1/1
Tube wall thickness (mm)	1.27	2.9	
Heat-transfer area (m^2)	4784 (51 500 ft^2)	192	1/24.92
	1.03	0.048	1/21.44
Inlet-plenum volume (m^3)	4.25	0.198	1/21.44
Outlet-plenum volume (m^3)	4.25	0.198	1/21.44
Primary-side volume (m^3)	30.50 (1077 ft^3)	2.4	1/15.25
Secondary-side volume (m^3)	157.33 (5556 ft^3)	4.9	1/26.22

Table 4.4.7 Component Elevations of the CCTF

Component	PWR	CCTF	Discrepancy
Bottom of heated region in core (mm)	0	0	0
Top of heated region in core (mm)	660	3660	0
Top of downcomer (mm)	4849	4849	0
Bottom of downcomer (mm)	0	0	0
Centerline of cold leg (mm)	5198	4927	-271
Bottom of cold leg (inside) (mm)	4849	4849	0
Centerline of loop-seal lower end (mm)	2056	2047	-9
Bottom of loop-seal lower end (mm)	1662	1959	+297
Center of hot leg (mm)	5198	4927	-271
Bottom of hot leg (inside) (mm)	4830	4849	+19
Bottom of upper core plate (mm)	3957	3957	0
Top of lower core plate (mm)	-108	-50	+58
Bottom of tube sheet of steam-generator simulator (mm)	7308	7307	-1
Lower end of steam generator simulator plenum (mm)	5713	5712	-1
Top of tubes of steam generator simulator (avg.) (mm)	17952.7	14820	

Table 4.4.8 Initial Test Conditions

Parameter	Test Condition
Total power	7.87 MW
Linear power	1.18 kWm^{-1}
Radial power distribution	A 1.37 B 1.20 C 0.76
Containment pressure	0.2 MPa
Steam generator secondary pressure	5.3 MPa
Downcomer wall temperature	468 K
Vessel internals temperature	423 K
Primary piping temperature	406 K
Lower plenum liquid temperature	394 K
ECC liquid temperature	310 K
ECC injection type	Lower plenum and cold leg injection
Pump K factor	15
ECC injection rates, durations, and injection locations	Accumulator flow: 0.104 m^3s^{-1} from 81.0 to 94.0 s into lower plenum* Accumulator flow: 0.088 m^3s^{-1} from 94.0 to 107.0 s into cold legs* LPCI flow: 0.0116 m^3s^{-1} from 107.0 to 979.0 s into cold legs*
Initial water level in lower plenum	0.86 m
Initial water level in steam generator secondary side	7.4 m
Power decay	Constant, from 0 to 90.5 s* ANS 1.0 + actinide (30 s after scram), from 90.5 to 690.5 s* Linear decay, from 690.5 to 898.0 s*
Reflood initiation time	90.5 s*
Peak clad temperature at reflood initiation	1074 K at TE31Y17

* Time in this table is defined as time after test initiation.

Table 4.4.9 Chronology of Testing Events for CCTF Run 54

Event	Time After Test Initiation (s)	Time Relative to Reflood Initiation (s)
Test initiated (Heater rods power on) (Data recording initiated)	0	-90.5
Accumulator injection initiated	81.0	-9.5
Power decay initiated (Bottom of core recovery) (Reflood initiated)	90.5	0.0
Accumulator injection switched from lower plenum to cold leg	94.0	3.5
Accumulator injection ended and LPCI injection initiated	107.0	16.5
Maximum PCT time	123.0	32.5
All heater rods quenched	552.5	462.0
Linear power decay initiated	690.5	600.0
Power off	898.0	807.5
LPCI injection ended	979.0	888.5
Test ended (Data recording ended)	1032.0	941.5

Table 4.4.10 Summary of Test Conditions for SCTF Run 719 (S3-15)

Parameter	Test Condition
System pressure	0.2 MPa
Initial total core power	7.12 MW
Radial power distribution (bundle 1/2/3/4/5/6/7/8)	1.36/1.2/1.1./1.0 0.91/0.86/0.81/0.76
Decay power	1.02 x ANS + 1.02 x actinides
Initial peak cladding temperature (at initiation ECC injection)	1134 K
ECC injection mode	Lower plenum injection
Upper head injection	None
UCSP injection	None
Lower plenum injection flow rate	37 kg s^{-1} for 13 s 37 to 13 kg s^{-1} over 15 s 13 to 4.1 kg s^{-1} over 70 s 4.1 to 3.75 kg s^{-1} over 10 s 3.75 kg s^{-1} for 500 s
Water temperature	353 K for 36 s 393 K for remainder of test
Injection period	608 s
Cold leg injection	None
Lower plenum liquid level	1.2 m, saturated at 393 K

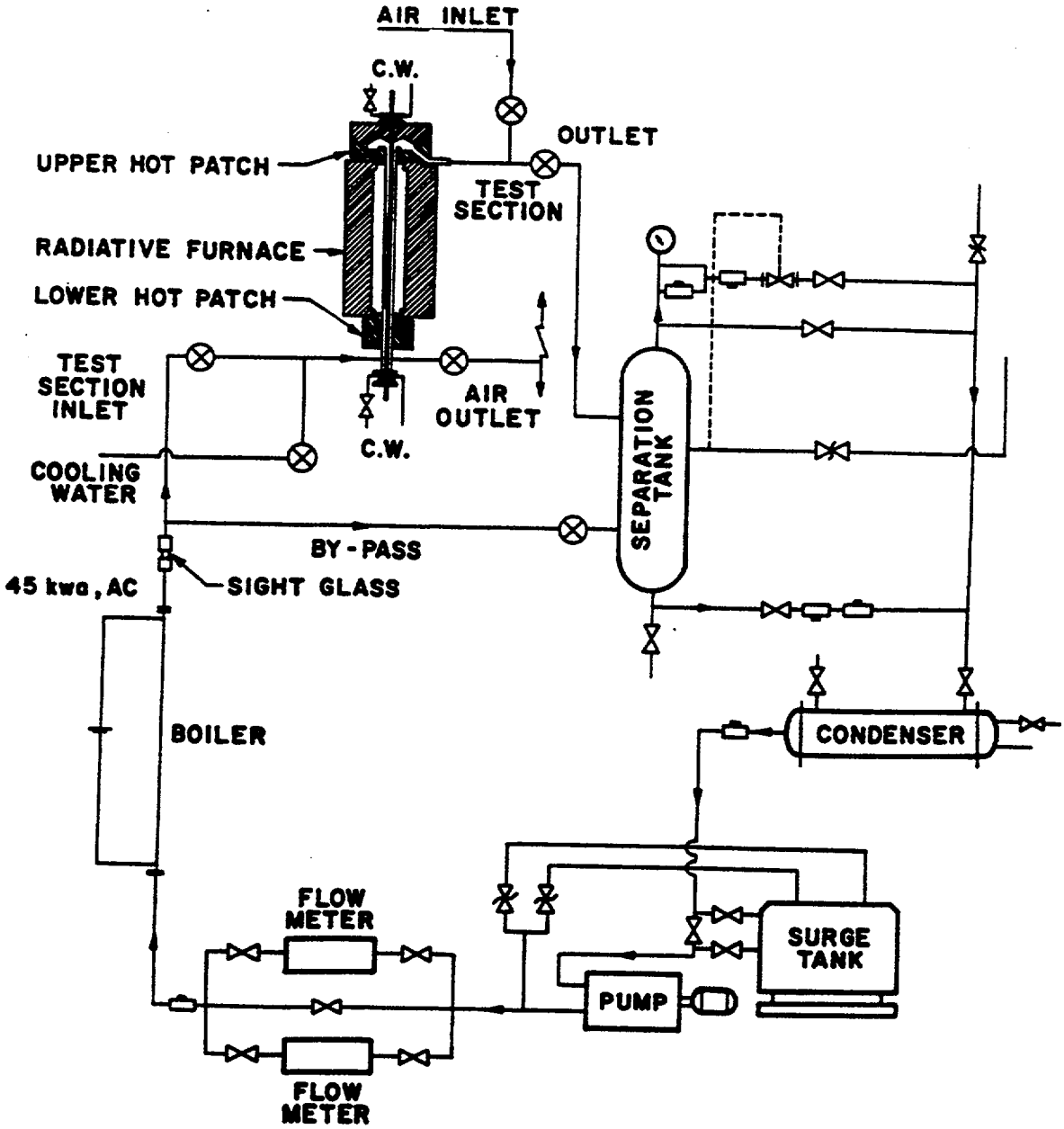

Figure 4.4.1 Two-Phase Heat Transfer Test Loop

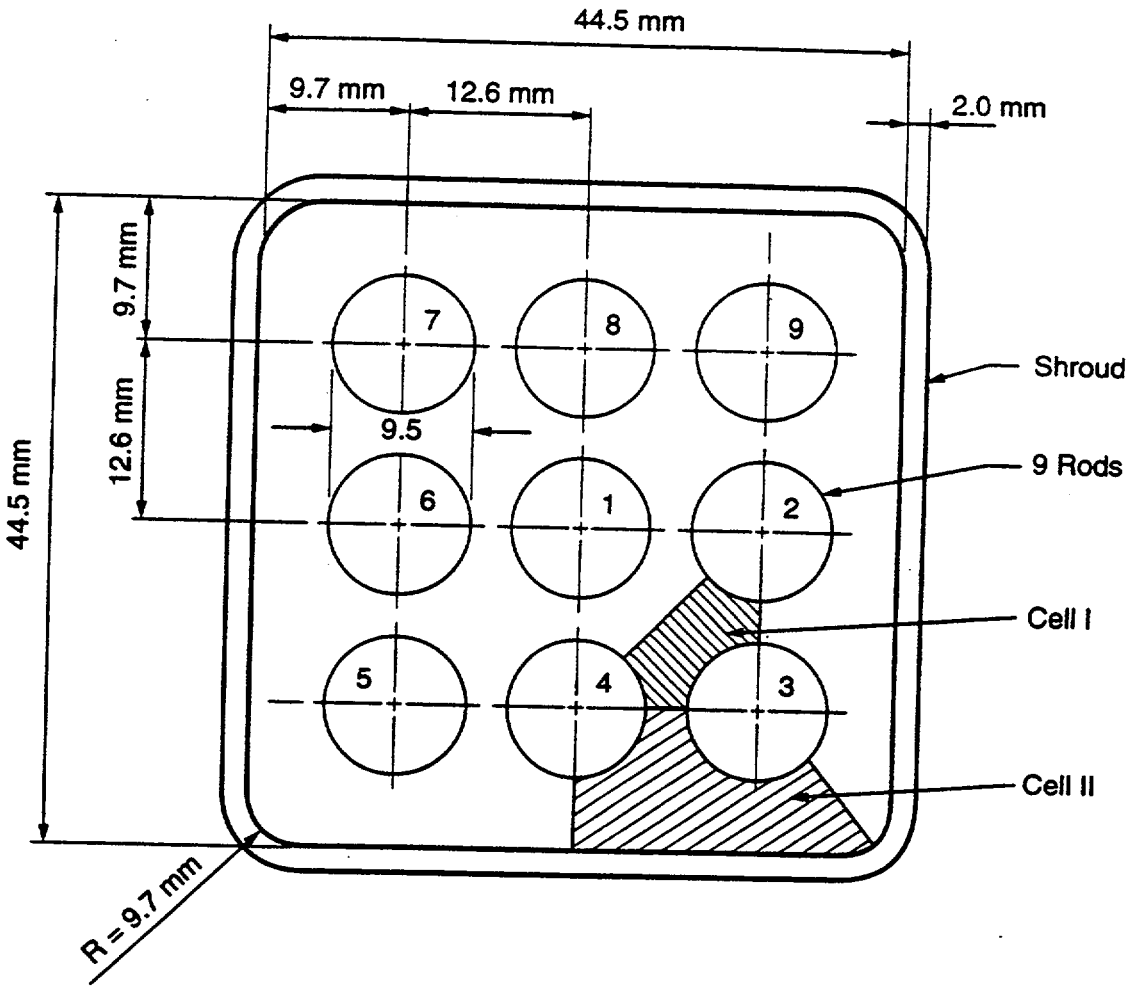

Figure 4.4.2 Cross-Sectional View of the Lehigh Test Bundle

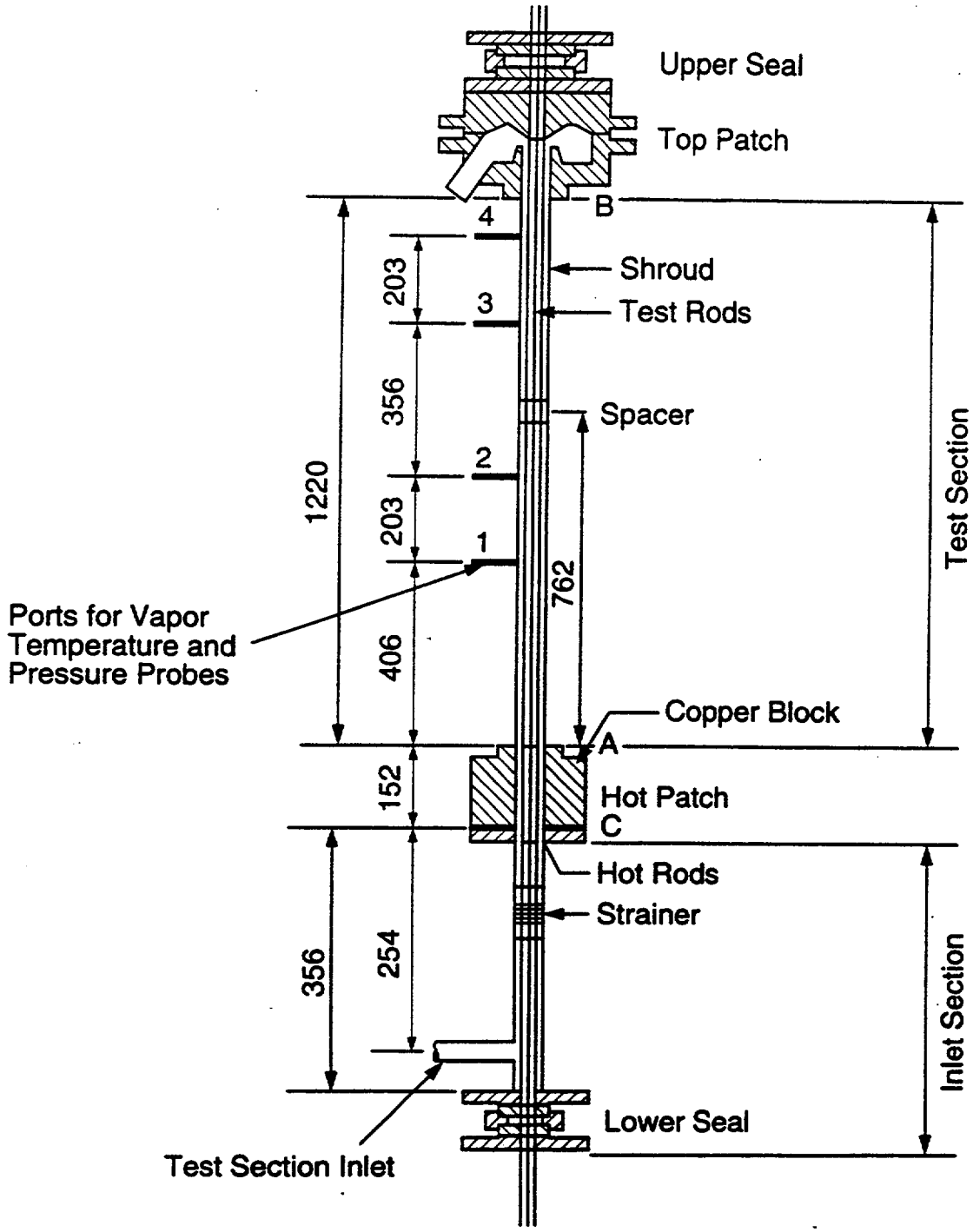

Figure 4.4.3 Lehigh Rod Bundle Test-Section Schematic

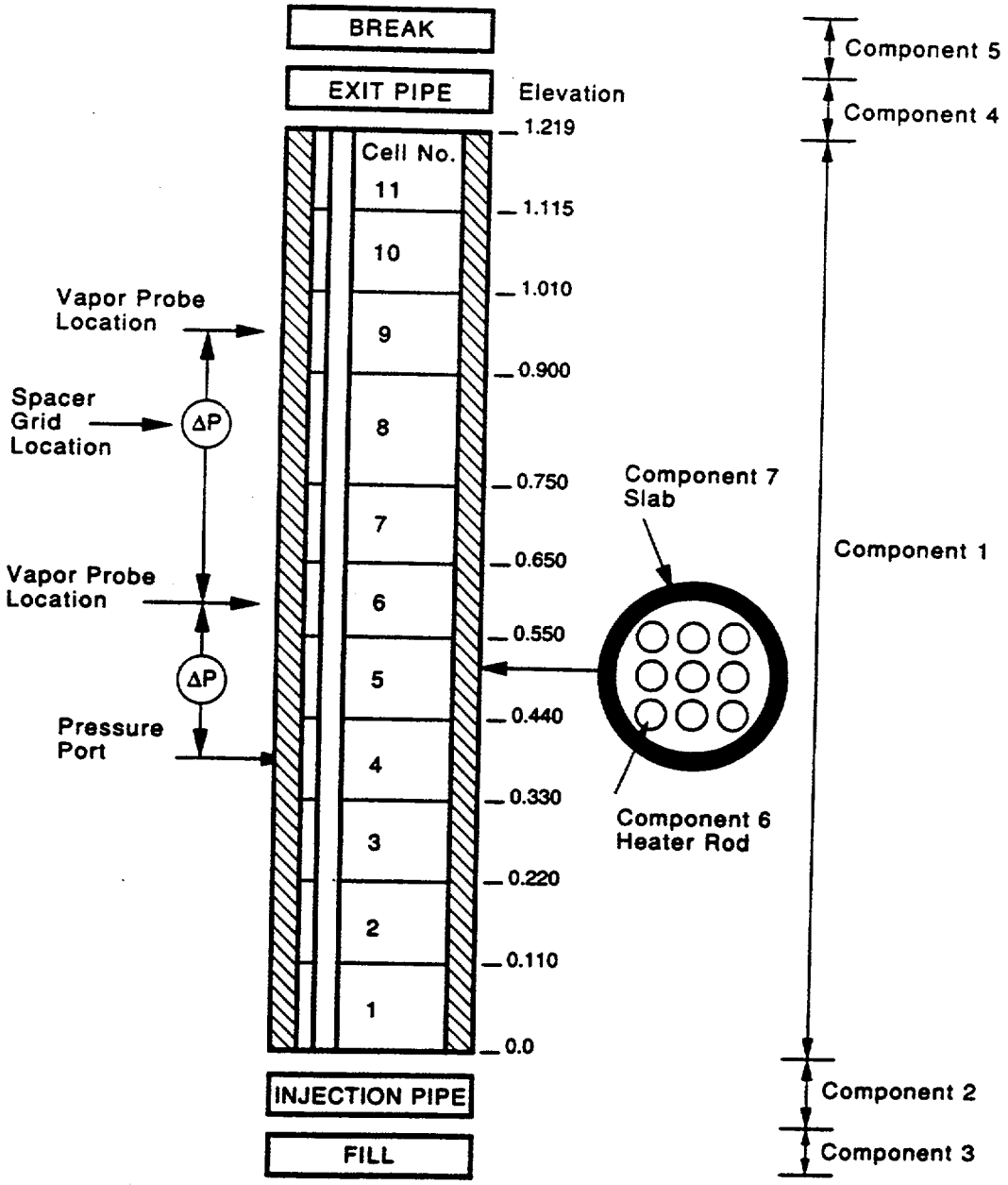

Figure 4.4.4 Lehigh Rod Bundle Facility Input Model Schematic

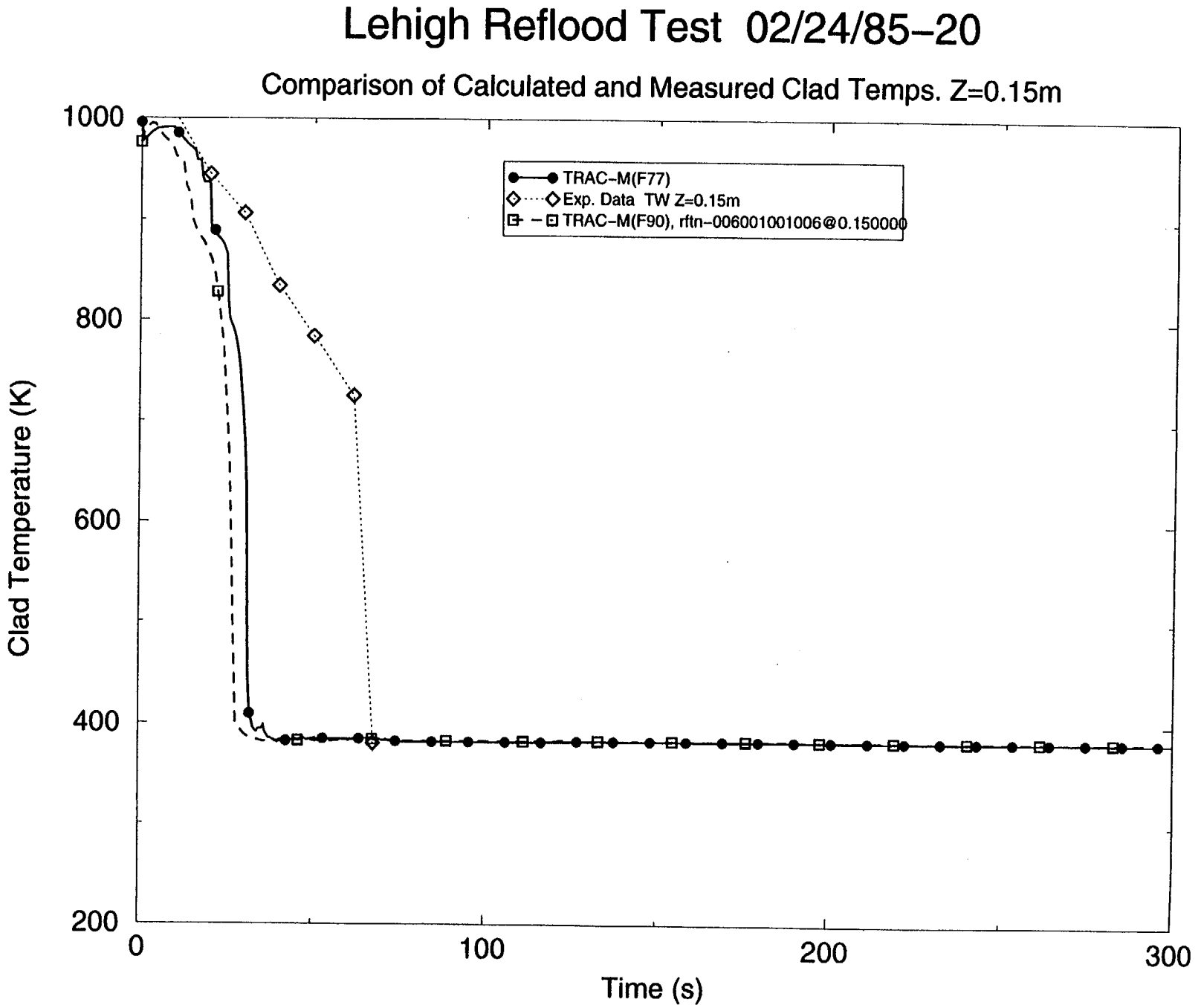

Figure 4.4.5 Comparison of Calculated and Measured Clad Temperatures (Z = 0.15 m) for Lehigh Reflood Test 02/24/85-20

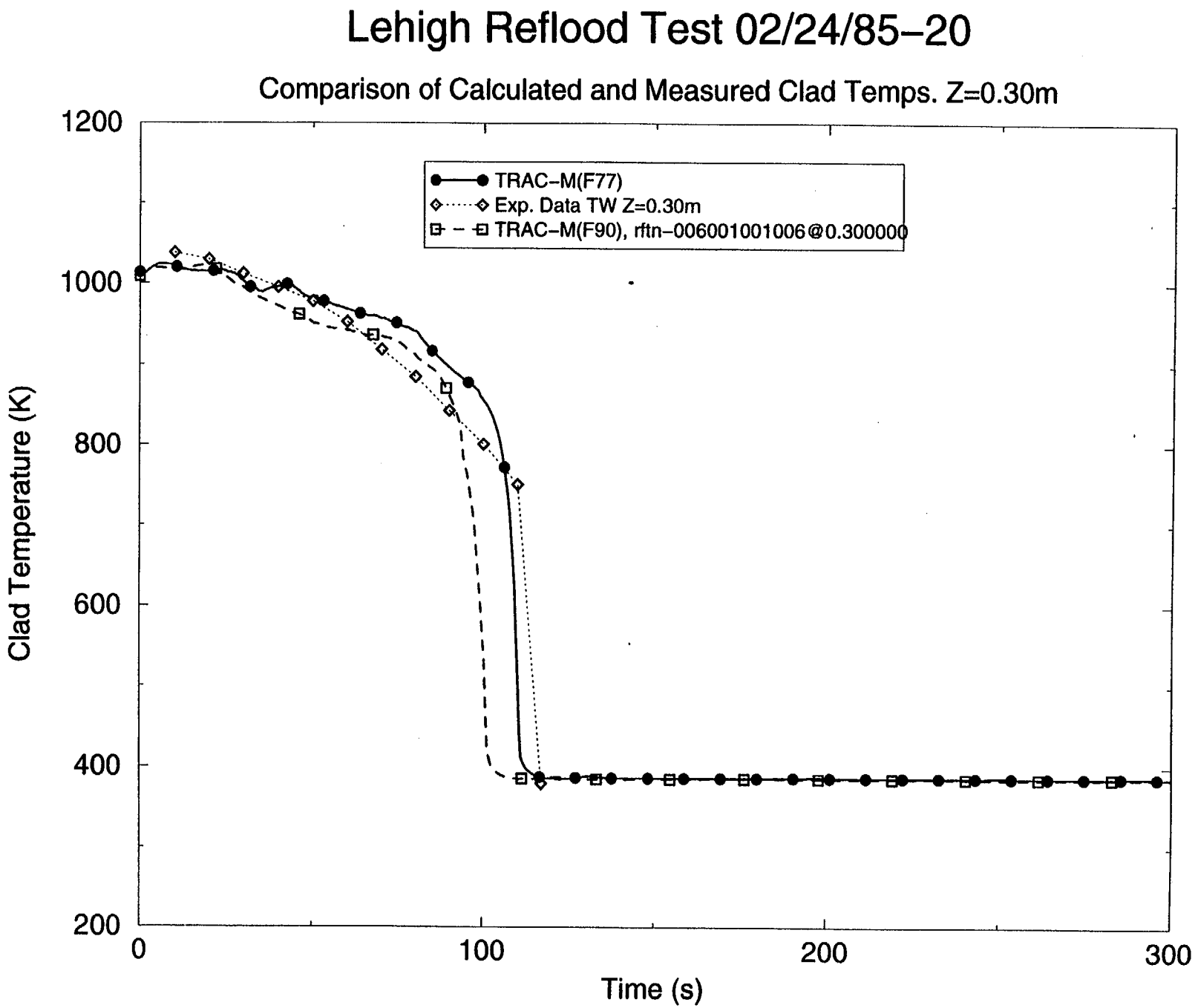

Figure 4.4.6 Comparison of Calculated and Measured Clad Temperatures (Z = 0.30 m) for Lehigh Reflood Test 02/24/85-20

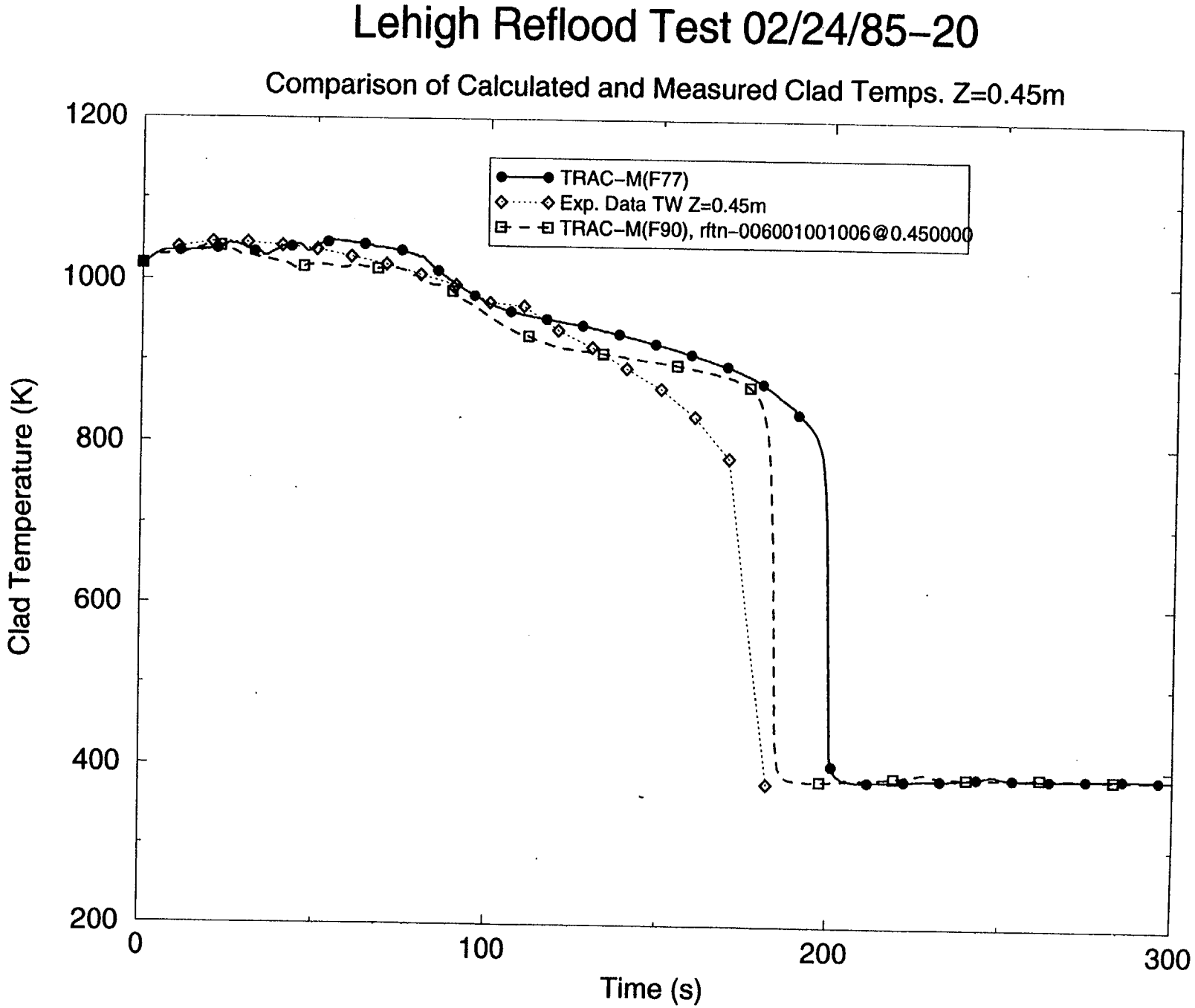

Figure 4.4.7 Comparison of Calculated and Measured Clad Temperatures (Z = 0.45 m) for Lehigh Reflood Test 02/24/85-20

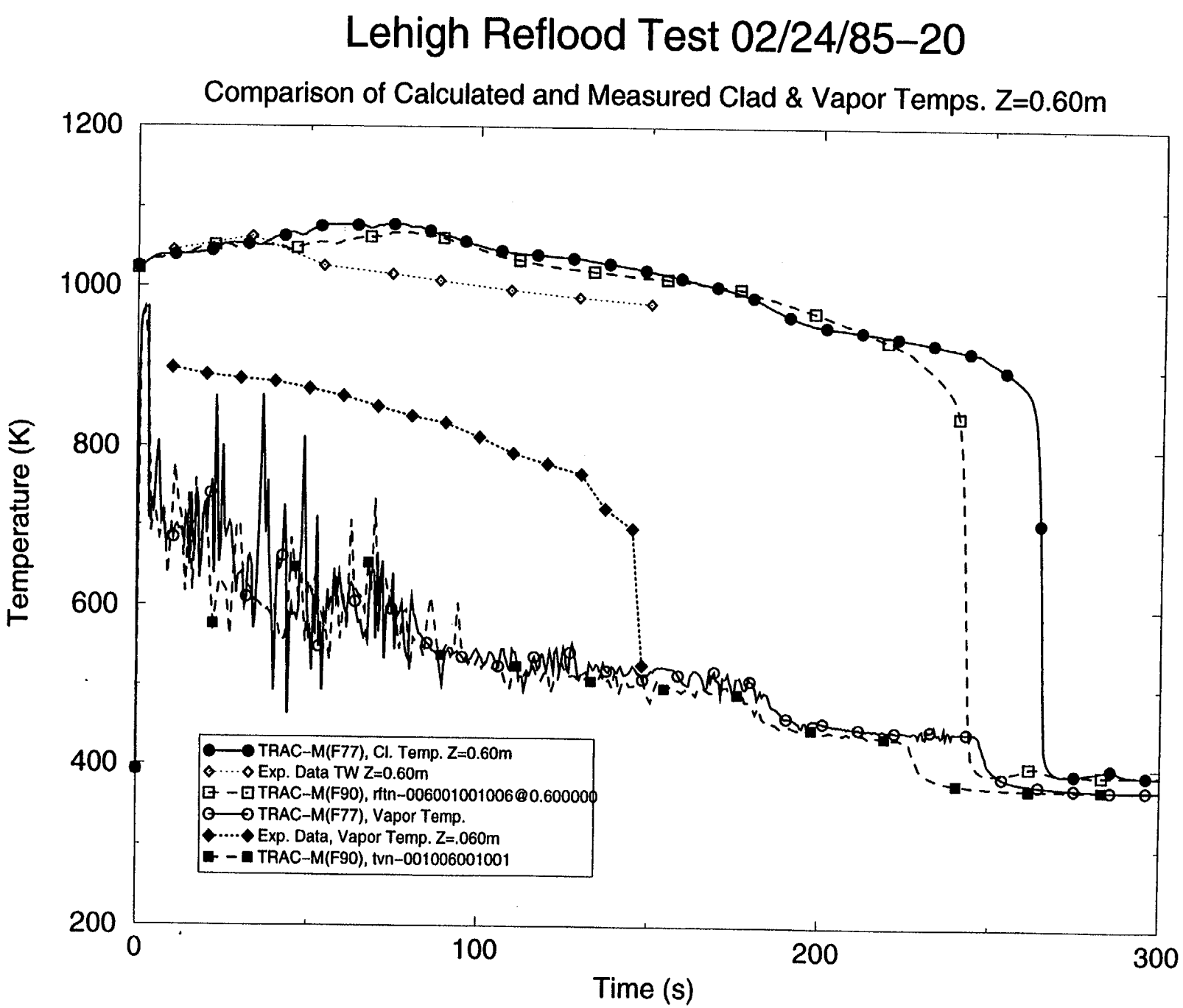

Figure 4.4.8 Comparison of Calculated and Measured Clad Vapor Temperatures (Z = 0.60 m) for Lehigh Reflood Test 02/24/85-20

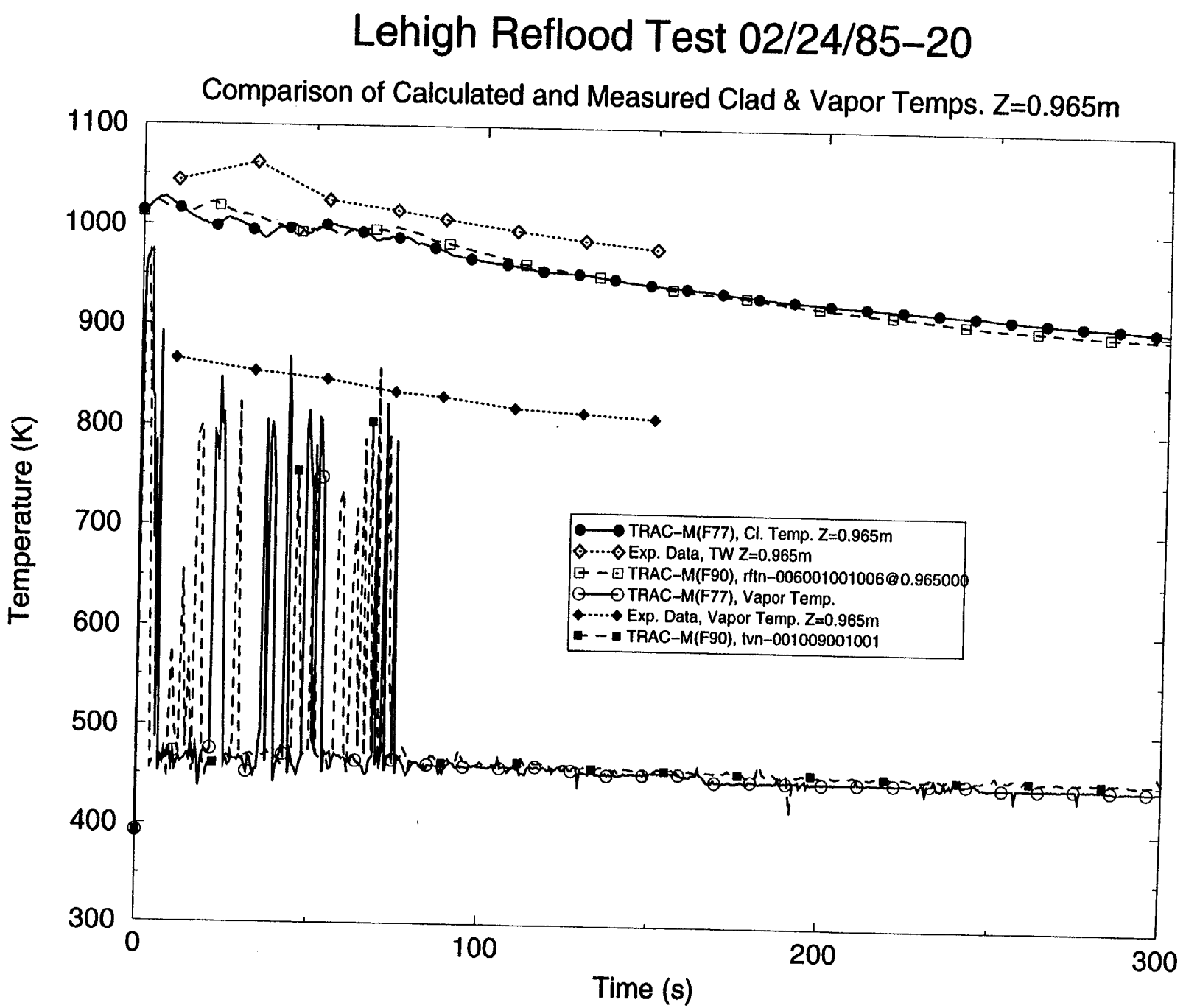

Figure 4.4.9 Comparison of Calculated and Measured Clad & Vapor Temperatures (Z = 0.965 m) for Lehigh Reflood Test 02/24/85-20

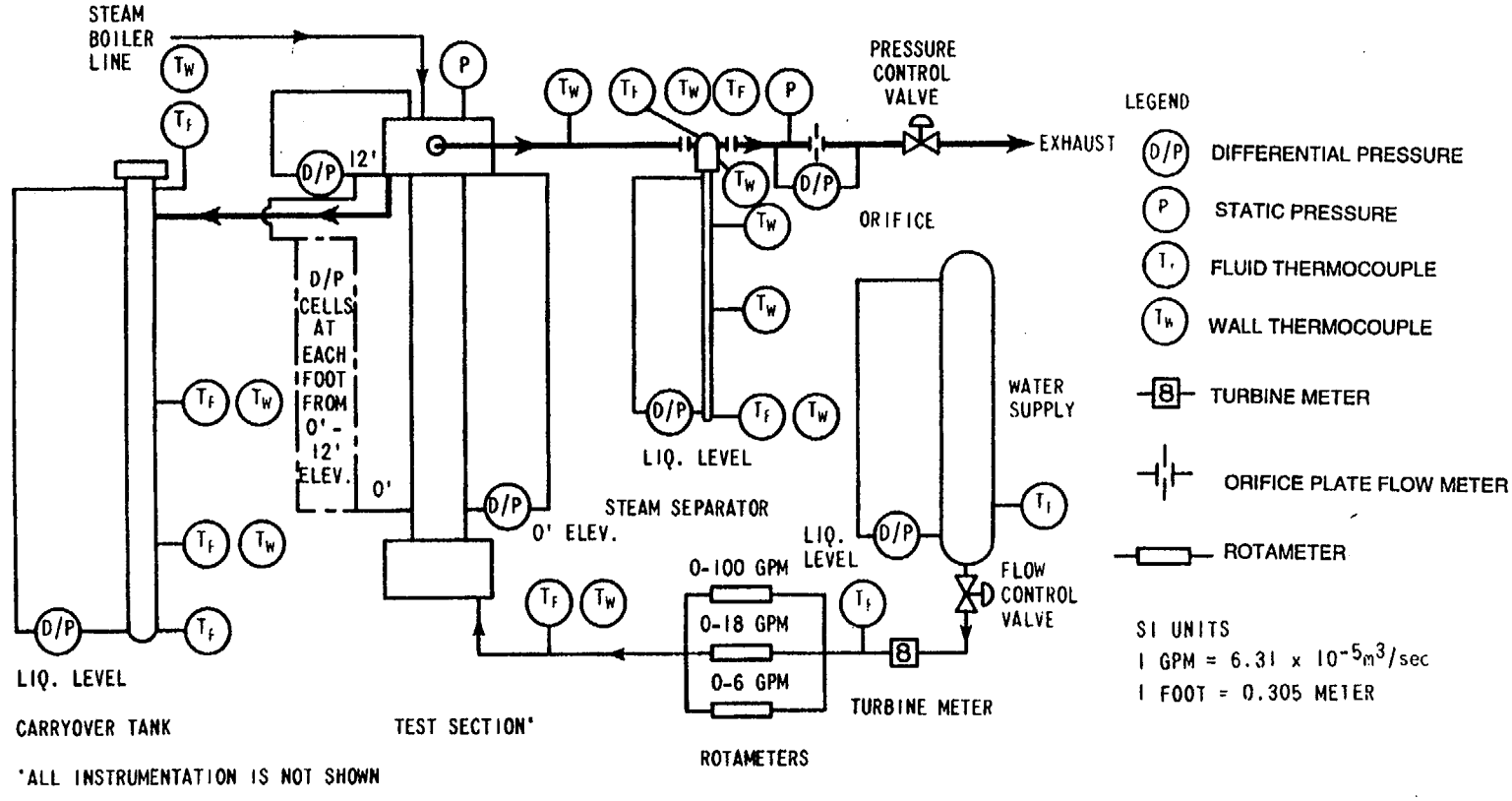

Figure 4.4.10 FLECHT-SEASET System Configuration

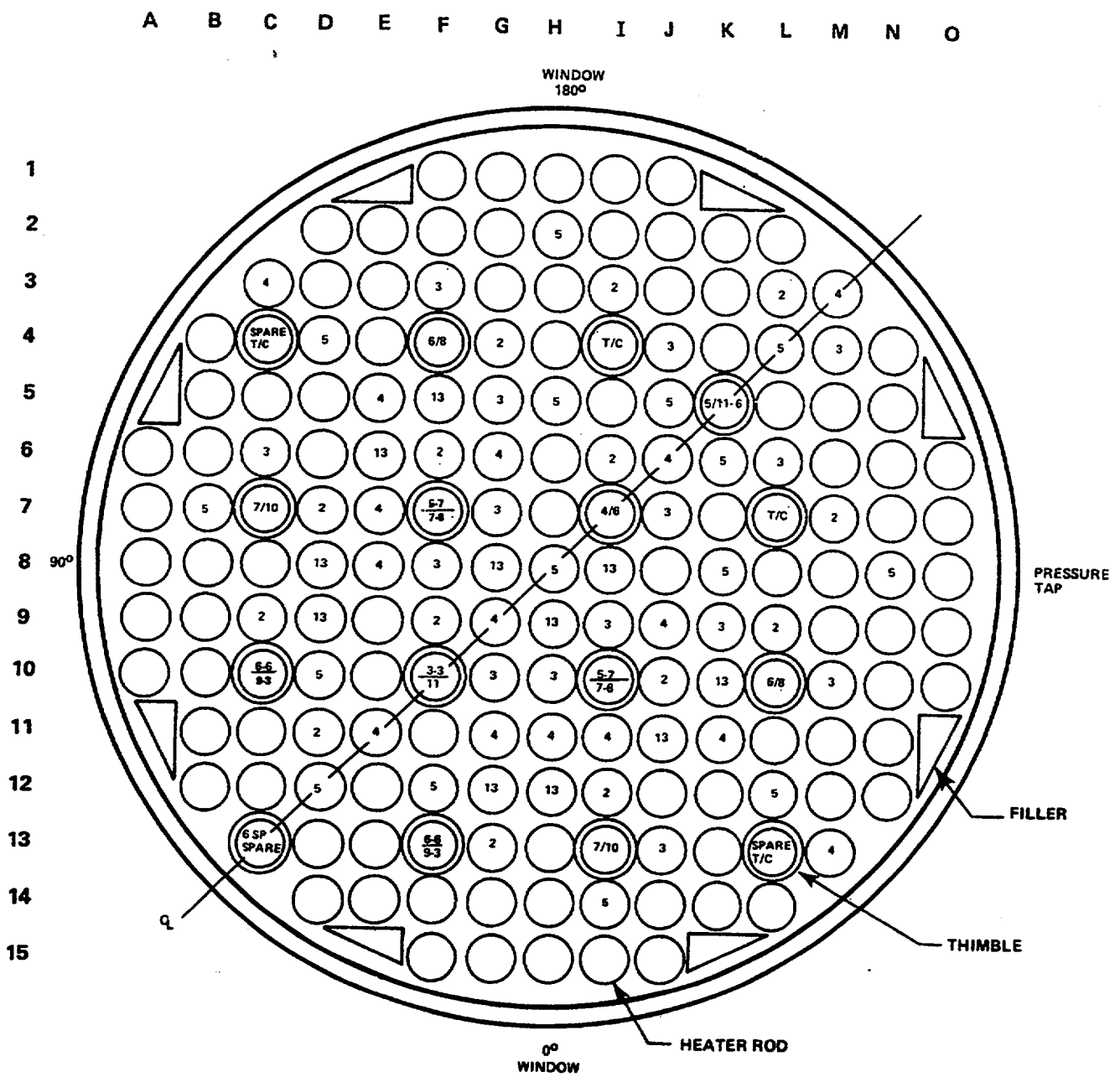

Figure 4.4.11 FLECHT-SEASET 161 Rod Test Bundle

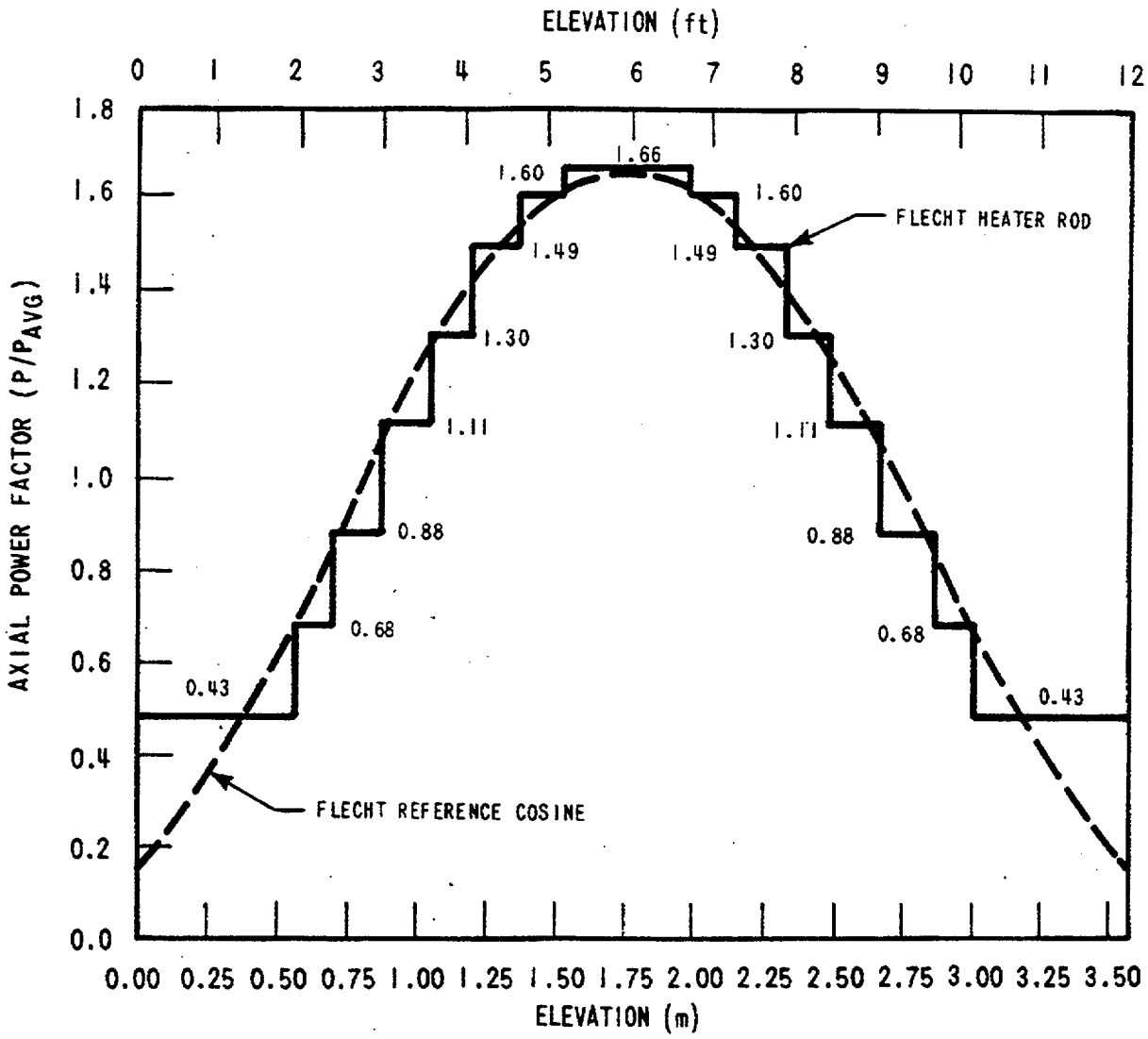

Figure 4.4.12 FLECHT-SEASET Axial Power Shape

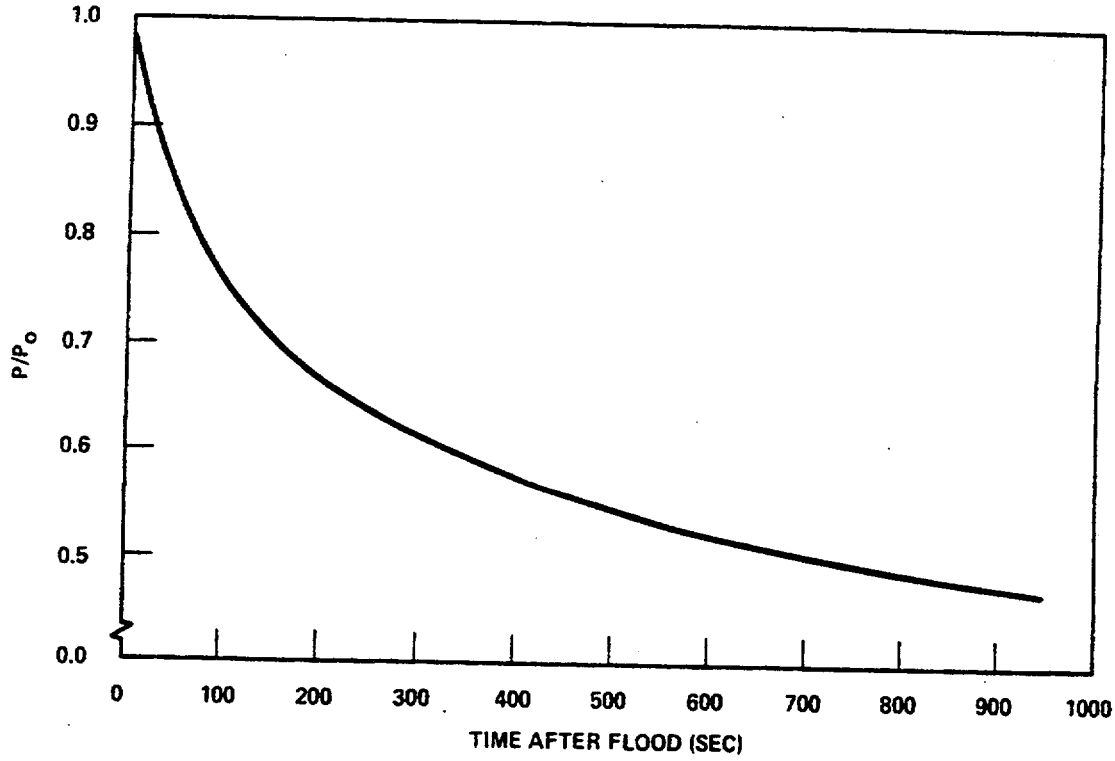

Figure 4.4.13 Decay Power Curve (ANS + 20%)

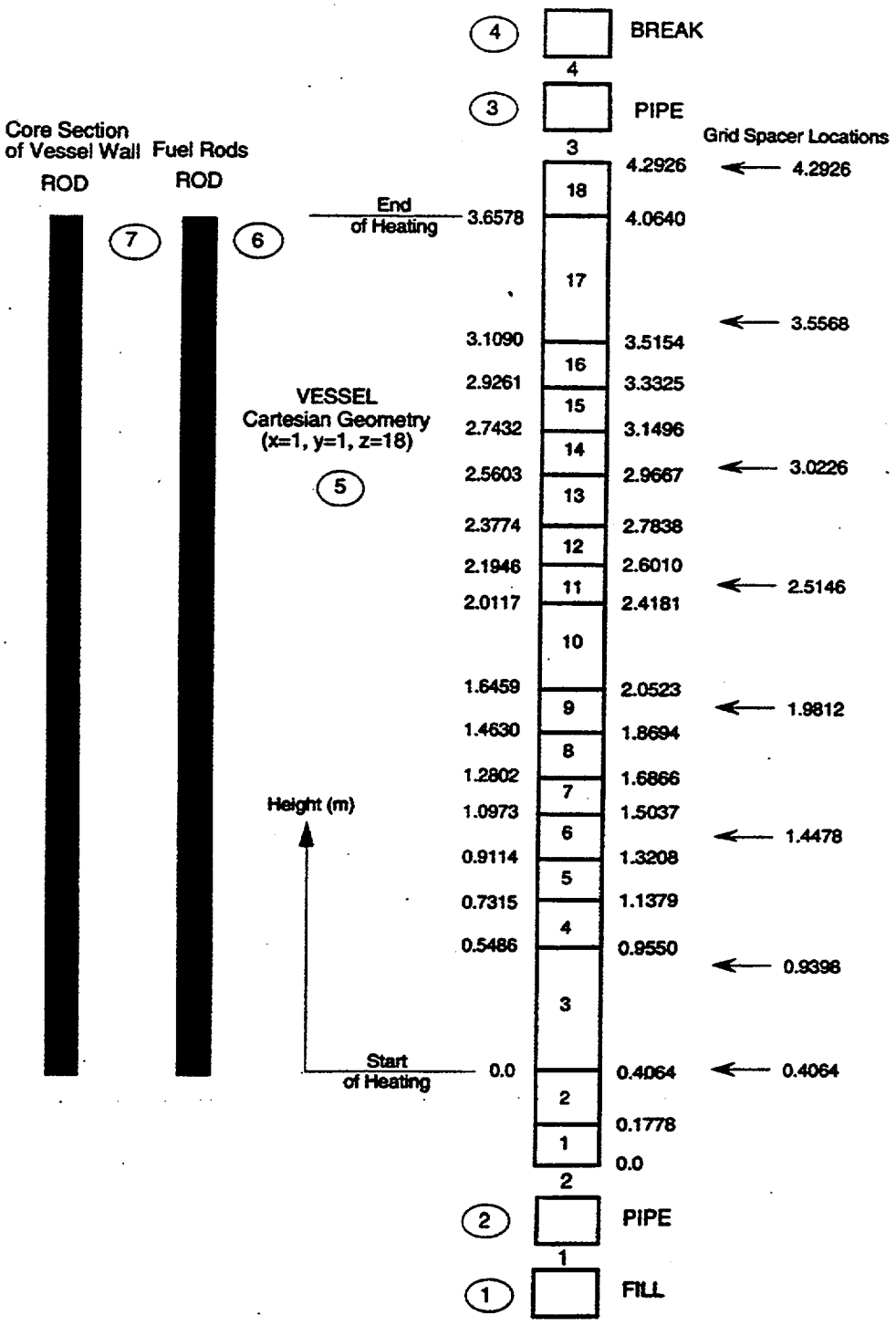

Figure 4.4.14 TRAC-M Input Model Schematic for FLECHT-SEASET Run 31504

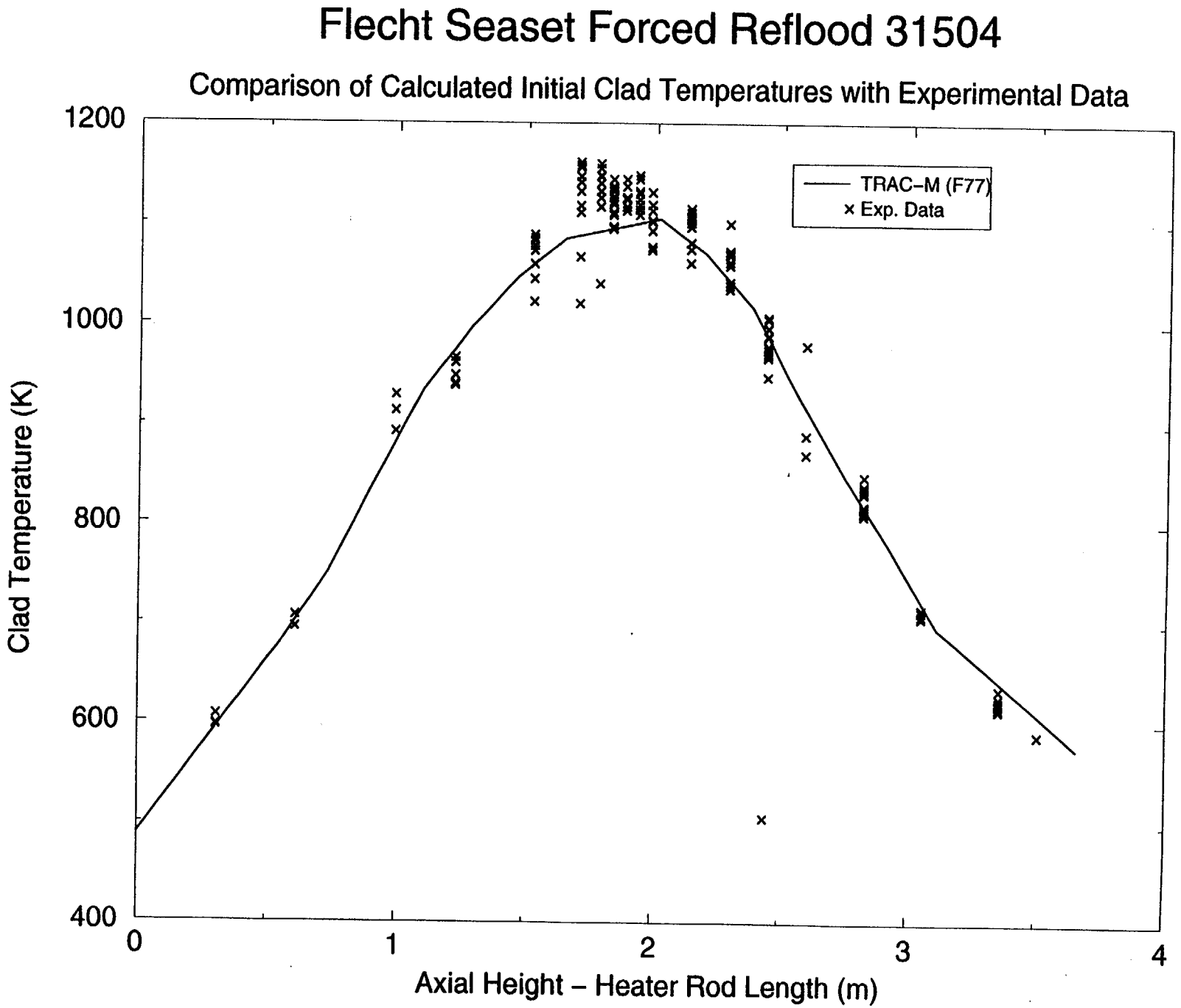

Figure 4.4.15 Initial Axial Temperature Variation

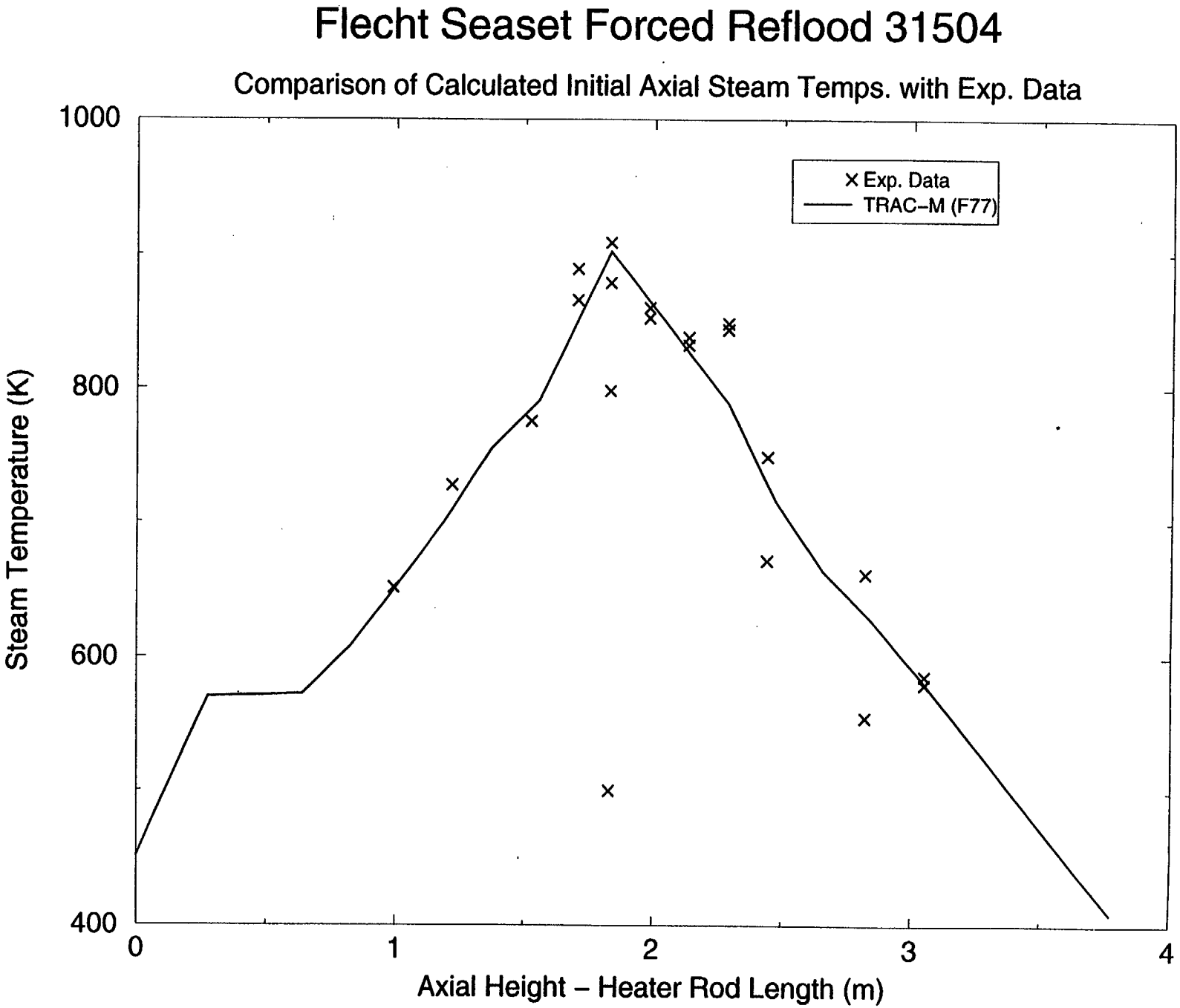

Figure 4.4.16 Initial Axial Steam Temperature Variation

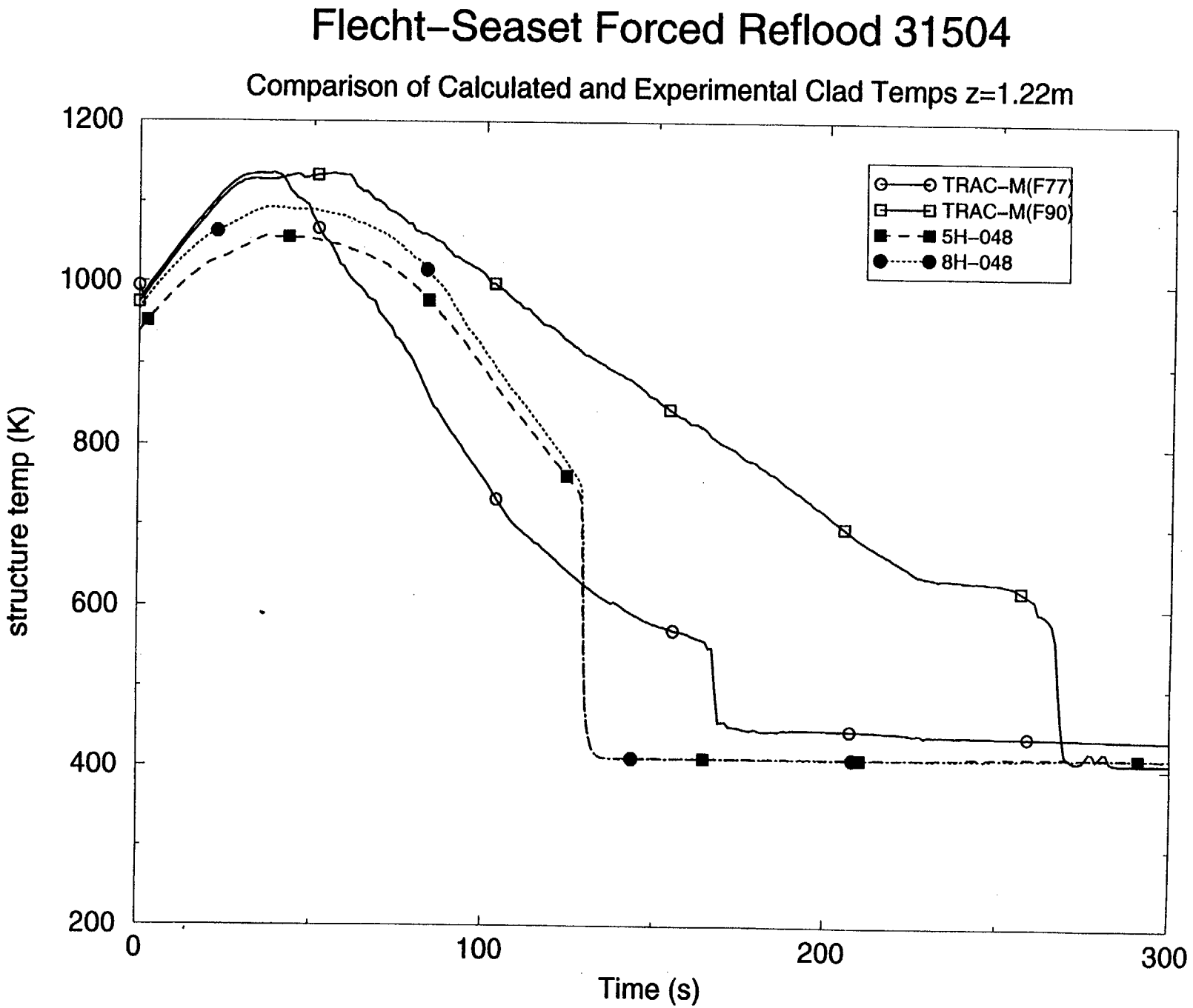

Figure 4.4.17 Comparison of Calculated and Experimental Clad Temperatures @ z = 1.22 m

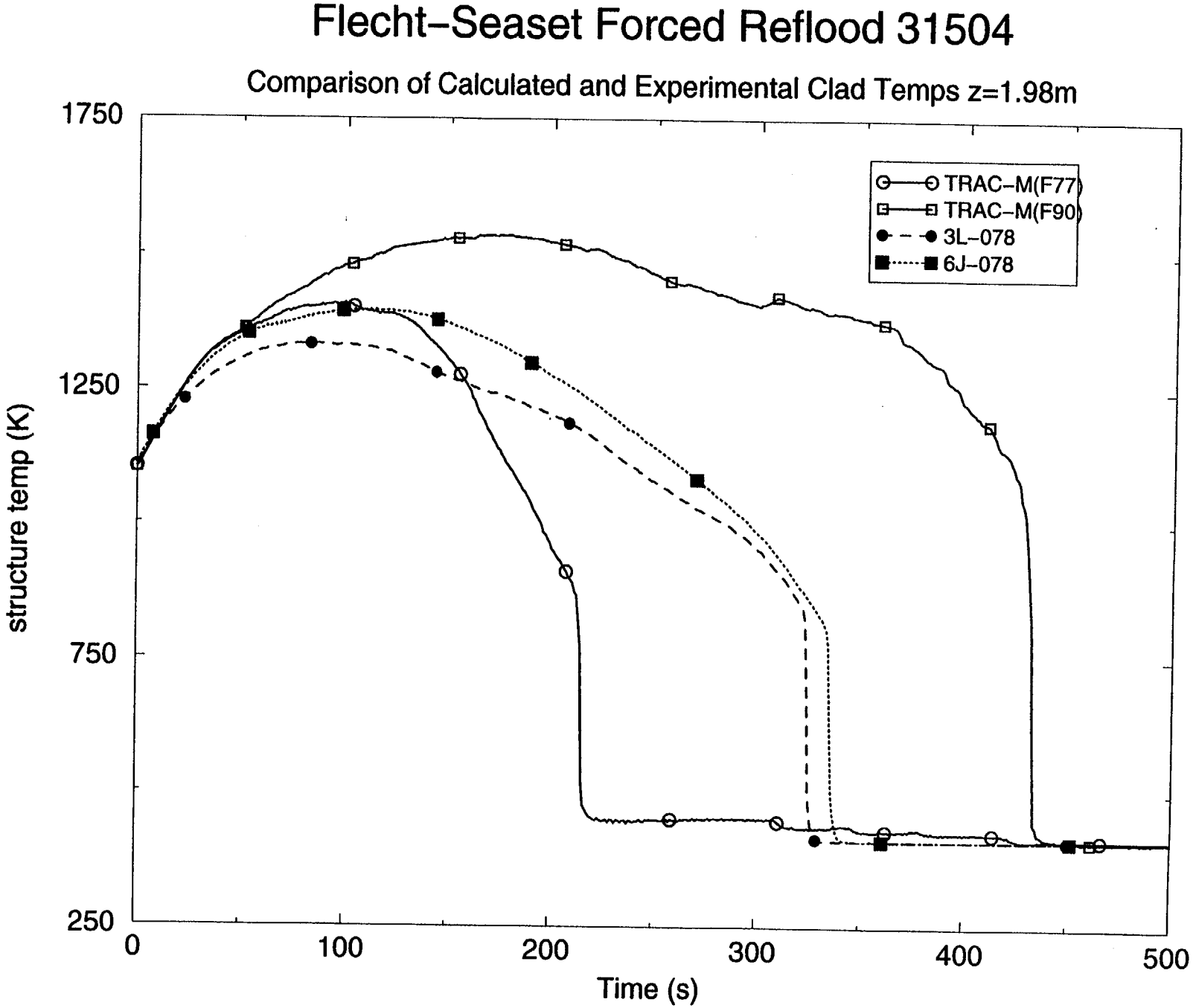

Figure 4.4.18 Comparison of Calculated and Experimental Clad Temperatures @ z = 1.98 m

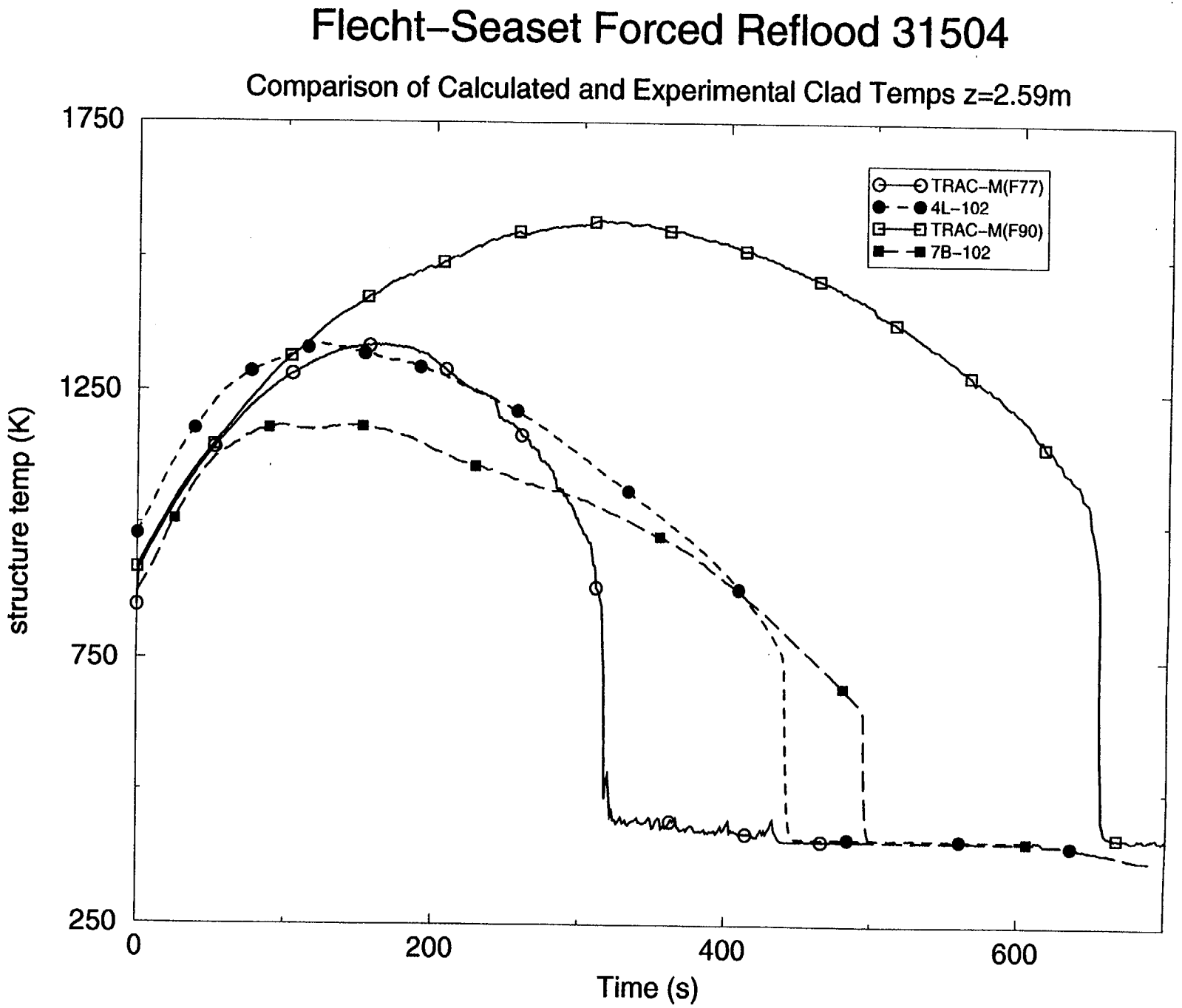

Figure 4.4.19 Comparison of Calculated and Experimental Clad Temperatures @ z = 2.59 m

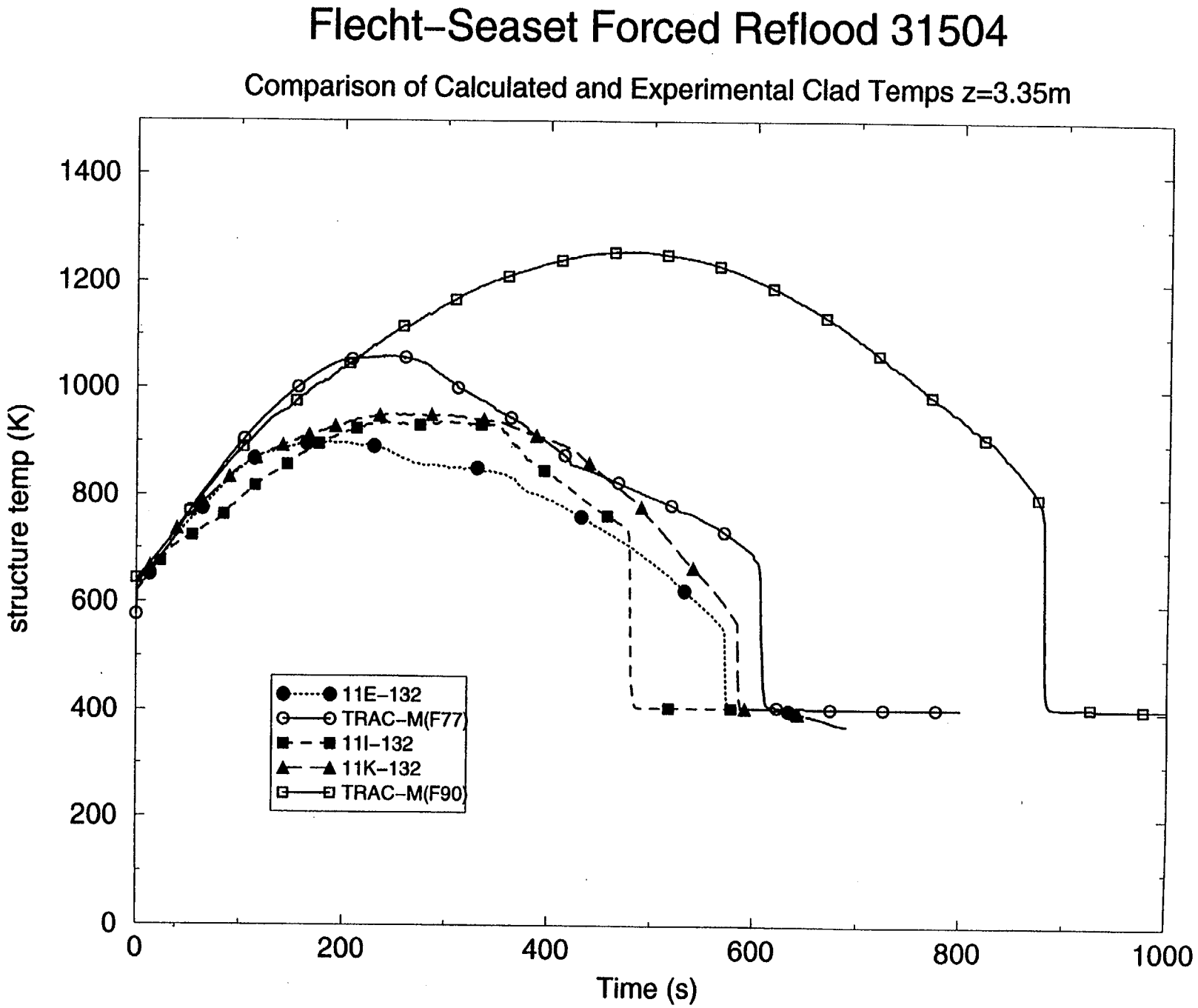

Figure 4.4.20 Comparison of Calculated and Experimental Clad Temperatures @ z = 3.35 m

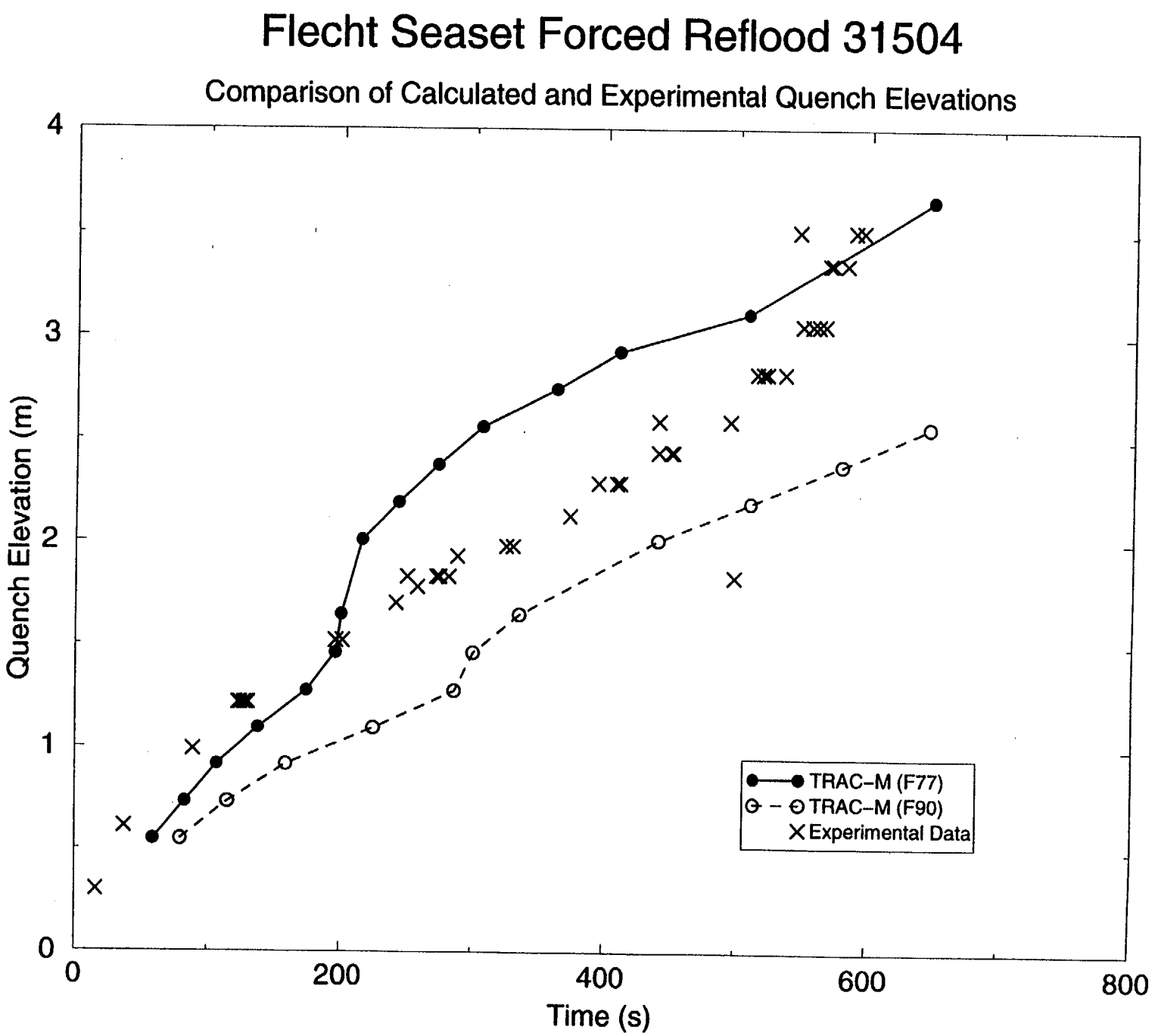

Figure 4.4.21 Calculated and Measured Quench Front Propagation

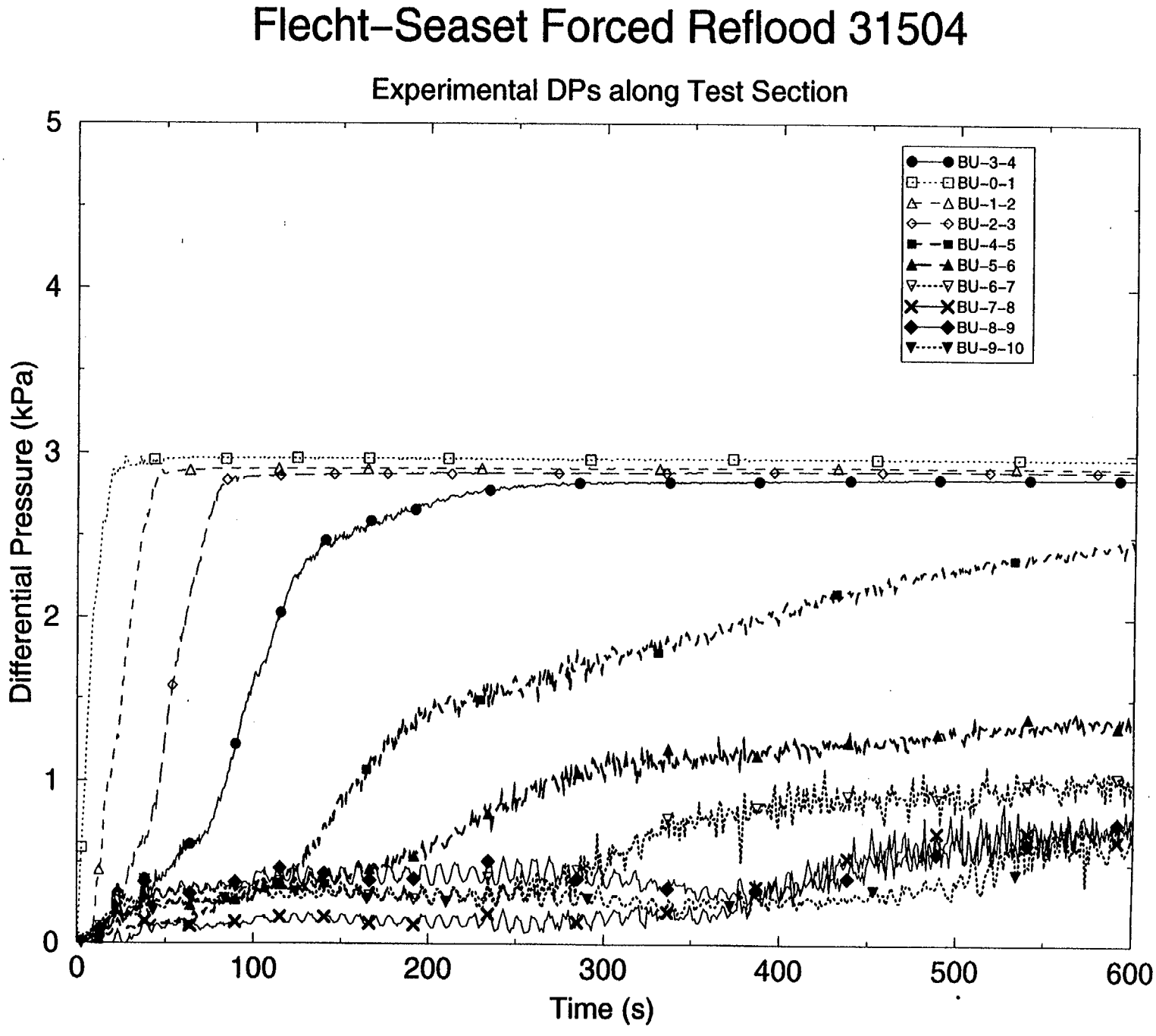

Figure 4.4.22 Experimental Differential Pressure Measurements Along the Test Section

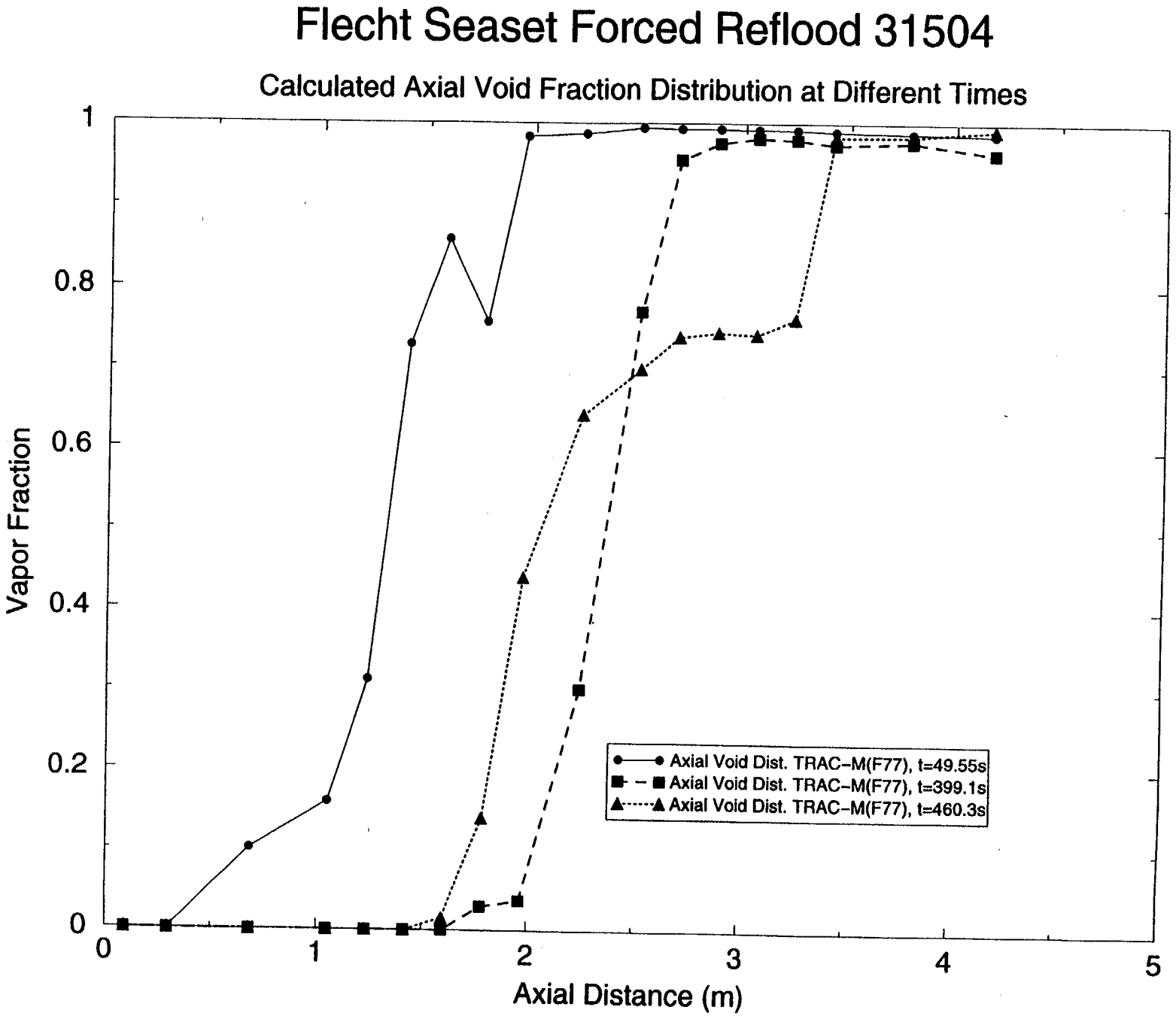

Figure 4.4.23 Calculation of Axial Void Fraction Distribution by TRAC-M(F77)

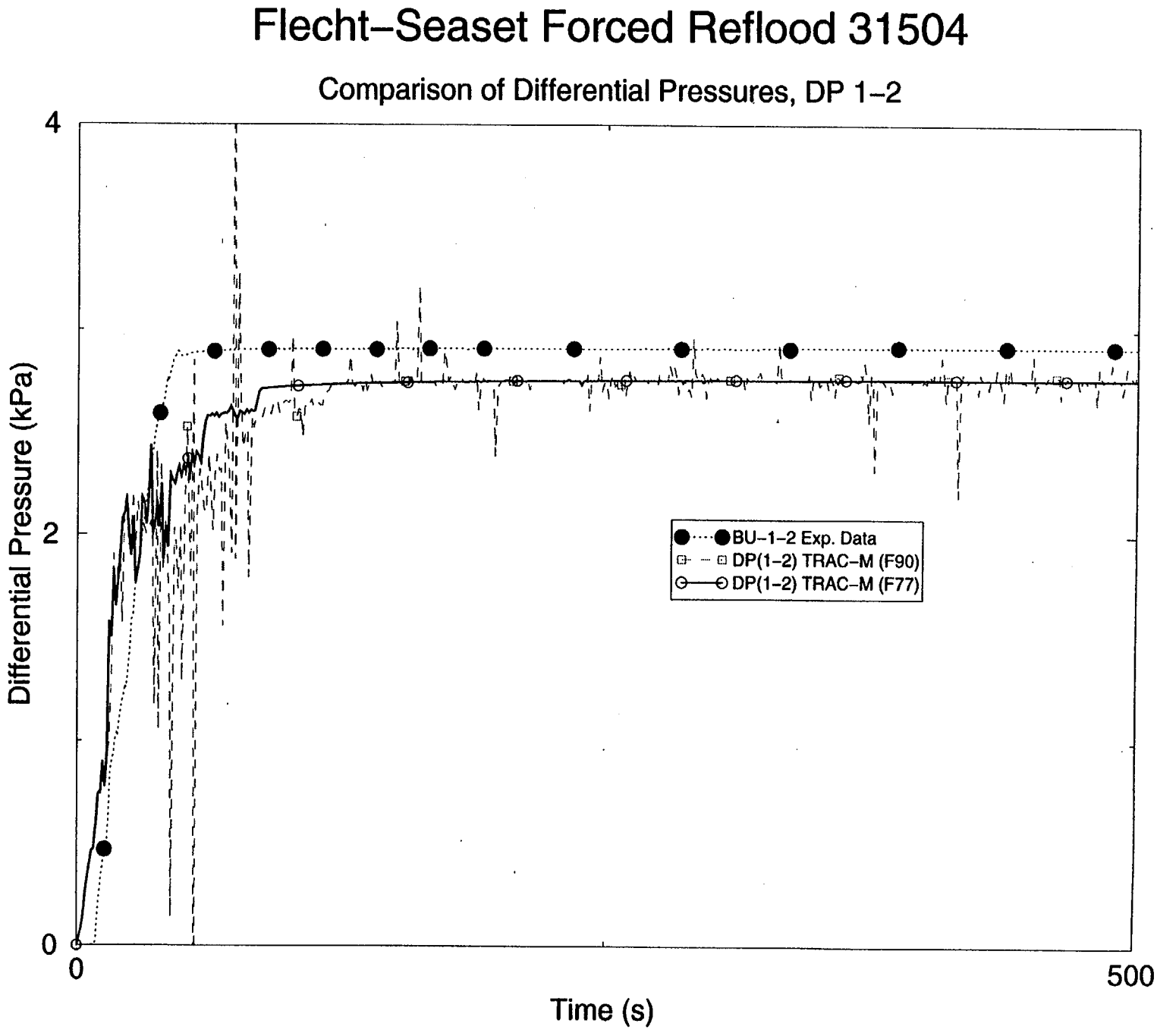

Figure 4.4.24 Comparison of Differential Pressures (Taps 1 - 2)

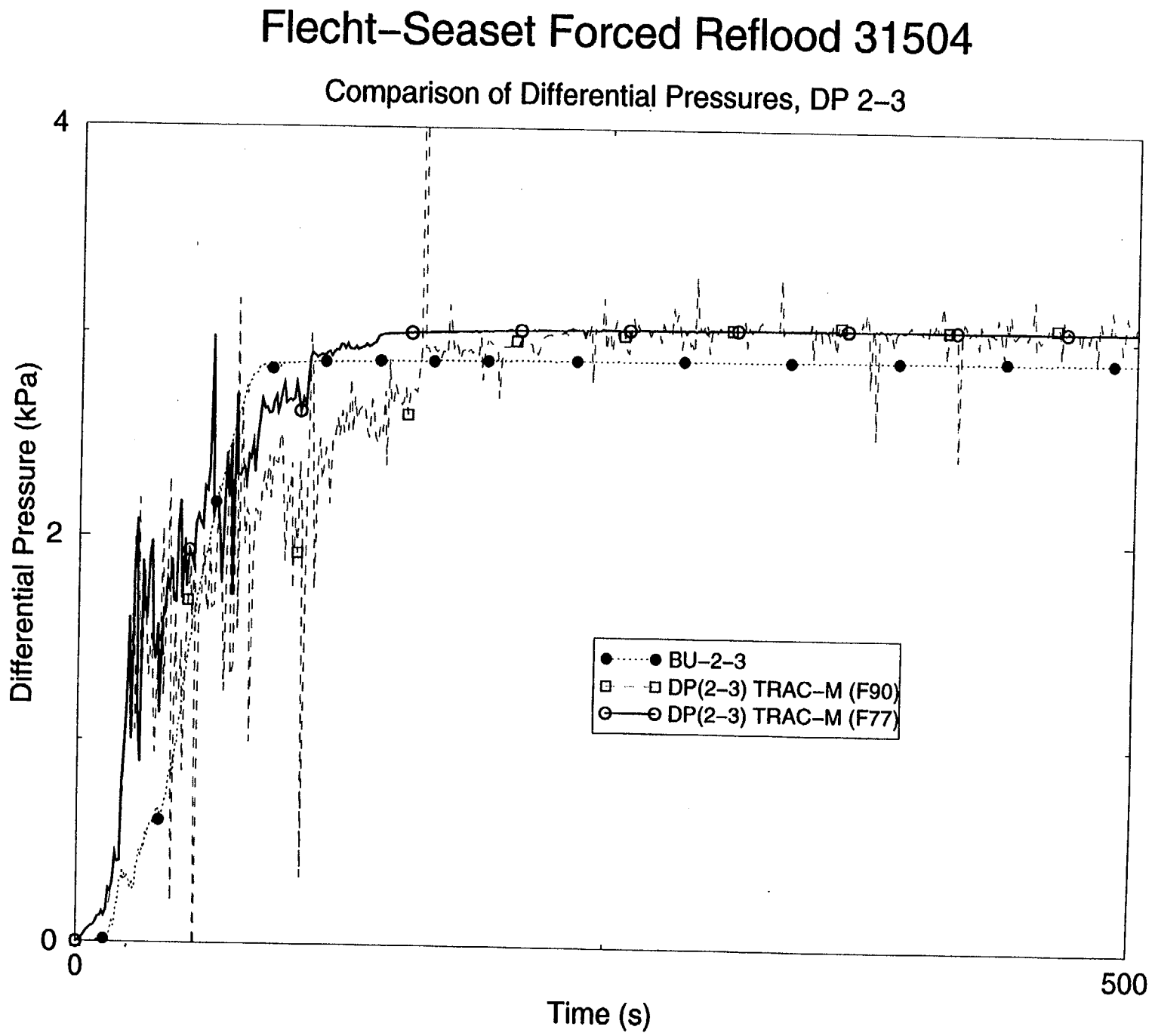

Figure 4.4.25 Comparison of Differential Pressures (Taps 2 - 3)

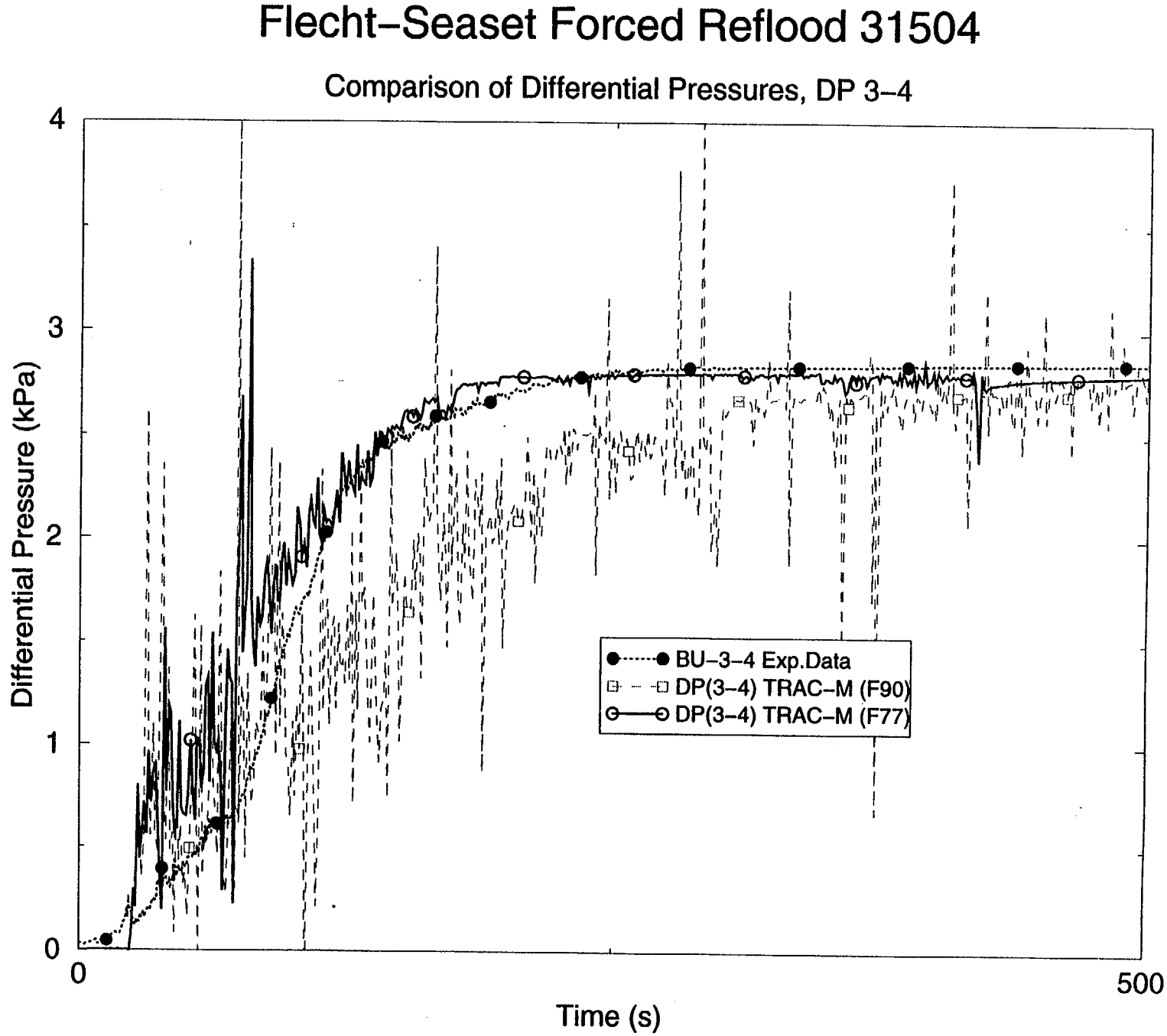

Figure 4.4.26 Comparison of Differential Pressures (Taps 3 - 4)

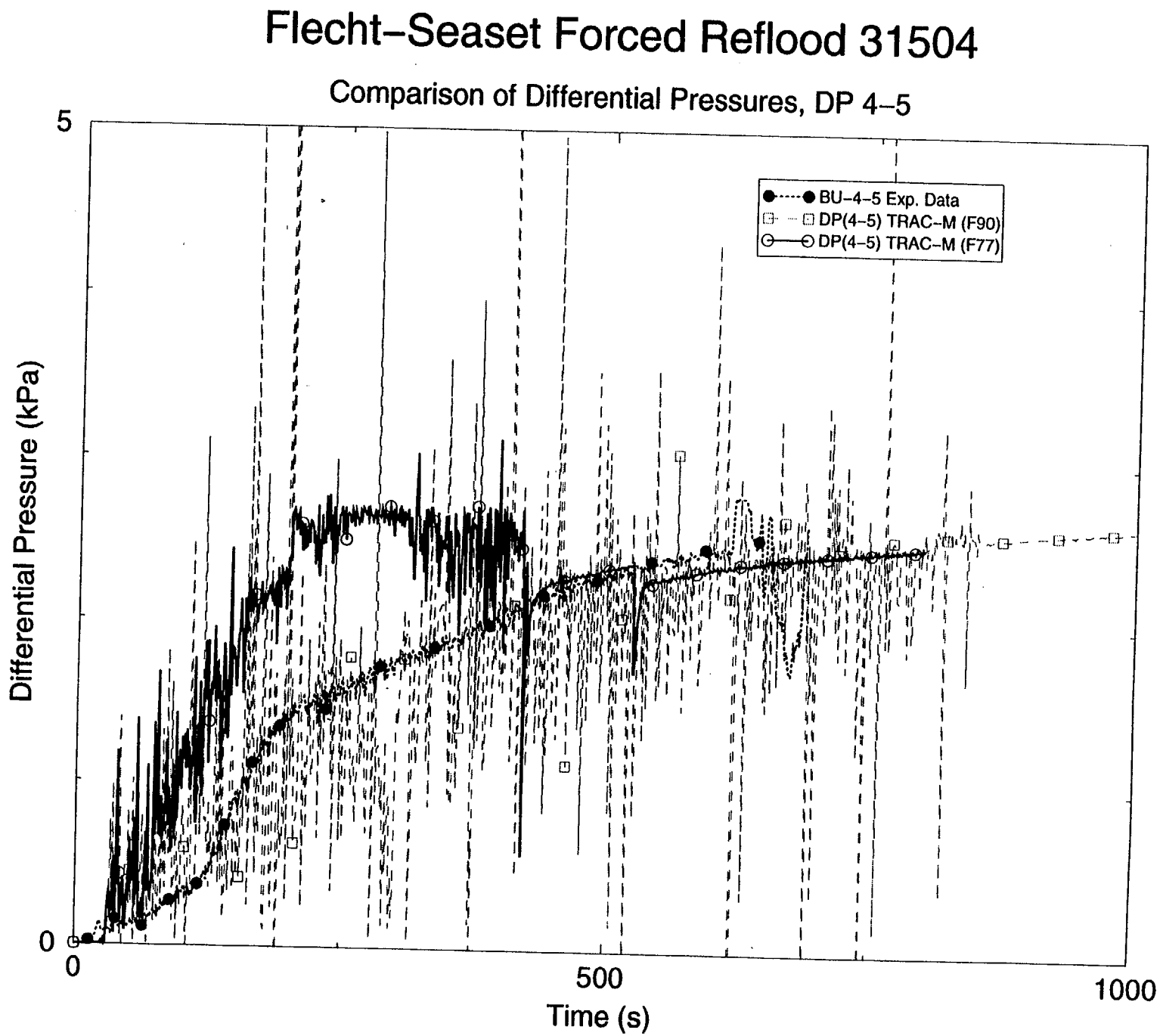

Figure 4.4.27 Comparison of Differential Pressures (Taps 4 - 5)

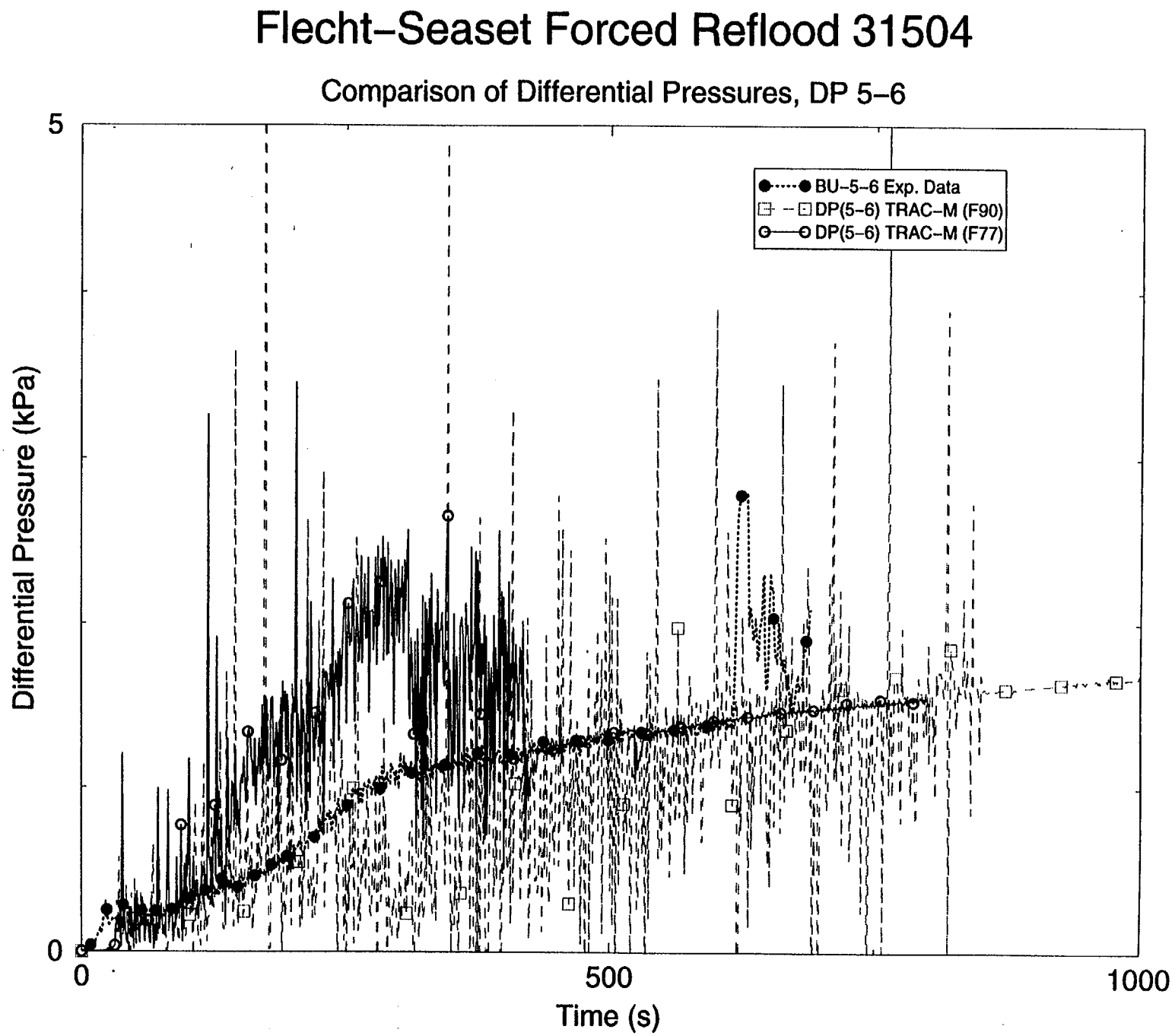

Figure 4.4.28 Comparison of Differential Pressures (Taps 5 - 6)

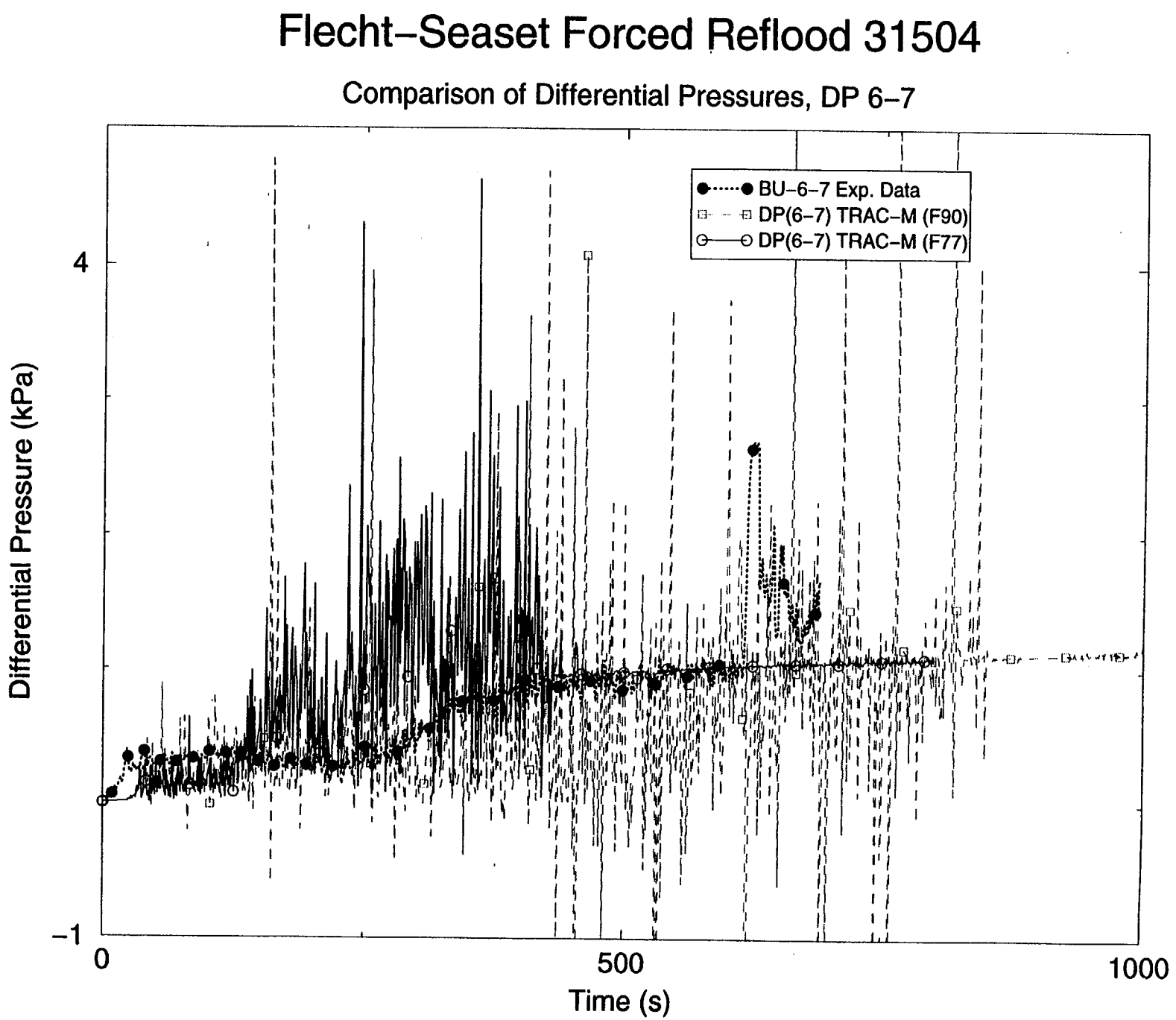

Figure 4.4.29 Comparison of Differential Pressures (Taps 6 - 7)

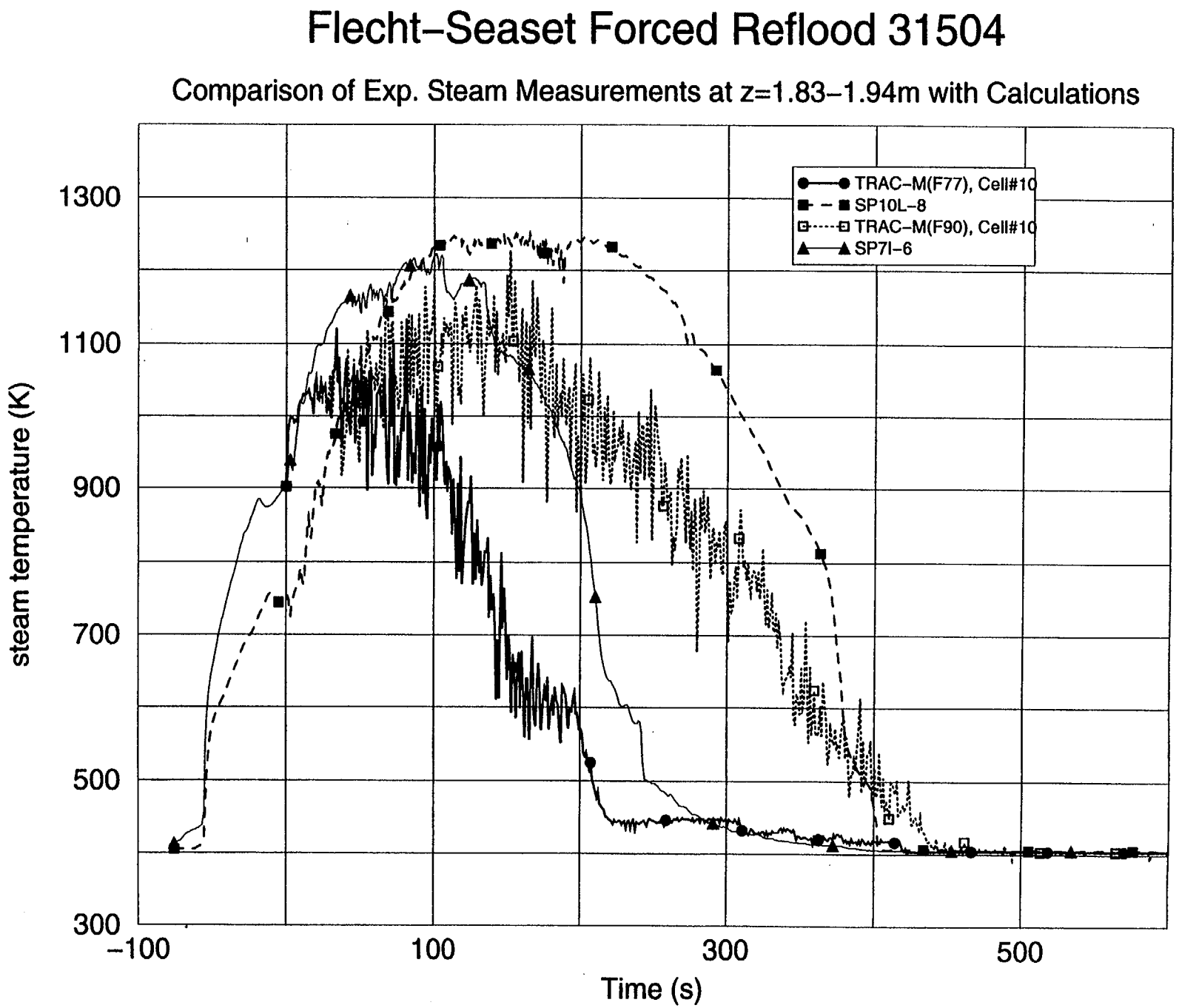

Figure 4.4.30 Steam Temperatures (Z = 1.83 - 1.94 m)

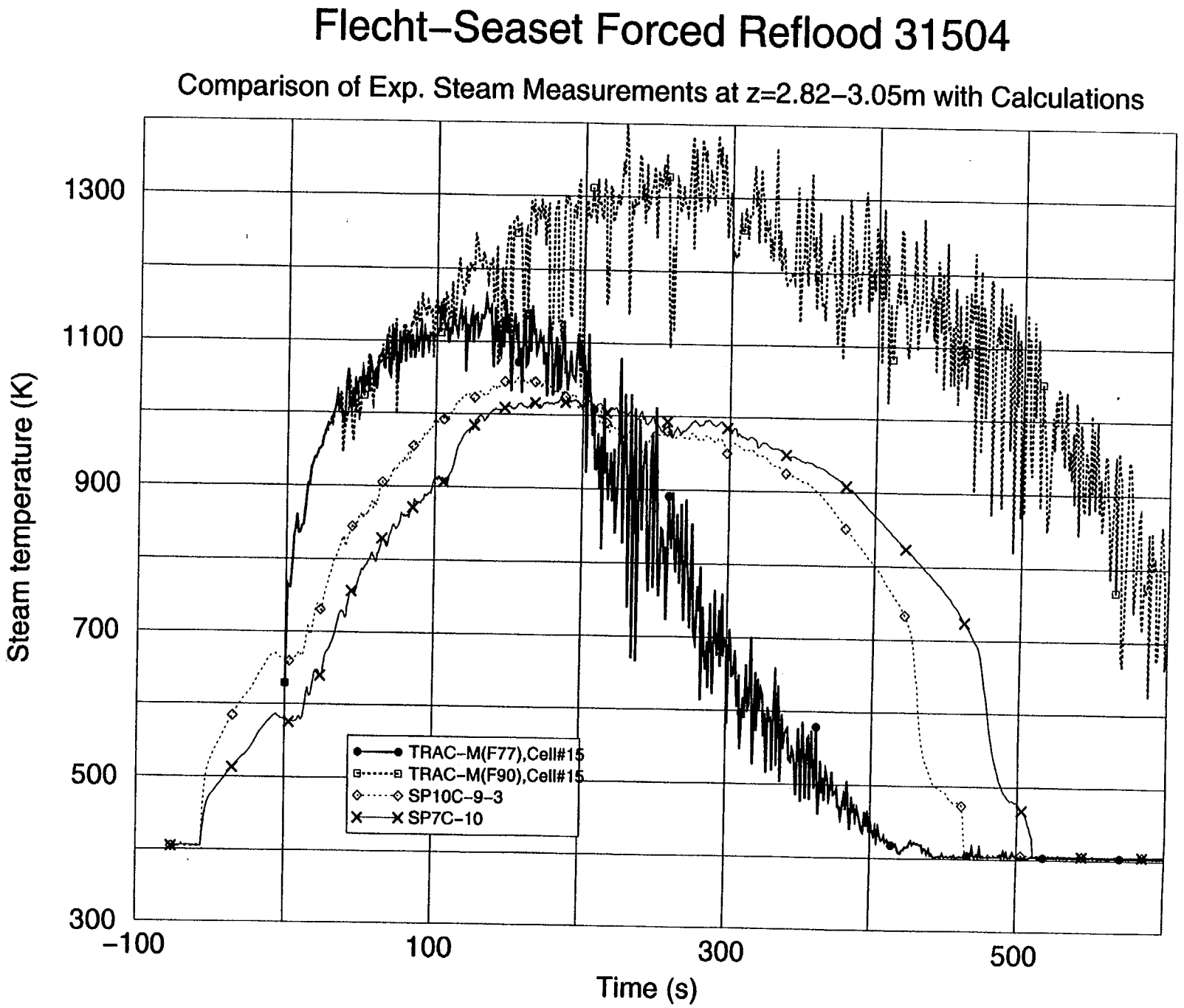

Figure 4.4.31 Steam Temperatures (Z = 2.82 - 3.03 m)

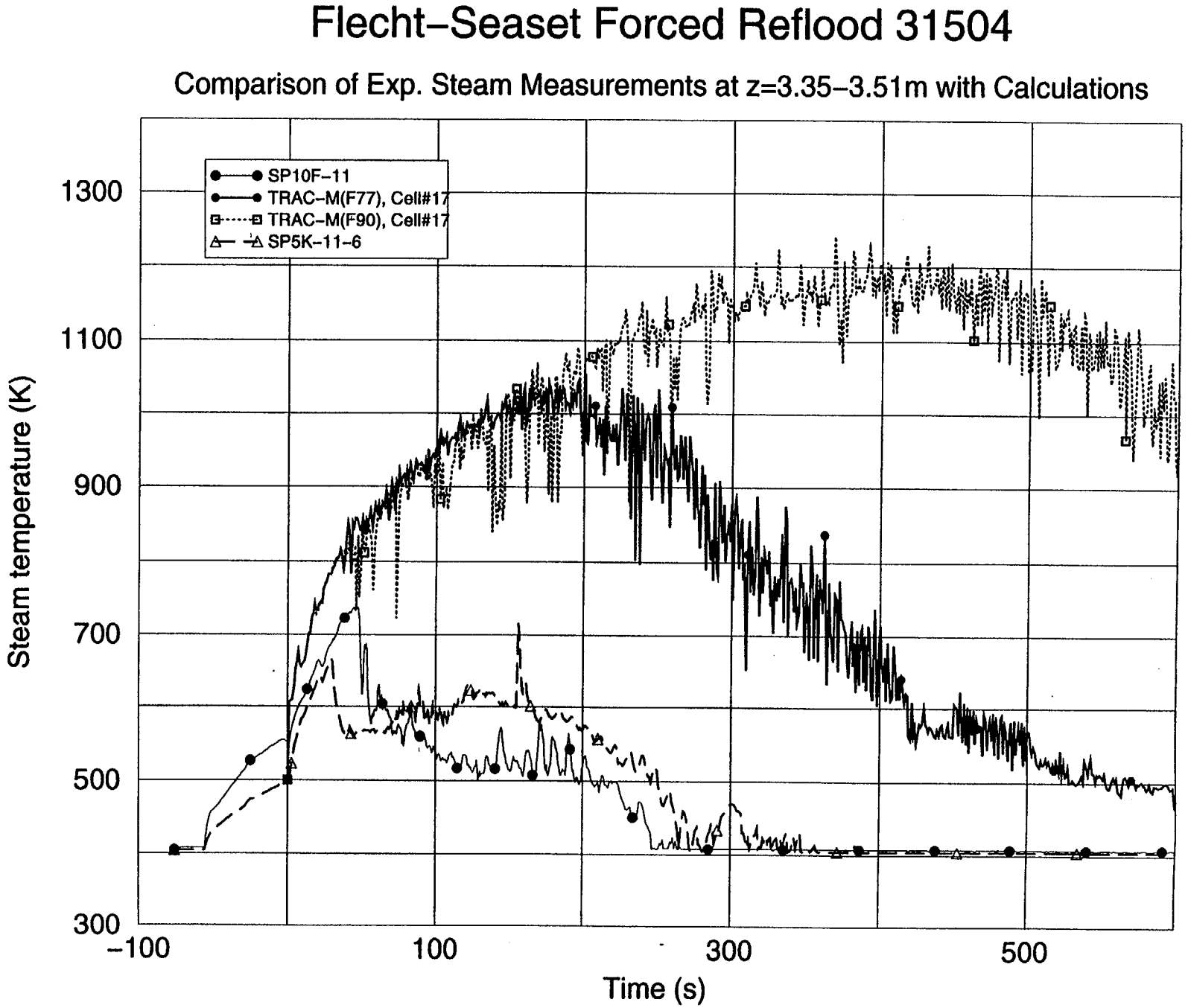

Figure 4.4.32 Steam Temperatures (Z = 3.35 - 3.51 m)

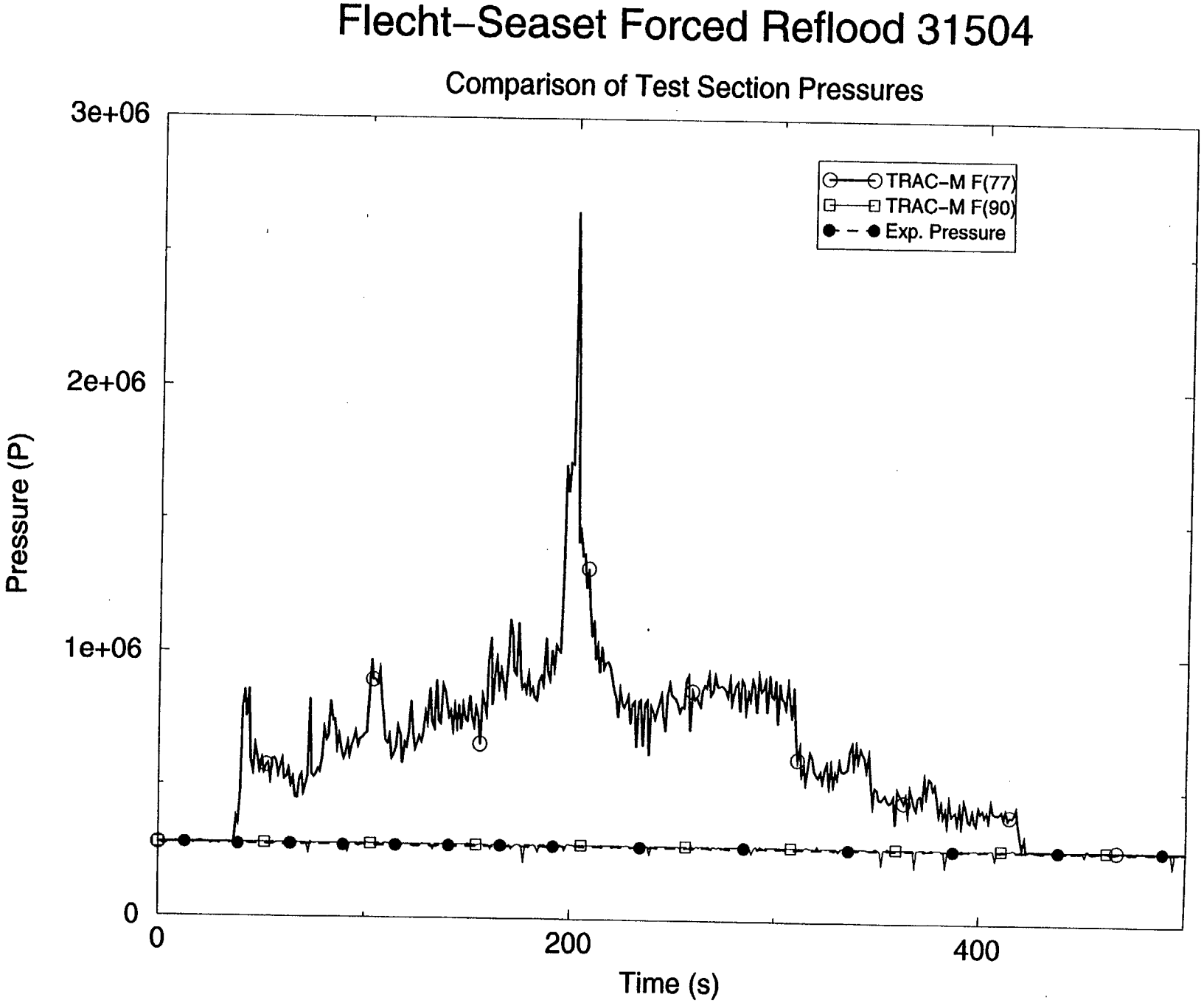

Figure 4.4.33 Comparison of Test Section Pressures

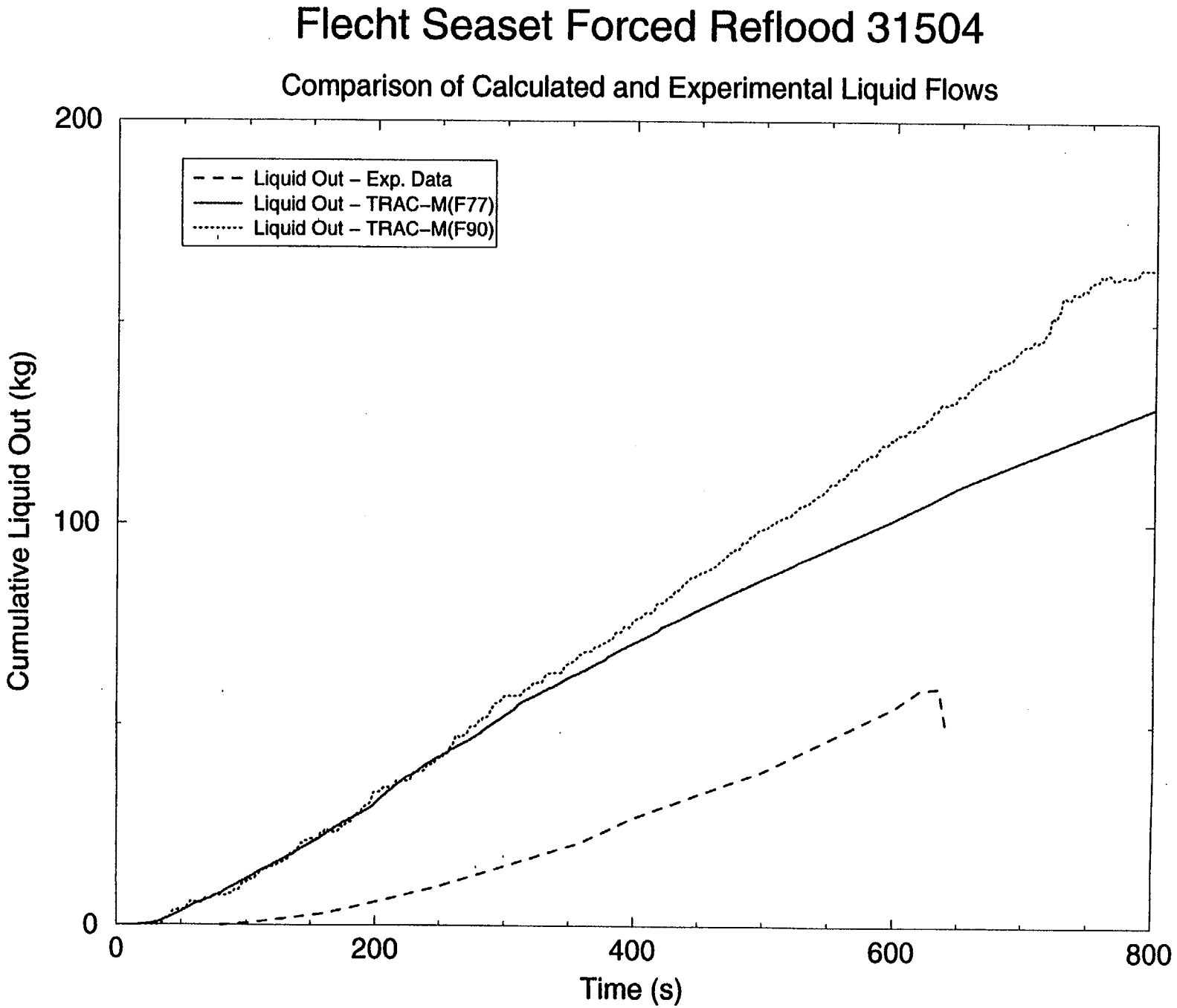

Figure 4.4.34 Comparison of Liquid Carryouts

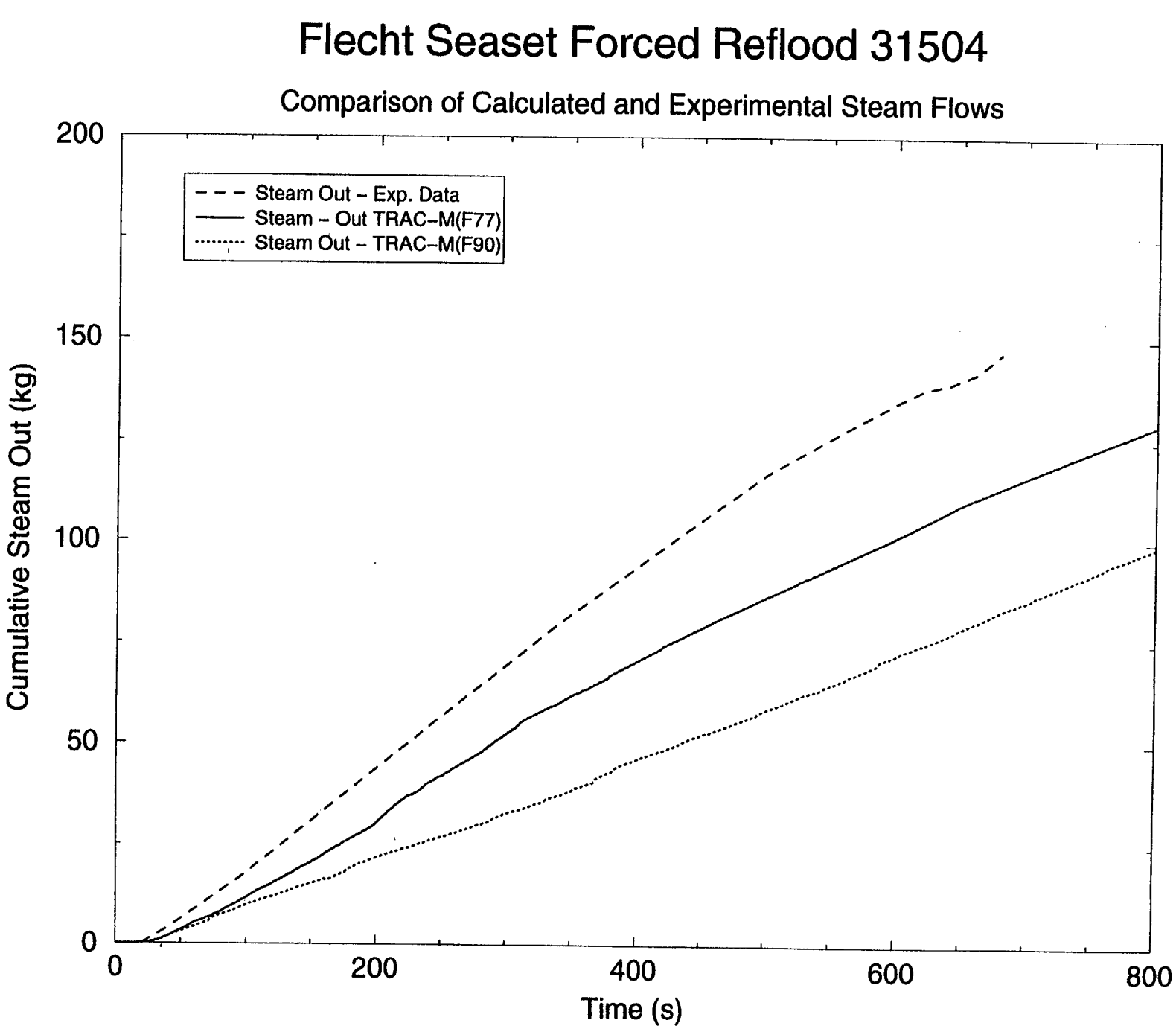

Figure 4.4.35 Comparison of Steam Carryouts

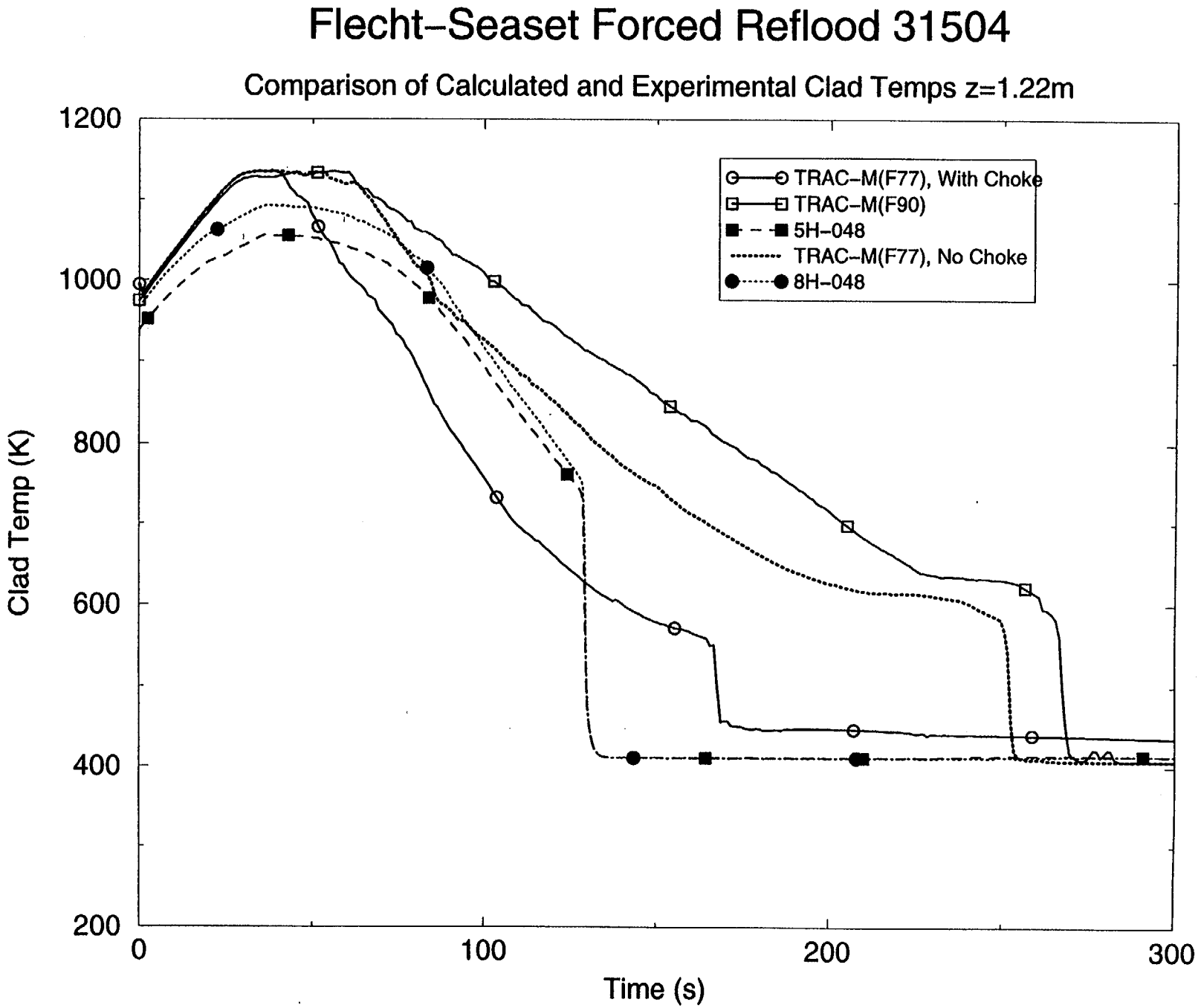

Figure 4.4.36 TRAC-M(F77) Clad Temp. Predictions with and without Choking @ z = 1.22 m

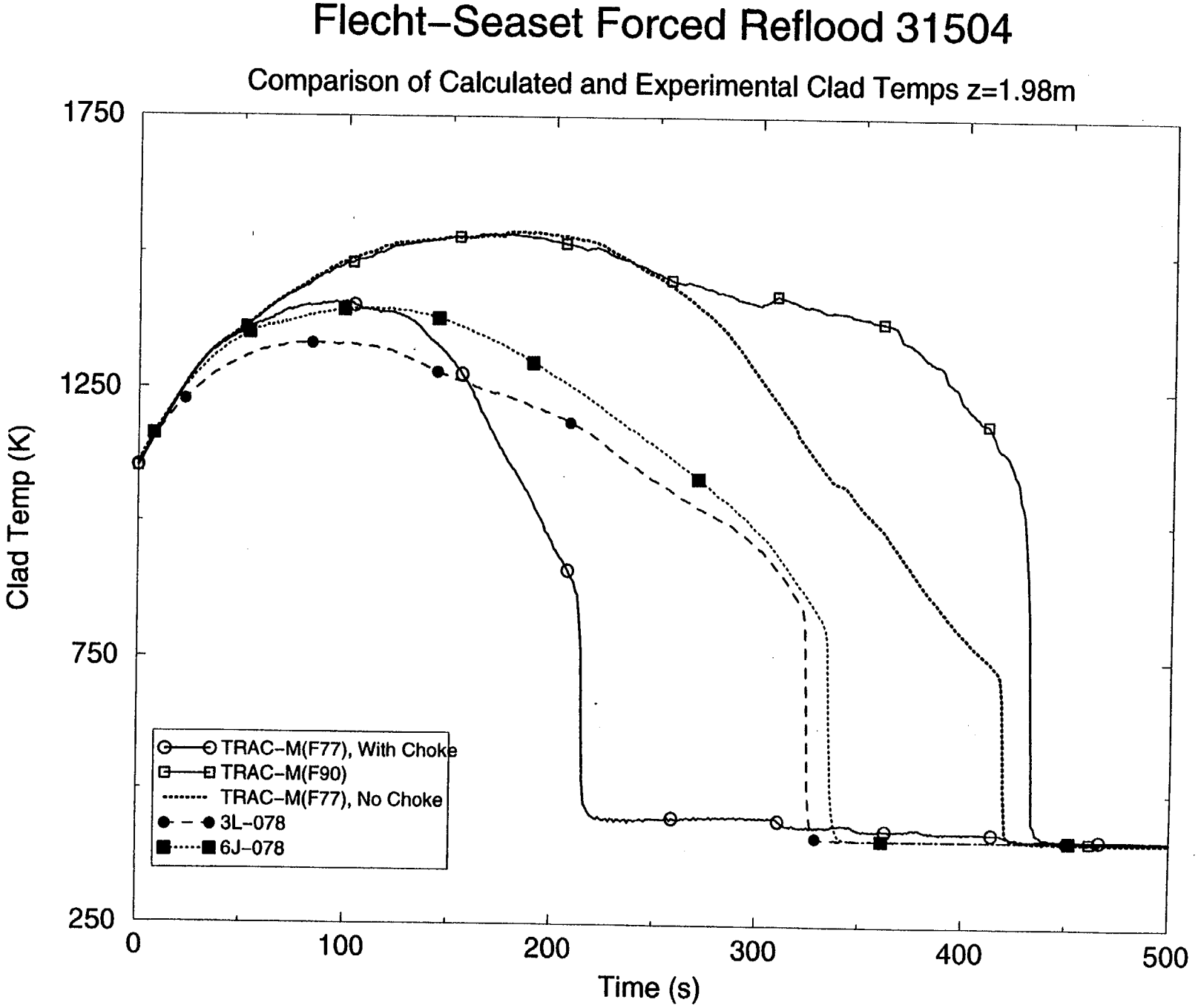

Figure 4.4.37 TRAC-M(F77) Clad Temp. Predictions with and without Choking @ z = 1.98 m

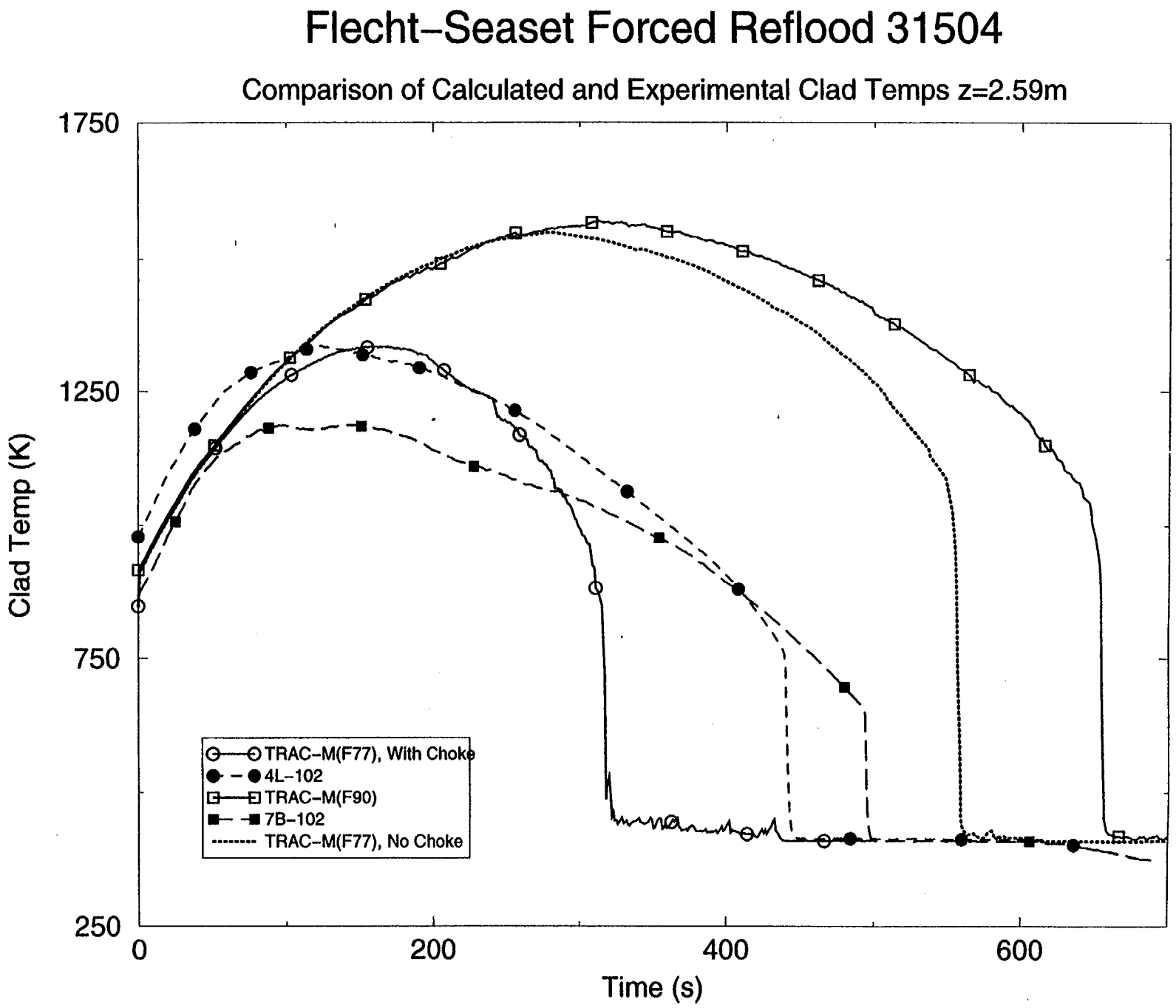

Figure 4.4.38 TRAC-M(F77) Clad Temp. Predictions with and without Choking @ z = 2.59 m

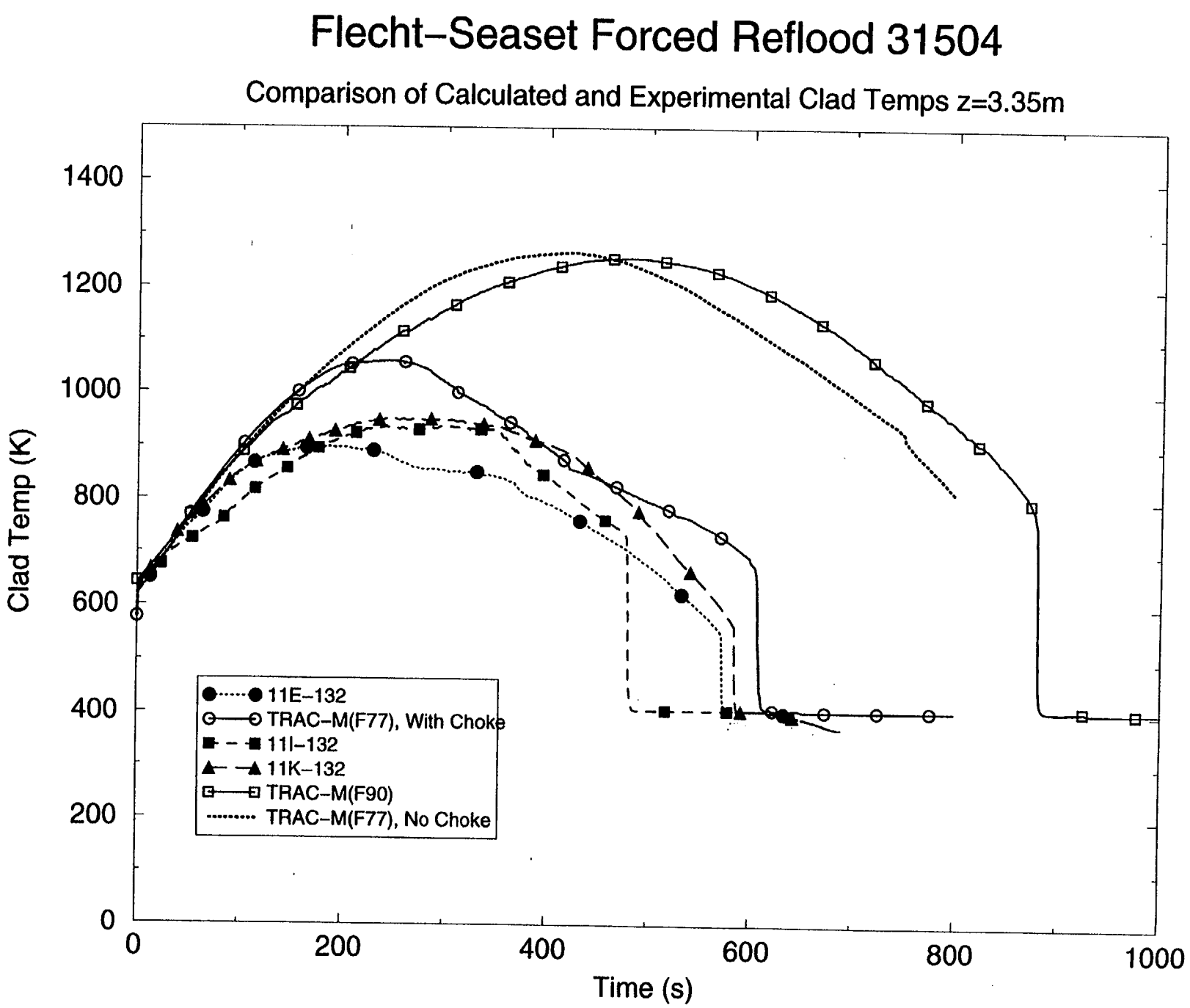

Figure 4.4.39 TRAC-M(F77) Clad Temp. Predictions with and without Choking @ z = 3.35 m

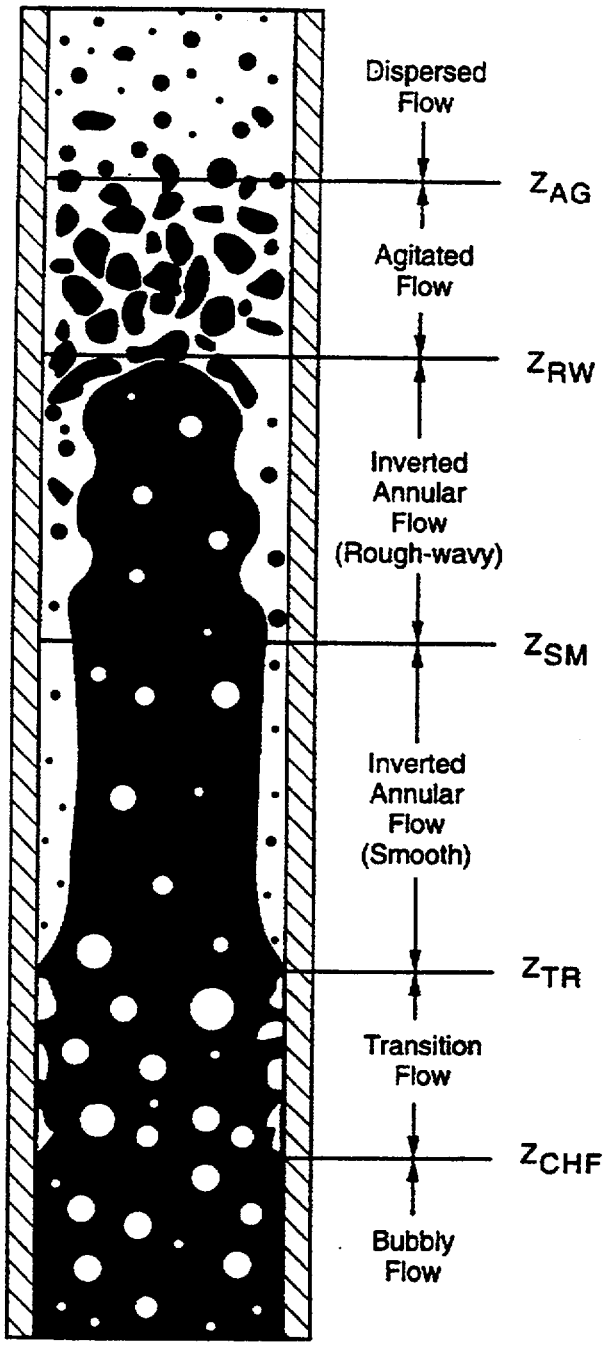

Figure 4.4.40 TRAC-M Reflood Flow Regime Map

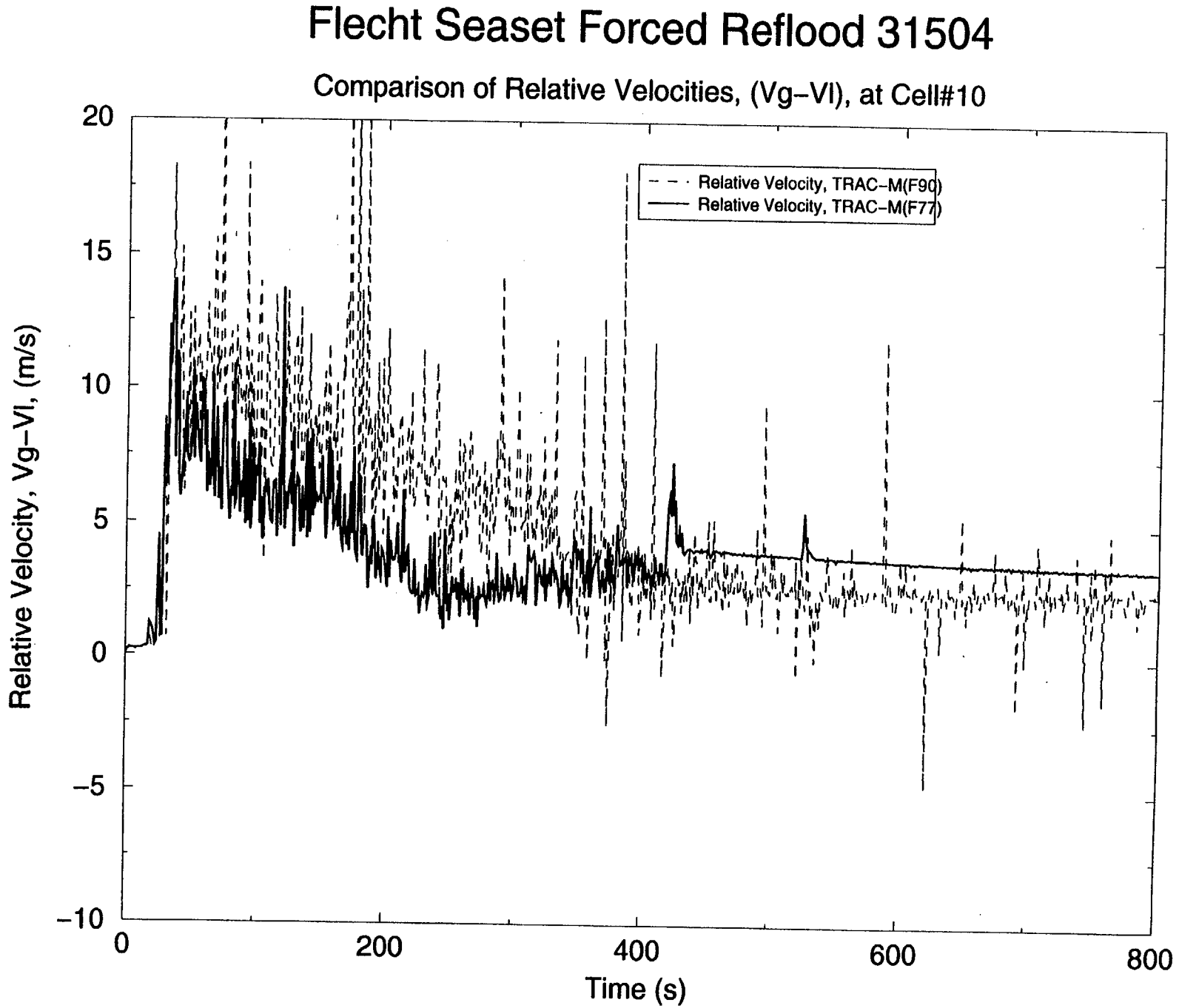

Figure 4.4.41 Calculated Relative Velocities at Cell 10

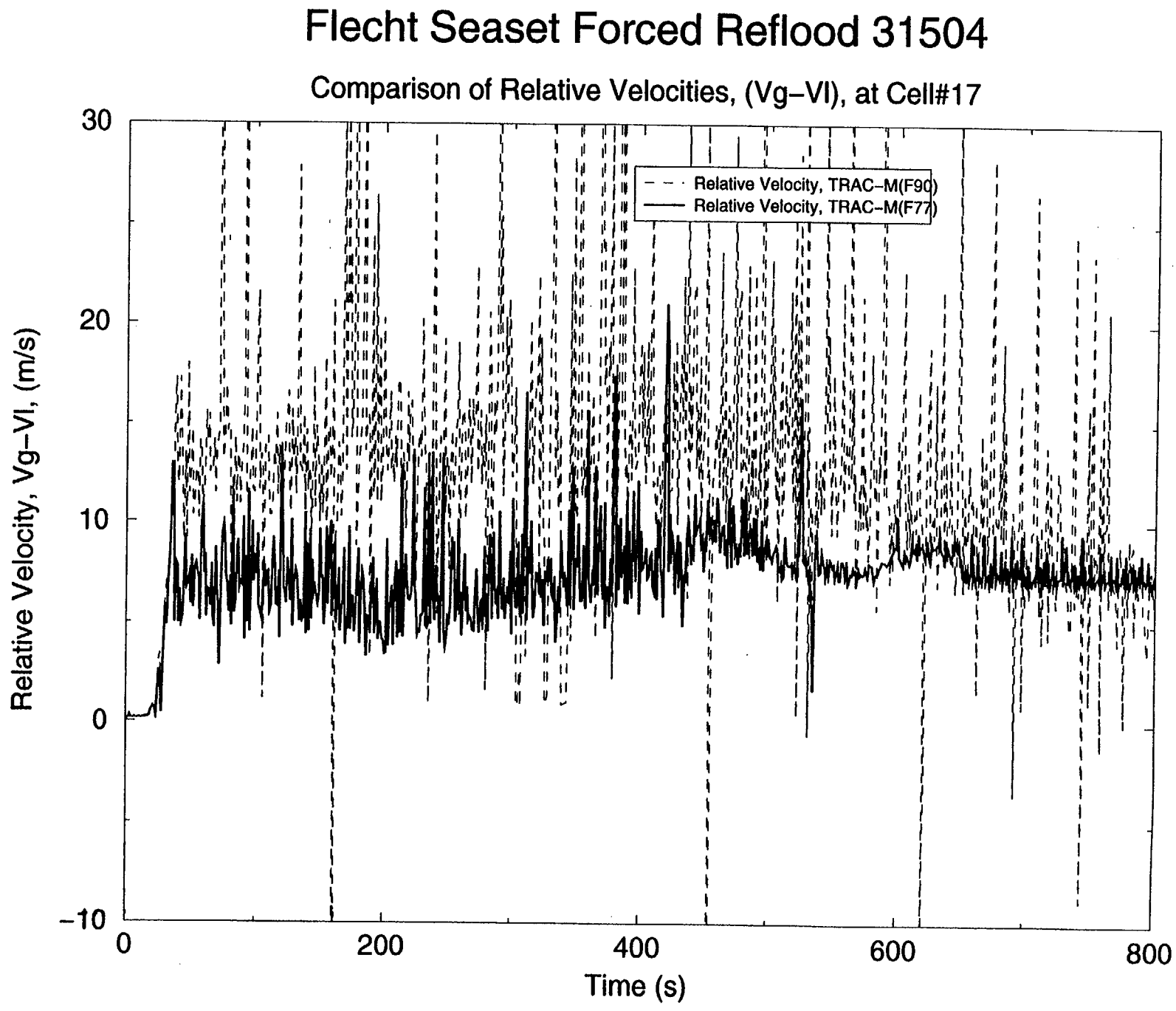

Figure 4.4.42 Calculated Relative Velocities at Cell 17

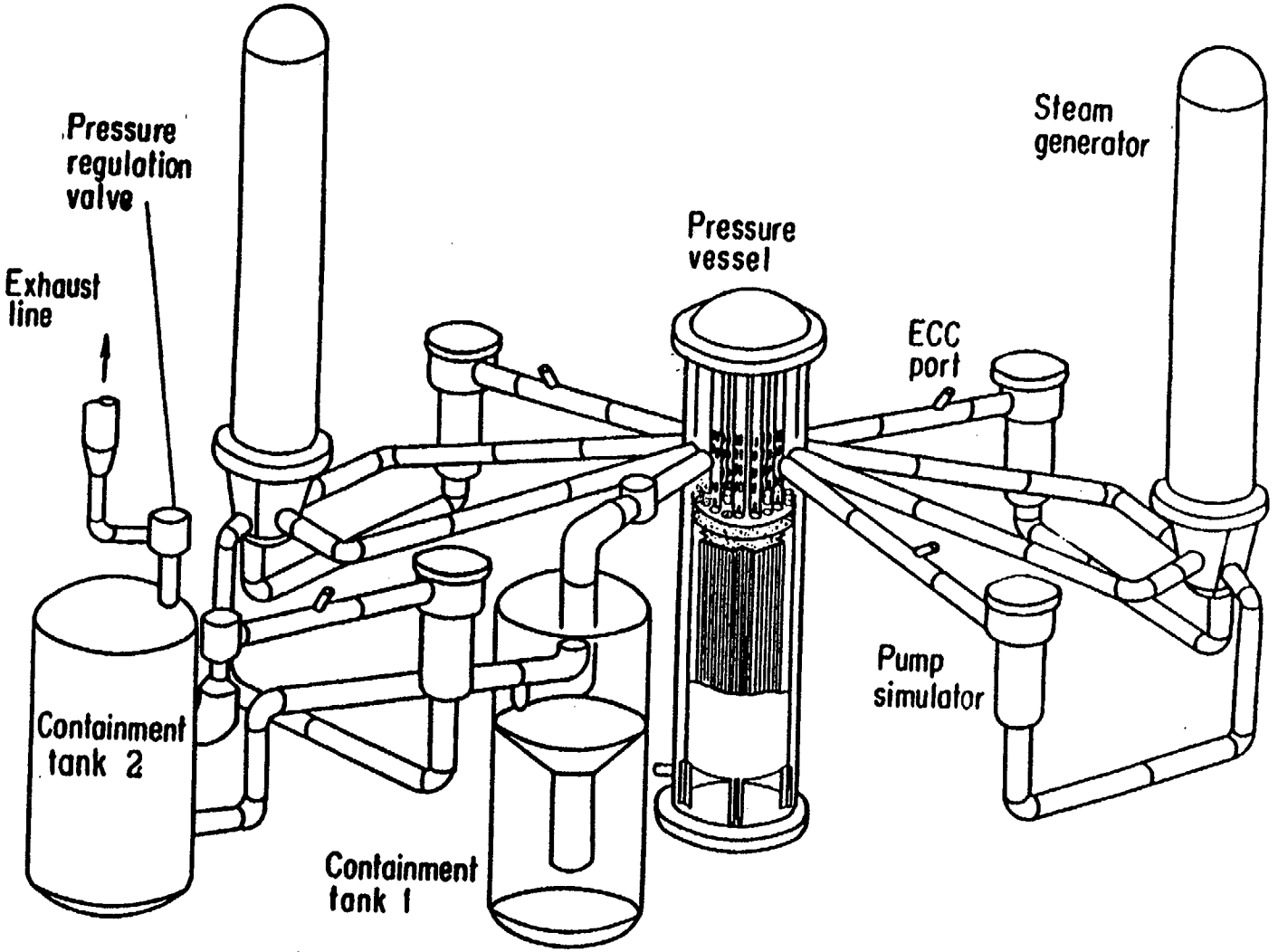

Figure 4.4.43 Isometric View of CCTF

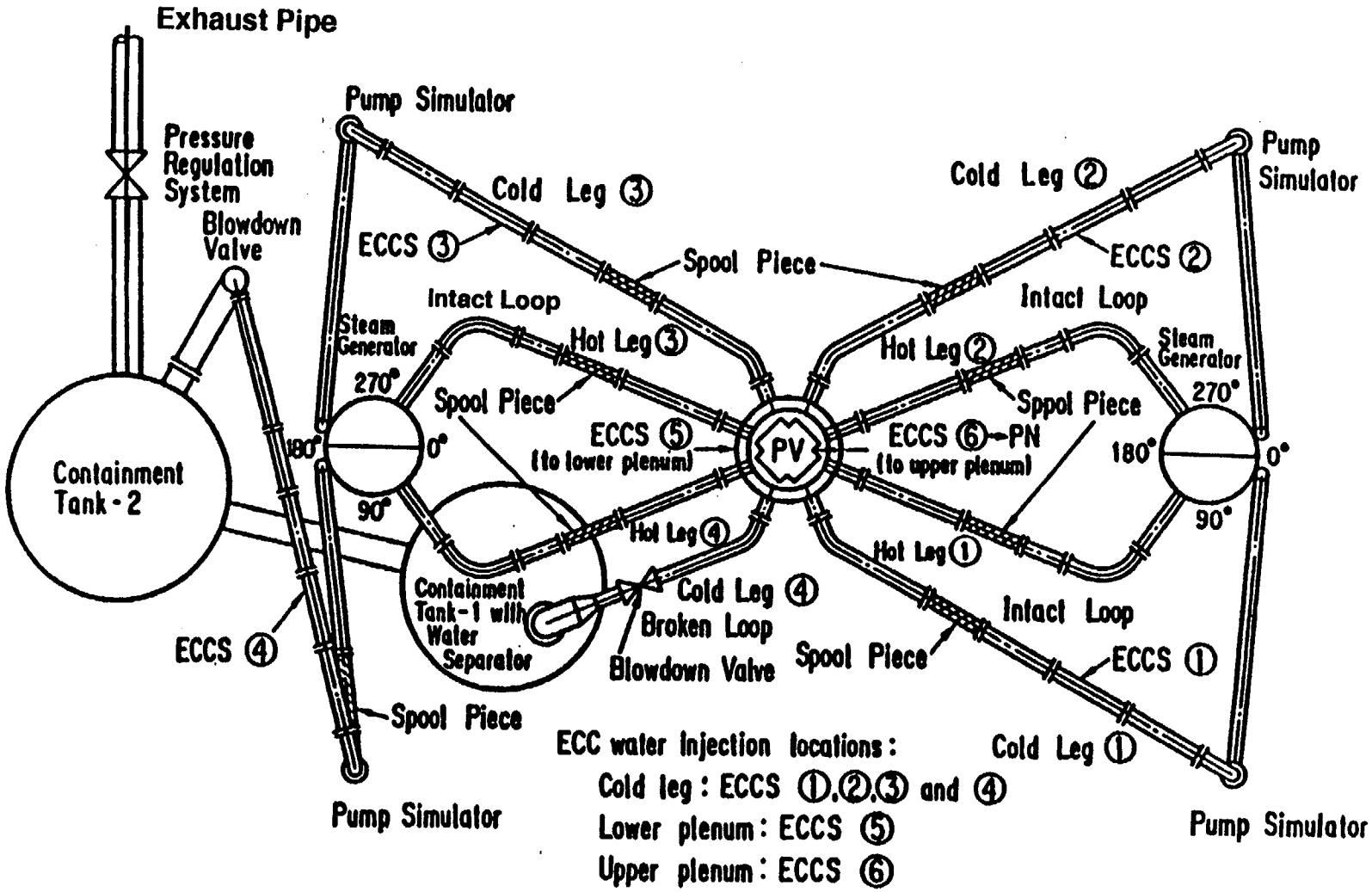

Figure 4.4.44 Top View of Primary-Loop Piping Layout

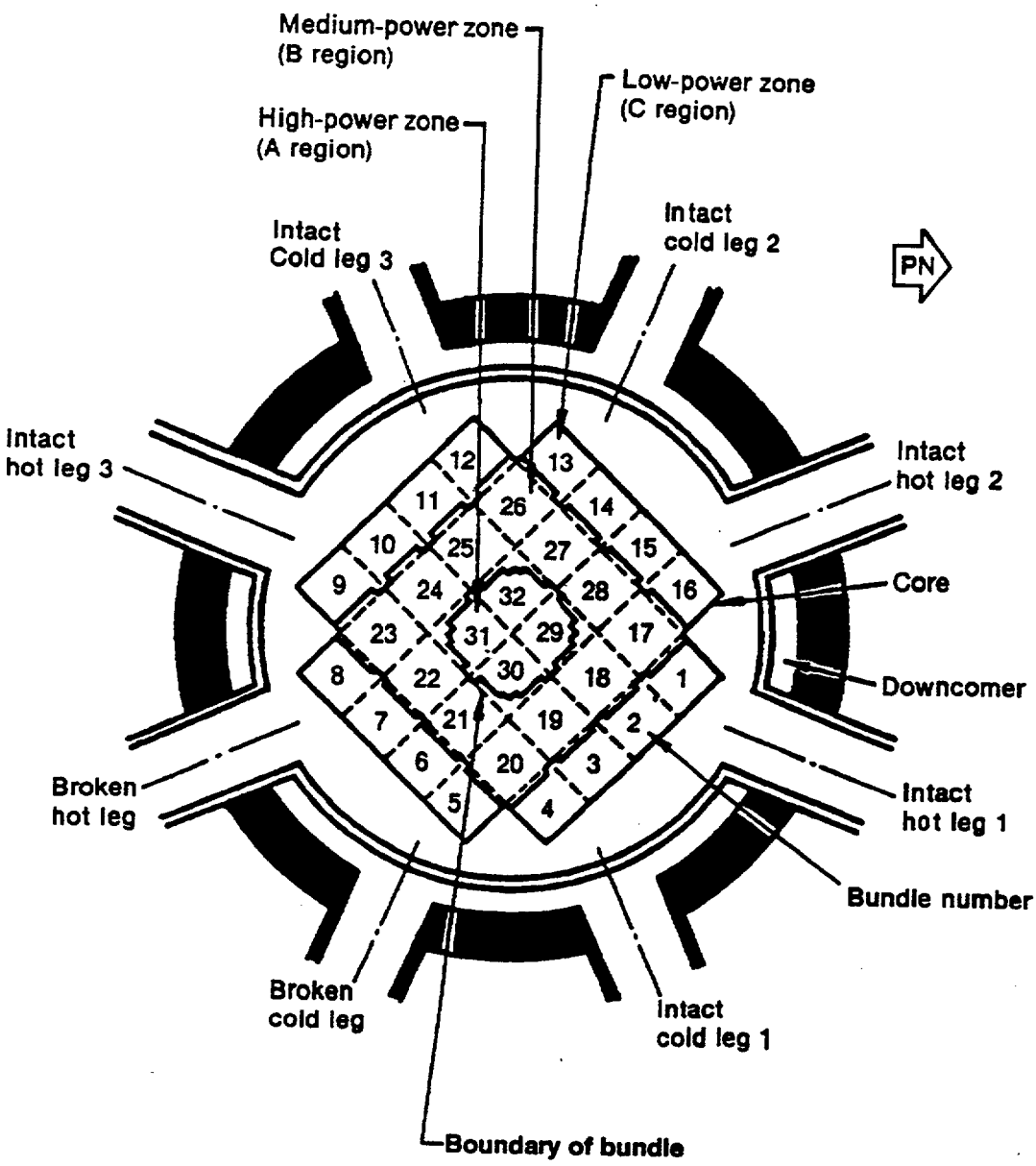

Figure 4.4.45 Cross-Section of the CCTF Pressure Vessel Through the Core-I Vessel Core and Primary-Loop Nozzles

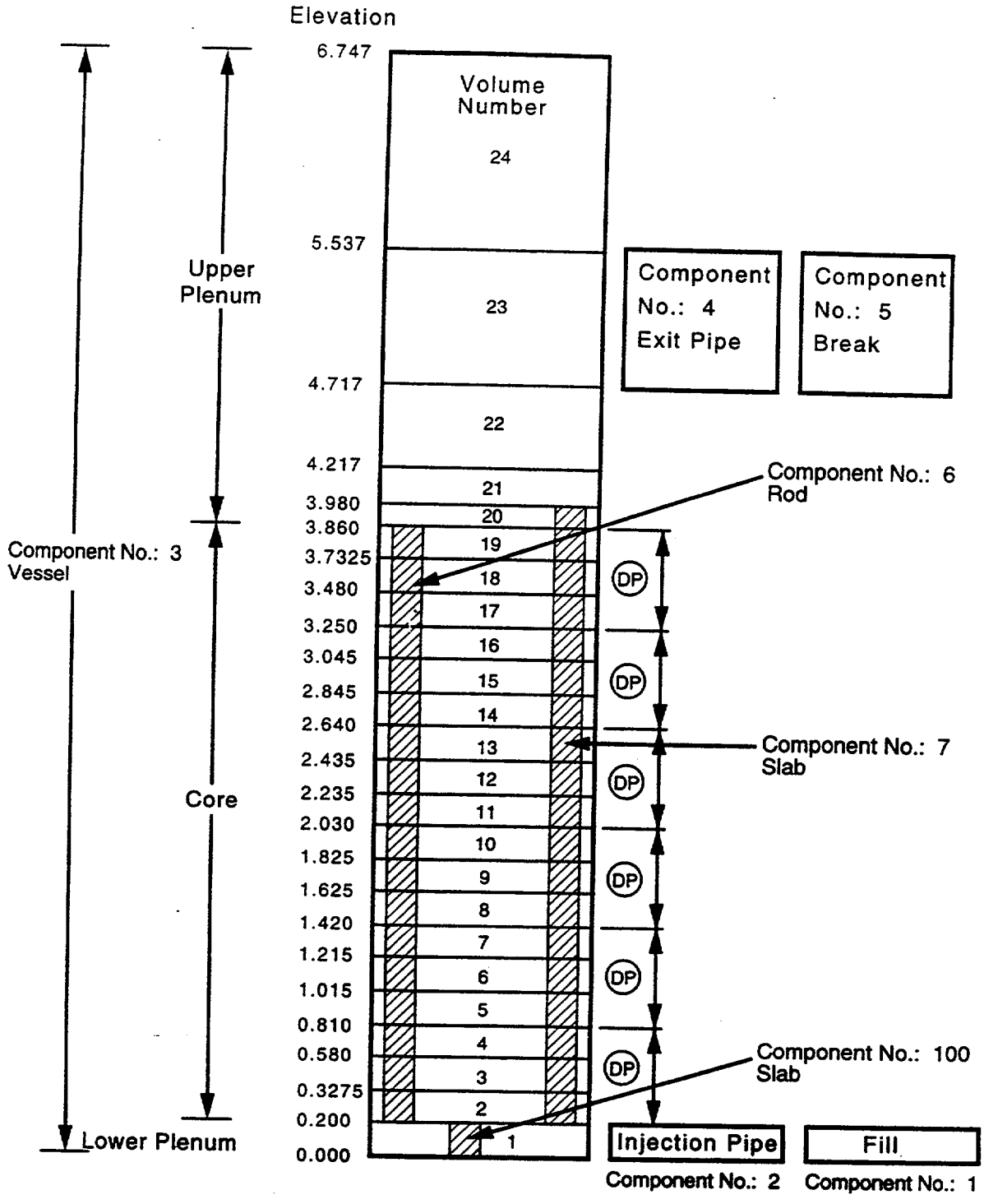

Figure 4.4.46 CCTF Input Model Schematic

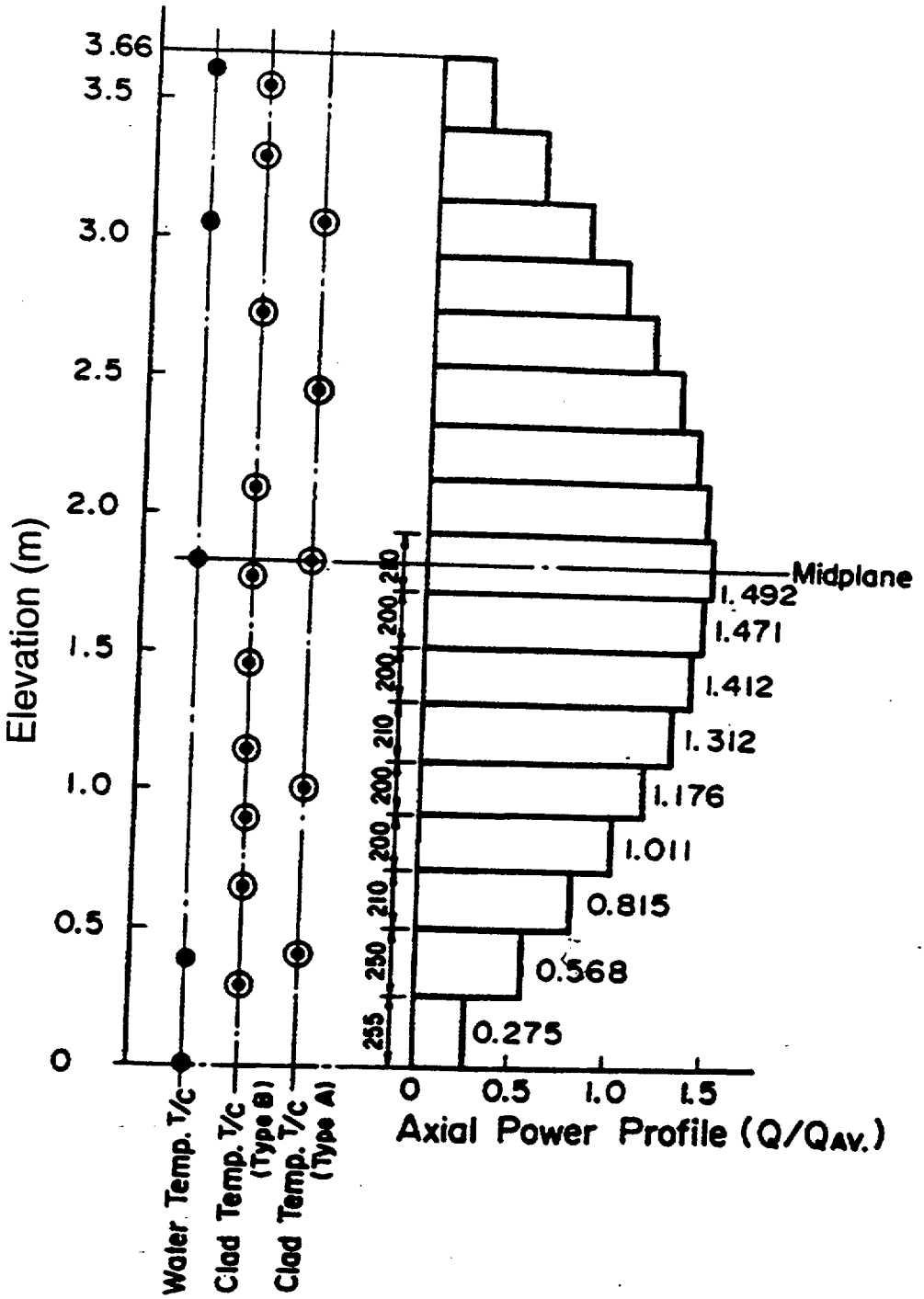

Figure 4.4.47 TRAC Model of the CCTF Run 14 Power Profile and Instrument Locations

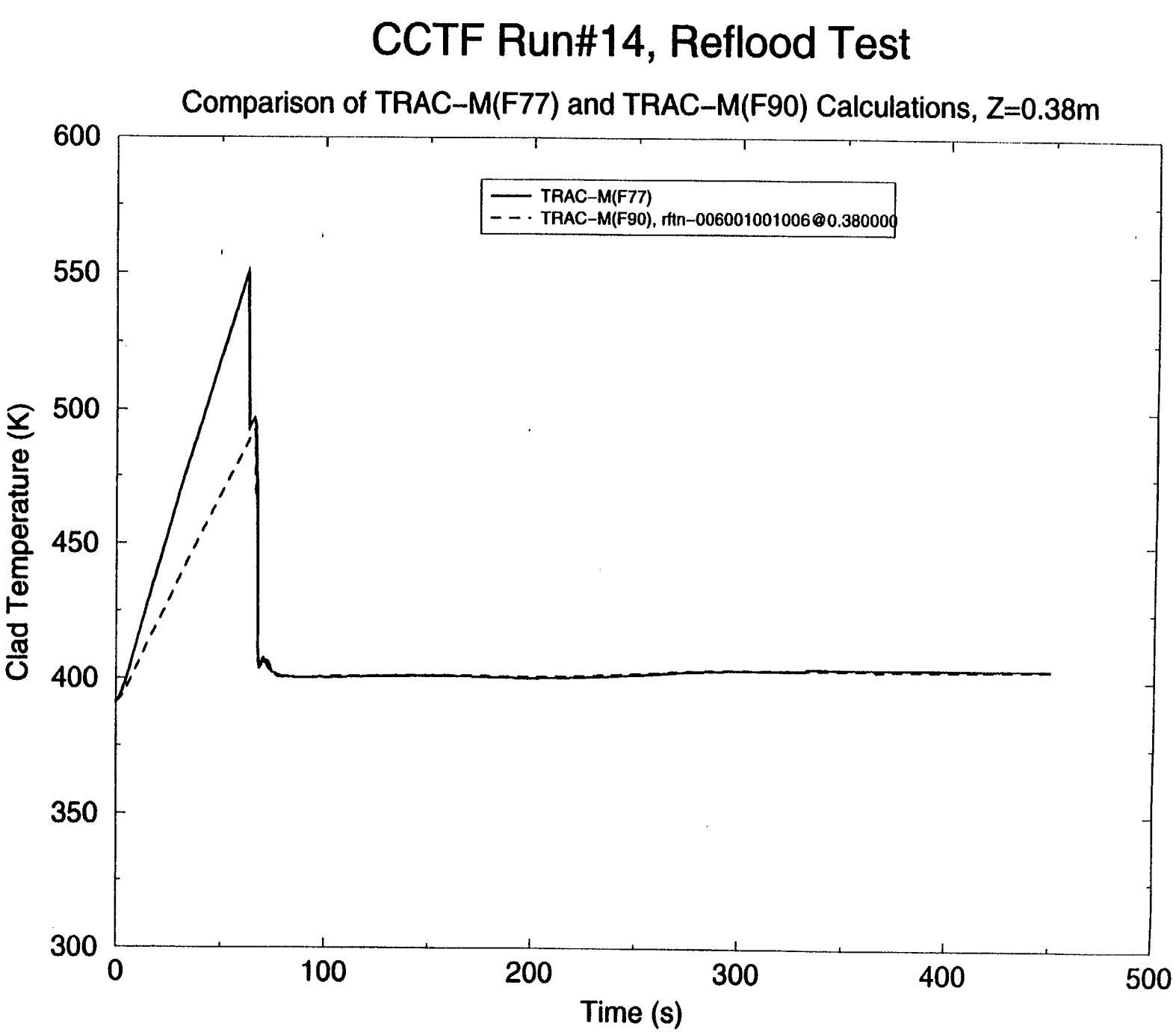

Figure 4.4.48 CCTF Run 14, Reflood Test –
Comparison of TRAC-M(F77) and TRAC-M(F90) Calculations (Z=0.38m)

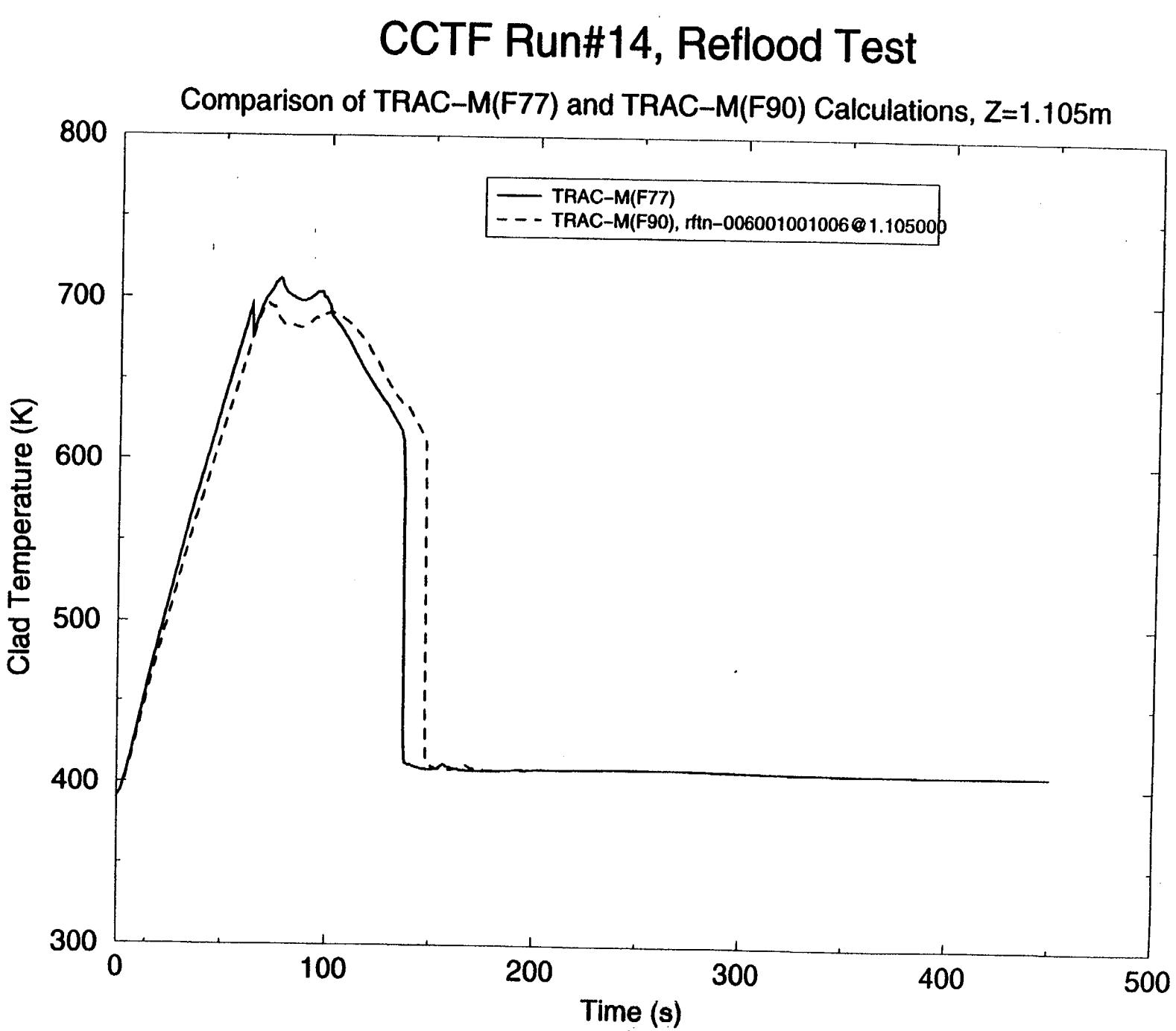

**Figure 4.4.49 CCTF Run 14, Reflood Test –
Comparison of TRAC-M(F77) and TRAC-M(F90) Calculations (Z=1.105m)**

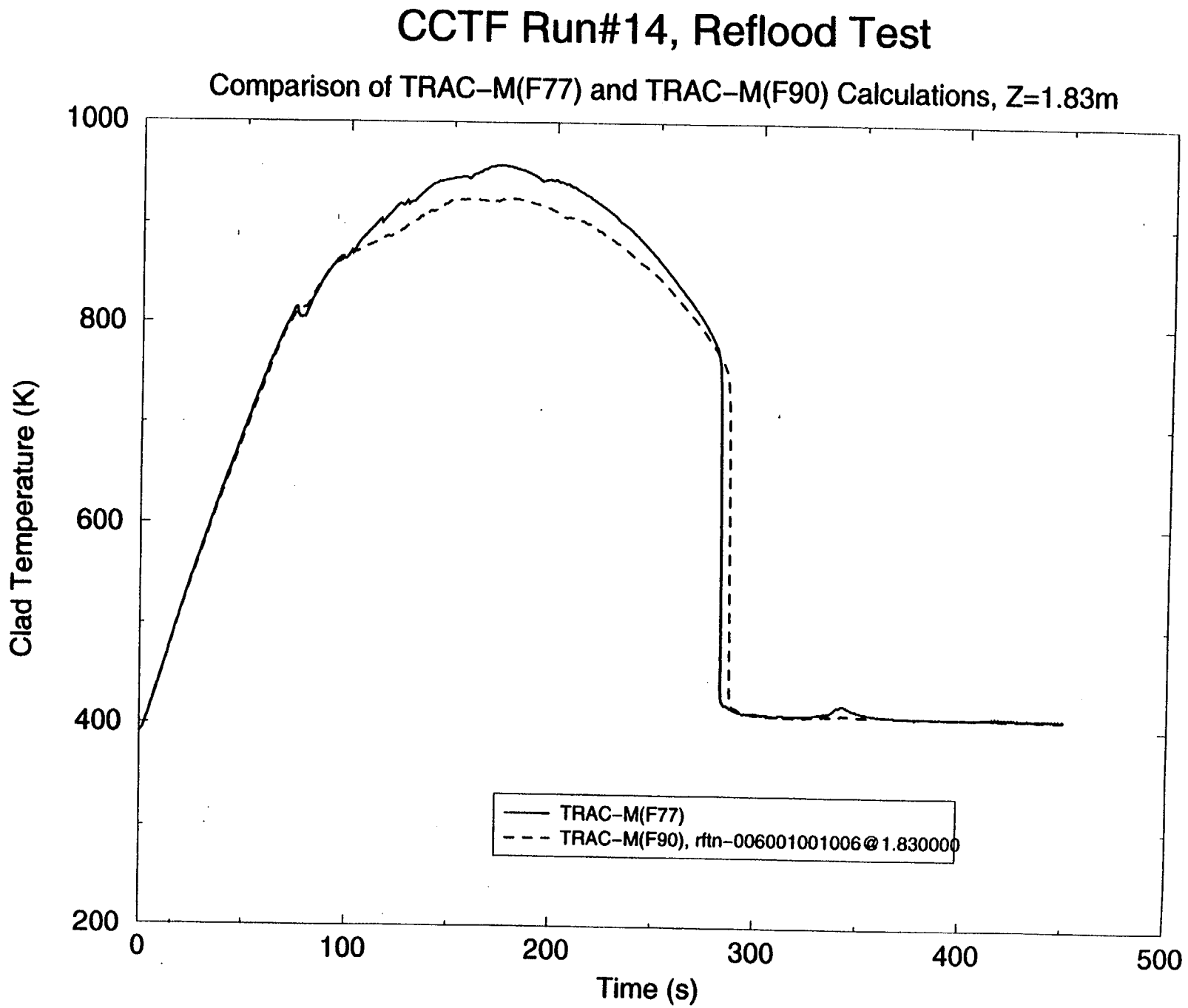

**Figure 4.4.50 CCTF Run 14, Reflood Test –
Comparison of TRAC-M(F77) and TRAC-M(F90) Calculations (Z=1.83m)**

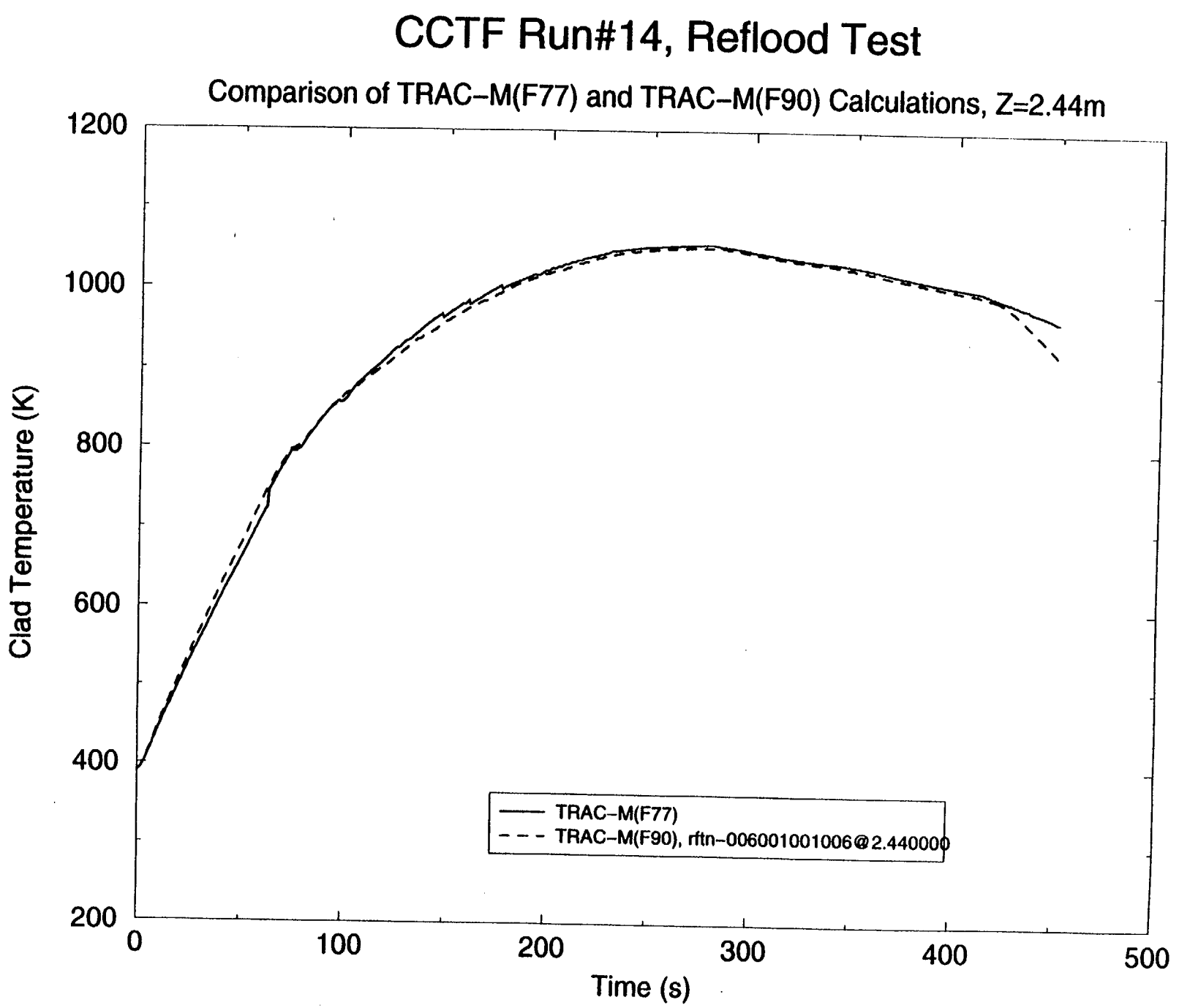

Figure 4.4.51 CCTF Test Run 14, Reflood Test – Comparison of TRAC-M(F77) and TRAC-M(F90) Calculations (Z=2.44m)